2020

Shifty protons and wandering electrons

Eliscia Fought
Iowa State University

Shifty protons and wandering electrons

by

Ellie Lynn Fought
(Eliscia Lynn Fought)

A dissertation submitted to the graduate faculty

in partial fulfillment of the requirements for the degree of

DOCTOR OF PHILOSOPHY

Major: Physical Chemistry

Program of Study Committee:
Theresa Windus, Major Professor
Mark Gordon
Xueyu Song
Levi Stanley
Vincenzo Venditti

The student author, whose presentation of the scholarship herein was approved by the program of study committee, is solely responsible for the content of this thesis. The Graduate College will ensure this thesis is globally accessible and will not permit alterations after a degree is conferred.

Iowa State University

Ames, Iowa

2020

TABLE OF CONTENTS

ACKNOWLEDGMENTS

The final two and a half months of my graduate career have been spent quarantined with my wife and two-year old. Needless to say, this is not how I envisioned this moment. Therefore, let me first say thank you to everyone involved at Iowa State and Ames Laboratory for adapting to this new reality and making this process easier to navigate.

Thank you to all of my committee members, past and present: Malika Jeffries-El, Jason Chen, Vincenzo Venditti, Levi Stanley, Xueyu Song, and Mark Gordon for all of your support. A special thanks to Mark Gordon for your mentorship and endless collection of stories. I would also like to thank all of my collaborators for all the hard work and chemical insight they've displayed. To the current and former members of the Windus Group, I'm grateful for your company and the knowledge and experience you've shared with me. To Annabelle Lolinco, especially, who's become an integral part of my support system, thank you for the comradery and cooking lessons. To all my family and adopted family near and far, you may not know what I do, but you've cheered me on anyway. To Theresa Windus, who's been the best PI that I could have hoped for. I'm very lucky to have had a major professor who was also a mentor and genuinely good human. I'm grateful for your patience, leadership, and knowledge, and I have thoroughly enjoyed my time in your lab. To Megan and Alex, thank you for the love and joy you bring me every day.

Work at the Ames Laboratory was supported by the Department of Energy under Contract No. DE-AC02-07CH11358 and in part by the Air Force Office of Scientific Research under the AFOSR award FA9550-12-1-0476. The Ames Laboratory is operated

for the DOE by Iowa State University. The document number assigned to this dissertation is IS-T 3272. Detailed funding information for specific projects is included in each chapter's acknowledgement section.

ABSTRACT

Møller-Plesset second order perturbation theory (MP2) is one of the most widely used electron correlation methods in computational chemistry. The rising cost of computing demands that computational chemists develop novel cost-saving strategies to reduce the time and energy associated with the most widely used methods in the field. Multiple studies are presented evaluating the effects of two particular strategies (dynamic voltage and frequency scaling and oversubscription) when used with specific MP2 algorithms. Additionally, a collection of experimental collaborations is presented covering a wide range of chemical topics, including organic synthesis, stereochemistry of 1,2-masked diols, nuclear magnetic resonance characterization of silicon nanocrystals, and inorganic catalysis involving cobalt.

CHAPTER 1: INTRODUCTION

General Introduction

Over the last three decades, there have been dramatic improvements in both computing power and data storage capacity. With this increase in computational power, the field of computational chemistry has emerged as a fundamental discipline in the field of chemistry as a whole. Upgrades in computer hardware have led to the use of higher accuracy methods with larger and larger chemical systems. Computational chemists are uniquely situated between computer science and chemistry, and this relationship is reflected throughout this dissertation.

The chemistry side of computational chemistry often comes in the form of collaborations with experimentalists both inside and outside the chemical sciences. The computational chemistry presented in this dissertation is primarily governed by quantum mechanics which can be used to calculate numerous molecular properties. The role of computational chemists in these collaborations is three-pronged: corroboration, explanation, and prediction. Through electronic structure and molecular properties calculations, computational chemists can reinforce data obtained by several experimental characterization methods such as X-ray crystallography and infrared (IR) spectroscopy. There are also several computational methods that provide information not readily obtained in a laboratory, such as the structure of a transition state or the shape of the molecular orbitals. Computational chemistry has gained significant attention as a predictive technique in several different industries, most prominently pharmaceuticals

and mining, improving the efficiency of synthesis in the lab and simultaneously reducing financial and environmental costs.

A major consideration throughout the computational sciences is the energy costs associated with powering and cooling the computer hardware. As a consequence, computational chemists strive to develop faster and more energy efficient methods. Computer science is one avenue for computational chemists to achieve these goals, providing a variety of tools and techniques for analyzing hardware and software. Through this analysis, a better understanding is gained of how the hardware is utilized during execution of various chemistry algorithms. This knowledge can then be applied to development of or experimentation with novel computer science methods with the goal of reducing execution times and improving energy efficiency.

Quantum Mechanics

A key tenet of quantum mechanics is the wave-particle duality of matter. All objects, large and small, are subject to this wave-particle duality, but only at the atomic and subatomic scales does it become necessary to take this principle into account. By treating subatomic particles, such as electrons, like waves, one may use a wavefunction to obtain crucial information about the object such as energy, momentum, and shape of the orbitals in which they reside. A system's wavefunction is often defined as

$$\Psi(\boldsymbol{r}, \boldsymbol{R}, t) = \psi(\boldsymbol{r}, \boldsymbol{R})\phi(t) \quad (1)$$

where $\psi(\boldsymbol{r}, \boldsymbol{R})$ is a function of space, and $\phi(t)$ is a function of time t. Absent the presence of a time-dependent potential acting on the system, the total wavefunction can be simplified as a function of only the electronic ($\boldsymbol{r}$) and nuclear ($\boldsymbol{R}$) coordinate vectors,

written as $\Psi(\boldsymbol{r}, \boldsymbol{R})$. Another tenet of quantum mechanics is the quantization of bound systems. In other words, observable quantities, such as energy and momentum, are only found at discrete levels. Determining a system's observables can be achieved using the observable's corresponding linear operator ($\hat{A}$) in an eigenvalue equation such as

$$\hat{A}\Psi(\boldsymbol{r}, \boldsymbol{R}) = A\Psi(\boldsymbol{r}, \boldsymbol{R}) \tag{2}$$

When operator $\hat{A}$ acts upon the wavefunction, the wavefunction is returned along with an eigenvalue (A), which represents the observable of interest. The most relevant (widely used/applicable) observable, energy, for a time-independent wavefunction is determined using the time-independent Schrödinger equation (TISE),[1]

$$\hat{H}\Psi(\boldsymbol{r}, \boldsymbol{R}) = E\Psi(\boldsymbol{r}, \boldsymbol{R}) \tag{3}$$

where $\hat{H}$ is the Hamiltonian operator, and E is the total energy of the system. The molecular Hamiltonian is comprised of five terms:

$$\hat{H} = \hat{T}_e + \hat{T}_n + \hat{V}_{en} + \hat{V}_{ee} + \hat{V}_{nn}. \tag{4}$$

The first term is the electronic kinetic energy (in atomic units), defined as

$$\sum_{i=1}^{N} \frac{-\nabla_i^2}{2} \tag{5}$$

and is summed over N electrons. The second term in (4) is the nuclear kinetic energy,

$$\sum_{A=1}^{K} \frac{-\nabla_A^2}{2M_A}, \tag{6}$$

summed over K nuclei, each with a known mass M_A. In equations (5) and (6), ∇^2 is the Laplacian operator, where

$$\nabla^2 \equiv \frac{\partial}{\partial x^2} + \frac{\partial}{\partial y^2} + \frac{\partial}{\partial z^2}. \tag{7}$$

The third term in (4) is the electron-nuclear attraction

$$\sum_{i=1}^{N}\sum_{A=1}^{K}\frac{-Z_A}{|\boldsymbol{r}_i-\boldsymbol{R}_A|} \tag{8}$$

with nuclear charge Z_A, electronic coordinates $\boldsymbol{r}_i$, and nuclear coordinates $\boldsymbol{R}_A$. The fourth and fifth terms in (4) are the electron-electron repulsion

$$\sum_{i=1}^{N}\sum_{j>i}^{N}\frac{1}{|\boldsymbol{r}_i-\boldsymbol{r}_j|} \tag{9}$$

and the nuclear-nuclear repulsion

$$\sum_{A=1}^{K}\sum_{B>A}^{K}\frac{Z_A Z_B}{|\boldsymbol{R}_A-\boldsymbol{R}_B|}, \tag{10}$$

respectively. Equation (3) can be simplified by removing the electron-nuclear coupling using the Born-Oppenheimer approximation[2], also known as the adiabatic approximation. The mass of the nucleus is so much greater than the mass of the electron that it can be assumed that nuclei are stationary due to an electron's ability to instantaneously adjust to any nuclear motion. This assumption results in (6) being equal to zero, (8) being only parametrically dependent on the nuclear coordinates $\boldsymbol{R}$, and (10) becoming a constant, E_{nuc}. Therefore, the Hamiltonian operator becomes a function of only the electronic coordinates,

$$\hat{H}_{el} = \hat{T}_e + \hat{V}_{en} + \hat{V}_{ee}, \tag{11}$$

and when operating on the electronic wavefunction, Ψ_{el}, the electronic energy is obtained

$$\hat{H}_{elec}\Psi_{elec} = E_{elec}\Psi_{elec}. \tag{12}$$

The total energy can then be found by adding the nuclear energy (found using (10))

$$E_{tot} = E_{elec} + E_{nuc}. \tag{13}$$

Hartree-Fock

The Hartree-Fock (HF) method[3] is the standard algorithm for beginning to solve the time-independent Schrödinger equation. The original Hartree method[3a, b] employed a wavefunction consisting of a simple product of one-electron functions,

$$\phi_1(\boldsymbol{r}_1)\phi_2(\boldsymbol{r}_2)\phi_3(\boldsymbol{r}_3)...\phi_N(\boldsymbol{r}_4) \tag{14}$$

where each $\phi_i(\boldsymbol{r}_i)$ contains both a spatial component and spin component. These one-electron orbital functions are derived from a chosen basis set, described in further detail later in this chapter. However, (14) does not satisfy the requirement that the wavefunction be antisymmetric upon exchange of the electrons per the Pauli Exclusion principle, so a more appropriate wavefunction is necessary.[4] The key difference between the Hartree method and HF is the use of a Slater determinant[6]

$$\Psi_{HF} = \frac{1}{\sqrt{N!}}\begin{vmatrix} \phi_1(\boldsymbol{r_1}) & \phi_2(\boldsymbol{r_1}) & \dots & \phi_N(\boldsymbol{r_1}) \\ \phi_1(\boldsymbol{r_2}) & \phi_2(\boldsymbol{r_2}) & \dots & \phi_N(\boldsymbol{r_2}) \\ \vdots & \vdots & \ddots & \vdots \\ \phi_1(\boldsymbol{r_N}) & \phi_2(\boldsymbol{r_N}) & \dots & \phi_N(\boldsymbol{r_N}) \end{vmatrix} \tag{15}$$

for a wavefunction, which is, indeed, antisymmetric upon exchange.

HF is an iterative method rooted in the variational principle, meaning that energies found with HF will always be greater than or equal to the exact energy, E_0. The HF process involves iteratively minimizing the energy of each one-electron orbital in the averaged potential of the remaining electrons. Minimization is achieved using the HF equations of the form

$$\hat{F}(\boldsymbol{r_1})\phi_i(\boldsymbol{r_1}) = \varepsilon_i\phi_i(\boldsymbol{r_1}) \tag{16}$$

where ε_i is the energy of the *i*th orbital, and $\hat{F}$ is the Fock operator. The Fock operator is defined as

$$\hat{F}(\boldsymbol{r_1}) = \frac{\nabla_1^2}{2} + \sum_A^K \frac{-Z_A}{|\boldsymbol{r_1} - \boldsymbol{R}_A|} + \sum_{j=1}^{N/2} [2\hat{J}_j(\boldsymbol{r_1}) - \hat{K}_j(\boldsymbol{r_1})] \tag{17}$$

where $\hat{J}$ and $\hat{K}$ are the Coulomb and exchange operators, respectively, and are defined as

$$\hat{J}_j(\boldsymbol{r_1})\phi_i(\boldsymbol{r_1}) = \left(\int \phi_j^*(\boldsymbol{r_2}) \frac{1}{|\boldsymbol{r_1} - \boldsymbol{r_2}|} \phi_j(\boldsymbol{r_2}) d\boldsymbol{r_2} \right) \phi_i(\boldsymbol{r_1}) \tag{18}$$

$$\hat{K}_j(\boldsymbol{r_1})\phi_i(\boldsymbol{r_1}) = \left(\int \phi_j^*(\boldsymbol{r_2}) \frac{1}{|\boldsymbol{r_1} - \boldsymbol{r_2}|} \phi_i(\boldsymbol{r_2}) d\boldsymbol{r_2} \right) \phi_j(\boldsymbol{r_1}) \tag{19}$$

The Coulomb operator, $\hat{J}_j$, describes the repulsion due to electron *j*. The exchange operator is a permutation operator with no physical analog and results from the antisymmetric nature of the HF wavefunctions.[5]

As stated earlier, the HF energy, E_{HF}, is the upper bound for the exact ground state energy E_0. The HF limit is the best possible energy determined when using HF and is approached as the basis set becomes sufficiently complete. Since HF neglects the instantaneous repulsions between electrons and only calculates the average repulsive effects, a small (but not insignificant) energy, known as the correlation energy, is unaccounted for. The correlation energy is defined as

$$E_{corr} \equiv E_{HF} - E_0 \tag{20}$$

E_{corr} typically represents less than 1 percent of the total energy but is necessary for accurately describing chemical phenomena such as bond dissociation and dispersion effects.[5]

Basis Sets

Computational chemists use basis sets to build the Slater determinant wave functions used in HF calculations and beyond. In a quantum chemistry context, a basis

set is usually a set of one-electron functions used to build atomic and molecular orbitals. The smallest basis set (minimal basis) uses a single function to represent each atomic orbital (AO) but is very rarely used due to accuracy issues. All other basis sets use linear combinations of multiple functions to represent each atomic orbital. Linear combinations of atomic orbitals (LCAOs) are then used to generate molecular orbitals (MOs) for anything beyond a single atom. MOs have the form

$$\phi_i = \sum_{\mu} C_{\mu i} \chi_{\mu} \tag{21}$$

with each MO, ϕ, written as an expansion of AOs, χ, each with coefficient C. In chemistry, the two most common types of functions used to build basis sets are Slater-type orbitals (STOs) and Gaussian-type orbitals (GTOs). Slater-type functions are written as

$$\phi_{abc}^{STO}(x, y, z) = N x^a y^b z^c e^{-\zeta r} \tag{22}$$

where N is a normalization constant, the sum of a, b, and c represents the angular momentum, ζ is the orbital exponent, and r is the distance from the nucleus. STOs perform well, describing both short- and long-range behavior of the electrons (i.e., useful very close to or very far from the nucleus) but are computationally expensive.

A more computationally efficient method is to substitute STOs with linear combinations of GTOs, which have the form

$$\phi_{abc}^{GTO}(x, y, z) = N x^a y^b z^c e^{-\zeta r^2} \tag{23}$$

with an r^2 in the exponential instead of r.[6] The use of GTOs reduces the time required to calculate the necessary integrals, but GTOs are not as well-behaved close to or very far from the nucleus. Thus, multiple GTOs are required to represent a single STO and accuracy generally improves as the number of GTOs (or primitives) in each linear

combination increases. In addition to simply increasing the number of primitives, it is common for chemists to use "split-valence" basis sets, where multiple functions are used to represent the valence orbitals. The valence basis functions can then be improved further by the addition of polarization or diffuse functions. Polarization functions increase the directionality of an orbital, more accurately describing interactions. Diffuse functions give an electron more space and are particularly useful for cases such as anions where the effective nuclear charge is reduced.[7]

The most common split-valence basis sets were created by Pople et al.[8] Pople basis sets are identified using the notation X-YZG: X denotes the number of GTOs representing each core orbital, and Y and Z represent two individual basis functions with linear combinations of Y and Z GTOs, respectively, for the valence orbitals. The addition of a (*) at the end of a basis set name indicates the addition of polarization functions. When including polarization functions, the first (*) indicates the addition of *d* orbitals to heavy atoms and the second (*) adds *p* orbitals to light (H/He) atoms. The addition of polarization functions can also be written as X-YZG(d)/(d,p). As with polarization functions, when adding diffuse functions to heavy atoms, a single (+) is added before the G, with an additional (+) for light atoms, as well. The two most common Pople sets used in this work are 6-311G(d,p) used in Chapters 6 and 7, and 6-311+G(d) used in Chapters 9 and 10.[9] Both 6-311 basis sets would be referred to as a triple-zeta basis due to the 3 individual basis functions used to describe the valence electrons.

Another popular collection of basis sets seen throughout the following chapters was developed by Dunning and coworkers.[10] Unlike the Pople sets, which are optimized

using HF, the Dunning "correlation consistent" basis sets are optimized using configuration interaction singles and doubles (CISD). Dunning basis sets are known by their acronyms cc-pVXZ (X = D,T,Q,5,6) which means correlation consistent polarized Valence [Double/Triple/Quadruple/Quintuple/ Sextuple] Zeta. Each step up from double to triple, and so on, increases each type of function by one and adds a new higher order polarization function. Additionally, the cc-pVXZ basis sets can be augmented by adding diffuse functions, and this is notated using the prefix aug-. The most common Dunning basis sets used throughout this work are cc-pVTZ[10] as seen in Chapters 3 and 4, and aug-cc-pVTZ[11] used in multiple chapters, most notably when calculating NMR chemical shifts. For a much more comprehensive take on basis sets, the reader is directed to Frank Jensen's *Introduction to Computational Chemistry-Second Edition*,[12] as well as, Davidson and Feller (1986).[7]

Density Functional Theory

Throughout Chapters 5-10 many calculations were performed using density functional theory (DFT). DFT was introduced by Hohenberg and Kohn in 1964 as an alternative first-principles approach to quantum mechanics.[13] By knowing the exact ground state electron probability density (ρ_0), a function of only three variables (x, y, and z), they proved that one can calculate the exact ground state energy (E_0), wavefunction, and other molecular properties. In other words, the energy (as well as other properties) is a functional of the density function ρ_0,

$$E_0 = E_v[\rho_0] \tag{24}$$

where ν highlights the dependence of E_0 on some external potential $\nu(\boldsymbol{r})$. A functional is simply a function of functions–the input is a function, and the output is a number. Additionally, Hohenberg and Kohn proved that DFT is variational for density functions satisfying two conditions: integration of the trial density function (ρ_t) over all space is equal to the total number of electrons and $\rho_t(\boldsymbol{r}) > 0$. Thus, the lower bound of the energy is the exact ground state energy, $E_0 \leq E_\nu[\rho_t(\boldsymbol{r})]$. While Hohenberg and Kohn proved the theoretical feasibility of DFT, they provided no instruction for how to actually use it.

In 1965, Kohn and Sham provided the first practical method for determining ρ_0 and, consequently, E_0.[14] This is accomplished by first constructing a reference system of *n* noninteracting electrons each experiencing the same external potential, $\nu(\boldsymbol{r})$. The potential $\nu(\boldsymbol{r})$ is defined such that the reference system's density, $\rho(\boldsymbol{r})$, is equal to the exact ground state density $\rho_0(\boldsymbol{r})$. The DFT energy functional can then be written as

$$E_{DFT}[\rho] = T_S[\rho] + E_{\mathrm{ne}}[\rho] + J[\rho] + E_{\mathrm{xc}}[\rho] \tag{25}$$

where T_S is the exact kinetic energy functional, E_{ne} is the nuclear-electronic potential functional, J is the Coulombic potential functional, and E_{xc} is the exchange-correlation energy functional.[12] In theory, this equation would yield the exact solution, but the identity of the universal exchange-correlation functional, $E_{\mathrm{xc}}[\rho]$, has yet to be found. Thus, approximations must be made in the form the functionals used to calculate the E_{xc}; the accuracy of the exchange-correlation energy improves with the quality of the approximation. Because the E_{xc} is found using approximations, DFT lacks any systematic way to make improvements, which is a significant disadvantage compared to other correlation methods.

Various types of DFT functionals have been developed, the five main categories being: local-density approximation (LDA), local-spin-density approximation (LSDA), generalized gradient approximation (GGA), meta-GGA, and hybrid functionals. The LDA functionals rely completely on the electronic density at a given point in space. LSDA functionals are extensions of LDAs for spin-polarized systems, meaning the density is separated by spin into $\rho^{\alpha}$and ρ^{β}. LSDA functionals are typically more appropriate than LDA functionals for systems with unpaired electrons. Building off the LSDA functionals, GGAs additionally include the gradients (first derivatives) of the density in the approximations. The semi-empirical GGA functional KT2 was used in Chapters 7 and 8 to calculate NMR shielding values.[15] Expanding from GGAs, meta-GGA functionals also include the second derivative of the density (sometimes called the kinetic-energy density) in the approximations. Hybrid functionals use a combination of HF and GGA or meta-GGA to approximate the exchange-correlation energy. Two hybrid functionals featured in multiple chapters are B3LYP[16] and PBE0, [17] both of which are used extensively throughout computational chemistry. This descriptive list of functionals is not exhaustive. For a more in-depth discussion on the functionals listed, as well as others, the reader is directed to the extensive review by Mardirossian and Head-Gordon (2017).[18]

Time-Dependent Density Functional Theory

The discussion of DFT thus far has only included calculations involving the ground state of a chemical system. A variant of DFT used for excited-state calculations is time-dependent density functional theory (TDDFT) initially formulated by Runge and

Gross in 1984.[19] Excited-state calculations using TDDFT are based on the principle of the density response function, calculating how the exact electronic density function ρ changes in response to small fluctuations in an external potential.[20] The poles of the density response function correspond to the exact excitation energies of the chemical system. The pole of a function is a type of singularity where the value of the function increases without bound (i.e., a pole of $f(x)$ is a root of $f(x)^{-1}$ and vice versa).[21] TDDFT is an efficient and accurate method for calculating excited states involving single excitations. For more complicated excited states, such as those involving two or more electrons or charge transfers, TDDFT has significant accuracy issues that are well-established.[22] These precise issues were observed while performing the calculations presented in Chapters 9 and 10.

Configuration Interaction

One of the most accurate post-HF correlation methods is configuration interaction (CI). Multiple variants of CI exist, but in this work only CI-Singles (CIS) were used to calculate excited states.[23] CIS best practices recommend the use of an optimized geometry found using a highly accurate method and fairly large basis set. Then, a single-determinant SCF MO ground state wavefunction, Φ_0, is formed using that geometry. The orbitals found when calculating Φ_0 are then used to form the CIS linear variation function,

$$\psi_{\mathrm{CIS}} = c_0\Phi_0 + \sum_a \sum_i c_{ia}\,\psi_i^a \tag{26}$$

which is a linear combination of a set of singly excited Slater determinants, ψ_i^a, representing excitations from an occupied spin-orbital i to virtual spin-orbital a. The

variable c_{ia} is the variational coefficient for each excitation. Then, using the linear variation method the first several roots, or excited states, are calculated. These roots are then used to calculate the vertical excitation energy, $h\upsilon_{max}$, of each excitation level, which is the difference in energy between the ground state and a particular excited state.

When performing a CIS calculation, the output provides a list of each contributing combination of occupied and virtual orbitals for a specific excited state along with a weighting coefficient. Using this data, one may then determine what specific electron orbitals contribute the most for an excited state of interest. This information can then be compared to experimental spectra, such as those found with UV-Vis absorption spectroscopy.

Computational Methods

Throughout this work, several computational methods were used beyond the basic energy calculation. First, it is necessary to introduce the concept of a potential energy surface (PES), which is a multi-dimensional "mathematical function that gives the energy of a molecule as a function of its geometry."[24] The PES is a function of $3K$ - 6 ($3K$ – 5 for linear structures) coordinates for K nuclei, excluding the three translational and three (two for linear) rotational degrees of freedom.

When analyzing a PES, one typically begins by calculating the gradient, or partial first derivatives, of the energy with respect to the nuclear coordinates. If every component of the gradient is equal to zero, that geometry is said to be at a stationary point, which can be classified as a minimum or maximum. The minima on a PES can represent reactants, products, or intermediates in chemical reactions. Saddle points are

stationary points that are minima in some dimensions and maxima in others. First-order saddle points, also called transition states, are minima in every dimension but one. Determining the location of transition states can provide important information such as torsional and activation barriers.

The method of locating minima on a PES is called geometry optimization or energy minimization. Multiple mathematical techniques can be used for performing geometry optimizations depending on the computational resources available. The most popular methods are Newton-Raphson methods and quasi-Newton methods which are the default geometry optimization techniques found in all the software packages used throughout this work. For a more complete description of optimization methods, the reader is directed to Jensen, Chapter 12.[12]

The second derivative of the energy with respect to the nuclear coordinates is called the Hessian matrix and provides a plethora of information about a chemical system. While gradient calculations can determine the location of stationary points on a PES, Hessians determine the type of stationary point found. By diagonalizing the Hessian matrix, the harmonic frequencies, ω_i, of the molecule can be determined. These frequencies can be compared to experimentally determined infrared (IR) and Raman spectra. Diagonalizing the matrix is an eigenvalue problem, where each ω_i is the square root of each eigenvalue λ_i. If all frequencies are positive, then the stationary point is a minimum. For any *n* imaginary frequencies (negative frequencies), the stationary point is an *n*th-order saddle point.

Chemists have numerous analytical techniques to determine the structure and purity of chemical samples. One of the most widely used is nuclear magnetic resonance

(NMR) spectroscopy. All nuclei are electrically charged, but some nuclei also have spin depending on the numbers of protons and neutrons. Radio frequency pulses cause excitations (resonance) of the nuclei, and depending on the nucleus' electronic environment, the precise frequency required for resonance can shift. The higher the electron density surrounding the nucleus, the lower the frequency needed to achieve resonance. Chemists refer to this effect of the electrons as shielding.

Spectroscopic NMR results are reported as chemical shifts, which is a comparison of the shielding for the molecule of interest to a chosen reference structure, in most cases tetramethylsilane (TMS). To compute NMR chemical shifts, we first calculate the chemical shielding (CS) tensor. The CS tensor is a purely theoretical quantity and describes the shielding at a nucleus with surrounding electron density compared to the same bare nucleus.[25] The individual components of the CS tensor, σ_{ij}, are calculated with the second derivative of the total energy with respect to both the external magnetic field ($\boldsymbol{B}_{\text{ext}}$) and the magnetic moment $\boldsymbol{\mu}$:[26]

$$\sigma_{ij} = \frac{\partial^2 E}{\partial(\boldsymbol{B}_{ext})_i \partial \boldsymbol{\mu}_j}\bigg|_{\boldsymbol{B}=\boldsymbol{\mu}=0} \tag{27}$$

Without mitigation, the choice of the origin of $\boldsymbol{B}_{\text{ext}}$ (i.e., the gauge) can arbitrarily affect the results, thus the most popular method for these calculations is the gauge-including atomic orbital (GIAO) method.[27] Chemical shielding tensors are 3 x 3 matrices

$$\sigma = \begin{bmatrix} \sigma_{xx} & \sigma_{xy} & \sigma_{xz} \\ \sigma_{yx} & \sigma_{yy} & \sigma_{yz} \\ \sigma_{zx} & \sigma_{zy} & \sigma_{zz} \end{bmatrix}$$

and somewhat difficult to assign physical meaning, so what is actually calculated is the isotropic shielding constant found by

$$\sigma_i = \frac{\sigma_{xx} + \sigma_{yy} + \sigma_{zz}}{3} \tag{28}$$

The chemical shift (δ_i) is then found by finding the difference in chemical shielding constants between the reference nucleus and the nucleus of interest

$$\delta_i = \sigma_{ref}^{ppm} - \sigma_i^{ppm} \tag{29}$$

The ppm superscript indicates that the shielding constants are in units of parts per million.

NMR shielding calculations are typically performed using DFT, but other theories are available. The most common type of functional used for NMR property calculations are the semi-empirical GGAs parameterized with experimental NMR data for specific collections of elements. A single functional standard has not emerged for shielding constant calculations; however, in this work the functional of choice is KT2 developed by Keale and Tozer.[15]

Perturbation Theory and MP2

Perturbation theories have long been developed to deal with intractable many-body problems, such as planetary motion and the interactions of charged subatomic particles.[28] The main principle of perturbation theory (PT) is that many challenging problems are not that different from ones we already know how to solve; they only differ by some kind of small perturbation. This section will provide a general derivation of PT (of non-degenerate energy levels) followed by a more detailed discussion of Møller-Plesset PT.[29] For a complete and straightforward derivation of PT the reader is directed to Levine, Chapter 9.[5]

PT begins with the full Hamiltonian, $\hat{H}$, which can be partitioned into the unperturbed Hamiltonian, $\hat{H}_0$, and the perturbation, $\hat{H}'$,

$$\hat{H} = \hat{H}_0 + \lambda\hat{H}' \tag{30}$$

where λ is the tuning coefficient with a value between 0 and 1, dictating the weight of the perturbation. The presence of the perturbation doesn't just affect the Hamiltonian; both the wavefunction and energy are dependent on λ and are approximated using Taylor series. Using the following abbreviations for the *k*th order corrections for the wavefunction and energy (W_k):

$$\Psi_k \equiv \frac{1}{k!}\frac{\partial^k \Psi}{\partial \lambda^k}\bigg|_{\lambda=0} \tag{31}$$

$$W_k \equiv \frac{1}{k!}\frac{\partial^k E}{\partial \lambda^k}\bigg|_{\lambda=0} \tag{32}$$

Let Φ_i represent the zeroth-order wavefunction of state *i*, which is also an eigenfunction of $\hat{H}_0$. The expressions for the perturbed wavefunction and perturbed energy take the forms:

$$\Psi = \Phi_0 + \lambda\Psi_1 + \lambda^2\Psi_2 + \cdots + \lambda^k\Psi_k \tag{33}$$

$$E = E_0 + \lambda W_1 + \lambda^2 W_2 + \cdots + \lambda^k W_k \tag{34}$$

The Taylor series (to the first few terms) for Ψ and E are substituted into the TISE, using the expression for $\hat{H}$ found in equation (30), and the terms are grouped by the order of λ. The equations for the zeroth, first, and second orders of λ are found to be:

$$\lambda^0: \quad \hat{H}_0\Psi_0 = E_0\Psi_0 \tag{35}$$

$$\lambda^1: \quad \hat{H}_0\Psi_1 + \hat{H}'\Psi_0 = E_0\Psi_1 + W_1\Psi_0 \tag{36}$$

$$\lambda^2: \quad \hat{H}_0\Psi_2 + \hat{H}'\Psi_1 = E_0\Psi_2 + W_1\Psi_1 + W_2\Psi_0 \tag{37}$$

A general expression for λ^n is derived[12] to be

$$\lambda^n: \quad \hat{\mathrm{H}}_0\Psi_n + \hat{\mathrm{H}}'\Psi_{n-1} = \sum_{i=0}^{n} W_i\,\Psi_{n-i}. \tag{38}$$

Using equations (35)-(37), the first- and second-order correction to the energy and first-order correction to the wavefunction can then be derived. The first-order correction to the energy is

$$W_1 = \langle\Phi_0|\hat{\mathrm{H}}'|\Phi_0\rangle \tag{39}$$

which is the average of the perturbation operator over the unperturbed wavefunction. Then the equation for the first-order correction to the wavefunction is

$$\Psi_1 = \sum_{i\neq 0} \frac{\langle\Phi_i|\hat{\mathrm{H}}'|\Phi_0\rangle}{E_0 - E_i}\Phi_i \tag{40}$$

with a sum over all eigenstates *i* except for the ground state Φ_0. E_0 and E_i are the unperturbed energies for the ground state and state *i*, respectively. The second-order correction to the energy is found to be

$$W_2 = \sum_{i\neq 0} \frac{\langle\Phi_0|\hat{\mathrm{H}}'|\Phi_i\rangle\langle\Phi_i|\hat{\mathrm{H}}'|\Phi_0\rangle}{E_0 - E_i}. \tag{41}$$

With these general expressions from PT, the discussion now moves on to Møller-Plesset second order perturbation theory (MP2).

Møller-Plesset Perturbation Theory

In quantum mechanics, one of the most significant and challenging problems is the accurate calculation of interactions between the electrons. One of the most popular post-HF correlation methods is Møller-Plesset PT (MPPT), specifically MP2. MP2 was originally proposed in 1934[29] by Møller and Plesset but was largely ignored by the

computational chemistry community until the 1970s[30] and early 1980s.[31] In MP2, the unperturbed Hamiltonian, $\hat{H}_0$, is the sum of the one-electron Fock operators as defined in (17) above. Another key feature of MP2 is its use of the ground-state HF wavefunction as the unperturbed wavefunction, Φ_0. It can be shown that the sum of the zeroth- and first-order energies is equal to the HF energy:

$$E_0 + E_1 = \langle \Phi_0 | \hat{H}_0 + \hat{H}' | \Phi_0 \rangle = E_{HF} \tag{42}$$

thus, the second-order correction is needed to improve upon the HF energy.

In the unperturbed ground-state wavefunction, Φ_0, all n electrons reside in the n lowest-energy orbitals. All other states take the form of excitations from the lower energy occupied orbitals into the higher energy virtual orbitals. Møller and Plesset proved in their 1934 paper that the expression for the second-order correction to the ground-state energy, W_2, only requires consideration of the doubly excited states, Φ_{ij}^{ab}. The doubly excited states differ from Φ_0 only in the replacement of occupied one-electron orbitals ϕ_i and ϕ_j with virtual orbitals ϕ_a and ϕ_b, respectively. The singly-excited states vanish due to Brillioun's Theorem[4] and variational conditions for off-diagonal Fock matrix elements. The triply excited states and higher disappear due to the Slater-Condon rules.[32] The expression for the second-order correction to the energy is

$$E_{\mathrm{MP2}} = \sum_{i<j}^{occ} \sum_{a<b}^{vir} \frac{\left(\langle \phi_i \phi_j | \phi_a \phi_b \rangle - \langle \phi_i \phi_j | \phi_b \phi_a \rangle \right)}{\varepsilon_i + \varepsilon_j - \varepsilon_a - \varepsilon_b} \tag{43}$$

where ε_n is the eigenvalue of the Fock operator for orbital ϕ_n. Significant time savings can be achieved by using the frozen core approximation. A complete MP2 calculation would involve computing electron repulsion integrals (ERIs) for all occupied and virtual

orbitals. Using the frozen core approximation limits excitations to only those between the occupied valence orbitals and virtual orbitals.

MP2 is not a variational method, thus, there is always a risk that the MP2-corrected energy is less than the true ground-state energy, unlike HF. MP2 is size extensive, meaning the energy found for *n* identical, non-interacting molecules is equal to *n* times the energy of a single molecule. While MP2 is the most popular MPPT method, higher orders have been derived.[33] Practical application of MP*n* methods ends at fourth order MPPT, MP4.

Implementations of MP2

Computer algorithms implementing MP2 have a common organization as shown in Figure 1, regardless of the quantities being calculated. MP2 algorithms begin with an SCF MO calculation to obtain the HF wavefunction, HF energy, and virtual orbitals. The ERIs in the AO basis, $(\mu\nu|\lambda\sigma)$, must then be transformed to ERIs in the spin-orbital MO basis, $(ia|jb)$. These transformations take place in quarter transformations, each step

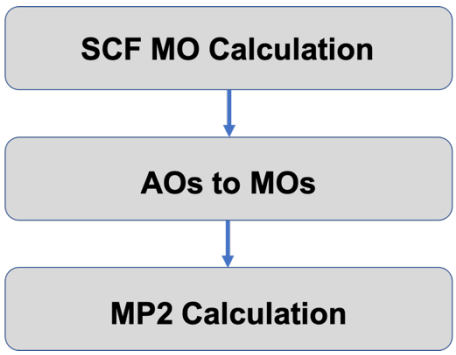

Figure 1. Standard MP2 algorithm structure

transforming a single index from AOs to MOs, as shown

$$(ia|jb) = \sum_{\sigma} C_{\sigma b} \left\{ \sum_{\lambda} C_{\lambda j} \left[\sum_{\upsilon} C_{\nu a} \left(\sum_{\mu} C_{\mu i} \, (\mu\upsilon|\lambda\sigma) \right) \right] \right\} \tag{44}$$

where C is the corresponding MO coefficient. The last stage in any MP2 algorithm is the calculation of the MP2 property of interest, such as the energy or gradient. A more comprehensive description of the MP2 energy and gradient algorithms can be found in Chapters 3 and 4 of this dissertation.

Development of MP2 algorithms increased rapidly in the 1980s with multiple implementations of the energy and gradient being produced. The key difference among the various algorithms lies in the treatment of the AO to MO transformation, which is one of the most computationally expensive steps with scaling of $O(N^5)$ for N basis functions. Direct MP2 algorithms[34] transform and store all ERIs in the memory, saving time by eliminating I/O between memory and the hard disk. Semi-direct MP2 algorithms[35] store the half-transformed ERIs on disk, then return them to memory as needed for the last two quarter transformations. Utilization of the disk, typically much larger than the memory, in semi-direct MP2 allows for calculations involving much larger molecules. The other common MP2 implementation is RI-MP2, which uses the resolution of the identity approximation.[36] An extended description of RI-MP2 can be found in Chapter 2 of this thesis.

Computer Science

A significant amount of computational chemistry falls under the purview of computer science. Along with modeling and theory development, computational

chemists are perpetually on a quest to improve the performance of their calculations, making them faster and more energy efficient. One obvious approach to achieving faster (and perhaps) more energy efficient calculations is upgrading the hardware on which they are executed. However, integrated circuits have not been improving generation to generation as rapidly as they had been for the last half century.[37] Integrated circuits incorporate metal-oxide semiconducting field-effect transistors (MOSFETs).[38] MOSFETs operate on the principle of varying the charge concentration, using a capacitor, in between a gate terminal and body, as illustrated in Figure 2.[39] A voltage is first applied to the gate terminal (G in the Figure) and until the required threshold voltage (V_T) is reached, which is dependent on the dielectric constant of the capacitor, the MOSFET is in the "off" state. Once the potential difference is sufficient, a conducting path forms between the source (S) and drain (D) terminals, and the MOSFET is in its "on" state.

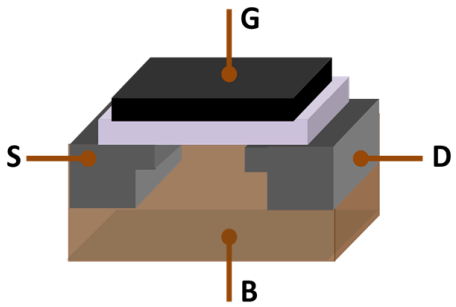

Figure 2. MOSFET showing gate (G), body (B), source (S) and drain (D) terminals. The gate is separated from the body by an insulating layer (white).[38]

Two tenets of computer engineering and design have been Moore's Law[40] and Dennard Scaling.[41] Moore's Law, introduced in 1965 by Gordon Moore, predicted a doubling in the number of transistors on an integrated circuit every two years. Closely related to Moore's Law, Dennard scaling (or MOSFET scaling) is a scaling theory proposed in 1974 by Robert Dennard stating that as transistors get smaller, the power

density remains constant. In other words, central processing units (CPUs) were getting faster without requiring any additional energy. Both Moore's Law and Dennard scaling began to breakdown in the mid-2000s due to ever-shrinking MOSFETs. In the most current Intel microarchitecture, nicknamed "Sunny Cove", the 10th generation chip has transistors just 10nm in length.[42] The ability to pack an increasing number of transistors onto an integrated circuit has its benefits, leading to higher computational efficiency, smaller required chip areas, or both. However, at these incredibly small sizes, control over the electrical overhead has begun to wane.

As the size of the transistors decrease, the magnitude and range of the voltage applied to the gate terminal must also be reduced. These prohibitive voltage windows restrict the machines from being able to fully turn off the applied voltage. This relatively new phenomenon is known as subthreshold conduction. Another unexpected consequence of reducing MOSFET size is gate-oxide leakage due to quantum mechanical tunneling. The insulating layer between the gate and the body has become so thin that electrons are now able to tunnel straight through, even below the threshold voltage.

The largest and most serious consequence of nanoscale MOSFET technology is the production of heat. The design of the integrated circuits incorporating very high densities of transistors is leading to the production of large amounts of thermal energy that is difficult to remove quickly. At high enough temperatures computer components become unstable and may be permanently damaged. To protect the components from prolonged exposure to heat, cooling fans and heat sinks must be integrated into machine design, inevitably leading to higher energy costs. These fundamental challenges require

computational scientists to be creative and develop strategies that use the available hardware in a novel and effective way.

The remainder of this section includes a description of the hardware and software used throughout the work presented in this dissertation, followed by a discussion of the strategies implemented.

Hardware

A majority of the experiments performed in Chapters 2-4 of this dissertation were executed on 6-core Intel E5-1650 *Sandy Bridge* nodes.[43] This microarchitecture will be used as a working example for this discussion. A diagram of an E5-1650 node can be found in Figure 3. Within a node are the cores (CPUs), L_1, L_2 and L_3 caches, and ports for the dynamic random access memory (DRAM), hard drive (disk), and internode communication. To operate efficiently, the CPUs must be able to access instructions and information as quickly as possible, minimizing lag time when moving from one task to the next. The cache memory, which is partitioned into three tiers of increasing size, was designed to accommodate this need. The smallest and fastest L_1 and L_2 caches are located directly on the core. The last level cache (LLC) L_3 has slightly higher latency, much larger storage capacity and is shared by all the cores within a node. The DRAM stores data and application information currently in use and has an even higher latency than the LLC. Data movement to and from the hard drive is referred to as I/O (input/output) as labeled in Figure 3. The hard drive is considered permanent storage and has data transfer rates an order of magnitude slower than any level of cache; therefore, the hard drive should be used judiciously when storing runtime data. Infiniband[44] (IB) is

a high throughput, low latency communication technology ubiquitously used throughout high performance computing (HPC). IB allows for fast communication between nodes which is essential for efficient parallel computing.

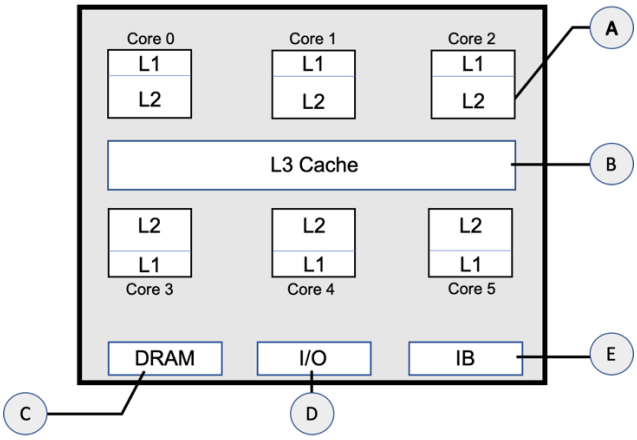

Figure 3. Basic schematic of a six-core Intel E5-1650 node with the following components: (A) core (CPU) containing both L_1 and L_2 cache; (B) L_3 cache; (C) DRAM connection; (D) hard drive connection; (E) Infiniband connection.

Software

Computational chemists have a wide array of computational software packages at their disposal, but the two featured throughout this dissertation are NWChem,[45] developed at Pacific Northwest National Laboratory, and the General Atomic and Molecular Electronic Structure System (GAMESS)[46] maintained by the Gordon Group at Iowa State University. Both software packages provide similar functionality, but each have some unique features such as the Tensor Contraction Engine[47] in NWChem and Effective Fragment Potential[48] calculations in GAMESS. Interpreting the results of quantum mechanical calculations, such as geometry optimizations, can be challenging without some kind of visualization software. *MacMolPlt*[49] is an open-source visualization graphical user interface available on multiple platforms and was the most common visualization software used throughout this dissertation. *MacMolPlt* can be

used to build and view molecular systems, view steps of an optimization, animate vibrational modes, generate electrostatic potential maps for a given set of MOs, and more.

MPI,[50] or Message Passing Interface, is a standardized message-passing protocol essential for parallel programming. A number of open-source and proprietary implementations of MPI exist that can be utilized on a majority of computing platforms and support multiple programming languages. When a program is launched with MPI, MPI creates the number of processes requested by the user, and each process is usually assigned to a single CPU. MPI organizes the processes into groups called communicators that allow the processes to send and receive messages within the group. While performing calculations and other operations, a process may require some or all of the data from other processes. MPI allows for point-to-point (process ←→ process) and collective communications (one process ←→ all processes). Collective communications are synchronization points (barrier points) in a program where every process is required to have completed a certain task. Creating too many synchronization points can lead to bottlenecks in the execution if the computational load of the processes is not balanced.

Strategies

One strategy currently being deployed in a direct response to the increased production of heat and overall rise in energy costs is dynamic voltage and frequency scaling (DVFS).[51] DVFS is the runtime adjustment of the power and speed settings of the CPU, DRAM and other peripheral components. The "voltage" is in reference to the applied processor voltage described in the beginning of this section. "Frequency" refers

to the operational frequency (also called clock speed) of a particular component and is defined as the number of cycles completed per second. A cycle is a single electronic pulse with which a task or operation is performed. The motivation for using DVFS comes from the reality that different devices within a computer are not perpetually in use; thus, when a component is not active, the voltage applied or frequency it is operating at can be scaled down until it is needed again. DVFS can be performed manually or autonomously by the hardware. Intel chips, in particular, are preprogrammed with power-saving C-states[52] that dynamically throttle the applied voltage of the cores based on computational load and core temperature. A number of computing platforms also contain governors[53] that allow a user to manually adjust the clock speed of the CPUs

Another strategy used for improving CPU efficiency is multi-threading (MT), which is defined as the execution of multiple processes (or threads) by the CPU. Various implementations of MT have been developed. Hyper-threading[54] is one version of MT built into some Intel hardware and allows for up to two virtual threads per physical core, with the CPU controlling the distribution of the computational load. A hybrid MT implementation uses both MPI as well as OpenMP, which assigns threads to MPI processes. The tandem of MPI and OpenMP has been shown to greatly improve performance of certain quantum mechanical calculations,[55] but it can require a significant amount of additional programming to ensure thread safety. A simpler, more user-friendly implementation of MT is oversubscription. Oversubscribing requires no additional programming and is simply achieved by requesting more processes from MPI than physical cores available. Oversubscription has been shown[56] to be effective at improving the speed of coarse-grained applications (i.e., extended periods between synchronization

points), but can be detrimental to applications with shorter inter-barrier intervals. In Chapters 3 and 4 of this dissertation oversubscription was utilized to improve the speed and energy efficiency of semi-direct MP2 calculations.

Throughout the experiments with oversubscription, a number of performance measurements were taken. Using the Performance Counter Monitor (PCM)[57] toolkit, it was possible to observe (in user-defined intervals) energy usage, cache hits and misses, C-state residencies, and more. Via the Runtime Average Power Limit (RAPL)[54] available on Intel cores, PCM can track the DRAM power, as well as the per-core power of the CPUs. The rate of cache hits or cache misses is the number of times a processor searched a cache level for a specific piece of data (flag) and was either successful (hit) or unsuccessful (miss) within a given time interval. In the PCM output, C-state residencies correspond to the percentage of time a core was in a given C-state within a measurement interval.

Thesis Organization

This dissertation is organized into two distinct sections: computer science (Chapters 2-4) and chemistry collaborations (Chapters 5-9). Chapter 2 is a study of the effect of manual DVFS strategies on multiple implementations of MP2. Chapters 3 and 4 are a pair of studies on the effect of oversubscription on semi-direct MP2 when using one or more nodes. In Chapters 5-9, the author provided the computational analysis in complement to the experimental work, including but not limited to electronic structure calculations, vibrational analyses, NMR chemical shielding and excited state calculations.

References

1. Schrödinger, E. *Phys. Rev.* **1926**, *28* (6), 1049; Schrödinger, E. *Naturwissenschaften* **1926**, *14* (28), 664-666; Schrödinger, E. *Annalen der Physik* **1926**, *384* (6), 489-527; Schrödinger, E. *Annalen der Physik* **1926**, *384* (6), 361-376; Schrödinger, E., *Annalen der Physik* **1926**, *384* (6), 734-756.

2. Born, M.; Oppenheimer, R. *Annalen der Physik* **1927**, *389* (20), 457-484.

3. **(a)** Hartree, D. R. *Math. Proc. Camb. Philos. Soc.* **1928**, *24* (01), 89; **(b)**Hartree, D. R. *Math. Proc. Camb. Philos. Soc.* **1928**, *24* (01), 111; **(c)** Fock, V. *Z. Für Phys.* **1930**, *61* (1–2), 126–148; **(d)** Fock, V. *Z. Für Phys.* **1930**, *62* (11–12), 795–805.

4. Szabo, A.; Ostlund, N. S. *Modern Quantum Chemistry*; Dover Publications: New York, **1996**.

5. Levine, I., *Quantum Chemistry. Fifth ed*. Prentice Hall: New Jersey, **2000**.

6. Boys, S. F. **1950**, *200* (1063), 542–554.

7. Davidson, E. R.; Feller, D. *Chem. Rev.* **1986**, *86* (4), 681–696.

8. Hehre, W. J.; Stewart, R. F.; Pople, J. A. *J. Chem. Phys* **1969**, *51* (6), 2657.

9. Head-Gordon, M.; Pople, J. A.; Frisch, M. J. *Chem. Phys. Lett.* **1988**, *153*, 503.

10. Dunning, T.H.; *J. Chem. Phys.*, **1989**, *90*, 1007–1023.

11. Kendall R. A.; Dunning Jr., T. H.; and Harrison R. J. *J. Chem. Phys.* **1992**, *96*, 6796-6806.

12. Jensen, F., *Introduction to Computational Chemistry. Second ed*.; John Wiley & Sons Ltd: West Sussex, England, **2007**.

13. Hohenberg, P.; Kohn, W., *Phys. Rev. B* **1964**, *136*, 864.

14. Kohn, W.; Sham, L. J. *Phys. Rev. A* **1965**, *140*, 1133.

15. Allen, M. J.; Keal, T. W.; Tozer, D. J. *Chem. Phys. Lett.* **2003**, *380*, 70.

16. Becke A. D. *J. Chem. Phys.* **1993**, *98*, 5648-5652; Lee, C.; Yang, W.; Parr, R. G.; *Phys. Rev. B* **1988**, *37*, 785-789; Vosko, S. H.; Wilk, L.; Nusair, M.; *Can. J. Phys*. **1980**, *58*, 1200-1211; Stephens, P. J.; Devlin F. J.; Chablowski C. F.; Frisch M. *J. Phys. Chem.* **1994**, *98*, 11623.

17. Perdew, J. P.; Ernzerhof, M.; Burke, K. *J. Chem. Phys*. **1996**, *105*, 9982–9985.

18. Mardirossian, N.; Head-Gordon, M.; *Mol. Phys.* **2017** *115* (19), 2315-2372.

19. Runge, Erich; Gross, E. K. U. *Phys. Rev. Lett.* **1984** *52*, 997.

20. Dreuw, A.; Head-Gordon, M. *Chem. Rev.* **2005** *105* (11), 4009-4037.

21. Pole (of a function). Encyclopedia of Mathematics. URL: http://www.encyclopediaofmath.org/index.php?title=Pole_(of_a_function)&oldid=31254.

22. (a) Tozer, D. J.; Amos, R. D.; Handy, N. C.; Roos, B. J.; Serrano- Andres, L. *Mol. Phys.* **1999**, *97*, 859; (b) Dreuw, A.; Weisman, J. L.; Head-Gordon, M. *J. Chem. Phys.* **2003**, *119*, 2943; (c) Dreuw, A.; Head-Gordon, M. *J. Am. Chem. Soc.* **2004**, *126*, 4007.

23. Foresman, J. B.; Head-Gordon, M.; Pople, J. A.; Frisch, M. J. *J. Phys. Chem.* **1992**, *96,* 135.

24. Sherrill, D. *Potential Energy Surfaces.* URL: http://vergil.chemistry.gatech.edu/courses/chem6485/pdf/pes-lecture.pdf.

25. Widdifield, C. M.; Schurko, R. W. *Concept Magn. Reson. A* **2009,** *34* (2), 91-123.

26. Schreckenbach, G.; Ziegler, T. *J. Phys. Chem.* **1995**, *99* (2), 606-611.

27. Ditchfield, R. *Mol. Phys*. **1974**, *27*, 789–807.

28. Bogolyubov, N. N. Pertubration Theory. Encyclopedia of Mathematics. URL: http://www.encyclopediaofmath.org/index.php?title=Perturbation_theory&oldid=11676.

29. Møller, C.; Plesset, M. S. *Phys. Rev.* **1934** 46: 618-622.

30. Binkley, J. S.; Pople, J. A. *Int. J. Quantum Chem.* **1975**, *9*, 229–236.

31. Bartlett, R. J. *Ann. Rev. Phys. Chem.* **1981***, 32,* 359-401.

32. Slater, J. C. *Phys. Rev.* **1929**, *34*, 1293-1322; Condon, E. U. *Phys. Rev.* **1930**, *36*, 1121-1133.

33. Pople, J. A.; Binkley, J. S.; Seeger, R. *Int. J. Quantum. Chem. Symp.* **1976**, *10*, 1–19; Bartlett, R. J.; Shavitt, I. *Chem. Phys. Lett.* **1977**, *50*, 190–198; Bartlett, R. J.; Purvis, G. D. *J. Chem. Phys.* **1978**, *68*, 2114–2124; Krishnan, R.; Pople, J. A. *Int. J. Quantum Chem.* **1978**, *14*, 91–100; Krishnan, R.; Frisch, M.; Pople, J. A. *J. Chem. Phys.* **1980**, *72*, 4244–4245; Kucharski, S.; Bartlett, R. J. *Adv. Quantum Chem.* **1986**, *18*, 281–344; Kucharski, S.; Noga, J.; Bartlett, R. J. *J. Chem. Phys.* **1989**, *90*, 7282–7290; Raghavachari, K.; Pople, J. A.; Replogle, E. S.; Head-Gordon M. *J. Phys. Chem.* **1990**, *94*, 5579–5586; He, Z.; Cremer, D. *Int. J. Quantum Chem.* **1996**, *59*, 15–29; He, Z.; Cremer, D. *Int. J. Quantum Chem.* **1996**, *59*, 31–55; He, Z.; Cremer, D. *Int. J. Quantum Chem.* **1996**, *59*, 57–69.

34. Head-Gordon, M.; Pople, J. A.; Frisch, M. J. *Chem. Phys. Lett.* **1988**, *153*, 503-506; Saebø, S.; Almlöf, J. *Chem. Phys. Lett.* **1989**, *154*, 83–89.

35. Frisch, M. J.; Head-Gordon, M.; Pople, J. A. *Chem. Phys. Lett.* **1990**, *166*, 281-289.

36. Bernholdt, D. E.; Harrison, R. J.; *Chem. Phys. Lett.* **1996**, *250*, 477-484.

37. Waldrop, M. M. The Chips Are down for Moore's Law. *Nature* **2016**, *530* (7589), 144–147.

38. (a)Kahng, D. U. S. Patent No. 3,102,230 (Filed 31 May 31, 1960, issued August 27, 1963); (b) Kahng, D. Sze, S.M. Semiconductor Devices: Pioneering Papers. **1991** 583-59; (c) Sah, C. T., Proceedings of the IRE **1961** 49(11), 1623-1634; (d) Hofstein, S. R.; Heiman, F. P. Proceedings of the IEEE. **1963**, 51, 1190 -1202.

39. MOSFET structure: https://en.wikipedia.org/wiki/MOSFET#/media/File:MOSFET_Structure.png

40. Moore, G.; *Electronics Magazine*, **1965**, 8, 38-41.

41. Dennard, R. H.; Gaensslen, F.; Yu, H. N.; Rideout, V. L.; Bassous, E.; LeBlanc, A. *IEEE Journal of Solid State Circuits*, **1974**, 256-268.

42. Intel – Products formerly Ice Lake. URL: https://ark.intel.com/content/www/us/en/ark/products/codename/74979/ice-lake.html

43. Sandy Bridge Die Architecture. URL: https://en.wikichip.org/wiki/intel/microarchitectures/sandy_bridge_(client)#System_Agent_2

44. Introduction to Infiniband. URL: https://www.mellanox.com/pdf/whitepapers/IB_Intro_WP_190.pdf

45. Valiev, M.; Bylaska, E. J.; Govind, N.; Kowalski, K.; Straatsma, T. P.; Van Dam, H. J. J.; Wang, D.; Nieplocha, J.; Apra, E.; Windus, T. L.; De Jong, W. A. *Comput. Phys. Commun.* **2010**, *181*, 1477-1489.

46. Schmidt, M. W.; Baldridge, K. K.; Boatz, J. A.; Elbert, S. T.; Gordon, M. S.; Jensen, J. H.; Koseki, S.; Matsunaga, N.; Nguyen, K. A.; Su S. J.; Windus, T. L.; Dupuis, M.; Montgomery, J. A. *J. Comput. Chem*. **1993**, *14*, 1347-1363.

47. Hirata, S. *J. Phys. Chem. A*. **2003**, *107*, 9887-9897.

48. Gordon, M. S.; Freitag, M. A.; Bandyopadhyay, P.; Jensen, J. H.; Kairys, V.; Stevens, W. *J. Phys. Chem. A.* **2001**, *105*, 2, 293-307.

49. Bode, B. M. and Gordon, M. S. *J. Mol. Graphics Mod.* **1998**, *16*, 133-138.

50. "MPI: A Message Passing Interface". Proceedings of Supercomputing '93. Portland, Oregon, USA. 878–883.

51. Talamudupula, S. K. *IJSRSET,* **2017**, *3*, 28–35.

52. Kidd, T. Power Management States: P-States, C-States, and Package C-States. URL: https://software.intel.com/en-us/articles/power-management-states-p-states-c-states-and-package-c-states#_Toc383778910, **2014**.

53. Linux CPUFreq Governors. URL: https://access.redhat.com/documentation/en-us/red_hat_enterprise_linux/6/html/power_management_guide/cpufreq_governors#governor_types, **2017**.

54. Annavarami, M.; Grochowski, E.; Shen, J. *Intel software programmer's guide-combined volumes 3a and 3b*, IEEE Computer Society, **2014**.

55. Shan, H.; Williams, S.; Jong, W.; Oliker, L. PMAM 15: San Francisco, CA, USA, **2015**.

56. Iancu, C.; Hofmeyr, S.; Blagojevic, F.; Zheng, Y. *IEEE International Symposium on Parallel & Distributed Processing*, **2010**, 1–11.

57. Performance Counter Monitor. URL: https://github.com/opcm/pcm

CHAPTER 2. POWER PROFILING AND EVALUATING THE EFFECT OF FREQUENCY SCALING ON NWCHEM

A conference proceeding of SpringSim-HPC 2016

Vaibhav Sundriyal, Ellie L. Fought, Theresa L. Windus, and Masha Sosonkina

ELF and TLW are responsible for all work on Bolt, VS and MS completed all work on Styx.

Abstract

Modern high-performance computing system designers are becoming increasingly aware of the energy requirements for computing while needing to lower the operational costs and raise reliability. At the same time, high-performance application developers are taking proactive steps towards less energy consumption without a significant performance loss. One way to accomplish this is to change the processor frequency dynamically during application execution. In this paper, a representative HPC application, NWChem, is considered with the aim to investigate its compute and memory intensiveness along with the energy-saving potential of various stages of execution. This work presents energy consumption characteristics of three different algorithms within NWChem that compute the Møller-Plesset (or many-body) perturbation theory second-order correction (MP2) to the Hartree-Fock energy (HF), which radically differ in their computer resource usages. Power consumption measurements are obtained with the application of dynamic voltage and frequency scaling (DVFS) to both processor and memory to determine the runtime behavior of the three MP2 algorithms. Finally, a

frequency scaling strategy is proposed and tested. For a 55-atom system, this strategy yields energy savings of up to 10.1% with a modest performance degradation of 2.4%.

Introduction

Power consumption has become a major concern for modern and future supercomputers. Current top petascale computing platforms in the world typically consume power on the order of several megawatts, which at current energy prices may cost on the order of several million U.S. dollars. In the quest for exascale performance, the power consumption growth rate must slow down and deliver more calculations per unit of power. To address this challenge, power and energy optimizations are needed in modern computing platforms at all levels: application, system software, and hardware.

It is well-established that the CPU and memory subsystem are the major energy consumers in a computing system. For example, the CPU consumes about 50% of the total power as was investigated in [9], considering both static and dynamic power consumption. Memory power consumption is also a significant component in a computer server power profile and is comparable to or may even surpass processor power consumption for memory-intensive workloads. An early study [13] has reported that, on an IBM p670 server, the average memory power consumption is 1223 watts, compared to the average processor power consumption of 840 watts.

The current generation of Intel processors provides various P-states for dynamic voltage and frequency scaling (DVFS) and T-states for introducing processor idle cycles (throttling). For example, the Intel “Haswell” micro-architecture provides fifteen P-states fp(1), . . . , fp(15), while the DRAM modules used in this work provide four P-states fm(1), . . . , fm(4) arranged in descending order of their frequency values. The delay of

switching from one state to another depends on the relative ordering of the current and target states, as discussed, e.g., in [18]. The user may write a specific value to model-specific registers (MSRs) to change the P- or T-states of the processor. The "Haswell" micro-architecture estimates power and energy consumption of the CPU and memory through the built-in MSRs, which certainly facilitates power-measurement efforts.

At this time, existing computer systems do not support software-controlled DVFS of memory devices. Recent studies [3] have explored DVFS of memory devices by modifying the DRAM timing registers to emulate different frequencies. In this work, it was determined experimentally that memory frequency can be scaled through the BIOS, which will allow estimation of the runtime effects of changing memory frequency of an application and developing a performance model. Since memory power consumption is increasingly a concern in the industry, it is believed a more flexible DVFS support may appear in the near future.

Various approaches exist to intelligently employ DVFS in scientific parallel applications. The more sophisticated applications scale processor frequency on different intervals of application runtime while attempting to predict accurately the performance effects from the DVFS. Such approaches may be broadly classified into two types: One that first divides the application into execution intervals of predefined duration and then uses the performance counters to determine a suitable frequency for them [8], [10], [11]; and the other that first determines communication intervals in parallel applications that use either explicit message passing [7], [14] or global address-space primitives [25] and then scales the frequency for those intervals, usually based on the variation of the MIPS (million instructions per second) metric at different P-states. Oversubscribing the

compute cores can also be thought of as a possible method to save energy [12], but it may not be applicable broadly.

NWChem [24] is an ab initio computational chemistry software package that provides many methods for computing the properties of molecular and periodic systems using standard quantum mechanical descriptions of the electronic wave- function or density. In this work, the power consumption characteristics of three different algorithms within NWChem that compute the Møller-Plesset (or many-body) perturbation theory second-order correction (MP2) to the Hartree-Fock energy are determined. By applying processor- and memory- frequency (denoted here as PF and MF, respectively) scaling to the execution, the compute and memory intensiveness of the algorithms are determined which may help in developing appropriate strategies for obtaining energy savings. In particular, future implementations of the algorithms can be written with both time to solution and power consumption in mind.

With the advent of the Sandy Bridge family of processors, Intel has introduced capabilities for both on-board power meters and power clamping. The Intel Running Average Power Limit (RAPL) [1] now provides a standard interface for measuring and limiting processor and memory power by the hardware, operating system, or within applications using Intel RAPL APIs along with a wall power meter, runtime power consumption traces are recorded for the three algorithms to determine power consumption variation during different stages of execution. Based on the runtime behavior of the inputs, a simple frequency scaling strategy is proposed which resulted in a maximum energy savings of 14.5%.

The rest of paper is organized as follows. Section II describes the architecture of the NWChem package. Section III discusses the power consumption characteristics of three different MP2 algorithms with their runtime behavior when PF and MF are modified. Sections IV and V provide related work and conclusions, respectively.

NWChem Architecture

The computational work was performed using NWChem, a scalable, portable, open-source computational chemistry soft- ware package. NWChem was designed to be used on multiple platforms and with different computer hardware. However, the prime design target is high performance computers and efficient use of all of the hardware components on those platforms. The software is written mostly in Fortran77 with some Fortran90 using object oriented programming ideas such as data encapsulations, object creation and annihilation, and class interfaces. NWChem uses the Global Array tools [16] to manage distributed memory in a non-uniform memory architecture (NUMA) paradigm.

Møller-Plesset Second Order Perturbation Theory [19], [26], or MP2, is an electron correlation method used in association with the self-consistent field, or Hartree Fock (HF) method, in quantum chemistry. MP2 is based on the foundational Rayleigh-Schro¨dinger perturbation theory using the Fock oper- ator as the unperturbed operator, and is one of the most widely used quantum mechanical correlation methods available. The HF method is an iterative procedure that assumes that each electron is in a mean field of the other electrons and, therfore, ignores the instantaneous correlations of the electrons with one another. The MP2 method is a correction to include this correlation energy.

There are three common MP2 algorithms used in NWChem: semi-direct, direct, and resolution of the identity MP2 [6], [17], [2], or RI-MP2.

In two of the MP2 methods (direct and semi-direct) within NWChem, an order N5 transformation of the atomic orbital integrals to the molecular orbital integrals is required, where N is the number of atomic orbital basis functions for the molecule of interest. This is the computational bottleneck for these MP2 energy methods. The direct MP2 performs all calculations and stores all of its integrals and other data to local memory. Any integrals that cannot be stored in memory are recalculated when they are subsequently needed in the calculations. For semi-direct MP2 some transformed integrals get stored in memory or recalculated and some (expensive ones) get written to disk. The semi-direct method is widely used, particularly because of its lower memory requirements. Both direct MP2 and semi-direct MP2 use identical mathematical algorithms in their calculations and mostly differ in the integral storage.

RI-MP2, on the other hand, uses the resolution of the identity mathematical approximation to transform four-center integrals to three-center integrals. For a complete basis set ϕ_n,

$$\sum_{n=1}^{\infty} |\phi_n >< \phi_n| = 1 \qquad (1)$$

where this sum is a projection operator known as the resolution of the identity. In the case of MP2, the resolution of the identity is used when calculating four-center AO integrals, usually in the form of $< ij \mid kl >$, where i, j, k, and l represent one-electron atomic basis functions. When the projection operator is used, we essentially multiply by one and

transform the four-center integrals into a sum over the product of two three-center integrals:

$$\sum_{n=1}^{\infty} < ij|\phi_n >< \phi_n|kl > \quad (2)$$

Each of the three-center integrals requires less time to compute, but results in more terms to calculate. The usual basis sets used in these calculations are far from complete, so to more adequately account for the approximations being made, a much larger auxiliary basis set (the one used for the RI approximation) must be used. This approximation also changes the order N^5 MO integral transformation into an order N^4 operation. However, the final energy evaluations is still order N^5 due to the extra multiplications involved to approximate the four-center integrals. The NWChem implementation also uses on order N^2 total memory and order N^3 disk storage (much less than the semi-direct method, but more than the direct method).

Experimental Results

The experiments were performed on two computing platforms based on their capabilities of performing MF scaling. For the PF scaling, the experiments were performed on a node of the computing platform named Bolt which comprises 18 Infiniband QDR-connected compute nodes, each with 64 GB of main memory and an Intel Xeon CPU E5–1650 "Sandy Bridge" six-core processor. For evaluating the effect of MF scaling, a computing platform named Styx was used, which has an Intel i5–4590 "Haswell" quad-core processor and 8 GB of main memory with timing specification 9-9-9-24. The processor frequency ranged from 3.3 GHz to 0.8 GHz; the frequency range for

memory was from 1.6 GHz to 0.8 GHz. For measuring the node power and energy consumption, a Wattsup power meter was used with a sampling rate of 1 Hz.

The chemical systems chosen for this work are a series of large, biologically relevant, diols, or carbon chains containing two −OH functional groups. The molecule energies were calculated using the Dunning cc-pVDZ basis set [4]. Although NWChem allows for extensive runtime control via directives in the input files, only two optional directives were used in this work. One optional parameter specified the maximum memory per physical process, and the other imported previously optimized molecular orbital vector files to aid in the first few steps of the calculations.

In this paper, the test cases are referred to by the system size, i.e., the number of atoms in the system (31, 40, 43, or 55), and by the MP2 algorithm employed: The test-name suffix "s" stands for semi-direct, "d"—for direct, and "r"—for RI- MP2. Table 1 provides the information that is most relevant to computational load. Specifically, this is the number of basis functions per molecule, for both the standard and auxiliary bases. Each test was executed at least three times to determine reproducibility of the results and the average values of those runs are presented in the paper.

Table 1. The test systems referred to by their number of atoms (system size), the number of atomic basis functions as well as, for the RI-MP2 method, the number of auxiliary basis functions.

System Size (atoms)	Basis Functions	Basis Functions (Auxiliary Basis)
31	263	598
40	335	800
43	359	858
55	473	1106

Bolt

Figures 1 to 3 depict the execution times for each of the four test system sizes using the three MP2 algorithms, respectively, at minimum and maximum processor frequencies run on a single (six-core) node. The effect of PF scaling changes depending on the type of MP2 being implemented. Execution times for RI- and direct MP2 double when running at the minimum frequency as compared to the maximum frequency. When using semi-direct MP2, the gaps between execution times at the minimum and maximum frequencies steadily decrease as the size of the system increases. These variations in how the three MP2 algorithms behave under different PFs demonstrate a need for a judicious application of PF scaling.

Hyperthreading was disabled on both platforms being used, but the effect of oversubscription of the CPUs was investigated on Bolt to determine potential energy savings. In addition to the calculations performed by calling six processes (one process per core), inputs for each of the three algorithms were also executed by using 12, 18, and 24 processes. It was found that oversubscription had either no effect or was adversely affecting performance for both RI-MP2 and direct MP2. However, for the semi-direct algorithm, execution times actually began to shorten. The effect becomes more pronounced as the system size (i.e. number of basis functions) increases, as well. Table II illustrates the effect for 55s, or 473 basis functions, where oversubscription provided over 20% savings in execution (wall clock) time and nearly a 15% savings in total energy consumed per execution. In this case, the oversubscription makes sense by increasing the overlap of computation and I/O as the semi-direct method is more I/O intensive than the other two methods.

Table 2. Number of processes in oversubscription tests with percent energy savings and percent decrease in execution time on Bolt

Processes	Energy Savings (%)	Decrease in Execution Time (%)
12	9	12.9
18	12.8	15.8
24	14.6	21.3

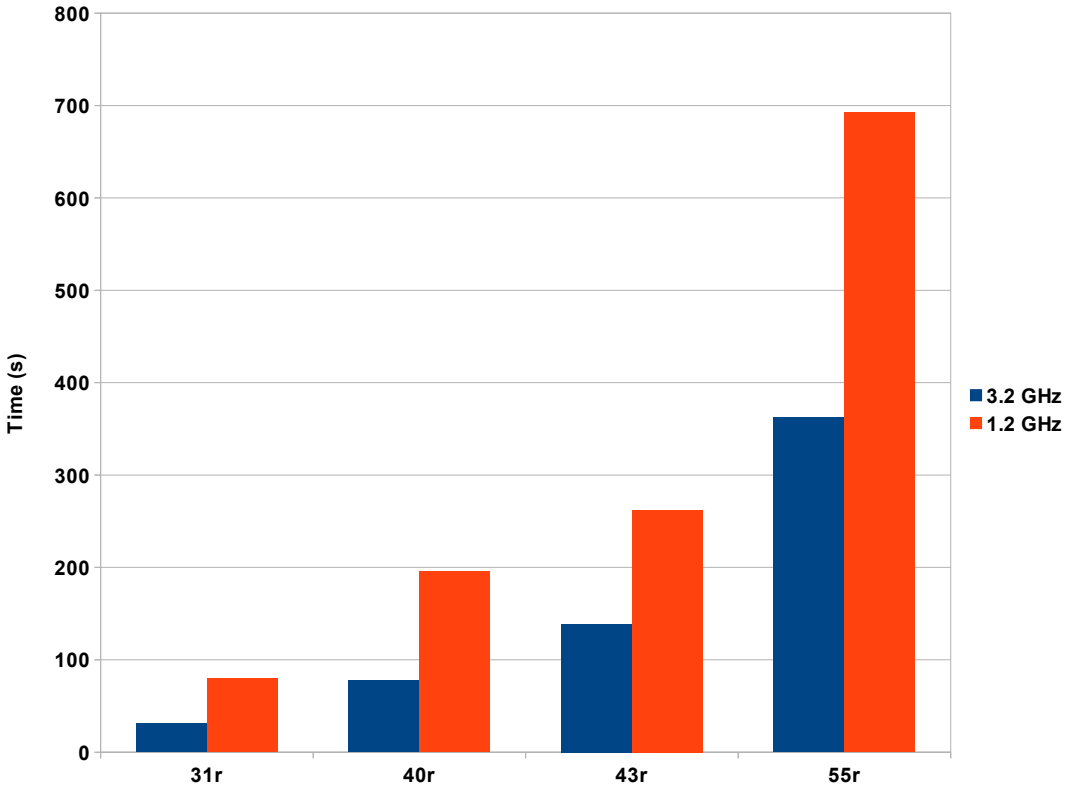

Figure 1. Job completion time for all four RI-MP2 inputs at the minimum and maximum processor frequencies on Bolt

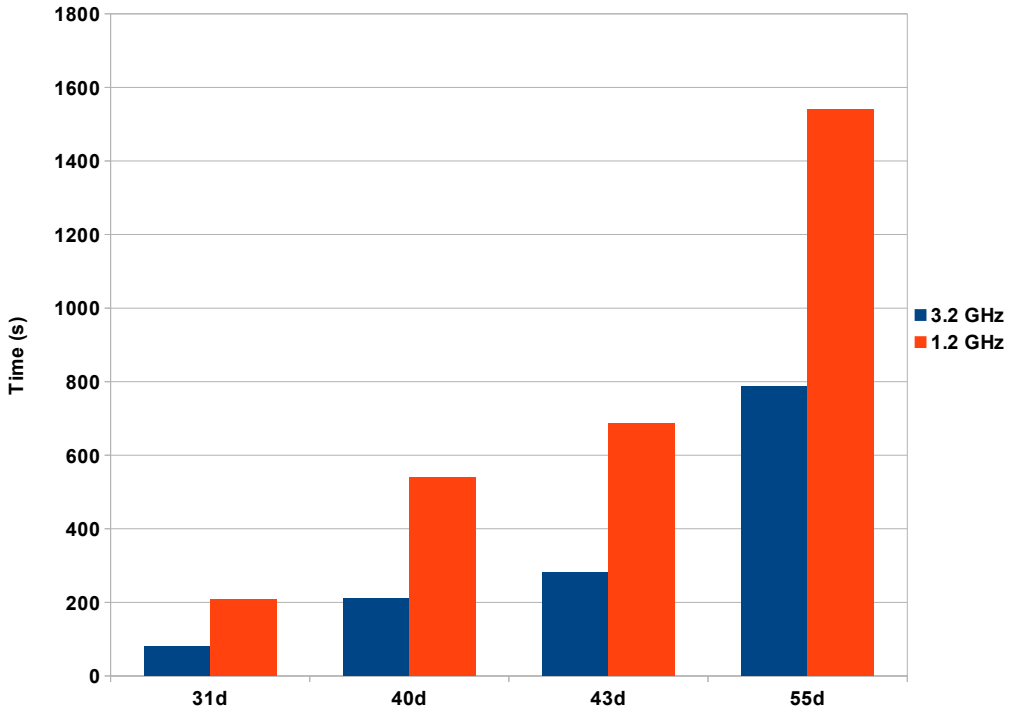

Figure 2. Job completion time for all four direct MP2 inputs at the minimum and maximum processor frequencies on Bolt.

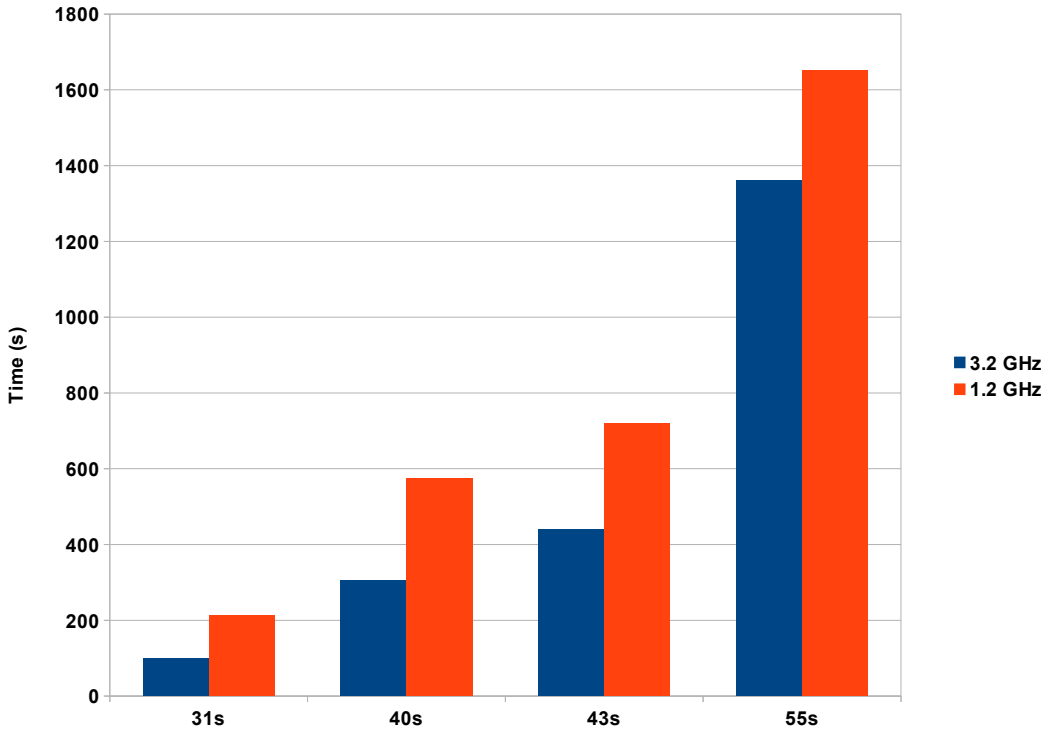

Figure 3. Job completion time for all four semi-direct MP2 inputs at the minimum and maximum processor frequencies on Bolt.

The power consumption traces for the total system power, CPU power, and memory power are depicted in Figs. 4 to 6 for the RI-MP2, direct, and semi-direct algorithms for the largest system of 55 atoms, respectively, executed on six cores of a single node of Bolt. In each of Figs. 4 to 6, the black vertical line divides the trace into HF and MP2 sections, which do not overlap. The direct algorithm spends the least time idling since it does not get involved in I/O whereas the semi-direct one frequently idles owing to heavy I/O activity. In the HF sections of all runs, the memory power consumption increases significantly due to the many put/get/accumulates associated with forming and diagonalizing the Fock matrix. The MP2 section is rather compute intensive for all the three algorithms with total power consumption staying uniformly high for the RI-MP2 and direct algorithms while, for semi-direct, it swings from 100 to 180 watts. These swings in the consumption have been correlated to I/O activity in the method.

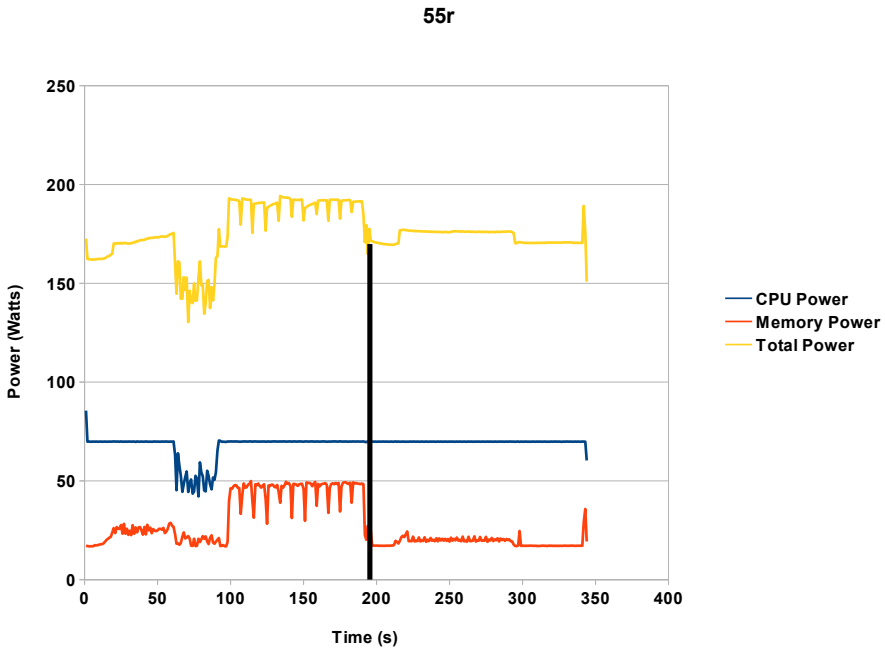

Figure 4. Variation in power consumption of different compute node components for RI-MP2 algorithm on Bolt.

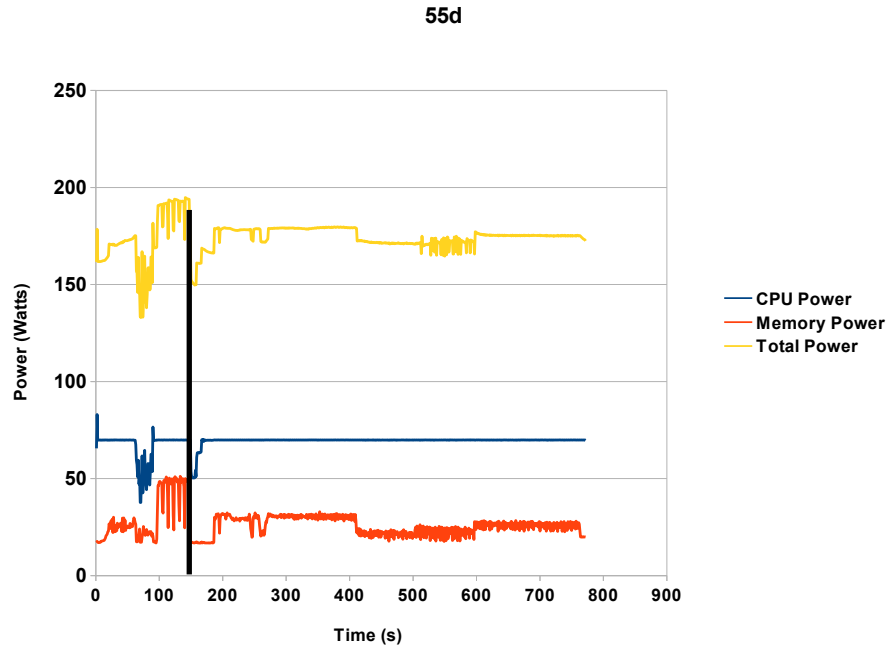

Figure 5. Variation in power consumption of different compute node components for RI-MP2 algorithm on Bolt.

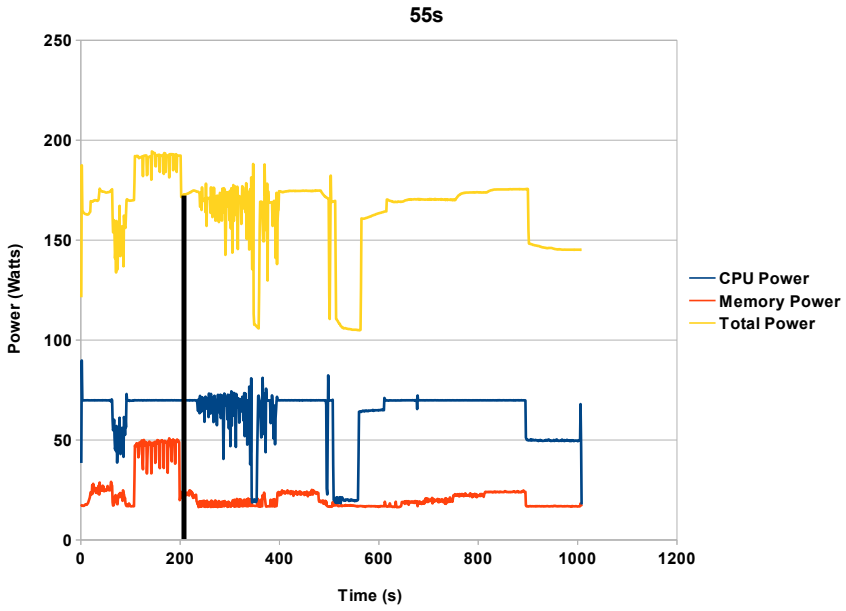

Figure 6. Variation in power consumption of different compute node components for semi-direct MP2 algorithm on Bolt.

Styx

Figure 7 depicts the change in execution time for the 55-atom system calculated by the three different MP2 algorithms, when PF and MF were modified. The *x*-axis of Fig. 7 represents the PF and MF pairs, in GHz. It can be observed that all three algorithms appear more sensitive to the PF scaling compared to the MF one. Specifically, for the latter, while keeping the PF at the maximum, the average performance degradation is 6.2% for the three algorithms. On the other hand, in the case of PF scaling while keeping the MF at the maximum, the corresponding average performance loss is 90.4%. These results indicate that MF scaling is more suitable for the three MP2 algorithms than the PF one is. This is not surprising given these algorithms are more compute intensive. Nevertheless, it is useful to examine the three algorithms in more detail.

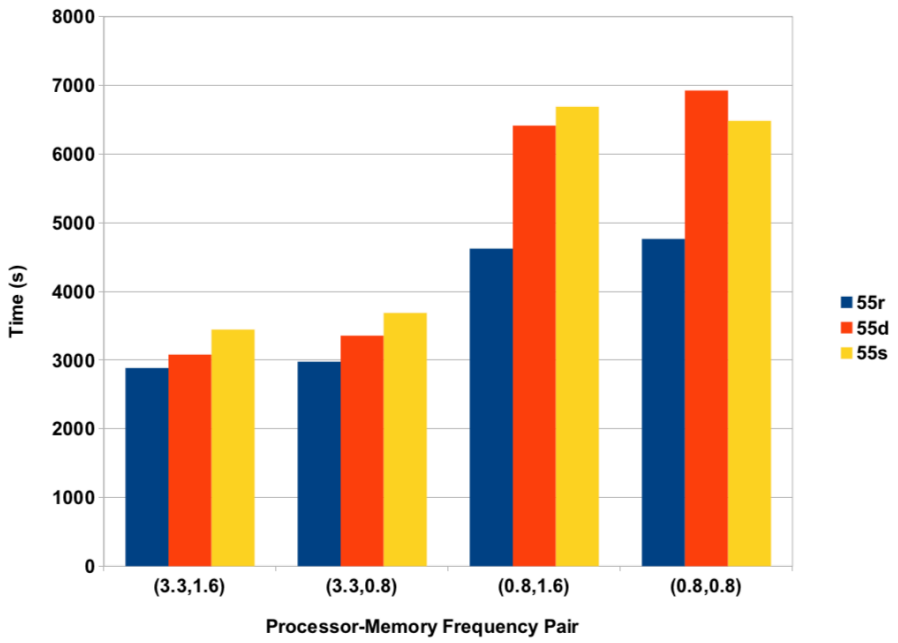

Figure 7. Variation in execution time for the 55-atom system using the three MP2 algorithms for different processor-memory frequency pairs on *Styx*.

For the largest 55-atom system, Figure 8 presents the effect of PF and MF scaling distinguishing the HF and MP2 computations in each of the three algorithms investigated here. Observe that, in all the cases, the MP2 portion is quite insensitive to the MF scaling yielding an average performance loss increase of 11% across all the three algorithms when MF was reduced to its lowest value of 0.8 GHz while at the maximum PF of 3.3 GHz. On the other hand, when the PF was reduced to its minimum of 0.8 GHz, while keeping the MF at 1.6 GHz, the average performance loss across all the three algorithms was 240%. Interestingly, in all the cases tested here, the HF computation is rather insensitive to either PF or MF scaling since HF exhibits an average performance degradation of only 3% during the executions when the MF is scaled and an acceptable 12% of degradation during the PF-scaled executions.

Based on the behavior exhibited by the HF and MP2 sections under the frequency scaling, as shown in Fig. 8, a simple frequency-scaling strategy may be proposed as follows to save energy:

− In the HF section: lower the PF to the minimum while keeping MF at the maximum.

− In the MP2 section, lower the MF to the minimum and set the PF to the maximum.

Specifically, the reduction in power consumption is higher when the PF is scaled rather than when the MF is. Hence, it makes sense to reduce the PF whenever possible. Since the HF section is insensitive to either PF or MF scaling, the PF is reduced in the proposed strategy. Reducing both, however, may cause a considerable performance loss in HF. (cf., e.g., the first and seventh bars in Fig. 8(a)). Since the MP2 section is too sensitive to the PF scaling, only the MF scaling was chosen in the proposed strategy.

Figure 9 shows the performance degradation and change in energy consumption for the three MP2 algorithms when oper- ated under the proposed strategies compared to the baseline case in which both PF and MF were set at their highest levels. The performance loss is ~11% for each algorithm. The proposed strategy saves 14.2% and 6% energy for the RI- MP2 and direct algorithms, respectively. For the semi-direct, however, the energy consumption increases by 1.8%, which may be explained by a relatively high I/O in the MP2 stage during which only little power is consumed (cf. Fig. 6). As noted earlier, oversubscription is a useful method to decrease the overall computational time for the semi-direct algorithm, which decreases the overall power consumption more effectively.

Related Work

There have been two general approaches to obtaining energy savings during parallel application execution. The first approach is to focus on identifying stalls during the execution by measuring architectural parameters from performance counters as proposed in [8], [10], [11]. The second approach determines the communication phases to apply DVFS as, for example, in [14], [7] and [21]. Etinski et al. [5] propose a technique that applies both DVFS and over-clocking to the CPUs to save energy and to improve execution time. A common shortcoming of these approaches is that they ignore MF scaling and, subsequently, cannot save energy for applications which are not MF intensive. Even though it is preliminary in nature, this problem has been addressed in this work at the application level.

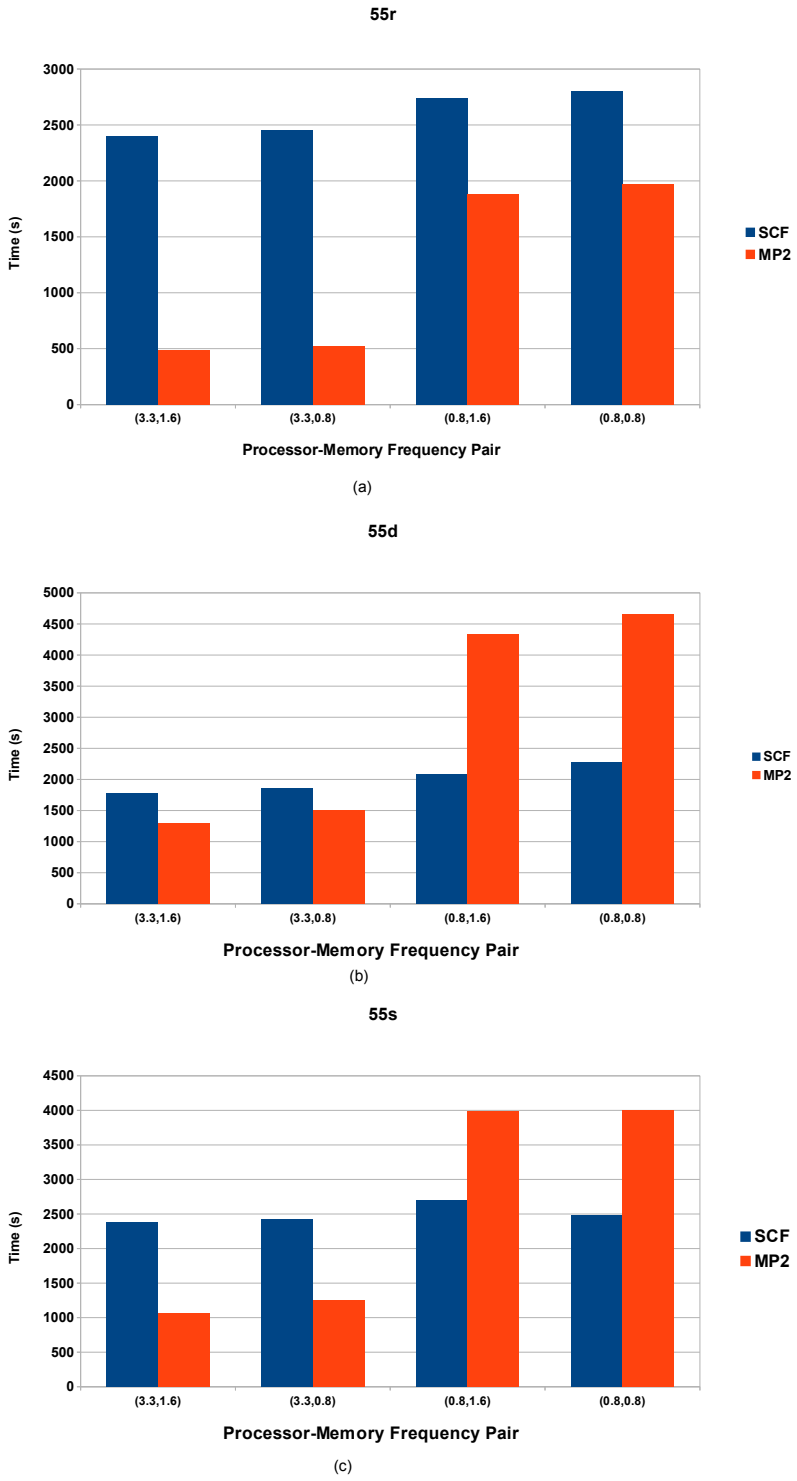

Figure 8. Variation in HF and MP2 execution times for the 55-atom system using a) RI-MP2, b) direct and c) semi-direct algorithms for different processor-memory frequency pairs on Styx.

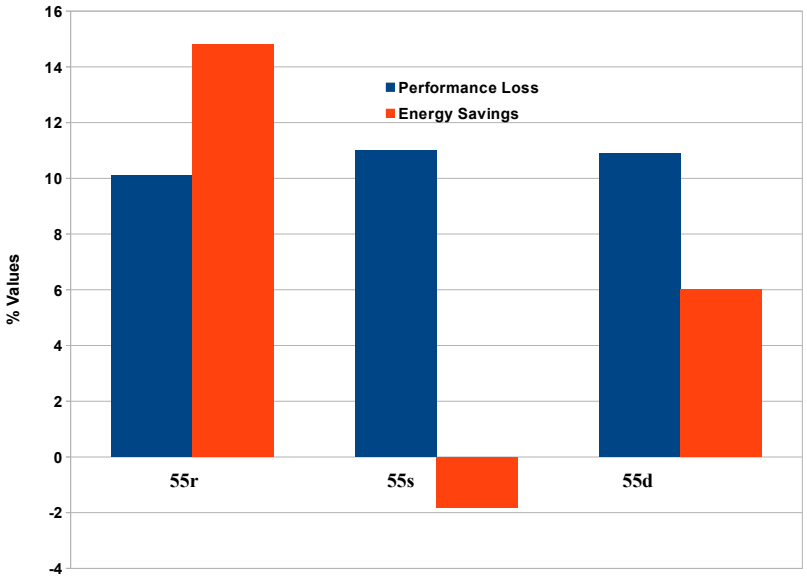

Figure 9. Performance degradation and energy savings for the 55-atom system calculated by the three MP2 algorithms under the proposed frequency-scaling strategy on Styx.

Authors in [25] design a high performance power aware communication library using Aggregate Remote Memory Copy Interface (ARMCI) which is the communication runtime system of the Global Arrays framework used in NWChem. In [22] the authors perform power profiling for the quantum chemistry application GAMESS [20] and propose a theoretical model which provides the relationship between performance loss tolerance and energy consumption based on the workload. The MPI collective communication operations are specifically targeted to save energy in [23]. Since exascale computing is being limited by power consumption, there have been some novel approaches which instead of limiting the energy consumption, focus on the power budget and attempt to improve performance under that constraint, employing the RAPL power limiting features. Authors in [15] propose a runtime system conductor that dynamically

distributes available power to different compute nodes and cores based on the available slack to improve performance.

Conclusions and Future Work

This work studies the power consumption characteristics of NWChem for three different algorithms: RI-MP2, direct, and semi-direct MP2, where the last two methods differ in the treatment of memory and disk storage of the integrals and intermediate data. Their execution time, recorded on two distinct computing platforms, was investigated as to the effects of PF and MF scaling on the HF and MP2 sections of the calculations of systems ranging from 31 to 55 atoms. It was observed that the HF and MP2 sections were relatively insensitive the to PF and MF scaling, A simple energy-saving strategy was also proposed, aiming to benefit from the findings that the HF section was relatively PF-insensitive whereas the MP2 one was MF-insensitive. This strategy yielded energy savings of 14.2% with a moderate performance degradation of 10%. For the semi-direct algorithm, oversubscription of the cores proved to be an effective method due to decreased computational time. Up to 15% savings were found in total energy consumed with a 20% decrease in execution time.

NWChem is one of the prominent quantum chemistry applications and enjoys a large user community. Hence, the findings of this paper are beneficial to an important scientific domain and a wide class of HPC applications. However, a deeper analysis of the MP2 algorithms is needed to fine tune the application of the energy-saving strategy. Since modern DRAM devices still do not have support for frequency scaling through

software, the DRAM power-limiting capability provided by the RAPL API may be used to widely employ the strategy.

Acknowledgments

This work was supported in part by the Air Force Office of Scientific Research under the AFOSR award FA9550-12-1-0476, by the National Science Foundation grants 0904782, 1047772, 1516096, by the U.S. Department of Energy, Office of Advanced Scientific Computing Research, through the Ames Laboratory, operated by Iowa State University under contract No. DE-AC02-07CH11358, and by the U.S. Department of Defense High Performance Computing Modernization Program, through a HASI grant.

References

1. M. Annavarami, E. Grochowski, and J. Shen. Intel software programmer's guide-combined volumes 3a and 3b. Washington, DC, USA, 2014. IEEE Computer Society.

2. D. E. Bernholdt and R. J. Harrison. Large-scale correlated electronic structure calculations: the ri-mp2 method on parallel computers. *Chem. Phys. Lett.*, 250:477–484, 1996.

3. H. David, C. Fallin, E. Gorbatov, U.R. Hanebutte, and O. Mutlu. Memory power management via dynamic voltage/frequency scaling. In *Proceedings of the 8th ACM International Conference on Autonomic Computing*, pages 31–40, 2011.

4. T.H. Dunning. Gaussian basis sets for use in correlated molecular calculations. i. the atoms boron through neon and hydrogen. *J. Chem. Phys.*, 90:1007–1023, 1989.

5. M. Etinski, J. Corbalan, J. Labarta, M. Valero, and A. Veidenbaum. Power-aware load balancing of large scale mpi applications. In *Parallel Distributed Processing, 2009. IPDPS 2009. IEEE International Symposium on*, pages 1–8, May 2009.

6. M. Feyereisen, G. Fitzgerald, and A. Komornicki. Use of approximate integrals in ab initio theory. an application in mp2 energy calculations. *Chem. Phys. Lett.*, 208:359, 1993.

7. V.W. Freeh and D.K. Lowenthal. Using multiple energy gears in MPI programs on a power-scalable cluster. In *Proceedings of the tenth ACM SIGPLAN symposium on Principles and practice of parallel programming*, pages 164–173, 2005.

8. R. Ge, X. Feng, W. Feng, and K.W. Cameron. CPU MISER: A performance-directed, run-time system for power-aware clusters. In *Parallel Processing, 2007. ICPP 2007. International Conference on*, page 18, Sep. 2007.

9. R. Ge, X. Feng, S. Song, H.C. Chang, D. Li, and K.W. Cameron. PowerPack: Energy profiling and analysis of high-performance systems and applications. *Parallel and Distributed Systems, IEEE Transactions on*, 21:658–671, 2010.

10. C.H. Hsu and W. Feng. A power-aware run-time system for high- performance computing. In *Supercomputing, 2005. Proceedings of the ACM/IEEE SC 2005 Conference*, page 1, nov 2005.

11. S. Huang and W. Feng. Energy-efficient cluster computing via accurate workload characterization. In *Cluster Computing and the Grid, 2009. CCGRID '09. 9th IEEE/ACM International Symposium on*, pages 68– 75, May 2009.

12. C. Iancu, S. Hofmeyr, F. Blagojevic, and Y. Zheng. Oversubscription on multicore processors. In *Parallel Distributed Processing (IPDPS), 2010 IEEE International Symposium on*, pages 1–11, 2010.

13. C. Lefurgy, K. Rajamani, F. Rawson, W. Felter, M. Kistler, and T.W. Keller. Energy management for commercial servers. *Computer*, 36(12):39–48, December 2003.

14. M.Y. Lim, V.W. Freeh, and D.K. Lowenthal. Adaptive, transparent fre- quency and voltage scaling of communication phases in MPI programs. In *Proceedings of the 2006 ACM/IEEE conference on Supercomputing*, 2006.

15. A. Marathe, P. E Bailey, D. K Lowenthal, B. Rountree, M. Schulz, and B. R deSupinski. A run-time system for power-constrained hpc applications. In *To appear in the proceedings of ISC*, 2015.

16. J. Nieplocha, B. Palmer, V. Tipparaju, M. Krishnan, H. Trease, and E. Apra. Advances, applications and performance of the glabal arrays shared memory programming toolkit. *International Journal of High Performance Computing Applications*, 20:203–231, 2006.

17. J. Almlo f O. Vahtras and M. W. Feyereisen. Integral approximations for lcao-scf calculations. *Chem. Phys. Lett.*, 213:514–518, 1993.

18. J. Park, D. Shin, N. Chang, and M. Pedram. Accurate modeling and calculation of delay and energy overheads of dynamic voltage scaling in modern high-performance microprocessors. In *2010 International Symposium on Low-Power Electronics and Design (ISLPED)*, pages 419–424, 2010.

19. P.J.Knowles, J.S.Andrews, R.D.Amos, N.C.Handy, and J.A.Pople. Re- stricted mllerplesset theory for open-shell molecules. *Chem. Phys. Lett.*, 186:130136, 1991.

20. M. W. Schmidt, K.K. Baldridge, J.A. Boatz, S.T. Elbert, M.S. Gordon, J.H. Jensen, S. Koseki, N. Matsunaga, K.A. Nguyen, S. Su, T.L. Windus, M. Dupuis, and Jr. J.A. Montgomery. General atomic and molecular electronic structure system. *J. Comput. Chem.*, 14:1347– 1363, November 1993.

21. V. Sundriyal, M. Sosonkina, A. Gaenko, and Z. Zhang. Energy saving strategies for parallel applications with point-to-point communication phases. *J. Parallel Distrib. Comput.*, 73(8):1157–1169, August 2013.

22. V. Sundriyal, M. Sosonkina, F. Liu, and M.W. Schmidt. Dynamic frequency scaling and energy saving in quantum chemistry applications. In *Proceedings of the International Parallel and Distributed Processing Symposium (IPDPS 2011)*, May 16-20 2011.

23. V. Sundriyal, M. Sosonkina, and Z. Zhang. Achieving energy efficiency during collective communications. *Concurrency and Computation: Practice and Experience*, 25(15):2140–2156, 2013.

24. M. Valiev, E.J. Bylaska, N. Govind, K. Kowalski, T.P. Straatsma, H.J.J. Van Dam, D. Wang, J. Nieplocha, E. Apra, T.L. Windus, and W.A. de Jong. Nwchem: A comprehensive and scalable open-source solution for large scale molecular simulations. *Computer Physics Communications*, 181(9):1477 – 1489, 2010.

25. A. Vishnu, S. Song, A. Marquez, K. Barker, D. Kerbyson, K. Cameron, and P. Balaji. Designing Energy Efficient Communication Runtime Systems for Data Centric Programming Models. In *Proceedings of the 2010 IEEE/ACM Int'l Conference on Green Computing and Communications & Int'l Conference on Cyber, Physical and Social Computing*, GREENCOM-CPSCOM '10, pages 229–236, Washington, DC, USA, 2010. IEEE Computer Society.

26. W.J.Lauderdale, J.F.Stanton, J.Gauss, J.D.Watts, and R.J.Bartlett. Many- body perturbation theory with a restricted open-shell hartreefock refer- ence. *Chem. Phys. Lett.*, 187:2128, 1991.

CHAPTER 3. SAVING TIME AND ENERGY WITH OVERSUBSCRIPTION AND SEMI-DIRECT MØLLER-PLESSET SECOND ORDER PERTURBATION METHODS

A paper published in the *Journal of Computational Chemistry*, **2017**, 38 (11), 830–841.

Ellie L. Fought, Vaibhav Sundriyal, Masha Sosonkina, and Theresa L. Windus

Abstract

In this work, the effect of oversubscription is evaluated, via calling 2n, 3n, or 4n processes for n physical cores, on semi-direct MP2 energy and gradient calculations and RI-MP2 energy calculations with the cc-pVTZ basis using NWChem. Results indicate that on both Intel and AMD platforms, oversubscription reduces total time to solution on average for semi-direct MP2 energy calculations by 25-45% and reduces total energy consumed by the CPU and DRAM on average by 10-15% on the Intel platform. Semi-direct gradient time to solution is shortened on average by 8-15% and energy consumption is decreased by 5-10%. Linear regression analysis shows a strong correlation between time to solution and total energy consumed. Oversubscribing during RI-MP2 calculations results in performance degradations of 30-50% at the 4n level.

Introduction

The ability to perform quantum mechanical (or *ab initio*) calculations for very large chemical systems on very large computational resources has made significant progress over

the last 20 years.[1,2] However, the time required to complete the calculations can be lengthy, taking days to even months to complete, and the financial costs of operating the large computational resources can become prohibitive. A 2015 report[3] found that the top petascale computing platforms consume several Gigawatts of electricity every year, equating to millions of U.S. dollars at today's energy prices. Even modestly-sized computational clusters can cost hundreds of thousands of dollars a year to power. Thus, using these high performance computing platforms in the most efficient manner – both in terms of power and in the throughput of computations within a particular power constraint – has become necessary in scientific computing.

Several strategies have been employed in an attempt to either reduce energy consumption over the course of the calculations or shorten execution times. Two prominent strategies are the use of accelerators and dynamically changing hardware parameters. The use of accelerators, such as graphics processing units (GPUs) and Intel's Xeon Phi, has become one of the most effective strategies for reducing execution times for a variety of calculations.[4-6] Since the static power consumption (the power consumed when the computer is not running a job, i.e. the power just to keep the machine up and running) can account for up to 50% of the power consumption,[7] reducing the time to solution will usually lower the energy requirements for the full job. In addition, these accelerator units inherently use less power per unit of computation than their usual CPU counterparts. Eisenbach[8] recently reported reductions in both time-to-solution and energy-to-solution of 8.6x and 7.3x respectively using GPUs for property calculations of very large chemical systems. In the second method, dynamic voltage and frequency scaling (DVFS) of the central processing unit and memory has recently been shown[9] to

reduce energy consumption of calculations with only modest performance degradation. Through judicious application of DVFS strategies within specific phases of different Møller-Plesset Second Order Perturbation Theory (MP2)[10] algorithms, this technique has exhibited up to a 10% overall savings in energy consumption. A 2016 report demostrated[11] the ability of DVFS to reduce energy use up to 20% using Coupled Cluster and Density Functional Theory algorithms with as little as 1% performance degradation.

In this work, we explore the use of oversubscription of the processors as yet another method to decrease the total time to solution and lower the overall power consumption of a computational job. In addition to being an effective tool, it is also a relatively simple method to use on today's computational resources. Oversubscription is one of many manifestations of multi-threading and involves executing tasks by calling for more *processes* (or threads) than the number of physical cores that exist, typically as some integer multiple of the system's available physical cores. In a computer architecture context, "multithreading is the ability of a CPU, or a single core in a multi-core processor, to execute multiple processes or threads" simultaneously.[12] Previous applications of multithreading in computational chemistry have involved very large biological systems (>1000 atoms) such as proteins and required additional middleware software,[13] such as OpenMP. Other computer science approaches involve job scheduling strategies or algorithms designed to incorporate multithreading to more efficiently use cluster resources.[14,15] Another strategy of note involving the TERA MTA architecture employed multithreading by reprogramming Hartree-Fock, successfully speeding up execution times by as much as 8x.[16] One appeal of oversubscribing is that no additional hardware or software is required and only a small number of environment

variables need to be set appropriately. To be clear, no changes are required in either the computational code or operating system. In 2010, Iancu showed[17] that moderate levels of oversubscription had positive effects on coarse-grained applications, or applications with many millisecond inter-barrier intervals. Coarse-grained applications were shown to speed up or be unaffected when executed with oversubscription. The reason for the performance gain is that the operating systems have become very efficient at swapping idling tasks (those doing I/O, for example) with other active tasks to ensure that the processor is kept busy. This observed behavior was both architecture and programming model independent, and throughput was increased by as much as 27% when oversubscribing at 2, 4, and 8 tasks per physical core.

We chose to test the effects of oversubscription on MP2 algorithms within the NWChem computational chemistry package, version 6.5.[18] MP2 is a suitable candidate for many reasons. First, MP2 is one of the computationally cheapest correlation methods beyond density functional theory, with the added benefit of being part of a systematically improvable ansatz. Additionally, multiple algorithms exist for the MP2 single point energy calculations within NWChem, with semi-direct and the resolution of the identity MP2 (RI-MP2) approximation being the two energy algorithms examined in this work due to their differing hardware requirements. The semi-direct MP2 method calls on both the local memory and the hard disk to perform the integral transformations, and, therefore can have lengthy periods of I/O. Alternatively, RI-MP2 employs the mathematical theory of the resolution of the identity to approximate four-center molecular integrals with products of three-center integrals[19] - all integral transformations taking place in memory. Employing the RI-MP2 method requires the use of a larger auxiliary basis set and has the

highest requirements for memory access of the two MP2 algorithms. Since these are two fairly standard methods, the reader is referred to the references for the details of the theory. However, details of the hardware requirements for different parts of the algorithms will be examined and explained during the rest of the paper.

In this paper, we will demonstrate the very real ability of oversubscription to improve the performance of semi-direct MP2 algorithms. We employ these strategies with no additional hardware or software, only changing the number of MPI processes called. On the Intel platforms, as much as a 45% reduction in execution time (total wall time) for MP2 semi-direct energy calculations and up to a 25% reduction in execution time for MP2 semi-direct gradient calculations were observed. RI-MP2 on the other hand did not show these same improvements for reasons given throughout the paper. The rest of the paper is organized in the following manner: The computational approach including the hardware, software and test chemical systems is described in the next section. This is followed by the results of the testing, which is followed by the conclusions.

Methods

Hardware

This work was performed on two distinct platforms to show generality of the use of oversubscription across computational systems. The first system, Bolt, contains 6 Intel E5-1650 cores with 64 GB of DDR3 RAM @ 1600 MHz. The second platform, TheBunny, consists of a dual-socket, 24 core NUMA node containing AMD Opteron 6344 Abu Dhabi processors, also with 64 GB of DDR3 RAM @1866 MHz. Both platforms have 7200 rpm SATA disks. Only one node on each platform was used to

perform the tests. More information in cache levels, physical memory and architecture can be found in the supporting information (SI). Certainly communication between nodes is important to the overall performance of the software, however, most of the power usage is on the node and it is easier to obtain power information from one node than from multiple nodes. Future work will examine the effects of the communication infrastructure on the power usage.

Software

On Bolt, iMPI version 5.0.217[20] was chosen as the message passing interface (MPI). The MPI chosen for use on the TheBunny was MVAPICH2-2.0.[21] As NWChem already contains internal BLAS and LAPACK libraries, for generality purposes, no external math libraries were included in the NWChem builds on either platform. The source code was compiled with GNU gcc and gfortran compilers, version 4.4.7[22], on Bolt and Intel's[23] icc and ifortran 2013, Update 5 on TheBunny. The different compilers were chosen based on their availability on the respective clusters. NWChem needs to be compiled appropriately and complete lists of environment variables for both architectures are included in the SI. Additionally, on Bolt, the Intel Running Average Power Limit (RAPL) software[24] was used to obtain both CPU and DRAM power usage throughout the calculations. All calculations were initiated via the `mpirun` command, with the `-np` option used to specify the number of processes to be used.

Within the NWChem input files, default settings and options were used with a few exceptions. First, a total memory directive was given allocating varying amounts of memory to be used depending on the size of the system. Larger amounts of memory

were used for the MP2 gradient calculations compared to the MP2 semi-direct energies. The amount of memory allocated for the individual systems can be found in the supporting information. Additionally, the orbitals were read in from previous self-consistent field (SCF) calculations using the tighter MP2 convergence tolerances to focus the calculations on the MP2 portion. Lastly, core orbitals were frozen as is standard for most MP2 calculations.

Chemical Systems

For this work, 18 different chemical systems of varying size and molecular shape were tested. Each system was categorized into one of 6 size categories, as well as one of three dimensions (3D, 2D, and 1D). This latter categorization was to determine whether screening effects have any influence on the overall benefit of oversubscription. A summary of all systems, including the chemical formula and number of basis functions corresponding to the cc-pVTZ spherical basis set,[25] can be found in Table 1. Due to the requirement of an auxiliary basis set for RI-MP2 calculations, the slightly smaller aug-cc-pVDZ basis was used for the orbital basis set with aug-cc-pVTZ as the auxiliary basis.[26] The coordinates as well as the memory allocated on both platforms for all 18 chemical systems can be found in the supplemental information. Each test set geometry was optimized at the MP2/cc-pVTZ level of theory.

Three different MP2 algorithms were tested on Bolt: semi-direct energy, semi-direct gradient, and RI-MP2 energy calculations. With 6 physical processes per node, three levels of oversubscription were tested by calling 6, 12, 18, and 24 virtual processes (i.e. 1*n*, 2*n*, 3*n*, and 4*n* respectively). For the semi-direct MP2 energy algorithm,

calculations for all 18 systems were performed. Based on the results on Bolt, only the semi-direct energy algorithm was tested on TheBunny. Calculations on TheBunny for each of the 18 test systems were performed using three levels of oversubscription, calling 24, 48, 72 and 96 virtual processes on 24 physical cores. All calculations were performed in triplicate and all times reported are averages of the three jobs.

Table 1. Identification and organization of 18 molecular systems for oversubscription tests into 3D, 2D and 1D categories. The first column gives the range of number of basis functions. For each of the center cells, the number of total basis functions and the chemical formula are given.

Sizes	1D	2D	3D
350-400	366 C_6H_9ON	382 C_9H_8	408 $C_6H_{12}O_2$
600-650	626 $C_9H_{19}O_2N$	618 $C_{15}H_{12}$	608 $C_{10}H_{22}$
800-850	858 $C_{13}H_{27}O_2N$	824 $C_{19}H_{16}O$	844 $C_{13}H_{26}O_3$
1000-1050	1056 $C_{20}H_{24}O_2N_2$	1022 $C_{19}H_{28}O_2$	1046 $C_{17}H_{34}O_2$
1200-1300	1262 $C_{22}H_{28}O_7$	1214$C_{24}H_{31}ON$	1306 $C_{21}H_{44}O_2$
1500-1600	1580 $C_{28}H_{40}O_6$	1608 $C_{31}H_{42}O_3$	1626 $C_{26}H_{54}O_3$

Results and Discussion

Semi-direct MP2 energy results-Bolt

For all 18 chemical systems evaluated, execution at every level ($2n$, $3n$, $4n$) of oversubscription was successful in reducing the total (wall) MP2 times of the semi-direct energy calculations on Bolt. The optimal number of virtual processes to call varies by chemical system, but the largest improvements in performance occurred at the $3n$ or $4n$ levels. For the 12 largest chemical systems tested, the average improvements in

performance range between 20 and 30 percent, in some cases representing over two hours in actual time saved. Furthermore, energy savings of up to 20 percent were observed in conjunction with oversubscribing at the 3*n* and 4*n* levels. The overall trends in performance improvement were consistent throughout all three spatial categories. However, as the spatial complexity of the molecules increased from 1D to 3D systems, the total MP2 execution time also increased, which was to be expected based on electron screening arguments. Figure 1 provides the average execution times of all 18 systems at each of the three oversubscription levels tested. The times in Figure 1 are normalized by the number of basis functions representing each system and the results are organized by dimension, size, and number of processes called.

On a subroutine level within the MP2 calculation, the effects of oversubscription are more pronounced. Within the semi-direct MP2 energy algorithm there are two main subroutines: "moin" and "make." The "moin" subroutine consists of the integral transformations from the atomic to molecular orbitals and accounts for 80-90% of the total MP2 calculation under normal conditions (one process per core). As the number of processes called increases, the total (wall) times for the moin subroutine drop dramatically. Average reductions in execution times range from 25-30% at the 2*n* level to 40-45% at the 4*n* level. This result is unsurprising due to the lengthy periods of I/O that can arise throughout the molecular integral transformations. These extensive periods of communication lead to inter-barrier intervals several seconds to minutes in length making this portion of the semi-direct MP2 energy algorithm an ideal candidate for use with oversubscription.

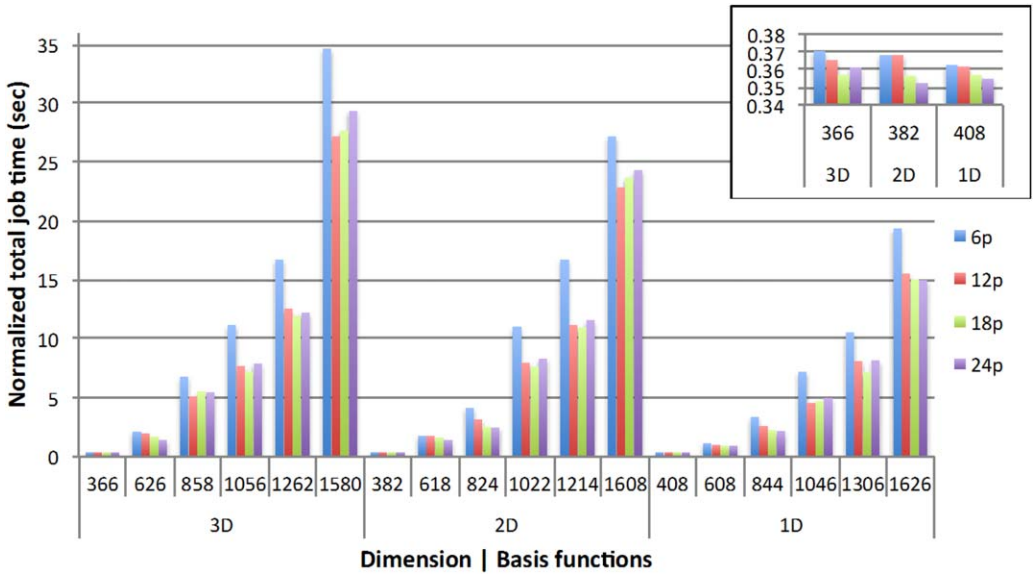

Figure 1. Average total execution times normalized by the number of basis functions for semi-direct MP2 energy calculations on Bolt (Intel). The times displayed are arranged first by dimension, then further organized by number of basis functions for each structure. The inset in the top right corner of the figure is an enlarged chart of the three smallest chemical systems.

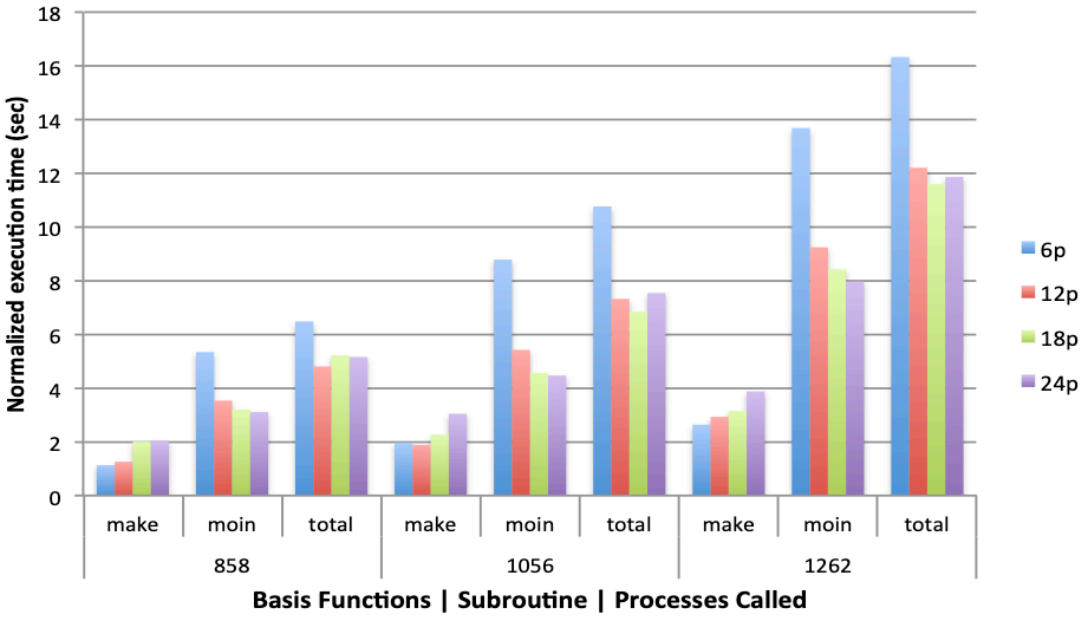

Figure 2. Average wall times for the "make" and "moin" subroutines, as well as the total MP2 time of the semi-direct MP2 energy calculations. The execution times have been normalized by dividing the average wall time by the number of basis functions used in the calculation.

Conversely, the "make" subroutine experiences rising execution times in conjunction with higher levels of oversubscription. The "make" subroutine accounts for the remaining 10-20% of the total MP2 time and consists of the formation of the MP2 energy using the newly transformed molecular integrals. At the highest oversubscription level, the "make" subroutine experiences performance losses ranging from 40-50%. However, considering the relatively small proportion of the total MP2 calculation that "make" represents, the overall effect is minimal.

The increases in "make" execution time may be due to the absence of any extended I/O periods and extended computational periods. Power trace analysis shows sustained CPU usage with the only I/O occurring at the very end of the subroutine. In a few rare cases, oversubscription actually reduces total "make" times, but we see no obvious explanation for this phenomenon. The cumulative effect of oversubscribing on semi-direct MP2 energy calculations is definitively positive, with total MP2 execution times consistently reduced (compared to execution under 6 processes) at every level for all but the smallest chemical systems. The time saved on the molecular integral transformations is consistently 5-10 times longer than the time added to the energy calculation, resulting in a net performance gain. In Figure 2, this trend is highlighted with a selection of 3D systems tested.

In addition to significantly reducing overall execution times, power trace analysis shows oversubscription also lowers the net energy requirements for semi-direct MP2 energy calculations. Nine of the 18 systems were evaluated, including the 600-650, 800-850, and 1000-1050 basis function subsets. Power evaluation for the larger systems were not performed since measuring the power of the components becomes cumbersome when

the calculations take longer than a few hours. The average total energy consumed by the CPU is around four times greater than the energy consumed by the DRAM. This power usage ratio is consistent across all sizes and dimensions measured. Oversubscribing leads to a 10-20% drop in the average DRAM energy consumed and a 10-15% drop in average CPU energy consumed, with average overall savings of 10-15% in power between the two components. Average energy savings for the two smaller subsets with oversubscription were 5-10% higher for the 2D and 3D systems compared to that of the 1D structures; however, within the 1000-1050 systems, average energy savings were comparable across all three dimensions. Figure 3 illustrates this trend, as well as provides a breakdown of each system executing under 1*n* and all three levels of oversubscription. Presented in Figure 3 are the relative percentages of energy consumed at the three levels of oversubscription compared to execution using 6 processes for the CPU, DRAM and the total (sum of the two components).

Closer investigation of the power consumption at the different levels of oversubscription provides insight as to where the energy savings are coming from. Provided in Figure 4 are power trace plots of the CPU and DRAM for the chemical system with 824 basis functions. When operating under only 6 processes, there are defined periods of reading and writing to disk during the "moin" subroutine, illustrated by the sharp drop in CPU power.

As the number of virtual processes increases, those periods of reading and writing become less defined until, at 24 processes, the different intervals are barely discernible. This suggests that the operating system is doing a good job of swapping out idle processes to keep the CPU busy. Linear regression, provided in Figure 5, shows a strong

relationship between the raw execution times in seconds and the total CPU energy, total DRAM energy, and the sum of the total energy consumed by the two components for all nine chemical systems evaluated. This linear relationship supports the idea that reducing the execution times will indeed result in lower energy requirements overall. Additional profiling of the CPU and memory components were performed on a select number of chemical systems using the vmstat tool within Linux. The vmstat profiling tool provides a breakdown of the CPU resources, including the percentages of CPUs in use by the user and the system, as well as the percentages of CPUs idling, waiting for I/O, and stalled. Measurements were taken once a second for the duration of the whole calculation. By plotting the per-second percentage of CPUs waiting for I/O over the course of the semi-direct energy jobs, differences between the levels of oversubscription are more apparent. Similar to the power trace analysis, it is only during the "moin" subroutine where significant effects of oversubscription are observed.

Throughout the molecular integral transformations, extended periods of I/O can appear, indicating the presence of bottlenecks. During these I/O-intensive intervals, CPU efficiency drops significantly due to the prolonged periods of waiting for I/O to be completed. As the oversubscription level rises, these intervals of waiting get shorter and the average percentage of CPUs waiting drops significantly. These trends are highlighted in Figure 6, which contains the percent of CPUs waiting for I/O versus time for 6 processes, as well as all three levels of oversubscription for the 1D system with 608 basis functions. The average CPU I/O wait time for a single processor was calculated for each of the three chemical systems profiled using the vmstat tool, and can be found in Table 2. Oversubscription was shown to reduce average wait times over 50% using 2n processes

and as much as 80% using 4n processes. These reductions in CPU wait time result in improved overall efficiency of the CPUs during extended periods of I/O.

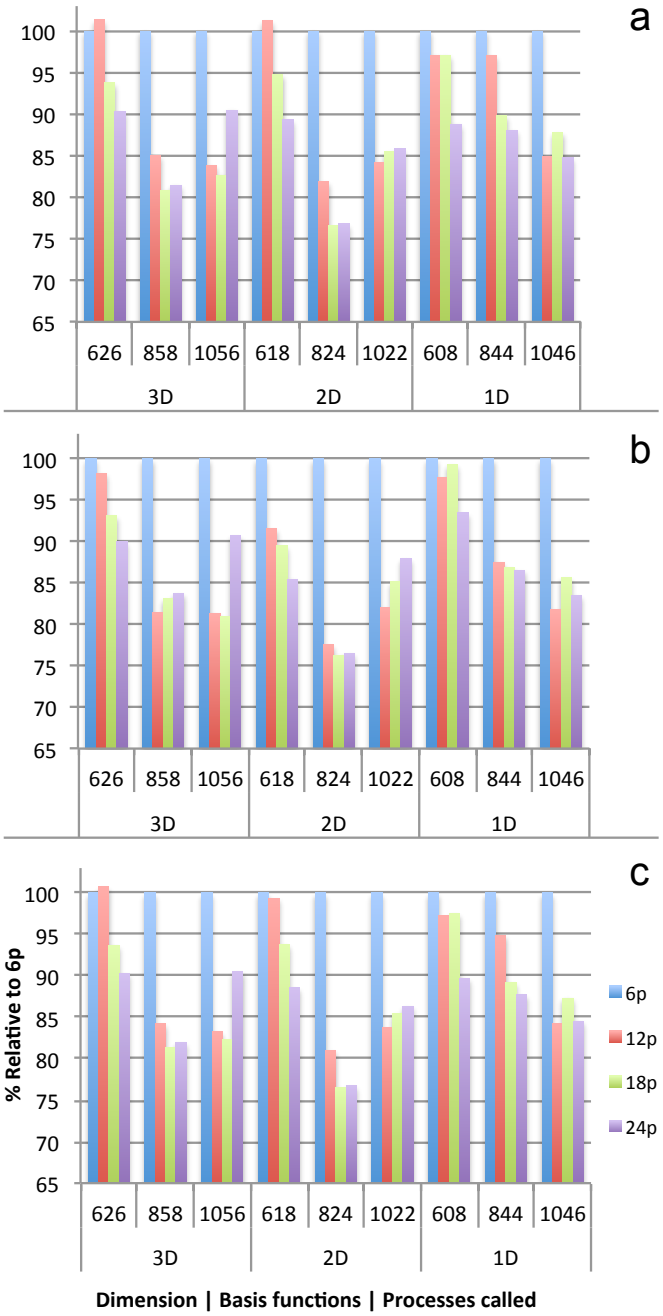

Figure 3. Relative percent of energy consumed by the (a) CPU, (b) DRAM, and (c) the sum of the two components for all nine chemical systems analyzed. Total average energy consumption drops by 10-20% depending on the level of oversubscription.

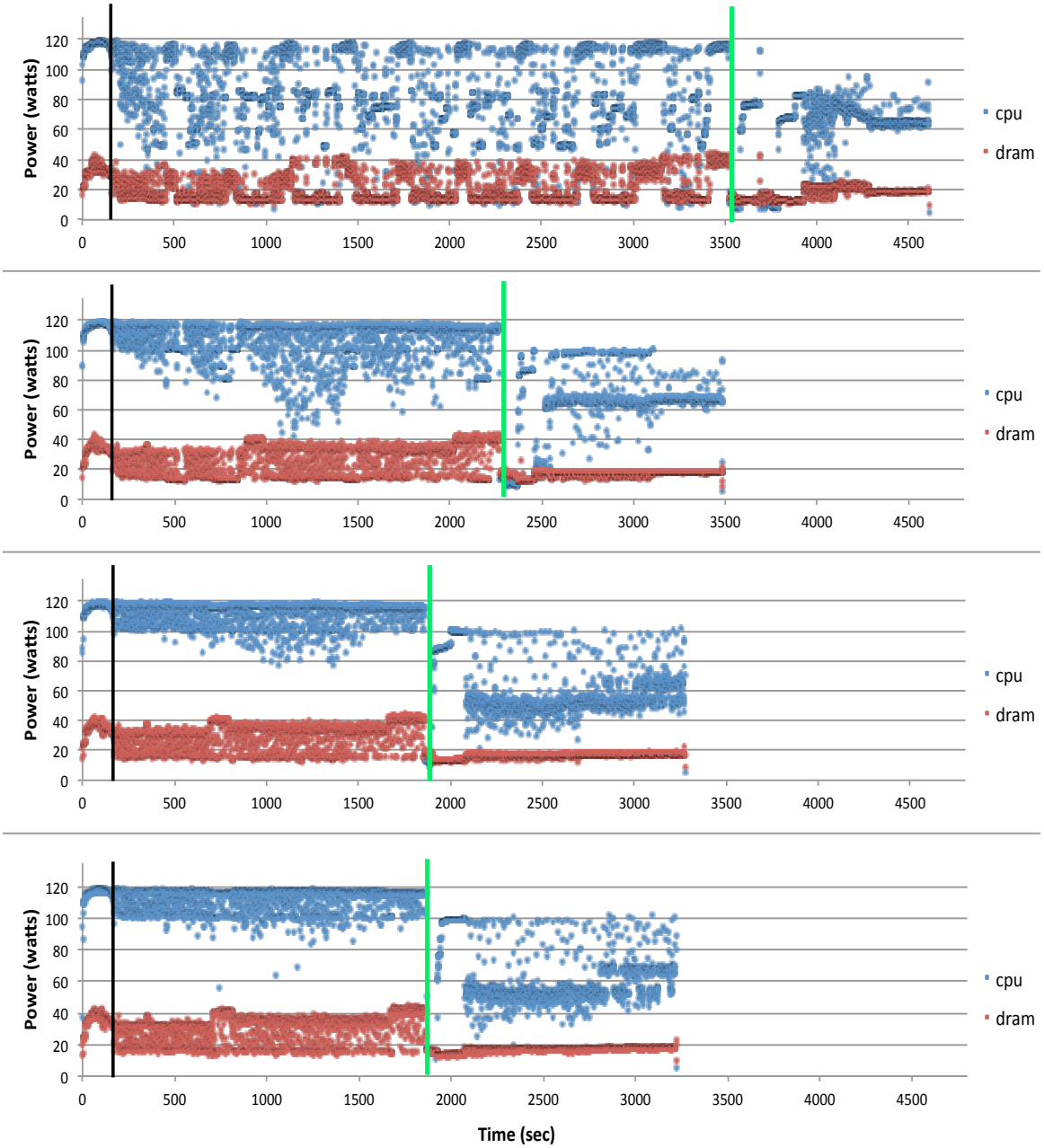

Figure 4. Power traces for the 3D system of 824 basis functions for both the CPU (blue) and the DRAM (red). Traces from top to bottom are: 6 processes, 12 processes, 18 processes, and 24 processes. As the oversubscription level rises the average power usage of both the CPU and memory become more uniform, causing an increase in instantaneous power but an overall drop in total energy consumption. The individual subroutines are separated by the green line with "moin" to the left and "make" to the right.

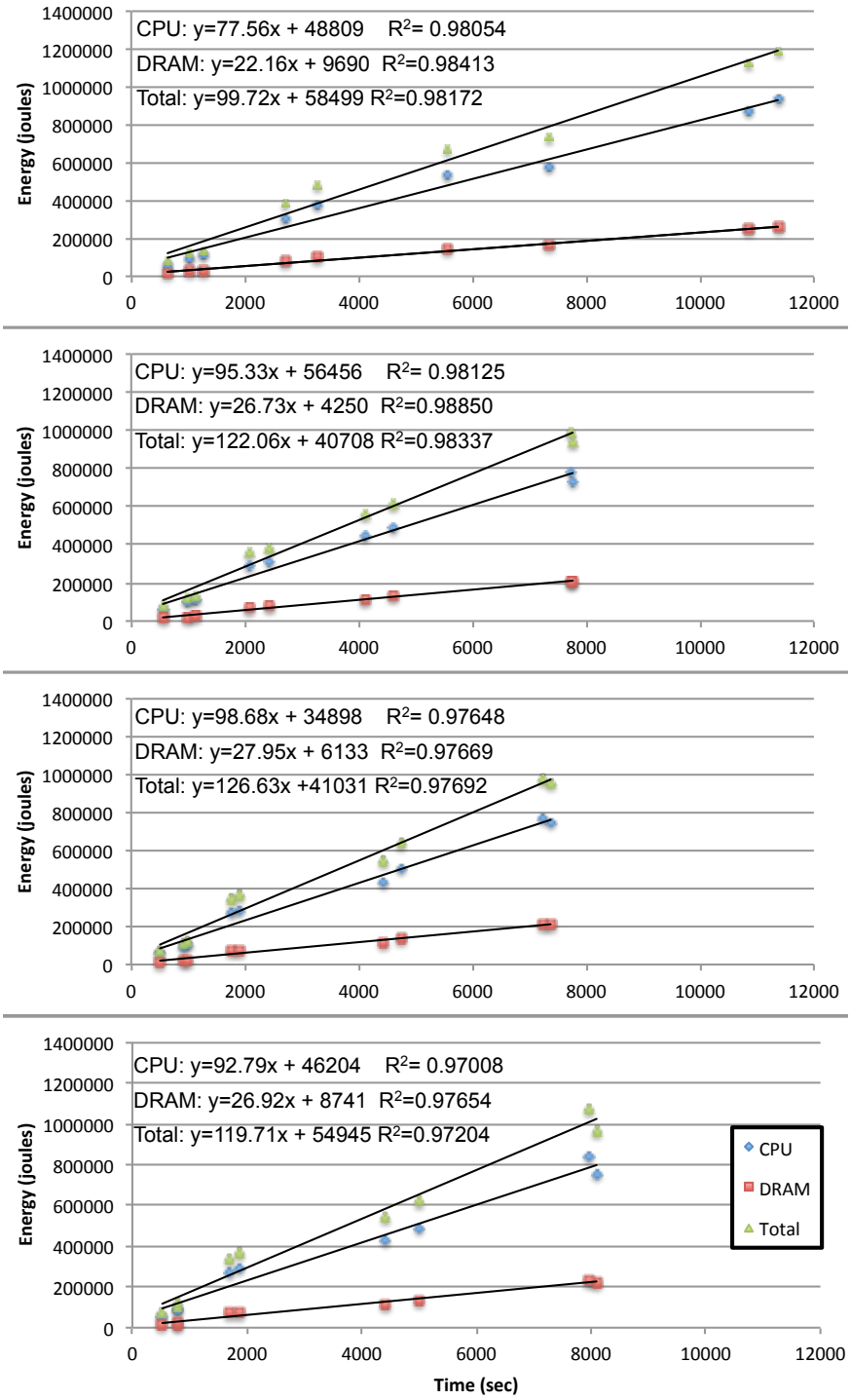

Figure 5. Linear regression plots showing total energy consumed versus total average execution times displayed from top to bottom for 6, 12, 18, and 24 processes respectively. For each level of oversubscription, the R^2 values are provided for the DRAM, CPU, and total energy (sum of two components).

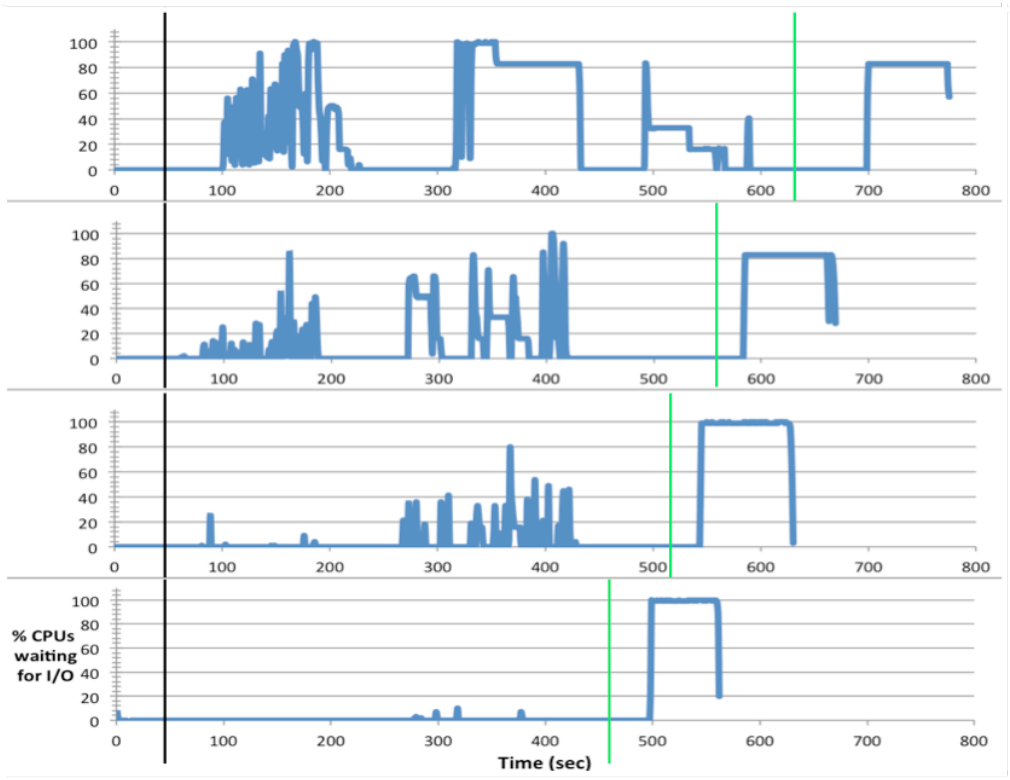

Figure 6. Percentage of CPUs waiting per second for the 608 basis function system. Plots from top to bottom: 6 processes, 12 processes, 18 processes, 24 processes. The black lines separate the plots into the three main subroutines from left to right: SCF energy, "moin," and "make."

Table 2. Average CPU wait time (sec) per physical process for 600-650 basis function subset.

Oversubscription level	608 functions	618 functions	626 functions
1n	229	319	361
2n	118	134	122
3n	96.8	79.8	111
4n	63.3	64.5	66.8

Semi-direct MP2 gradient results-Bolt

As with the semi-direct energy calculations, the execution time for the semi-direct MP2 gradient calculations were also shortened in conjunction with the use of oversubscription. Improvements in gradient wall times ranged from 8-15%, and the optimal amount of oversubscription again varied by chemical system. Figure 7

summarizes the average wall times for all systems tested normalized by dividing by the number of basis functions for each system. Trends in the total execution times are similar to those in the energy wall times with total computation times rising dramatically as the systems become more three-dimensional. The lower overall effectiveness of oversubscription on the gradient jobs can be explained by the higher complexity of the calculations. The semi-direct MP2 gradient algorithm consists of eleven main subroutines, the first two being the same two subroutines found within the semi-direct MP2 energy algorithm, "moin" and "make." Of the remaining nine subroutines, eight are compute-intensive. The "pija" forms the second-order density matrix, "wija" and "wijf" form the initial and final energy-weighted density matrices, "lai" and "laif" calculate the initial and final Lagrangian matrices, "cphf" is the coupled-perturbed Hartree-Fock calculation, and "nons" and "sep" calculate the non-separable and separable parts of the MP2 two-particle density matrix respectively. Following the formation of the initial Lagrangian matrix, the "back" routine is the back-transformation of the doubles coefficients a_{ij}^{ab} to the atomic orbital basis. Similar to the "moin" subroutine, the "back" transformation has considerable I/O throughout. As with the semi-direct energy calculations, "moin" execution times were reduced significantly, typically between 30-50%, with the greatest improvements occurring at the highest oversubscription levels.

Unlike the semi-direct energy calculations, the "moin" subroutine only accounts for 10-15% of the total execution times of the semi-direct gradients, so the overall benefit is not as obvious. Similarly, the "make" subroutine sees performance losses by as much as 40%, but also accounts for significantly less of the gradient calculation, never representing more than 10% of the total calculation time. The I/O-intensive "back"

subroutine also benefits significantly from oversubscription, with execution times reduced by 20-40%. Of the eight compute-intensive subroutines listed above, "nons" is the only one to benefit from oversubscription with modest performance improvements of 3-6%. None of the remaining seven subroutines experienced more than a 10% rise in execution time at any level of oversubscription, most displaying moderate increases of 2-5%. Furthermore, only three of these seven routines regularly account for more than 10% of the total compute time, namely "lai," "cphf," and "nons." It is noteworthy that the "lai" subroutine, which regularly accounted for more than 20% of total execution time was minimally affected by oversubscription. From this we concluded the duration of a particular subroutine is not necessarily a determining factor in the overall effect of oversubscribing.

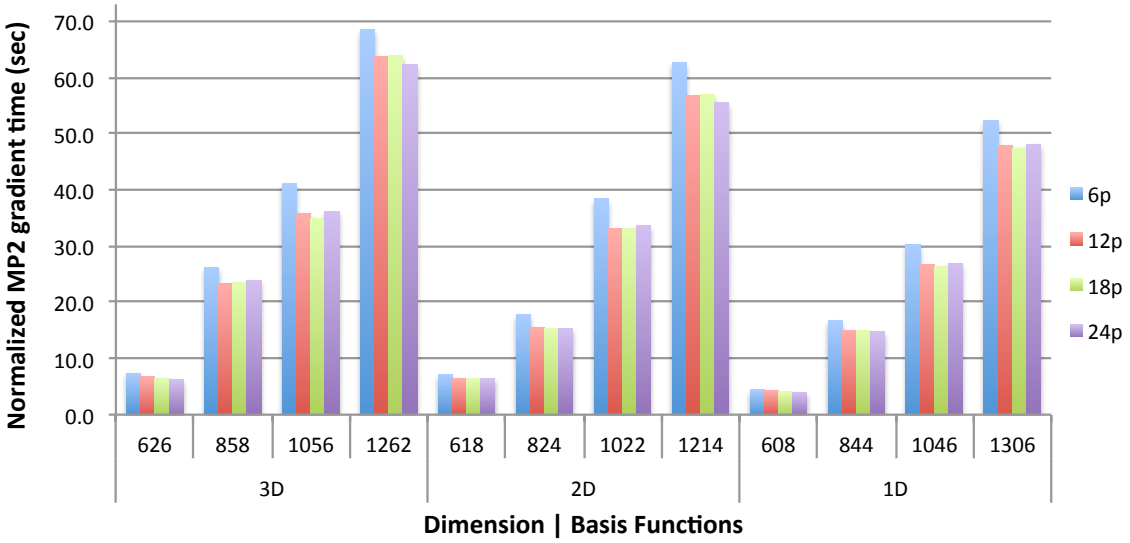

Figure 7. Average normalized total execution times for semi-direct MP2 gradient calculations on Bolt (Intel). The times displayed are arranged first by dimension, then by number of basis functions for each structure. Within the semi-direct gradient tests, performance improvements of 8-15% were observed.

Energy savings were also observed when testing the semi-direct MP2 gradients with oversubscription. The sum of the energies consumed by the CPU and DRAM resulted in average total energy savings of 5-10% with the largest savings occurring when using 3*n* processes. As with the semi-direct energy calculations, average total energy savings from oversubscribing are comparable across all three dimensional categories of structures. The total energy savings of the systems whose power was traced can be found in Figure 8. Regression analysis again shows a linear relationship between the total time to solution and total energy consumed with R^2 values around 0.9. Regression plots for the gradient calculations have been omitted for brevity, and can be found in the supporting information. Power trace analysis displays similar trends in the behavior of the I/O-intensive subroutines, "moin" and "back," where the individual periods of reads

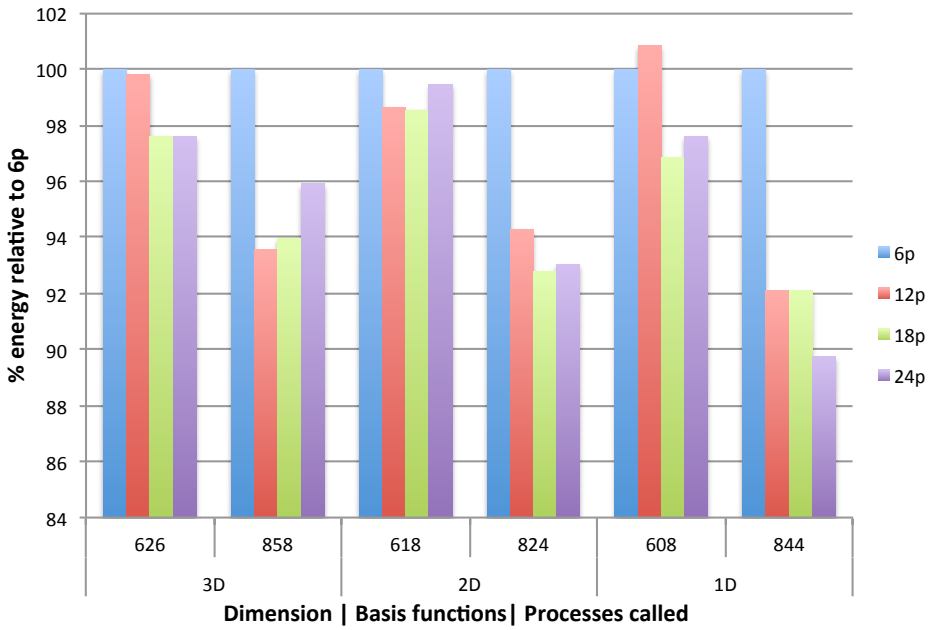

Figure 8. Relative total energy consumed for 6 different system sizes for semi-direct MP2 gradient calculations on Bolt. Total average energy is the sum of the CPU and DRAM average energy consumed at each size and number of processes called. Oversubscription of MP2 gradient calculations resulted in 5-10% total energy savings.

and writes become indistinguishable as process number increases and average power requirements become more uniform. Power trace plots for each level of oversubscription for the 2D, 618 basis function system can be found Figure 9. The individual power traces are broken down by subroutine, and contiguous subroutines with similar power requirements are grouped together.

Semi-Direct energy results-TheBunny

Semi-direct energy calculations on TheBunny produced similar trends as were observed Bolt. For all but the three smallest systems, oversubscription was successful in reducing total MP2 execution times. Unlike on Bolt, semi-direct MP2 energy calculations for the 350-400 basis function subset were adversely affected by all three levels of oversubscription. Both main subroutines were significantly impacted, with "moin" execution times rising by as much as 20%, resulting in total MP2 times increasing by as much as 42% when executing with 96 processes. For the remaining nine systems tested, oversubscribing reduced MP2 execution times by as much as 68%, with the largest improvements taking place with the biggest chemical systems. On TheBunny, as was observed on Bolt, oversubscription was consistently more effective in reducing total MP2 times for the more spatially complex systems. A key difference observed on TheBunny was the proportions of the total MP2 time each subroutine represented. The "moin" subroutine accounted for no less than 79% of the total MP2 times for any system, and at the largest sizes consistently represented more than 90% of the MP2 computation time. Therefore, it follows that the total MP2 wall times would be closely tied to "moin" execution times, and this relationship is illustrated in Figure 10, the percent change in

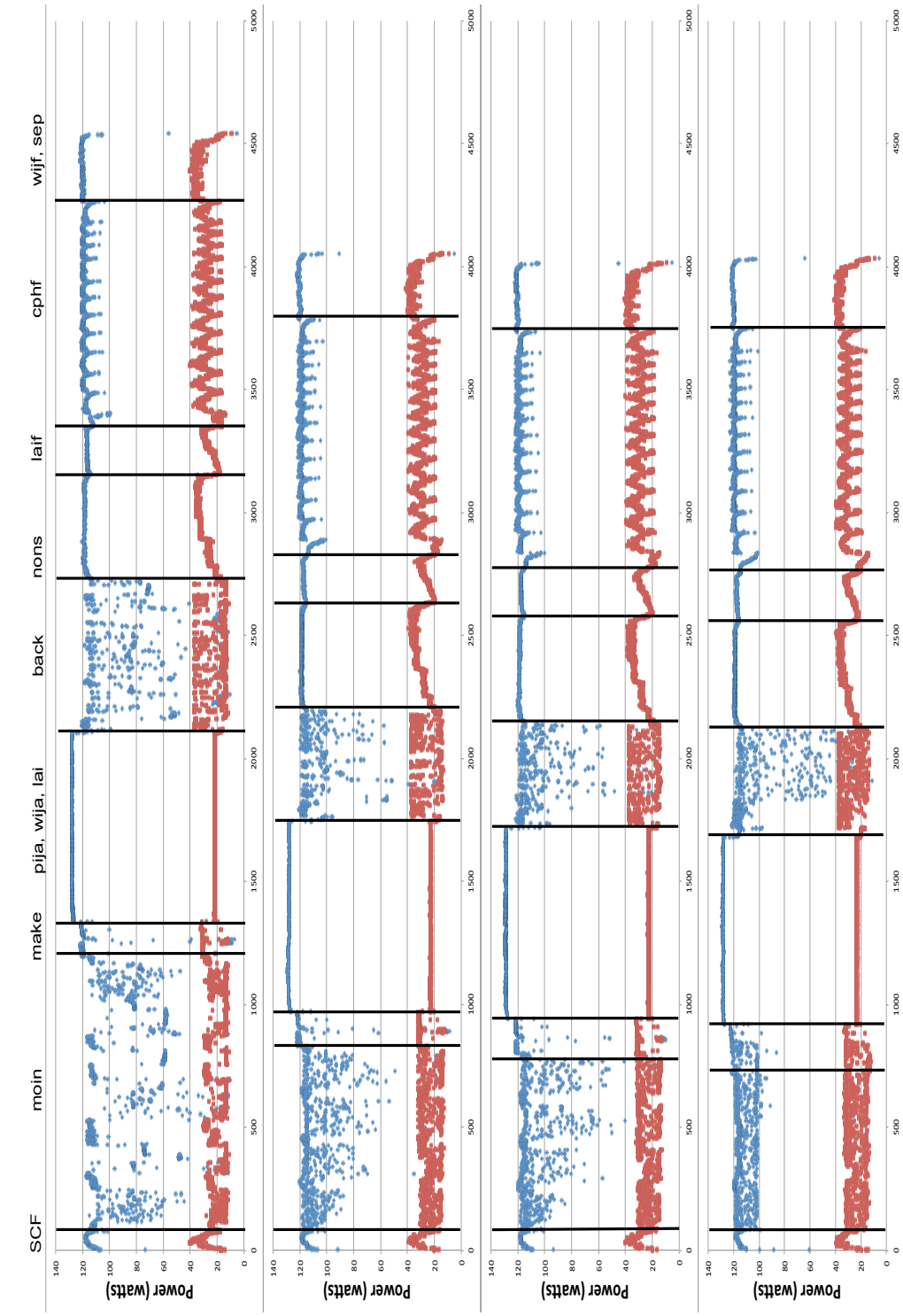

Figure 9. Power traces for the 2D system of 618 basis functions for both CPU (blue) and DRAM (red). Traces from top to bottom are: 6 processes, 12 processes, 18 processes, and 24 processes. The regions of time subroutines represent are separated by the black lines and are labeled at the top of the figure.

execution time for the "moin" subroutine and the total MP2 time of each system tested. The percent change shown is relative to the execution times when operating with 24 processes (1*n*).

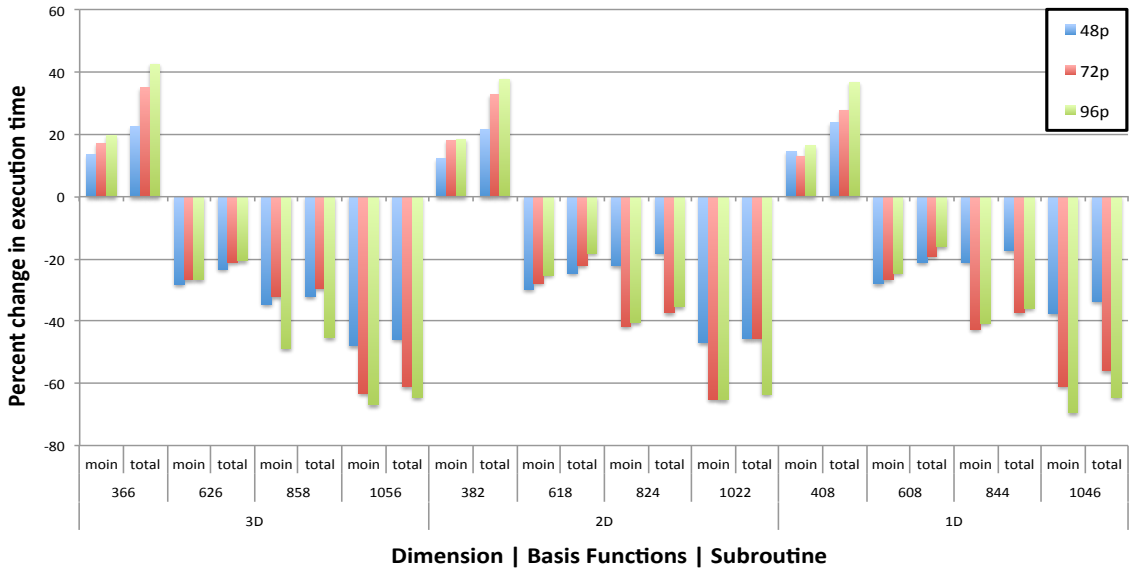

Figure 10. Percent change in execution times for semi-direct MP2 calculations on TheBunny compared to computation using 24 processes. The "moin" subroutine consistently accounts for more than 80% of the total MP2 calculation time, and for all but the 350-400 basis function subset is closely related to the change in total MP2 time.

RI-MP2 energy results-Bolt

The RI-MP2 energy calculations were negatively affected systematically by oversubscription, with execution times rising as the number of processes called increased. Total wall times increased when executing with 2*n* processes by 7-15%, at 3*n* by 22-35%, and at 4*n* by 28-50%. The extent to which execution times rose was partially dependent on the dimension of the structure. The linear chemical systems experienced as much as a 50% increase in wall times as compared to the more 3D structures that saw a maximum of 34%. These results are summarized in Figure 11 with average total execution times

organized by dimension and system size. A different basis set was used for these calculations due to the need for an auxiliary (fitting) basis set, so the chemical formulas and number of corresponding aug-cc-pVTZ basis functions for all six systems tested can be found in the supporting information. The RI-MP2 energy algorithm contains thirteen subroutines, and nine consistently required less than five seconds to complete. The dramatic increases in total execution times can be attributed to the "formA" subroutine, which regularly accounted for more than 85% of the added time to solution. This relationship between total time to solution and "formA" wall times is illustrated in Figure 12. The times provided are raw execution times as opposed to the normalized times provided for the semi-direct methods.

The vmstat profiling tool was also used with RI-MP2 calculations in an attempt to better understand why oversubscription was adversely affecting this method. In addition to providing a breakdown of system resources, the vmstat profiling tool also records the number of context switches per second. When running calculations with no

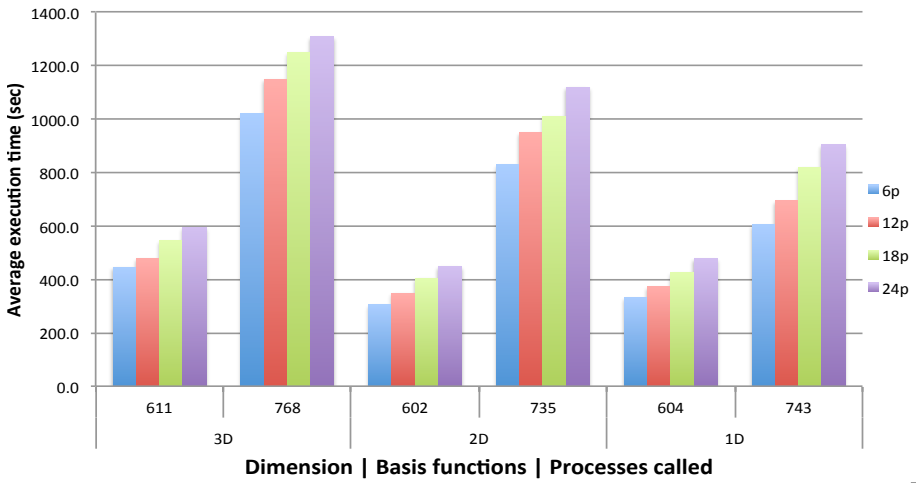

Figure 11. Average total wall times (sec) for RI-MP2 energy calculations. Times are organized first by dimension and then by system size. Linear chemical systems experienced the largest performance losses, as high as 50% at the 4*n* level.

oversubscription, the number of context switches is consistently between 1100-1500 per second. Oversubscribing at the 2*n*, 3*n*, and 4*n* levels, results in prolonged periods with rates of 105-107 context switches per second at the end of the calculations. These sustained periods of context switching coincide with the computations of the "formA" subroutine at each level of oversubscription. Additional analysis of the "formA" algorithm revealed multiple copies of patches of matrices to the memory, which results in large numbers of context switches when processor resources are divided. The increases in context switching could be explained in terms of the rate of transfer of data to the multiple tasks running on a single core. Since the main memory is able to supply data to the processes competing for the scheduling time slice at a much faster rate than a mechanical hard drive (due to its location being on-chip and the availability of multiple channels of data), the relative of context switches increases substantially.

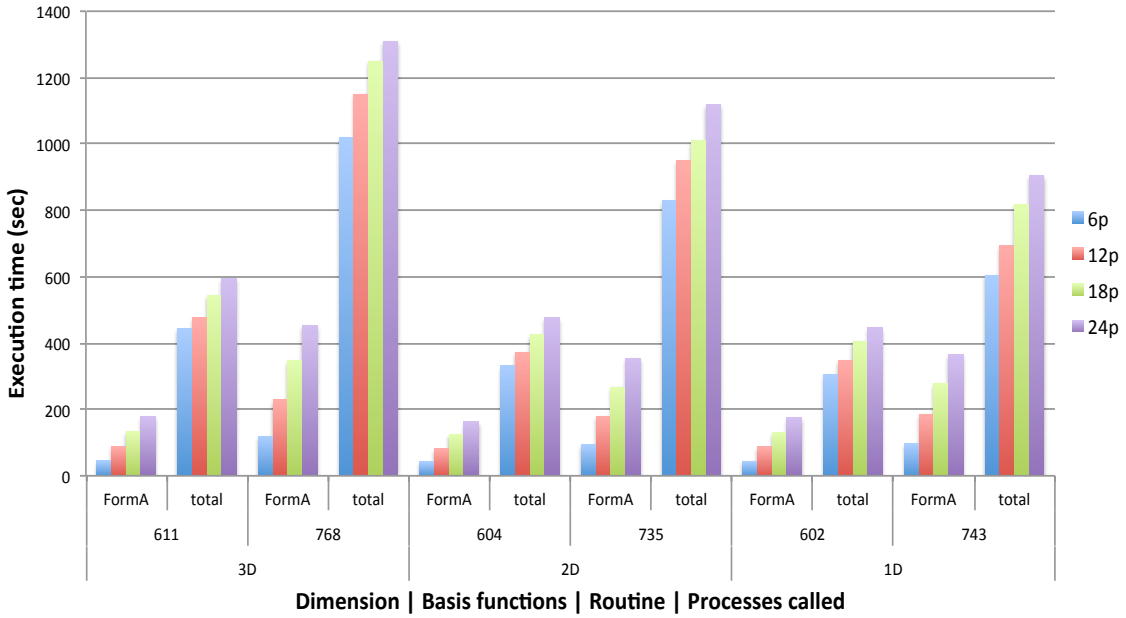

Figure 12. Raw average execution times for the "formA" subroutine and total RI-MP2 calculation for all 6 chemical systems tested separated by dimension and basis functions.

Conclusion

Throughout this work, it has been demonstrated that oversubscription in conjunction with semi-direct MP2 methods consistently reduced total time to solution. On both Intel and AMD platforms, significant performance improvements were observed when performing semi-direct MP2 energy calculations using the cc-pVTZ basis. On Bolt (Intel) total MP2 execution times were reduced on average by 25-45% with the largest improvements taking place at the 3*n* or 4*n* levels, most likely due to increased I/O throughput. On TheBunny (AMD) oversubscription was even more effective in improving performance with the largest systems experiencing a 45-65% drop in total MP2 wall times. The average improvements in performance were consistent across all three dimensions of chemical systems tested for both the Intel and the AMD architectures. On both platforms, the most significant effects of oversubscription were observed within the "moin" subroutine, which consists of the molecular integral transformations. Along with substantial time savings, power trace analysis showed oversubscription also reduced total energy consumption by the CPU and DRAM between 10-15% for the semi-direct MP2 energy calculations. Linear regression analysis shows a strong correlation between time to solution and total energy consumed, leading us to reasonably conclude that even modest reductions in execution time through oversubscription could result in non-negligible energy savings.

Semi-direct gradient calculations provided similar results, with average savings in total execution times of 8-15%. Only three of the eleven subroutines (moin, make, back) within the semi-direct MP2 gradient algorithm were regularly affected by oversubscribing, with most only experiencing changes as high as 5%. Notable energy

savings of 5-10% were also seen with oversubscription. Along with the semi-direct MP2 energy results, there is strong evidence that oversubscription can improve performance of I/O-intensive algorithms, such as "moin" and "back", while only modestly affecting the remaining subroutines. A more fine-grained application of oversubscription, specifically targeting I/O-intensive functions, has the potential for even larger savings of time and energy.

The results of oversubscription with RI-MP2 calculations demonstrate that this technique is not appropriate for all computational work. RI-MP2 execution times rose linearly as the level of oversubscription increased. The "formA" subroutine, which contains a large number of copy patches to memory, was the most adversely affected by oversubscribing. During the execution of the "formA" subroutine, context switching was found to rise dramatically at the $2n$, $3n$, and $4n$ levels, resulting in significant system overhead and performance degradation.

While I/O intensive algorithms are not usually prescribed for very large, high performance machines, chemists often have large amounts of disk on their local clusters. Therefore, this analysis could have a significant benefit to performance and energy usage of moderate sized resources for computations that involve disk I/O. These techniques may also be applied to higher-order methods that display extended periods of disk I/O or communication. Future work will analyze the conclusions of this work while also taking into account issues associated with communication between nodes.

Acknowledgments

This work was supported in part by the Air Force Office of Scientific Research under the AFOSR award FA9550-12-1-0476, by the U.S. Department of Energy, Office of Advanced Scientific Computing Research, through the Ames Laboratory, operated by Iowa State University under contract No. DE-AC02-07CH11358, and by the U.S. Department of Defense High Performance Computing Modernization Program, through a HASI grant.

Supporting Information

Provided in Supporting Information: Cartesian coordinates of all 18 chemical systems, memory allocated per molecule, number of RI basis functions for each molecule, cache sizes of L1, L2, and L3, environment variables used for the NWChem builds for each platform, and regression plots for the gradient calculations.

References

1. Anisimov, V. M.; Bauer, G. H.; Chadalavada, K.; Olson, R. M.; Glenski, J. W.; Kramer, W. T. C.; Aprà, E.; Kowalski, K. *J. Chem. Theory Comput.* **2014**, *10* (10), 4307–4316.

2. Bhaskaran-Nair, K.; Kowalski, K.; Moreno, J.; Jarrell, M.; Shelton, W. A. *J. Chem. Phys.* **2014**, *141* (7), 074304.

3. TOP500 Statistics. http://top500.org/statistics/efficiency-power-cores/ (accessed June 20, 2016).

4. Leang, S.; Rendell, A. P.; Gordon, M. S. *J. Chem. Theory Comput.* **2014**, *10*, 908-912.

5. Vogt, L.; Olivares-Amaya, R.; Kermes, S.; Shao, Y.; Amador- Bedolla, C.; Aspuru-Guzik, A. *J. Phys. Chem. A*. **2008**, *112*, 2049−2057.

6. De Prince III, E. A.; Hammond, J. R. *J. Chem. Theory Comput*. **2011**, *7*, 1287−1295.

7. Shimpi, A. L. The Sandy Bridge Review http://www.anandtech.com/show/4083/the-sandy-bridge-review-intel-core-i7-2600k-i5-2500k-core-i3-2100-tested/21 (accessed Jun 16, 2016).

8. Eisenbach, M. IEEE Xplore Full-Text PDF: http://ieeexplore.ieee.org/stamp/stamp.jsp?tp=&arnumber=7802509 (accessed Jan 3, 2017).

9. Sundriyal, V.; Fought, E.L.; Sosonkina, M.; Windus, T.L. *HPC '16,* Proceedings of the 24th High Performance Computing Symposium, Pasadena, CA, USA; Society for Computer Simulation International: San Diego, **2016**.

10. Head-Gordon, M.; Pople, J.A.; Frisch, M. *J. Chem. Phys. Lett.* **1988**, *153*, 503.

11. Lavrijsen, W.; Iancu, C.; Jong, W. D.; Chen, X.; Schwan, K. Proceedings of the Eleventh European Conference on Computer Systems - EuroSys '16 **2016**.

12. Multithreading https://en.wikipedia.org/wiki/multithreading_ (computer_architecture) (accessed Jun 3, 2016).

13. Zhang, X.;Wong, S. E.; Lightstone, F. C. *J. Comput. Chem.* **2013**, *34*, 915-927.

14. Utrera, G.; Corbalan, J.; Labarta, J. *J. Supercomput.* **2014**, *68,* 1113-1140.

15. Navarro, A.; Vilches, A.; Corbera, F.; Asenjo, R. *J. Supercomput.* **2014**, *70*, 756-771.

16. Bolding, B.; Baldridge, K.K. *Comp. Phys. Comm.,* **2000**, *128*, 55-66.

17. Iancu, C.; Hofmeyr, S.; Blagojević, F.; Zheng, Y. 2010 IEEE International Symposium on Parallel & Distributed Processing, **2010**, 1-11.

18. Valiev, M.; Bylaska, E. J.; Govind, N.; Kowalski, K.; Straatsma, T. P.; Van Dam, H. J. J.; Wang, D.; Nieplocha, J.; Apra, E.; Windus, T. L.; De Jong, W. A. *Comput. Phys. Commun*. **2010**, *181*, 1477.

19. Bernholdt, D. E.; Harrison, R. J.; *Chem. Phys. Lett.* **1996**, *250*, 477-484.

20. Intel® MPI Library. Version 5.0.2.044. https://software.intel.com/en-us/intel-mpi-library

21. MVAPICH-Network-Based Computing Laboratory. MVAPICH: MPI over InfiniBand, 10GigE/iWARP and RoCE. http://mvapich.cse.ohio-state.edu/

22. Free Software Foundation, Inc. GCC 4.4.7. https://gcc.gnu.org/gcc-4.4/

23. Intel® Parallel Studio C++ and Fortran Compilers. Composer XE 2013, Update 5. https://software.intel.com/en-us/intel-parallel-studio-xe

24. Annavarami, M.; Grochowski, E.; Shen, J. *Intel software programmer's guide-combined volumes 3a and 3b;* IEEE Computer Society: Washington D.C. **2014**.

25. Dunning, T.H.; *J. Chem. Phys.*, **1989**, *90*, 1007–1023.

26. Kendall R. A.; Dunning Jr., T. H.; and Harrison R. J. J. Chem. Phys. **1992**, *96*, 6796-6806.

CHAPTER 4: IMPROVING EFFICIENCY OF SEMI-DIRECT MØLLER–PLESSET SECOND ORDER PERTURBATION METHODS THROUGH OVERSUBSCRIPTION ON MULTIPLE NODES

A paper published in the *Journal of Computational Chemistry*, **2019**, 40 (24), 2146–2157.

Ellie L. Fought, Vaibhav Sundriyal, Masha Sosonkina, and Theresa L. Windus

Abstract

The purpose of this work is to evaluate the efficacy of oversubscription, at the 1*n*, 2*n*, and 3*n* levels for *n* physical cores, on semi-direct MP2 methods within NWChem when using two and three Intel nodes. Semi-direct MP2 energy and gradient calculations were performed on chemical systems ranging from 824-1626 basis functions using the cc-pVTZ basis set. Wall times for semi-direct MP2 energies were reduced by as much as 36% using two nodes and 44% using three nodes compared to no oversubscription. Total energy consumed by the CPU and DRAM was also reduced by as much as 12% using two nodes and as much as 20% using three nodes when oversubscribing. MP2 gradient wall times improved by as much as 16% using two nodes and 18% using three nodes compared to execution at the 1*n* level, however energy savings were insignificant. Intel performance-counter data shows a strong correlation between total wall time saved and less time spent in the idle state, indicating a more efficient use of the processors when oversubscribing.

Introduction

With the breakdown of Dennard scaling and the rise of exascale computing, power considerations will become increasingly important.[1] Power and energy requirements are rapidly increasing due to rising chip densities, processor frequencies and cooling costs. According to the most recent TOP500 report,[2] even the smaller HPC systems regularly drew 500-1000 kilowatts over the course of a year costing, in some cases, over a million dollars just to power the machines. These estimates do not even consider cooling costs, which have been reported to make up 25-50 percent of total power required by large data centers.[3] For computational scientists, implementing strategies that save energy and have little to no adverse effect on performance will be necessary, particularly with the rise of power-limited (vs. time-limited) access to computational resources. .

Dynamic voltage and frequency scaling (DVFS) has been shown to be an effective method for lowering overall power requirements of HPC systems.[4] A 2011 paper showed overall power requirements were reduced by 8 percent by mapping points of global synchronization within algorithms to when cores were expected to be in an idle state and manipulating the power states of the cores accordingly.[5] In 2016 it was reported[6] that DVFS, applied broadly to "amenable regions" of the NWChem computational chemistry code,[7] could save up to 20 percent in total energy requirements with less than one percent loss in performance. Another pair of recent articles[8] employ a similar strategy, applying DVFS to specific regions of Møller-Plesset second order perturbation theory[9,10] (MP2) algorithms lowered overall energy use by up to 10% with minimal costs to performance.

Multi-threading has also been used to improve computational performance. Multi-threading is the execution of multiple processes (or threads) via a single CPU or core. An early implementation of multi-threading in chemistry involving the Cray MTA architecture accomplished up to 8x speedups of the Hartree-Fock algorithm.[11] Multi-threading can be achieved many different ways with another common approach being the hybrid application of MPI and OpenMP for inter- and intranode communication, respectively. The introduction of OpenMP adds an additional level of parallelization allowing users to perform calculations on very large systems with more efficient parallel scaling.[12,13] While in some cases the addition of OpenMP threads improves performance, neither NWChem nor the Global Arrays toolkit are completely thread safe. The use of OpenMP with NWChem CCSD(T) calculations[14] was shown to improve performance, but extensive changes were required in every routine accessed during the calculations, and even variables within nested loops had to be updated. .

One of the simplest manifestations of multithreading is oversubscription achieved by calling more MPI processes (typically some integer multiple) than physical cores exist. Oversubscription allows the user to increase parallelism without any additional software or changes to the program or operating system. Iancu et al examined[15] the effects of oversubscription on both coarse- and fine-grained applications. Granularity, in this case, describes the relative length of interbarrier intervals, i.e. the duration between synchronization points within an algorithm. The authors reported improvements of system throughput of 27% with oversubscription. Coarse-grained applications experienced improvements or were unaffected, whereas fine-grained applications were more likely to experience performance degradations.

In 2017, we reported[16] on the effects of oversubscription on MP2 on a single node within the NWChem software package. MP2 is a popular and relatively inexpensive correlation method and has multiple implementations within NWChem. We chose to explore the effects of oversubscription on semi-direct MP2 and resolution-of-the-identity MP2 (RI-MP2) energy calculations, as well as semi-direct gradients. Semi-direct MP2 algorithms within NWChem contain both coarse- and fine-grained subroutines to evaluate. Using a single node, we achieved significant improvements in both execution time and energy use when oversubscribing with semi-direct MP2 algorithms within NWChem. On both Intel and AMD platforms, oversubscription led to improvements in time-to-solution of semi-direct MP2 energy calculations by 25-45%. Oversubscription also produced reductions in total energy used by the CPU and DRAM of 10-15%. Most, if not all, of the improvement in performance can be attributed to the *moin* subroutine, which consists of the integral transformations from atomic to molecular orbitals (MOs). Similar results were achieved for semi-direct MP2 gradients. Wall times improved by 8-15% and total energy consumed dropped by 5-10% through oversubscription. Improvements in total execution time resulted from more efficient utilization of the CPUs during the more computationally-intensive subroutines. Less time was spent waiting for communication when more processes were called resulting in significant time savings. While the number of processes increases with oversubscription, regression analysis showed a strong correlation between total wall time and energy consumed. Thus, shorter calculations consume less total energy.

The results of our tests when oversubscribing on one node are encouraging but not necessarily practical. When using only one node, there is no opportunity to evaluate

oversubscription's effects on internode communication. To better understand the applicability of oversubscription to a wider range of chemical systems and methods, it is pertinent to examine its performance when using multiple nodes. This paper seeks to evaluate just that by testing oversubscription in conjunction with semi-direct MP2 using two and three nodes. We limited our work to at most three nodes for the added control and highly detailed monitoring needed to evaluate the effects of the method. In our previous work, RI-MP2 experienced significant performance degradation when oversubscribing on a single node, thus we chose not to test RI-MP2 on multiple nodes.

Methods

Hardware

The platform used in this work, *Bolt*, consisted of Sandy Bridge nodes, each with six Intel Xeon E5-1650 cores and 64 GB of DDR3 RAM at 1600 MHz. The system contains a 7200 RPM SATA disk and node-to-node communication was accomplished with InfiniBand. This work was performed on a smaller, local cluster as opposed to a larger High Performance Computing (HPC) system for the added control over the operating system. With our local cluster, we were able to use performance monitors and had superuser control over the frequency scaling governor. Additional information regarding the hardware, such as cache sizes, can be found in the Supporting Information (SI).

Software

The MPI used for this work was MVAPICH2-2.2rc1.[17] Blocking must be enabled in MVAPICH in order to call more than one process per processor, and the MPI threads were not bound to the cores. The GNU gcc and gfortran compilers, version 4.4.7,[18] were used to compile the NWChem version 6.5 source code. The GNU gcc and gfortran were the default compilers in the operating system. Included in the NWChem software package are internal BLAS and LAPACK libraries, and no additional math libraries were used as an additional experimental control. Multiple performance monitors were used to evaluate the behavior of the system. Intel's Running Average Power Limit (RAPL)[19] was used to monitor the CPU and DRAM power usage over the course of the calculations. The Processor Counter Monitor application programming interface (API)[20] was used to track cache accesses, power state residency of the cores, frequency, etc. The *on-demand* frequency scaling governor was used for all calculations.

Very few optional directives were used within the NWChem input files. Per-processor total memory limits were used, with the amount based on the size of the system. Each system's total memory limit is provided in the SI. The path for a large local scratch directory was also provided. The converged SCF orbitals were preloaded to save time and the core orbitals were frozen for the MP2 calculation, a common practice for the method. NWChem was called using the mpirun command with two options: *-np* that specifies the total number of processes, and *-hostfile* that directs the processes to specific nodes or "hosts." Examples of the mpirun command and the structure of the hostfiles used can be found in the SI. For each calculation 1*n*, 2*n*, or 3*n* processes were called where *n* is the number of physical cores, thus *n* is 12 for two nodes and 18 for three

nodes. Unlike our previous work, we chose not to oversubscribe at levels higher than 3*n* for this work. When oversubscribing at the 4*n* level previously, minimal performance gains were made and in most cases, we observed performance losses compared to the 2*n* and 3*n* levels. The nodes used in this work were reserved via the queuing system and jobs were initiated locally from the nodes without the assistance of a scheduler. Each chemical system was tested using 1*n*, 2*n*, or 3*n* processes on one, two, and three nodes and each type of calculation was performed in triplicate. All times reported are averages of the three runs.

Chemical Systems

Twelve chemical systems were used in this work with sizes ranging from 37 to 83 atoms organized into four size groups and categorized as one-dimensional (1D), two-dimensional (2D), or three-dimensional (3D). Testing systems with various dimensionalities was done to evaluate the relationship between screening effects and the effectiveness of oversubscription. The chemical formula, number of basis functions using the cc-pVDZ basis,[21] and Cartesian coordinates for each system can be found in the SI. Table 1 provides the number of basis functions, chemical formula, and categorization for all 12 systems used. All chemical systems used for this work were also used in our previous work using one node for comparison purposes. MP2 energy calculations were performed for all 12 systems at the specified geometries, and in the interest of time, MP2 gradient calculations were performed for the six smallest systems.

Table 1. Identification of 12 chemical systems used to test oversubscription, organized by dimension. The first column gives range of sizes in basis functions. For the remaining three columns, the number of basis functions and chemical formula of each system is provided.

Sizes	3D	2D	1D
800-850	858 $C_{13}H_{27}O_2N$	824 $C_{19}H_{16}O$	844 $C_{13}H_{26}O_3$
1000-1050	1056 $C_{20}H_{24}O_2N_2$	1022 $C_{19}H_{28}O_2$	1046 $C_{17}H_{34}O_2$
1200-1300	1262 $C_{22}H_{28}O_7$	1214$C_{24}H_{31}ON$	1306 $C_{21}H_{44}O_2$
1500-1600	1580 $C_{28}H_{40}O_6$	1608 $C_{31}H_{42}O_3$	1626 $C_{26}H_{54}O_3$

Results and Discussion

MP2 has been shown to scale linearly at smaller numbers of nodes with no oversubscription.[22] Figure 1 shows that with both the semi-direct MP2 energy and gradient calculations, we see that same behavior in scaling. Perfectly linear scaling when increasing from one to two or three nodes would result in speedups of 2x or 3x respectively. The plots in Figure 1 show speedups hovering around 2x and 3x for both energy and gradient calculations.

Semi-Direct MP2 Energy

As with the calculations performed on a single node, significant performance improvements were accomplished when using oversubscription with semi-direct MP2 energy calculations on multiple nodes. Figure 2 provides normalized execution times for all twelve systems at each level of oversubscription for both two and three nodes.

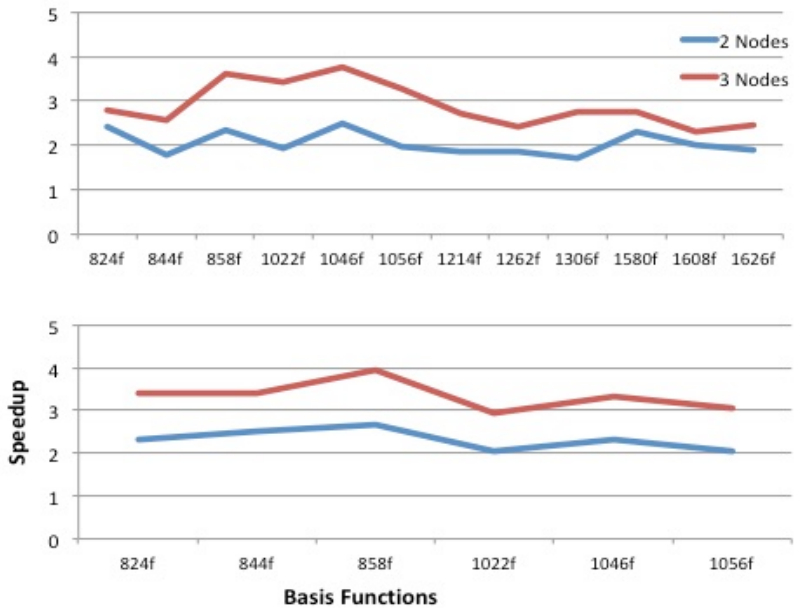

Figure 1. Top: speedups compared to one node for two and three nodes for semi-direct MP2 energy algorithm; bottom: speedups compared to one node for two and three nodes for semi-direct MP2 gradient algorithm with no oversubscription.

The execution times are normalized by dividing them by each system's number of basis functions. With both two and three nodes, time-to-solution and energy usage were lowered at every level of oversubscription for all twelve evaluated. Using two nodes, total wall times improved by an average of 27% at the 2*n* level and 36% at the *3n* level compared to execution with no oversubscription. At the 2*n* level, total execution times improved by a maximum of 40%, and at the 3*n* level, by as much as 44%. In most cases, the 3*n* level of oversubscription was more successful in reducing total execution times than the 2*n* level. With three nodes, total MP2 wall times improved by an average of 30% at the 2*n* level and 44% at the 3*n* compared to no oversubscription, with maximum improvements of 52% and 53% for 2*n* and 3*n* respectively. When oversubscribing with three nodes, execution at the 3*n* level outperformed 2*n* for all twelve chemical systems

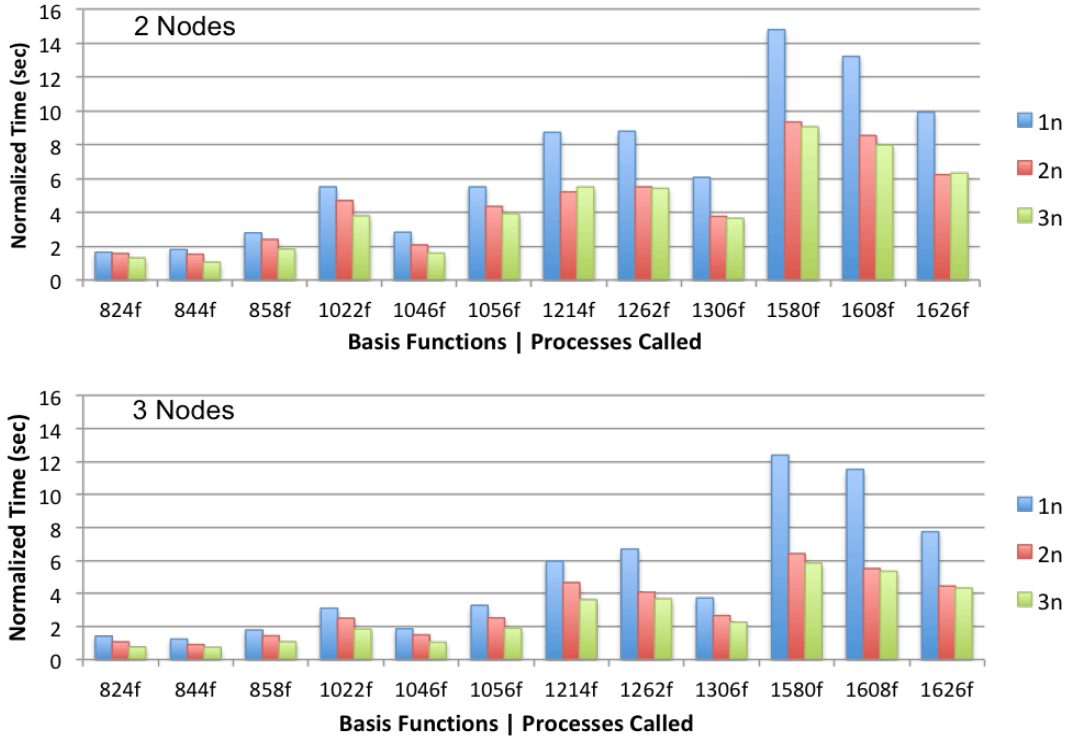

Figure 2. Total MP2 execution time at 1*n,* 2*n*, and 3*n* processes for all twelve chemical systems, normalized by the number of basis functions. The top chart represents two-node execution times and the bottom chart represents three-node execution times.

tested. For both two and three nodes, the average improvement in performance increased as the size of the chemical systems grew.

The semi-direct MP2 energy algorithm consists of two main components: the *moin* subroutine and *make* subroutine. The *moin* subroutine includes the transformation of the atomic orbitals (AOs) to the molecular orbitals (MOs) and requires extensive communication between the processes as well as I/O to disk. The *make* subroutine is the actual MP2 energy calculation using the newly transformed MOs and is much more fine-grained (and typically much faster) than the *moin* component. Without oversubscription, the *moin* subroutine accounts for over 80% of the total MP2 energy wall time, thus significant improvements to the *moin* subroutine would lead to time saved overall. For

all twelve chemical systems at each level of oversubscription, time-to-solution for the *moin* subroutine improved significantly. Figure 3 provides execution times for the *moin*, *make*, and total MP2 for three of the 3D chemical systems. As demonstrated in Figure 3, most, if not all, of the improvements in total MP2 execution time can be attributed to speedups in the *moin* subroutine. Using two nodes, the *moin* wall times were reduced by an average of 39% when oversubscribing and as much as 56% at the 3*n* level. When running on three nodes, *moin* wall times improved on average by 44%, and by as much as 61% at the 3*n* level, compared to no oversubscription. There was no discernible difference in performance between the dimensional subgroups, but like the total MP2 times, the effects of oversubscription were more pronounced as the size of the systems increased.

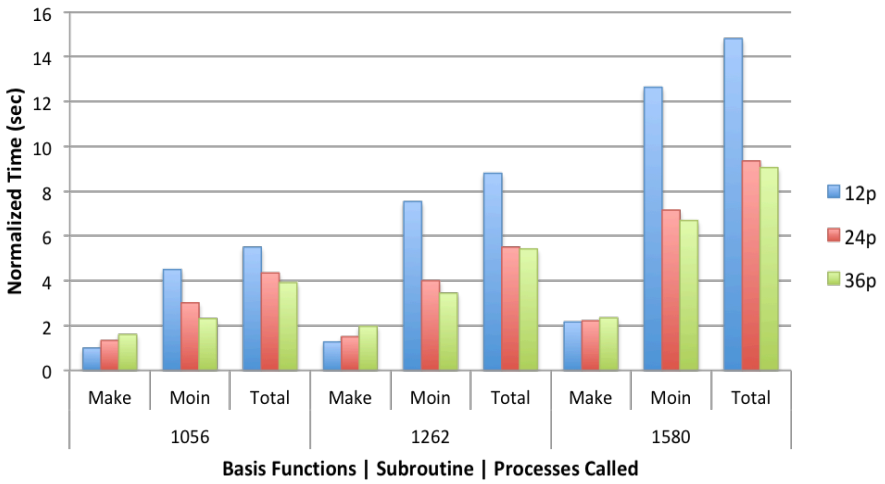

Figure 3. Normalized execution times for three 3D systems for *make, moin*, and total MP2 wall time using two nodes at each level of oversubscription.

Oversubscription of the *moin* subroutine results in more efficient use of the CPUs during the calculation of the first and second index integral transformations. Multiple passes are required to complete these transformations, and at the end of each pass, the

processes perform some I/O and wait for the remaining processes to finish before getting their next task. When operating with a smaller number of processes, the number of tasks required of each process is larger, and processes sometimes spend significant time waiting for all other processes to finish the pass. Through oversubscription, while one process is waiting for I/O, another process assigned to the same CPU is allotted its time slice and can perform its own tasks. Additionally, when oversubscribing the number of passes required to complete the transformations decreases proportionally. The work is divided across a larger number of processes, thus, the number of tasks per process is smaller and the required computations are completed in fewer passes. For example, the 824 basis function system at the 1*n* level using two nodes requires 342 passes, while the 2*n* level requires 170 passes and the 3*n* level requires 114 passes. Thus, the number of passes is cut by the factor of oversubscription. While each pass does get longer when oversubscribing, the duration does not double or triple as with the number of processes thus saving time during these routines. By oversubscribing the *moin* subroutine becomes more coarse-grained by requiring fewer global synchronization points.

In contrast, the *make* subroutine responded unpredictably with oversubscription. Some chemical systems experienced slight improvements, while others saw significant increases in *make* execution time. The *make* subroutine has short interbarrier intervals with multiple one-sided communication calls, thus significant improvements due to oversubscription would not be anticipated. The 1D systems experienced the smallest hit to performance when executing with both two and three nodes. The maximum performance drop due to oversubscription across all twelve chemical systems observed was 68% using two nodes and 58% using three nodes, both at the 3*n* level. Unlike the

moin subroutine, the functions within the *make* subroutine are not dependent on the number of processes called at start-up. The *make* subroutine contains much more one-sided communication than the *moin* subroutine with multiple gets, puts, and accumulates, the total numbers of which do not change with different levels of oversubscription.

The Performance Counter Monitor (PCM) API provides a breakdown of the Intel core C-states by the percentage of time spent in each state. The Intel C-states are pre-programmed power saving states of the cores based on usage and core temperature. The C0 state corresponds to the non-idle state when the core is actively executing instructions, whereas the C7 state corresponds to the idle state when maximum power savings are achieved.[23] Careful analysis of the core state residencies provides some insight on the benefits of oversubscription. For all levels of oversubscription, the cores spend over 85% of the total MP2 execution time in either the C0 or C7 C-state. When using two nodes, the total time spent in the C0 power state as the level of oversubscription increases is relatively unchanged, only increasing by as much as 3%. In Figure 4, we illustrate the consistency in C0 residency time across all levels of oversubscription when using two nodes and the significant reduction in time spent in the C7 state. The average time spent in the C7 power state drops considerably when oversubscribing, and the reduction in the time spent in C7 is highly correlated with the overall time saved on the calculations.

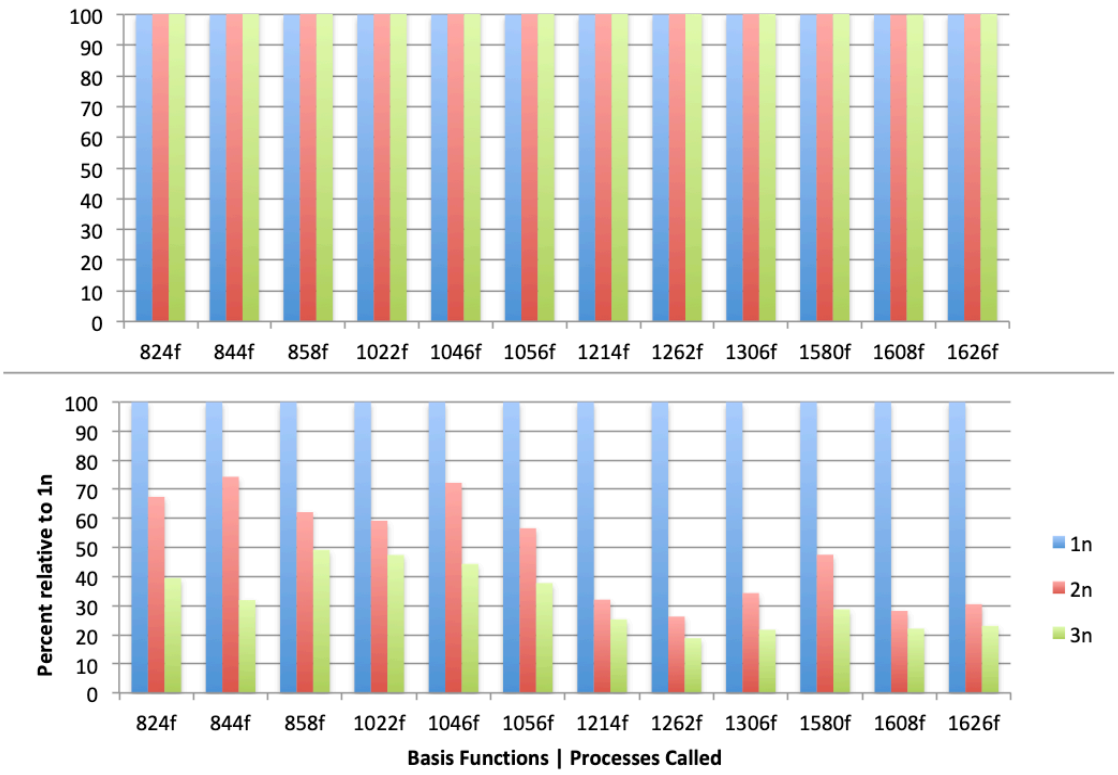

Figure 4. Percent relative time spent compared to 1*n* processes for all 12 chemical systems in (a) the C0 power state and (b) the C7 power state.

The plots in Figure 5 trace both the C0 and C7 percent residency over the course of the semi-direct energy calculations for the 1306 basis functions system at each level of oversubscription. The C-state residency traces show the overall reduction in time spent in the C7 power state when oversubscribing. The traces also show more prolonged periods of time spent in the C0 state as the level of oversubscription increases.

Further analysis of C-state residencies and total MP2 wall times show a direct relationship between reductions in time spent in the idle C7 state and overall time saved through oversubscription. The plots in Figure 6 compare the difference in C7 residency time to the total time saved relative to 1*n* processes for the 2*n* and 3*n* levels of oversubscription using two nodes. The time differences plotted in Figure 6 are highly

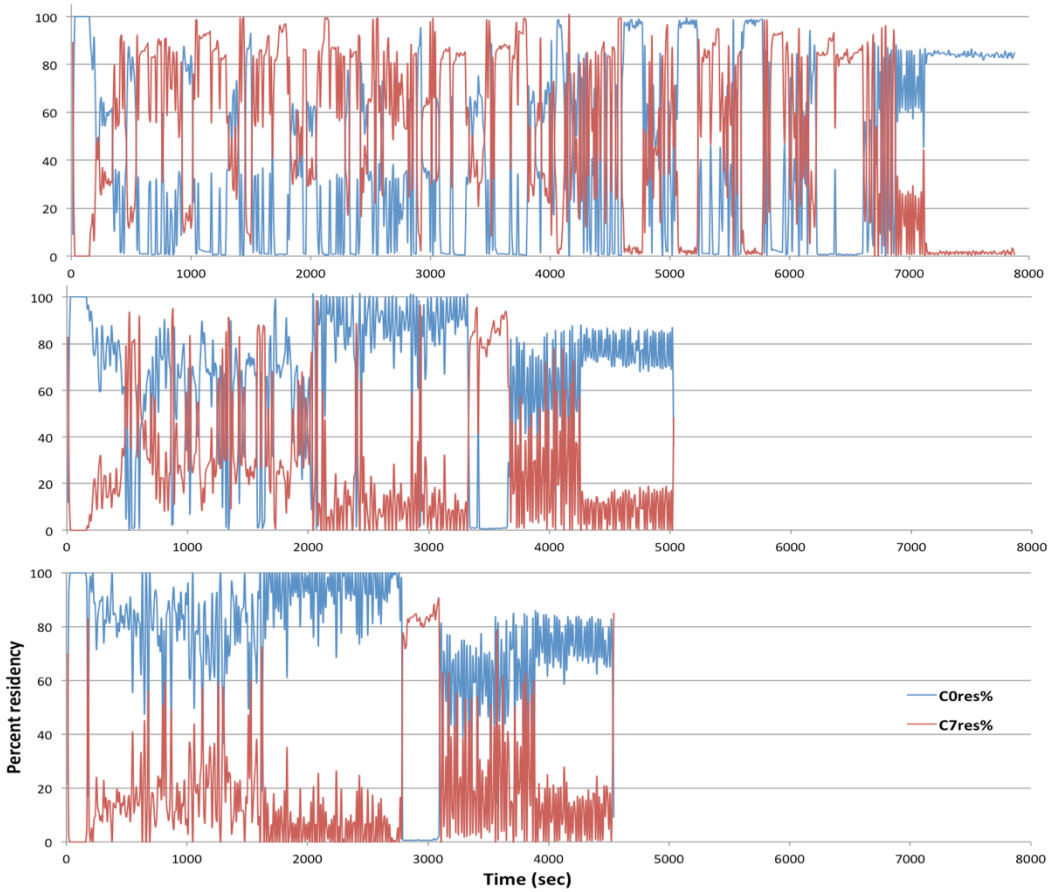

Figure 5. C0 and C7 residencies for a single socket for the 1306 basis functions system using two nodes. From top to bottom, the graphs are for 1n, 2n, and 3n levels of oversubscription, respectively.

correlated with R^2 values over 0.99 for both levels of oversubscription. The changes or lack thereof in C7 and C0 residency time, respectively, indicate an overall improvement in efficiency through oversubscription. The cores are doing the same amount of work while idling for less time overall.

Using the RAPL toolkit provided by Intel, we monitored the CPU and DRAM power consumption at one-second intervals. Figure 7 provides percent relative energy

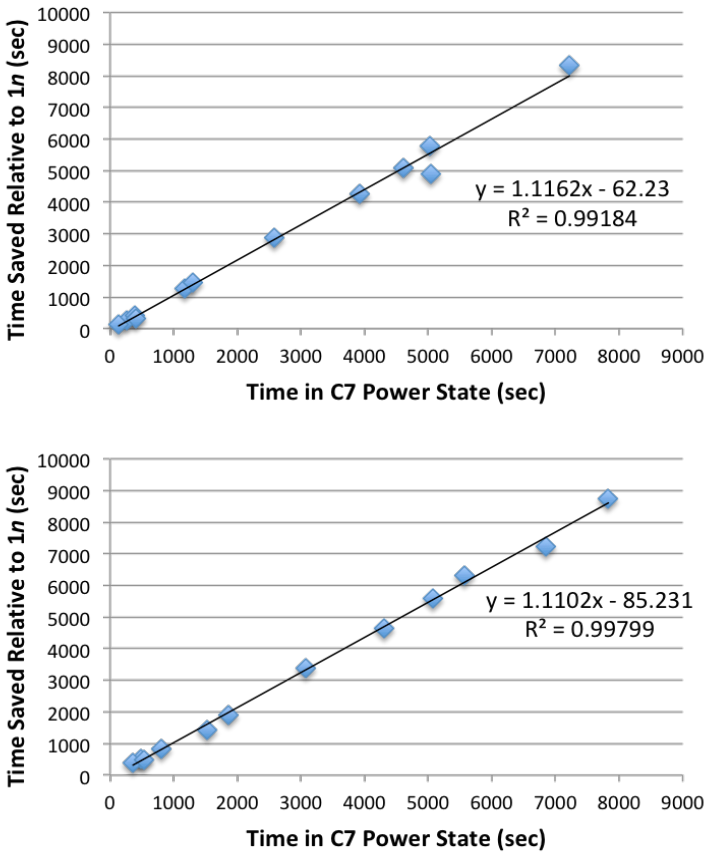

Figure 6. Total wall time saved versus time difference in C7 residency compared to 1*n* for 2*n* processes (top) and 3*n* processes (bottom) using two nodes.

consumed compared to no oversubscription for both two and three nodes. Similar to our results using one node, we report cumulative energy savings using two nodes of 5-10%, with more energy being saved as the size of the chemical system increases. With three nodes, even larger energy savings were achieved, with savings of 15-20% for the largest systems. When using two nodes, execution with 3*n* processes is more energy efficient for the smaller chemical systems, while for the larger systems the differences between the levels of oversubscription are negligible. When executing on three nodes, higher levels of oversubscription consistently correspond to larger total energy savings. These differences in energy savings can be attributed to time saved through oversubscription.

The speedups provided in Figure 8 illustrate the minimal difference in speedup between oversubscription at the 2*n* and 3*n* levels for the 1056 basis function system and larger when using two nodes. The speedups also show that unlike the behavior using two nodes, oversubscription at the 3*n* level on three nodes is consistently more advantageous than the 2*n* level. The reductions in total energy consumed when oversubscribing can be attributed to shorter wall times and less time spent idling during communication. Static power consumption of the system (i.e. when no user tasks are running) can exceed 50% of the power required by the same system when fully active.[24] Thus significant energy

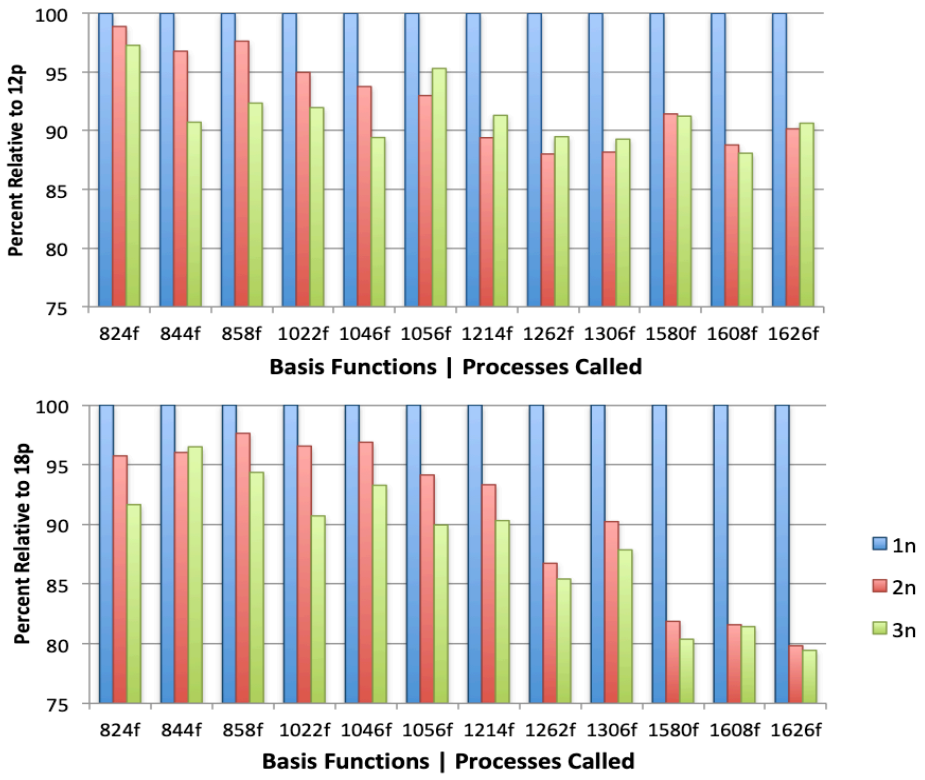

Figure 7. Percent energy used for all twelve chemical systems at each level of oversubscription relative to 1*n* processes for (top) two nodes and (bottom) three nodes.

savings can be attained by reducing the number and duration of idle periods throughout the calculations. As the level of oversubscription increases, the power consumption of both the CPU and DRAM is higher for longer periods of time, but the overall time is reduced. Figure 9 provides power traces for the same 1306 basis function system example (as in Figure 5) for both the CPU and DRAM at each level of oversubscription. These trends in wattage are consistent with the changes in the C-state residencies and further support the idea that oversubscribing is more efficiently using the CPUs compared to standard execution at 1*n*.

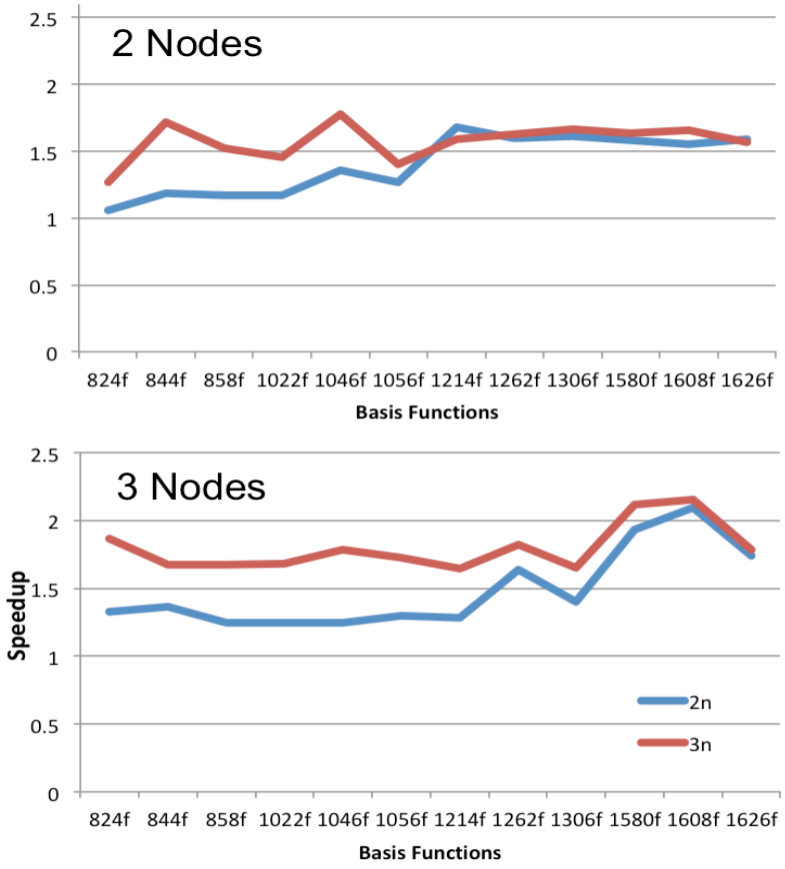

Figure 8. Speedups of the semi-direct MP2 algorithm in NWChem due to oversubscription on (top) two nodes and (bottom) three nodes

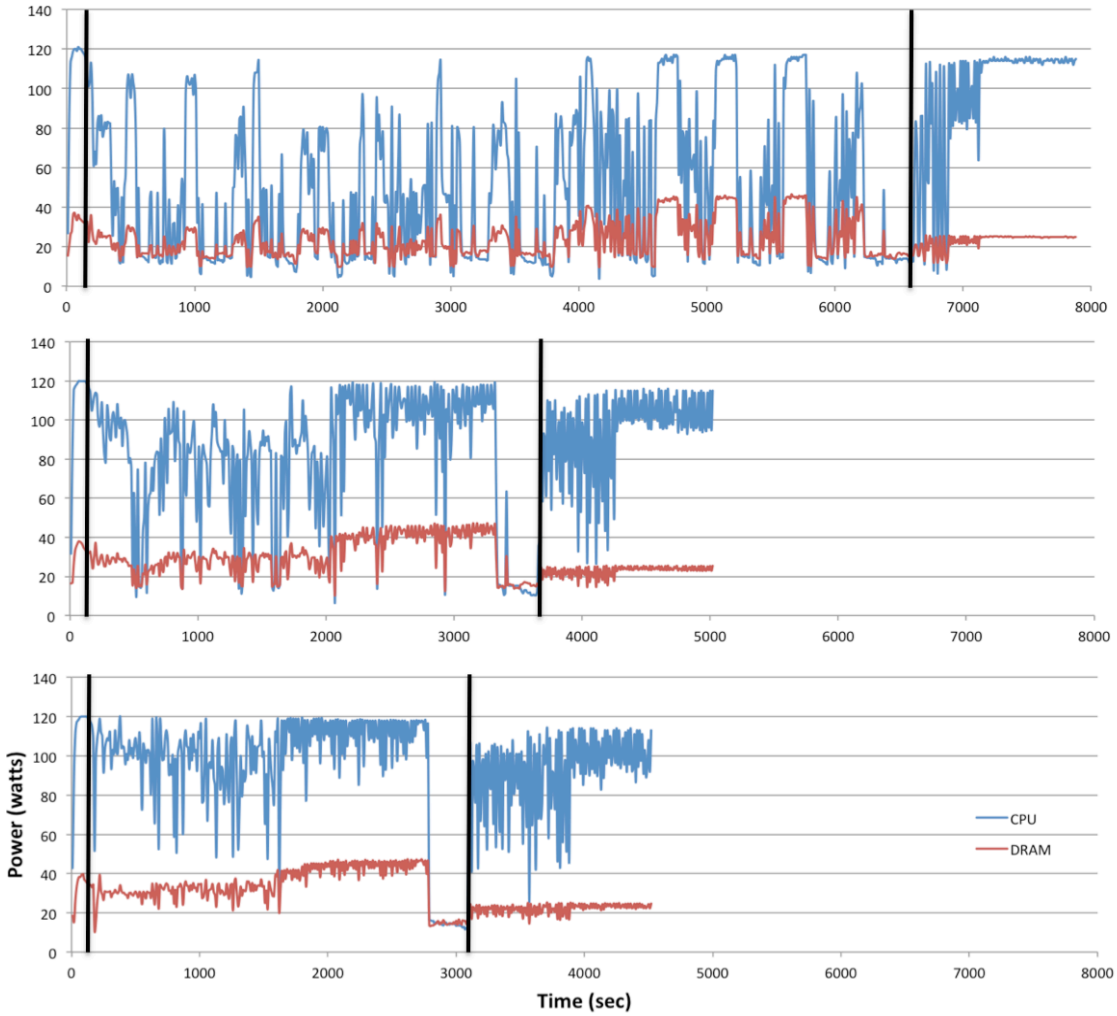

Figure 9. Traces for the CPU and DRAM energies at (top) 1*n*, (middle) 2*n,* and (bottom) 3*n* processes for the 1306 basis function system using two nodes. The black lines separate the subroutines into three sections: SCF energy calculation, *moin*, and *make*. Oversubscribing leads to minimal increases in the SCF wall times.

Both the CPU and DRAM experienced drops in total energy used, but it was the DRAM that saw the larger total savings. In some cases, the net savings in energy consumed by the DRAM was 50% more than the net savings in energy used by the CPU even though the DRAM typically draws only a fraction of the power drawn by the CPU. The charts in Figure 10 show a side-by-side comparison of the cumulative energy saved by the CPU and DRAM for the nine largest systems at both 2*n* and 3*n* when executing on

three nodes. As the level of oversubscription rises, the DRAM operates more efficiently. When oversubscribing, the rate of cache misses on a per process per second basis dropped, sometimes to less than half the rate at the 1*n* level. A table containing the rates of cache misses for both the L2 and L3 cache levels for all systems at each level of oversubscription can be found in the SI. The significant energy savings by the DRAM appears to come from the combination of shorter total execution times, as well as fewer

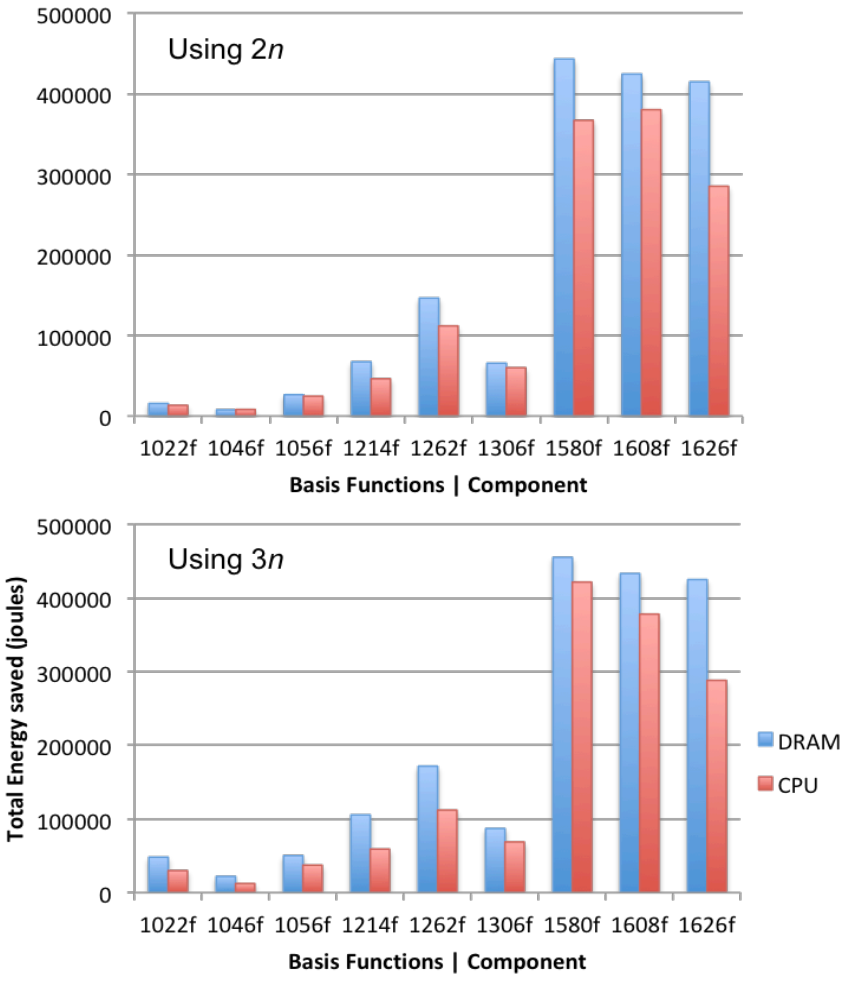

Figure 10. Comparison of absolute energy saved by DRAM and CPU relative to 1*n* using three nodes at the 2*n* and 3*n* levels for the nine largest chemical systems.

cache misses, resulting in fewer DRAM accesses per process. CPU frequency data

provides some explanation for the differences in energy savings between the DRAM and CPU. Figure 11 provides the average CPU frequency as a percent relative to the nominal frequency of the processor (3.2 GHz) during the *moin* subroutine at each level of oversubscription for all twelve chemical systems when using two nodes. At the 1*n* level, the CPUs operated at an average 43% of the nominal frequency. At the 2*n* level that average rose to 64%, and at the 3*n* level it rose to 80% of the nominal frequency. Thus, while the *moin* wall times were reduced significantly through oversubscription, the increase in the average operating frequency of the CPUs resulted in smaller energy savings than those experienced by the DRAM.

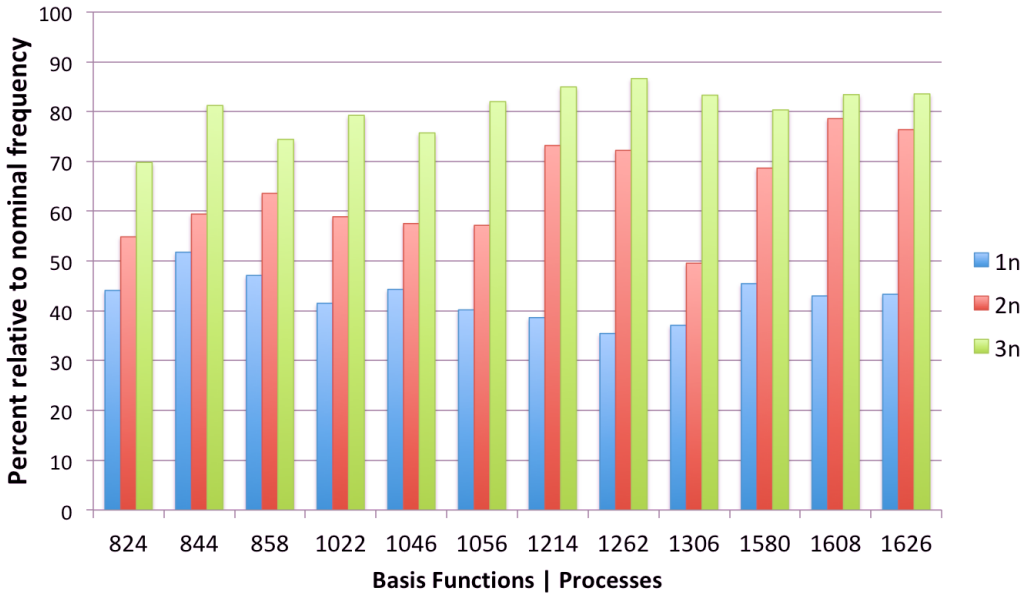

Figure 11. Average CPU frequency as a percent relative to the nominal frequency (3.2GHz) during the *moin* subroutine for all twelve systems at each level of oversubscription using two nodes.

Semi-Direct MP2 Gradients

Similar to execution on a single node[16] oversubscription results in significant improvements in total MP2 gradient wall times. Figure 12 provides normalized total execution times for all six systems examined using both two and three nodes. On two nodes MP2 gradient wall times were reduced 4-11% with an average of 8% when using 2*n* processes. At the 3*n* level, wall times dropped by 11-16% with an average of 14%. When executing on three nodes, gradient wall times reduced by 5-14% with an average of 8% at the 2*n* level. Using 3*n* processes on three nodes resulted in gradient wall time reductions of 10-18% with an average of 15%. In most cases, higher levels of oversubscription correspond to more total wall time saved. The semi-direct MP2 gradient

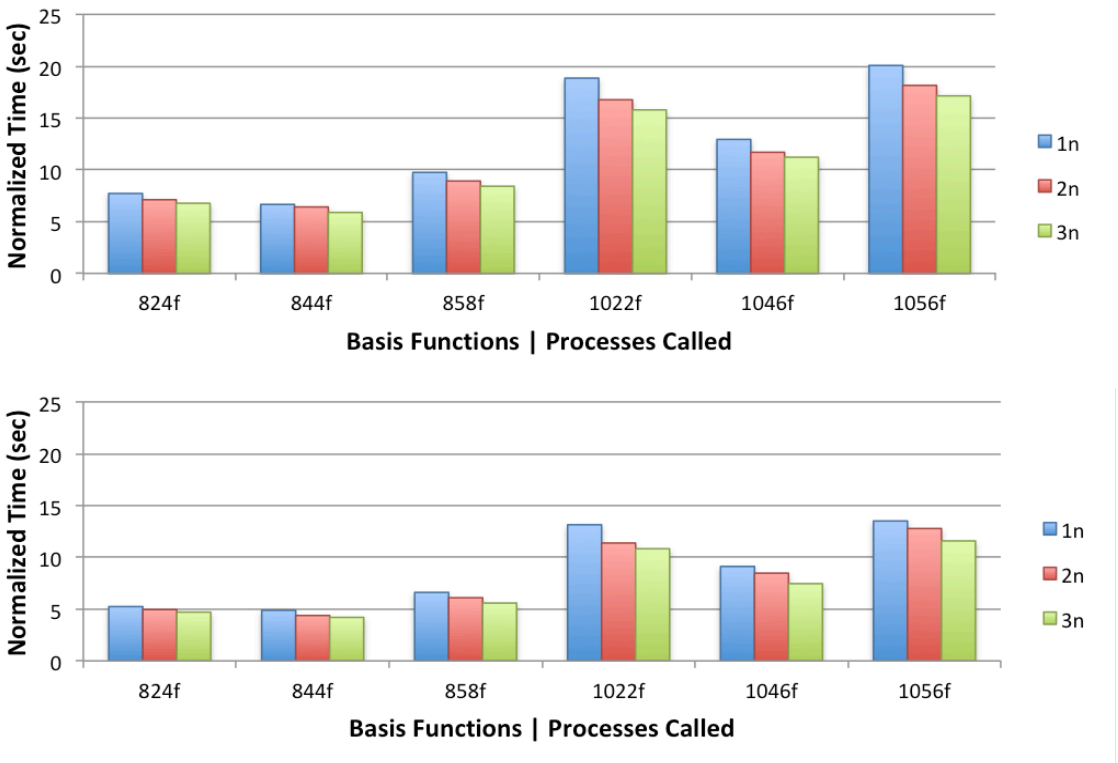

Figure 12. Normalized total execution times for semi-direct MP2 gradients for all six chemical systems tested at all three levels of oversubscription. The top represents two nodes and the bottom represents three nodes.

algorithm is comprised of eleven subroutines, the first two being the same *moin* and *make* as in the semi-direct energy calculation. As in the energy calculations, oversubscription reduces *moin* wall times by as much as 35% at the 2*n* level and as much as 52% at the 3*n* level.

Only one of the remaining nine subroutines has significant periods of I/O. The *back* subroutine, essentially the reverse of the *moin* routine, transforms the molecular orbitals back into atomic orbitals. Figure 13 provides normalized execution times for the *moin*, *back*, and total MP2 gradient at each level of oversubscription for the three largest chemical systems tested using two nodes. Using two nodes, oversubscription reduced *back* wall times 14-25% at the 2*n* level and 29-45% at the 3*n* level. With three nodes, *back* wall times improved by 12-32% at 2*n* and 30-39% at 3*n*. The reductions in *moin* and *back* execution time account for all of the improvements made in total gradient wall times.

The remaining eight subroutines are more coarse-grained than *make*, with less checkpointing and one-sided communication, but do not contain the same parallel loop structure observed in the *moin* and *back* subroutines that benefit from oversubscription. The subroutine accounting for the highest average percentage of time is the *lai*, which forms the initial Lagrangian matrix. The *lai* subroutine accounts for at least 25% of the total gradient execution level of oversubscription. The effect of oversubscription on the other seven compute-intensive subroutines is similar with changes in execution times of less than 5%.

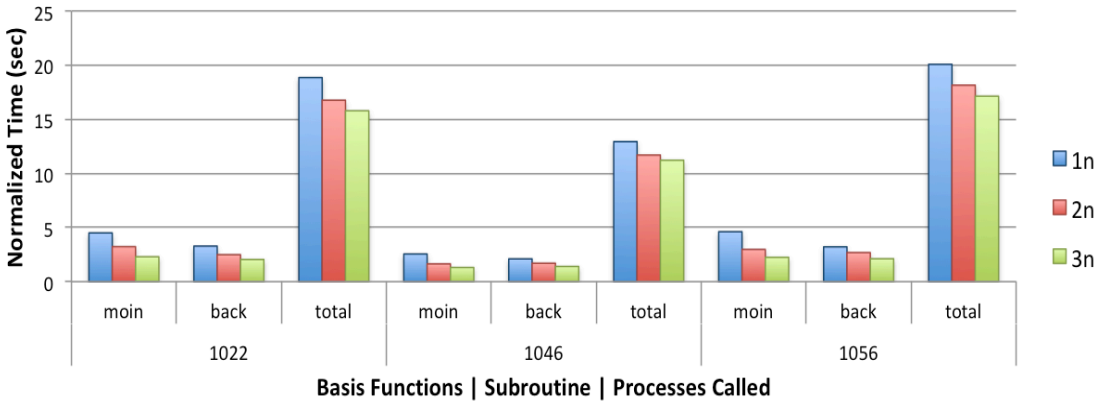

Figure 13. Normalized execution times for the 1000 basis function subset for the *moin*, *back*, and total MP2 gradient at all three levels of oversubscription using two nodes.

In our previous work on a single node, oversubscription of the semi-direct MP2 gradient calculations resulted in total energy savings of 5-10%. Using multiple nodes, RAPL analysis shows more inconsistent overall effects from oversubscribing. On both two and three nodes, total changes in energy consumed are no more than +/-2%. Figure 14 provides percent relative energy used compared to execution with no oversubscription for all six systems tested on two nodes. When performing semi-direct MP2 energy calculations, oversubscription consistently led to higher overall energy savings in the DRAM compared to the CPU, even though the CPU uses about three times as much total power. With the semi-direct MP2 gradient calculations, total CPU energy consumed rose as the level of oversubscription increased. The energy consumed by the CPU dropped for the subroutines benefiting from oversubscription, such as the time with no oversubscription, and that percentage rises to over 30% at the *3n* level. However, oversubscription has a minimal effect on *lai* wall times, with changes of less than +/-1% at either *moin* and *back*, which we attribute to much shorter execution times.

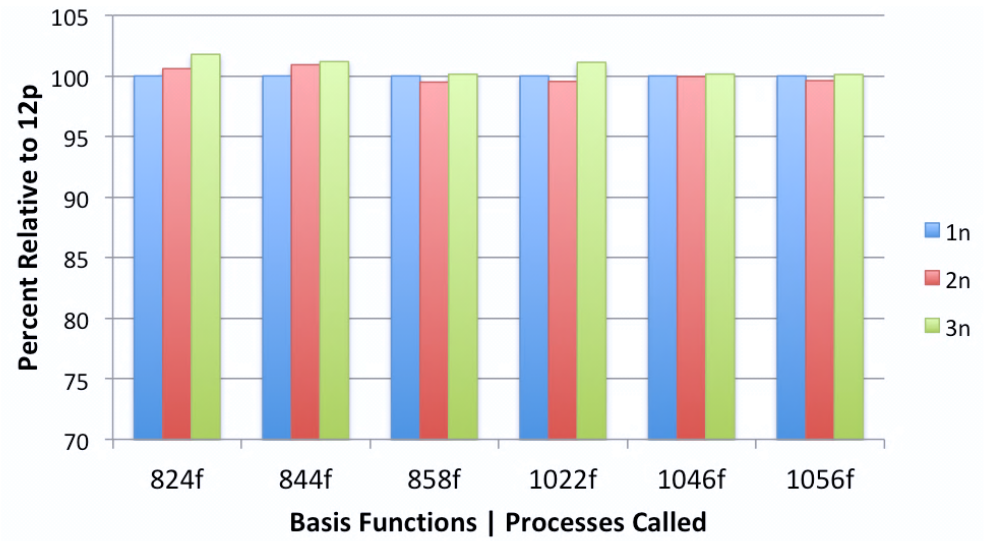

Figure 14. Percent relative energy used compared to no oversubscription using two nodes. All six systems tested are shown at each level of oversubscription.

However, for the remaining subroutines, the average energy consumed by the CPU slightly rose, eliminating any energy savings via *moin* and *back.* In contrast, with the exception of the smallest chemical system tested, the total energy consumed by the DRAM actually decreased as the level of oversubscription increased, balancing out the increases in energy used by the CPU and resulting in limited overall energy added or saved.

Conclusions

Throughout this work, oversubscription has been shown to be an effective strategy to improve efficiency of semi-direct MP2 methods using multiple nodes. Implementing oversubscription can be accomplished with no additional changes to the hardware or software and simply requires calling more processes via MPI. On both two and three nodes, execution at each level of oversubscription led to significant reductions in time to solution for both semi-direct MP2 energy and semi-direct MP2 gradient

algorithms within NWChem. Using two nodes, semi-direct MP2 energy calculations improved by an average of 27-36% when oversubscribing compared to execution at the 1*n* level. Using the RAPL toolkit, it was found that oversubscribing on two nodes saved an average of 5-10% total energy consumed by the CPU and DRAM. On three nodes, oversubscription improved total MP2 energy wall times 30-44% compared to execution with 1*n* processes. Oversubscription also saved significant energy using three nodes with average savings of 10% at both the 2*n* and 3*n* levels. On both two and three nodes, only modest improvements are observed when increasing the level of oversubscription from 2*n* to 3*n*. We suspect that by oversubscribing with 2*n* processes, the limit of maximum CPU efficiency is reached or nearly reached, thus further improvements at the 3*n* level are limited. For all twelve chemical systems tested almost all of the time savings occurred during the *moin* subroutine. The *make* subroutine was typically unaffected or negatively affected by oversubscription. Within the *moin* subroutine, oversubscription led to a reduction in synchronization checkpoints resulting in less time spent both waiting for communication and during communication. Oversubscribing led to longer interbarrier intervals between the checkpoints, effectively making the *moin* subroutine even more coarse-grained. Conversely, oversubscription had no effect on the total number of either one-sided or two-sided communication calls within the *make* subroutine and the resulting overhead helps to explain most of the performance losses observed.

Semi-direct MP2 gradient calculations also experienced significant time savings when oversubscribing. On two nodes, oversubscription saved an average of 8-13% with the greatest improvements happening at the 3*n* level. Executing on three nodes, oversubscription resulted in total wall time savings of 8-15%, with the largest

improvements at the 3*n* level, as well. Only two (*moin* and *back*) of the eleven subroutines within the semi-direct MP2 gradient algorithm in NWChem experienced performance improvements through oversubscription on multiple nodes. As with the semi-direct MP2 energy calculations, *make* experienced losses in performance with respect to time-to-solution and energy consumed. The remaining eight subroutines were mostly unaffected by oversubscription with maximum changes in performance of +/-5%. Unlike our previous work using a single node, total energy consumed by the CPU and DRAM was largely unchanged by oversubscribing on both two and three nodes. While execution times did not change significantly for eight of the subroutines in the MP2 gradient algorithm, energy consumed by the CPU increased slightly as the level of oversubscription rose, thus eliminating any energy savings that may have occurred during the *moin* and *back* subroutines.

Using the Performance Counter Monitor API, it was discovered that as the level of oversubscription increased for both MP2 energy and gradient calculations, the CPUs were in the idle C7 state for a smaller percentage of the time. Regression analysis for the semi-direct MP2 energies showed a correlation between less time spent in the idle C7 state with oversubscription and the total time saved on the calculations. This correlation indicates that the improvements in execution times arose from better utilization of the CPUs by spending less time idling as the work was divided among greater numbers of processes. RAPL analysis shows that for both the MP2 energy and gradient algorithms that the DRAM consistently saved more total energy than the CPU. These savings occurred despite the fact that the DRAM typically consumes about 25% of the total energy used by the CPU. PCM data for MP2 energy calculations on two nodes indicated

that the rate of cache misses per process dropped as the level of oversubscription increased for both the L2 and L3 cache. The combination of improved efficiency in accessing the DRAM and the shorter execution times when oversubscribing are most likely responsible for the energy savings observed. The average operating frequency of the CPUs rose significantly with the level of oversubscription resulting in smaller total energy savings by the CPU.

While oversubscription was successful at improving total wall times for both semi-direct MP2 energy and gradients on the platform described in this work, we acknowledge that systems with higher latency will most likely not benefit as greatly. However, a more judicious approach, targeting specific subroutines that benefit the most from oversubscribing could lead to even greater performance improvements even on newer, faster platforms.

Acknowledgments

This work was supported in part by the Air Force Office of Scientific Research under the AFOSR award FA9550-12-1-0476, by the U.S. Department of Energy, Office of Advanced Scientific Computing Research, through the Ames Laboratory, operated by Iowa State University under contract No. DE-AC02-07CH11358 and by the U.S. Department of Defense Performance Computing Modernization Program, through a HASI grant.

Supporting Information

Provided in Supporting Information: Cartesian coordinates of all 12 chemical systems, memory allocated per system, cache sizes of L1, L2, and L3, and environment variables used for the NWChem build. The structure of the hostfiles and a data table containing the average cache misses per process per second using two nodes are also available.

References

1. S. Kamil, J. Shalf, E. Strohmaier, IPDPS 2008 IEEE International Symposium. **2008**, 1–8.

2. TOP500 Statistics, November 2018. Available at: http://top500.org/statistics/efficiency- power-cores.

3. R. Sawyer. *Calculating Total Power Requirements For Data Centers;* White Paper for Schneider Electric's Data Center Science Center. **2016**

4. S. K. Talamudupula, *IJSRSET,* **2017**, *3*, 28–35.

5. D. Kerbyson, A. Vishnu, K. Barker, In: 2011 IEEE International Conference: Austin, TX, USA,, **2011**, 225–233.

6. W. Lavrijsen, C. Iancu, W. D. Jong, X. Chen, K. Schwan, In: Proceedings of the Eleventh European Conference on Computer Systems - EuroSysq '16: London, United Kingdom,, **2016**.

7. M. Valiev, E. J. Bylaska, N. Govind, K. Kowalski, T. P. Straatsma, H. J. J. Van Dam, D. Wang, J. Nieplocha, E. Apra, T. L. Windus, W. D. Jong, *Comput. Phys. Commun*. **2010**, *181*, 1477.

8. (a) V. Sundriyal, E. L. Fought, M. Sosonkina, T. L. Windus, In: HPC ’16, Proceedings of the 24th High Performance Computing Symposium. Society for Computer Simulation International: San Diego, Pasadena, CA, **2016**. (b) V. Sundriyal, E. L. Fought, M. Sosonkina, T. L. Windus, In: HPC '17 Proceedings of the 25th High Performance Computing Symposium, Virginia Beach, Virginia, United States. Society for Computer Simulation International: San Diego, Pasadena, CA, **2017**.

9. C. Møller, M.S. Plesset, *Phys. Rev.* **1934** *46*, 6182

10. M. Head-Gordon, J. A. Pople, M. Frisch, *J. Chem. Phys. Lett*. **1988**, *153*, 503.

11. B. Bolding, K. K. Baldridge**,** *Comput. Phys. Commun***. 2000,** *128***,** 55.

12. K. Ishimura, S. Ten-no, *Theor. Chem. Acc.* **2011,** *130*, 317-321.

13. M. Katouda, T. Nakajima, *J. Chem. Theory Comput*. **2013,** *9*, 5373-5380.

14. H. Shan, S. Williams; W. Jong, L. Oliker, In: Proceedings of the Sixth International Workshop on Programming Models and Applications for Multicores and Manycores - PMAM 15: San Francisco, CA, USA,, **2015.**

15. C. Iancu, S. Hofmeyr, F. Blagojevic´, Y. Zheng, IEEE International Symposium on Parallel & Distributed Processing, **2010**, 1–11.

16. E. L. Fought, V. Sundriyal, M. Sosonkina, T. L. Windus. *J. Comput. Chem*. **2017**, *38*, 830–841. DOI: 10.1002/jcc.24756

17. MVAPICH2-2.2rc1, http://mvapich.cse.ohio-state.edu

18. Free Software Foundation, Inc. GCC 4.4.7. Available at: https://gcc.gnu.org/gcc-4.4/

19. M. Annavarami, E. Grochowski, J. Shen, Intel Software Programmer’s Guide – Combined Volumes 3a and 3b; IEEE Computer Society: Washington, DC, **2014**.

20. Performance Counter Monitor. Available at: https://github.com/opcm/pcm

21. T. H. Dunning, *J. Chem. Phys*. **1989**, *90*, 1007.

22. R. Kendall, E. Apra, D. Bernholdt, E. J. Bylaska, M. Dupuis, G. Fann, R. Harrison, J. Ju, J. Nichols, J. Nieplocha, T. P. Straatsma, T. L. Windus, A. Wong, *Comput. Phys. Commun*. **2000**, *128*, 260.

23. T. Kidd**,** Power Management States: P-States, C-States, and Package C-States. Available at https://software.intel.com/en-us/articles/power-management-states-p-states-c-states-and-package-c-states#_Toc383778910, **2014.**

24. A. L. Shimpi, The Sandy Bridge Review. Available at: http://www.anandtech.com/show/4083/the-sandy-bridge-review-intel-core-i7-2600k-i5-2500k-core-i3-2100-tested/21, accessed on June 16, 2018.

CHAPTER 5. DIRECT SYNTHESIS OF THE PHENANTHROVIRIDONE SKELETON USING A HIGHLY REGIOSELECTIVE NITROQUINONE DIELS−ALDER REACTION

A paper published in *ACS Omega*, **2020** *5* (16), 9311-9315.

Huangchao Yu, Ellie L. Fought, Theresa L. Windus, and George A. Kraus

ELF and TLW are responsible for all computational work, HY and GK completed all work on synthetic work.

Abstract

A variety of nucleophiles react efficiently with in situ generated nitroquinones. The reaction with substituted resorcinols led to a direct synthesis of the phenanthroviridinone and lagumycin skeleton via a highly regioselective Diels-Alder reaction.

Introduction

Nitrogen-substituted quinones, both natural and synthetic, have shown useful biological activity. Among these compounds are the jadomycins **1** which exhibit activity against cancer cell lines and against bacteria and yeast.[1] Phomazarin **2** was isolated from *Phoma terrestris Hansen* (Pyrenochaeta terrestris Hansen). Its structure was determined by Boger through total synthesis.[2] Catalin **3**, also known as pirenoxine, is an anti-cataract agent.[3] These quinones are most commonly synthesized via halo- and aminoquinones.[4]

An alternative would be to utilize nitrobenzoquinone, shown in Scheme 1. A literature search showed that nitroquinones have been infrequently used in organic synthesis. Nitrobenzoquinone and its analogs have been employed in innovative syntheses by Parker,[5] Valderrama,[6] and Tapia[7]. We report herein that nitrobenzoquinone reacts readily with a wide variety of heterocycles and electron-rich aromatics.[8]

Scheme 1. Heterocyclic quinones

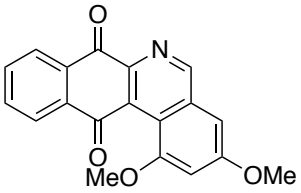

1

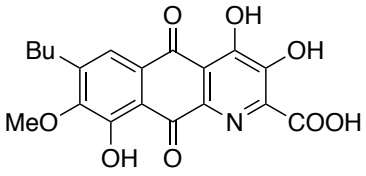

2

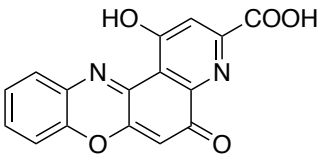

3

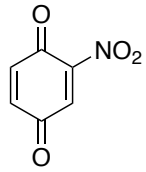

nitrobenzoquinone

Results And Discussion

The optimal conditions for the addition of aromatics to nitrobenzoquinone were determined using 1,3-dimethoxybenzene and 2-methylfuran. Among the oxidants evaluated for the in situ generation of nitrobenzoquinone, two equivalents of silver (I) oxide proved to be the most effective (Table 1). Other oxidants such as iron (III) chloride and manganese (IV) oxide did not provide promising yields. Dichloroethane emerged as the solvent of choice. The reaction was performed at ambient temperature overnight in the absence of light, and the product was isolated simply by loading the crude mixture

onto a silica column and eluting with an organic solvent. Nitrohydroquinone **4**, readily prepared

Table 1. Optimization of the reaction.

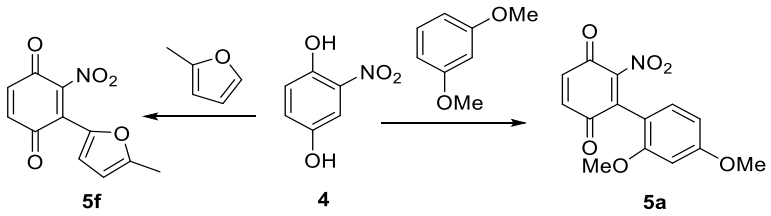

5f **4** **5a**

Entry	Product	Oxidant (200%)	Solvent	Yield[a]
1	5a	$FeCl_3$	$CHCl_3$	N.P.[b]
2	5a	$FeCl_3$	DMF	<5%
3	5a	MnO_2	$CHCl_3$	N.P.
4	5a	MnO_2	DMF	<5%
5	5a	Ag_2O	$CHCl_3$	51%
6	5a	Ag_2O	DCE	70%
7	5f	MnO_2	$CHCl_3$	N.P.
8	5f	MnO_2	Acetone	N.P.
9	5f	MnO_2	Et_2O	N.P.
10	5f	MnO_2	EtOAc	N.P.
11	5f	MnO_2	DMF	N.P.
12	5f	Ag_2O	$CHCl_3$	95%
13	5f	Ag_2O	DCE	97%

[a] Isolated yield

[b] No product detected

from commercially available 1,4-dimethoxybenzene,[8] was oxidized in situ to nitrobenzoquinone which reacted successfully with a range of electron-rich heterocycles such as furans, thiophenes and anilines. The results are illustrated in Scheme 2. All of the compounds in Scheme 2 are new compounds. The ready formation of 2,4,6-trisubstituted aryl quinones (**5b**, **5d**) is notable and likely a consequence of the high reactivity of nitrobenzoquinone. Other heteroaromatics such as pyrroles afforded the corresponding adducts in moderate yields. It is worth mentioning that aniline derivatives (**5j, 5l**) and tetrahydroquinolines (**5k**) reacted readily, presumably due to the electron donating effect of the nitrogen atom.

Scheme 2. Reaction scope

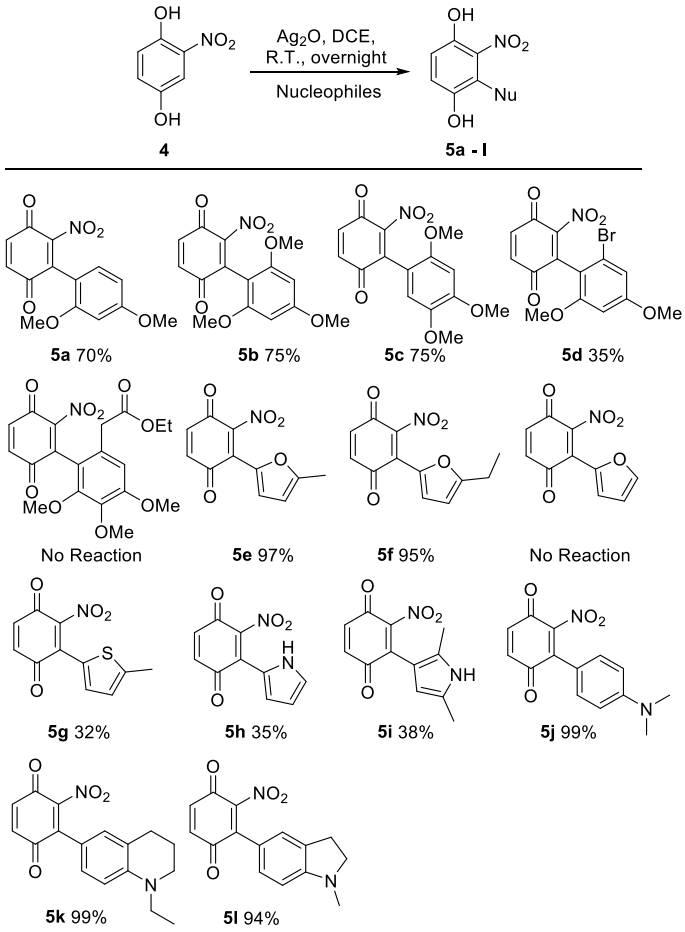

Surprisingly, the reaction between nitrobenzoquinone with phosphorus ylides afforded benzofurans **5m, 5n** and **5o**. The mechanism may involve a conjugate addition followed by an intramolecular cyclization and the expulsion of triphenylphosphine oxide. This chemistry provides an alternative route to nitro substituted benzofuran structures (Scheme 3).

Scheme 3. Synthesis of benzofuran

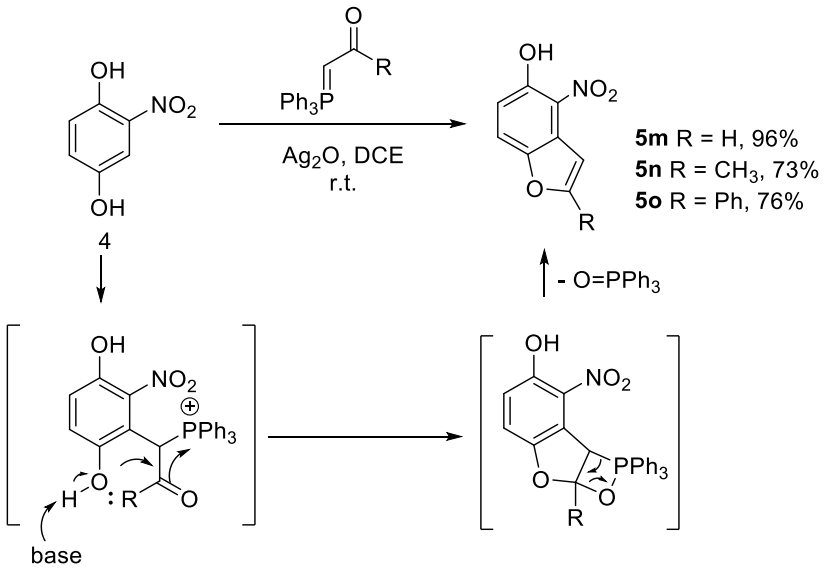

Synthetic Applications

With a good understanding of the reaction patterns of nitrobenzoquinone, a direct synthesis of the phenanthroviridone skeleton was attempted. The reaction of in situ generated nitrobenzoquinone with the tert-butyldimethylsilyl ether of 3,5-dimethoxybenzyl alcohol **6** afforded two products **7a** and **7b** in a 4:1 ratio which could not be separated (Scheme 4). A Diels-Alder reaction with the inseparable mixture of **7a** and **7b** favored the reaction at the double bond not bearing the nitro group, presumably because the bulky out-of-plane aryl group blocked the alternative site (Figures 1 and 2).

Moreover, the Diels-Alder reaction was highly regioselective, generating structures **8a** and **8b** as the only isomers, as evidenced by the oxidative conversion of **8a** to **11**.

Scheme 4. Regioselective Diels-Alder reaction

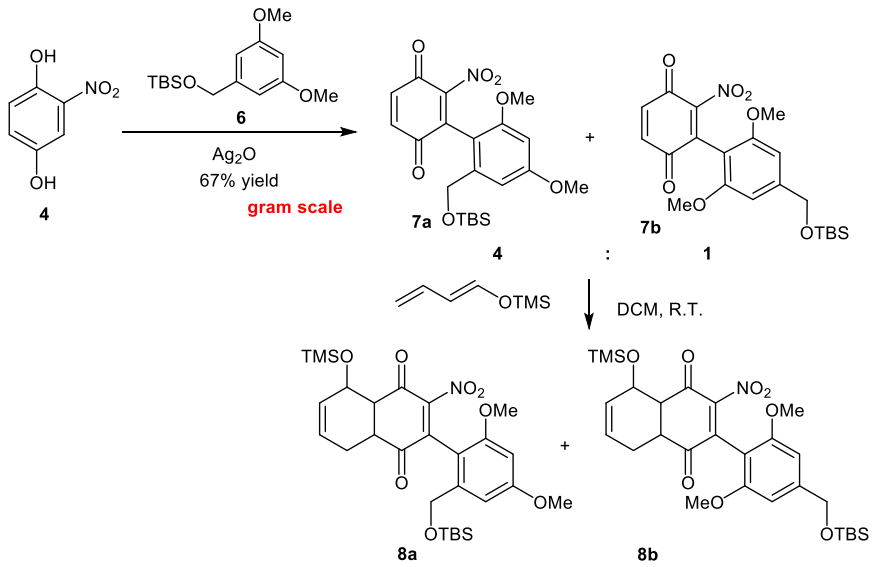

Mild acid mediated deprotection of the TMS group and oxidative aromatization by PCC produced a separable mixture of naphthoquinones **9a** and **9b** (Scheme 5). The nitro group in **9a** was readily reduced and the resulting product was oxidized with MnO_2 to form aminoquinone **10**. Deprotection of the silyl ether using TBAF followed by intramolecular imine formation with MnO_2 afforded the phenathroviridone skeleton **11**, as shown in Scheme 5. The structure of **11** was confirmed by single crystal diffraction experiment.

Scheme 5. Synthesis of Phenathroviridone skeleton

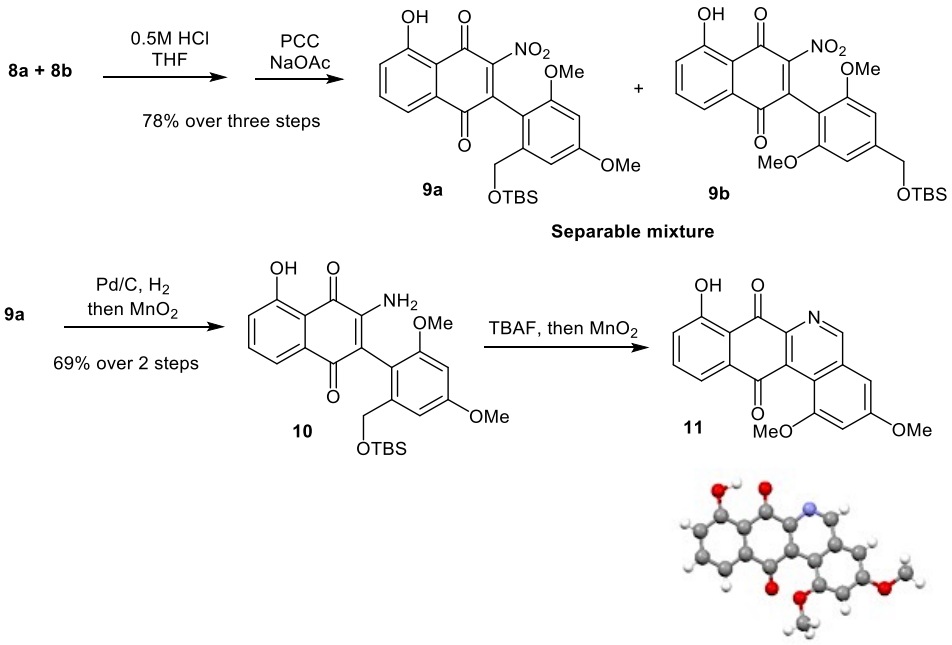

Using the common intermediate **10**, the lagumycin B skeleton **12** was synthesized by an acid catalyzed intramolecular cyclization process. This is shown in Scheme 6.

Scheme 6. Synthesis of the lagumycin B skeleton

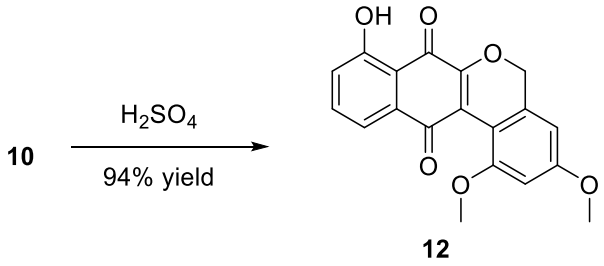

Origin of the Regioselectivity

The General Atomic and Molecular Electronic Structure System (GAMESS)[9] was used for all structural and vibrational analysis. B3LYP[10] density functional theory and

the 6-311G(d,p) basis set[11] were employed for all final reported values. All 3D figures and two-dimensional electrostatic potential surfaces were created using MacMolPlt.[12]

Two separate optimizations were performed on **5b**. The first optimization imposed no symmetric or rotational constraints and its lowest energy geometry can be found in Figure 1. When allowed to freely rotate, the nitro group distorts to 63.7 degrees out of the plane of the quinone, most likely due to the steric interactions between the nitro and carbonyl oxygens. The phenyl group also distorts from the expected 90 degrees to 58.8 degrees out of the plane of the quinone. Another feature of the low energy geometry is the positioning of the quinone oxygens, each distorted out of the plane of the ring, but in opposite directions. The oxygen at C1 presents a dihedral of 3.8 degrees, while the oxygen at C4 sits 8.4 degrees out of the plane of the ring. A Hessian calculation confirmed the structure is a minimum on the potential energy surface (PES) with zero imaginary frequencies.

A second optimization was performed on the same substituted quinone, imposing symmetric constraints using the C_S plane of symmetry, referred to as **5b_sym**. Optimizations were performed with both nitro oxygens in the plane of the quinone and the phenyl group perpendicular. The optimized geometry of **5b_sym** can be found in the Supporting Information. The symmetry optimized structure was found to be 13.7 kcal/mol higher in energy than the lowest energy (unrestricted) geometry. Torsional analysis shows that the relaxation of the nitro group out of the plane of the quinone accounts for ~6 kcal/mol. A Hessian calculation on **5b_sym** found 3 imaginary frequencies indicating the conformer is not a stationary point on the PES.

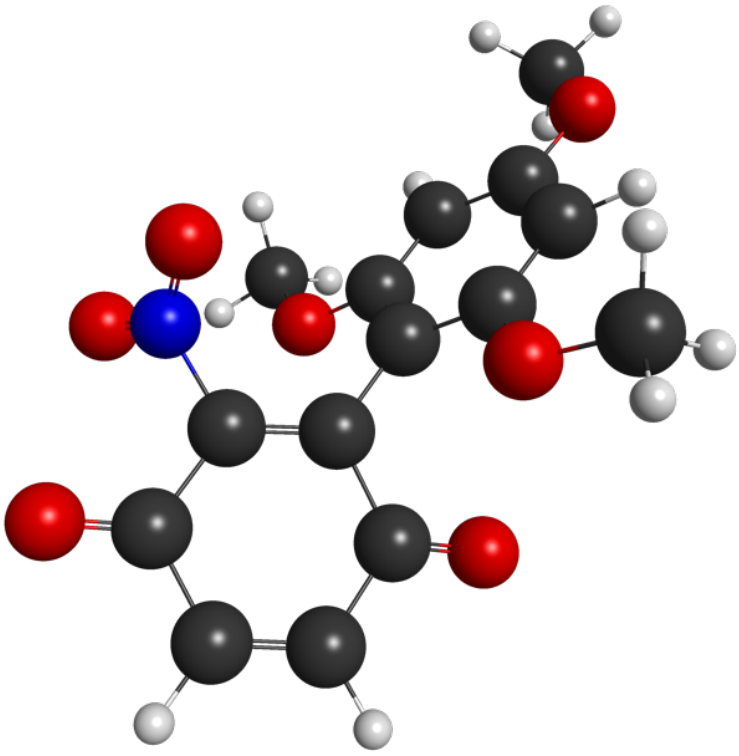

Figure 1. Lowest energy geometry for nitroquinone (5b) optimized using B3LYP and 6-311G(d,p).

The optimized molecular orbitals for 5b were used to calculate two-dimensional molecular electrostatic potentials (MEPs). The MEP is defined as the potential felt by a positive charge given the molecular charge density at a given point within a grid. These calculations were achieved by first rotating the structure so the ring containing the C5-C6 bond was situated in the *xy*-plane. A diagram depicting the locations of the MEP planes can be found in Figure 2. Then 2D MEPs were calculated 2Å above and 2Å below the plane of the ring and can be found in Figure 3 (a) and (b) respectively. As seen in Figure 3, at 2Å above the plane, the negative charge density is higher in the region around C6, whereas at 2Å below the plane, the charge density is much more evenly distributed.

Population analysis of the dienophile carbons show negligible differences between the C5 and C6 of the quinone, but both Mulliken and Löwdin populations show significant differences between the C1 and C4 of the diene. The populations and partial charges both indicate the terminal carbon, C4, is more electronegative than C1. A rudimentary frontier molecular orbital (FMO) analysis finds C4 of the diene aligned with C5 of the quinone ring and C1 of the diene aligned with C6 of the quinone; these data can be found in the Supporting Information. The electronegativity difference within the diene, the skewed MEP 2Å above the dienophile, and the FMO results are all consistent with the regioselectivity found in experiment.

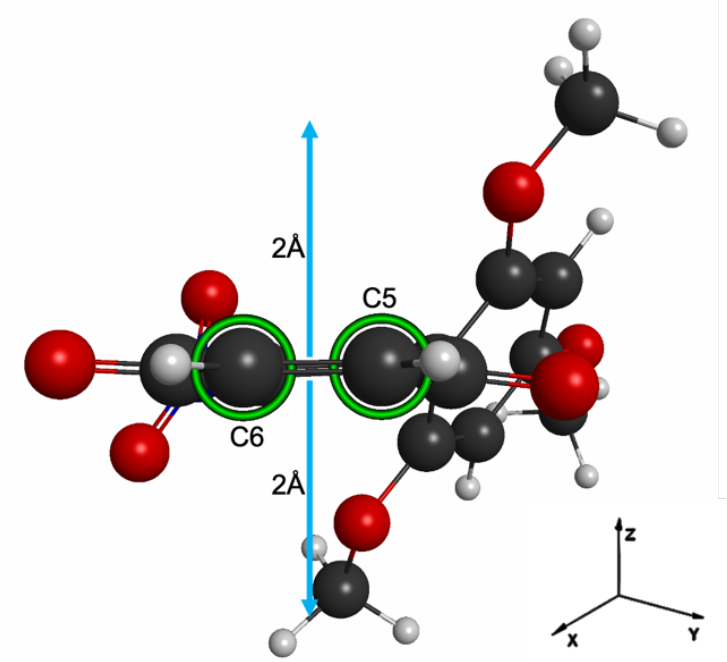

Figure 2. Head-on view of C5-C6 bond in 5b illustrating the location of the MEP planes 2Å above and below the plane of the nitroquinone ring. C5 and C6 are marked in green for clarity.

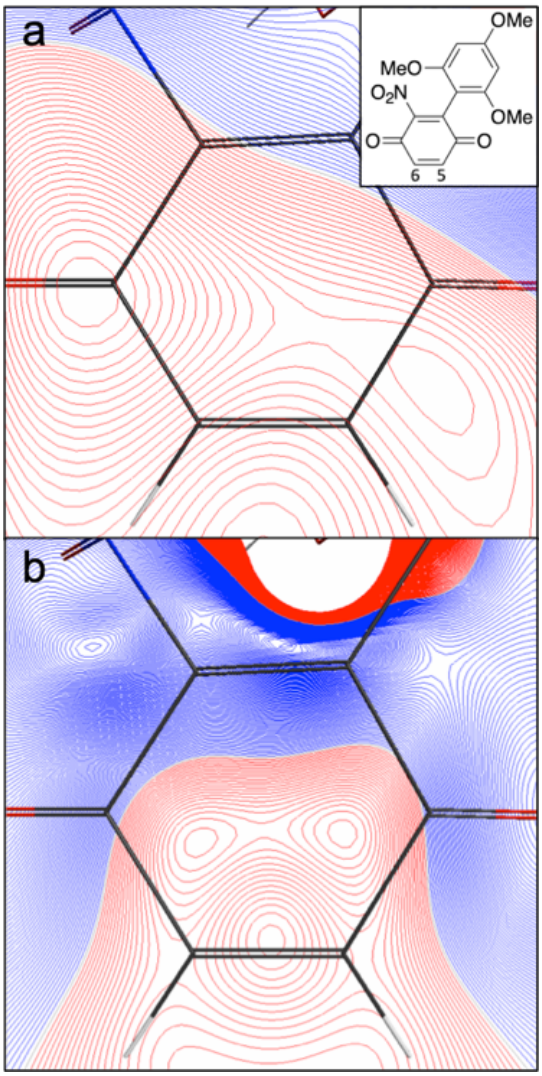

Figure 3. Two-dimensional molecular electrostatic potentials for nitroquinone (**5b**): (a) MEP calculated 2Å above the plane of C5-C6 double bond; (b) MEP calculated 2Å below the plane of the C5-C6 double bond. The red contours are regions of positive potential (negative charge density), and blue contours are regions of negative potential (positive charge density). The inset in the upper righthand corner of shows the orientation of the system with the C5 and C6 carbons labeled.

Conclusion

To conclude, the use of nitrobenzoquinone enabled a direct synthesis of the lagumycin B and phenathroviridone skeletons. The synthetic route is flexible and scalable and will permit the synthesis of other potential analogs.

Experimental

General Procedure for electron rich aromatics addition to nitroquinone 4.

2',4'-Dimethoxy-6-nitro-[1,1'-biphenyl]-2,5-dione (5a). To a 5 ml round bottom flask, 2-nitrobenzene-1,4-diol **4** (47 mg, 0.3 mmol, 1.0 equiv.) and silver (I) oxide (139 mg, 0.6 mmol, 2.0 equiv.) in dry DCE, 1,3-dimethoxybenzene (62 mg, 0.45 mmol, 1.5 equiv.) was added. The reaction mixture was allowed to stir at ambient temperature without light (the flask was fully covered by aluminum foil) overnight. After the reaction is finished (tracked by TLC), the crude mixture was loaded directly on a silica column. Using ethyl acetate/hexane (1:3) as eluent the desired product **5a** was isolated as a highly colored solid (61 mg, 70% yield). ^{1}H NMR (400 MHz, Chloroform-d) δ 7.06 (d, J = 8.5 Hz, 1H), 6.99 (d, J = 10.2 Hz, 1H), 6.92 (d, J = 10.3 Hz, 1H), 6.54 (d, J = 8.5 Hz, 1H), 6.49 (s, 1H), 3.84 (s, 3H), 3.73 (s, 3H). ^{13}C NMR (101 MHz, Chloroform-d) δ 184.64, 177.43, 163.98, 158.84, 137.54, 135.20, 134.82, 131.31, 109.12, 105.53, 99.27, 55.83, 55.76. HRMS (ESI-QTOF) calcd for $C_{14}H_{12}NO_6$ $[M + H]^+$ 290.0660, found 290.0656.

Acknowledgement

We thank the ISU Department of Chemistry for partial support of this research. This research was partially supported by the U.S. Department of Energy, Office of Basic Energy Sciences, Division of Chemical Sciences, Geosciences, and Biosciences for the Computational Chemical Sciences project. The Ames Laboratory is operated for the U.S. Department of Energy by Iowa State University under Contract No. DE-AC02-07CH11358.

Supporting Information

The Supporting Information is available on the ACS Publications website. Including experimental procedures, spectra, and computational results.

References

1. Jakeman, D. L.; Farrell, S.; Young, W.; Doucet, R. J.; Timmons, S. C. Bioorg. Novel jadomycins: incorporation of non-natural and natural amino acids. *Med. Chem. Lett.* **2005**, *15*, 1447-1449.

2. Boger, D. L.; Hong, J.; Hikota, M.; Ishida, M. Total synthesis of phomazarin. *J. Am. Chem. Soc*. **1999**, *121*, 2471-2477.

3. Biswas, N. R.; Mongre, P. K.; Das, G. K.; Sen, S.; Angra, S. K.; Vajpayee, R. B. Animal study on the effects of catalin on aftercataract and posterior capsule opacification. *Ophthalmic Research* **1999**, *31*, 140-142.

4. Chaves, M. H.; Santos, L. A.; Lago, J. H. G.; Roque, N. F. Alkaloids from Porcelia macrocarpa. *J. Nat. Prod*. **2001**, *64*, 240.

5. Parker, K. A.; Sworin, M. A convergent synthesis of indoloquinones. *Tetrahedron Lett.* **1978**, 2251-2254.

6. Benites, J.; Rojo, L.; Valderrama, J. A.; Taper, H.; Calderon, P. B. Part 1: Effect of vitamin C on the biological activity of two euryfurylbenzoquinones on TLT, a murine hepatoma cell line. *Eur. J. Med. Chem.* **2008**, *43*, 1813-1817.

7. Polgatti, V.; Valderrama, J. A.; Tapia, R. Studies on quinones. XIX. Improved synthesis of 2-nitro-1, 4-benzoquinone and its reaction with nucleophiles. *Synthetic Commun*. **1990**, *20*, 1085-1090.

8. Yu, H.; Kraus, G. A. An entry to indole quinones using in situ generated nitrobenzoquinone, *Tetrahedron Lett.* **2018**, *59*, 1424-1426.

9. Schmidt, M. W.; Baldridge, K. K.; Boatz, J. A.; Elbert, S. T.; Gordon, M. S.; Jensen, J. H.; Koseki, S.; Matsunaga, N.; Nguyen, K. A.; Su, S.; Windus, T. L.; Dupuis, M.; Montgomery, J. A. anothers General Atomic and Molecular Electronic Structure Systems. *J. Comput. Chem.* **1993**, *14*, 1347-1363.

10. Becke, A. D. Becke's three parameter hybrid method using the LYP correlation functional. *J. Chem. Phys.* **1993**, *98*, 5648-5652; Lee, C.; Yang, W.; Parr, R. G. Development of the Colle-Salvetti correlation energy formula into a functional of the electron density. *Phys. Rev. B.* **1988**, *37*, 785-789; Vosko, S. H.; Wilk, L.; Nusair, M. Accurate spin-dependent electron liquid correlation energies for local spin density calculations: a critical analysis. *Can. J. Phys.* **1980**, *58*, 1200-1211; Stephens, P. J.; Devlin, F. J.; Chabalowski, C. F.; Frisch, M. J. Ab initio calculation of vibrational absorption and circular dichroism spectra using density functional force fields. *J. Phys. Chem.* **1994**, *98*, 11623- 11627.

11. Krishnan, R.; Binkley, J. S.; Seeger, R.; Pople, J. A. Self-consistent molecular orbital methods. XX. A basis set for correlated wave functions. *J. Chem. Phys.* **1980**, *72*, 650-654.

12. Bode, B. M.; Gordon, M. S. *J. Mol. Graphics and Modeling.* **1999**, *16*, 133-138.

CHAPTER 6. COMPUTATIONAL AND NMR SPECTROSCOPIC EVIDENCE FOR STEREOCHEMISTRY-DEPENDENT CONFORMATIONS OF 2,2,6,6-TETRAMETHYLPIPERIDINYL-MASKED 1,2-DIOLS

A paper published in the *Journal of Organic Chemistry*, **2015**, 80, 9967−9972

Ellie L. Fought, Shreyosree Chatterjee, Theresa L. Windus, and Jason Chen

ELF and TLW contributed all computational results, SC and JC were responsible for all synthetic and spectroscopic results.

Abstract

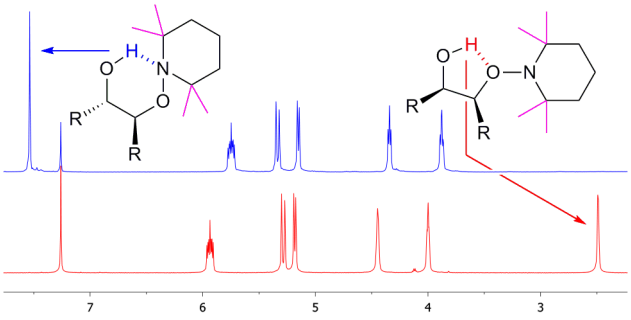

2,2,6,6-Tetramethylpiperidinyl-masked 1,2-diols exhibited stereochemistry-dependent hydroxyl proton chemical shifts: ca. 7 ppm for the *syn* diastereomer and ca. 2 ppm for the *anti* diastereomer. A computational search for low energy geometries revealed that the *syn* isomer favors a six-membered ring hydrogen bond to nitrogen and the *anti* isomer favors a five-membered ring hydrogen bond to oxygen. The computed low energy conformations were found to have a large difference in hydroxyl proton shielding that was reflected in the

experimental chemical shift difference. This chemical shift difference was observed in a broad range of solvents, and thus may be useful as a stereochemical probe. The stereochemistry-dependent conformation and chemical shift signature appeared to be due to a *syn* pentane interaction between the *gem*-dimethyl groups on the 2,2,6,6-tetramethylpiperidinyl moiety.

Introduction

Stereochemically-defined polyols are commonly found in natural products and bioactive molecules. Oxidative strategies for introducing alcohols or masked alcohols are appealing because they install additional functional groups. Many oxidants have been used to introduce alcohols, including osmium tetroxide,[1] selenium dioxide,[2] singlet oxygen,[3] and oxaziridine reagents.[4] More recently, the readily-available stable oxygen radical 2,2,6,6-tetramethyl-1-piperidinyloxy (TEMPO) has become increasingly popular as a precursor to an electrophilic oxygen reagent. TEMPO has been used to install 2,2,6,6-tetramethylpiperidinyl-masked alcohols through α-functionalization reactions of carbonyl compounds[5] and β-dicarbonyls[6] and vicinal difunctionalization reactions of alkenes[7] and α,β-unsaturated carbonyl compounds.[8]

We recently reported that α-oxyaldehydes generated by oxidative incorporation of TEMPO can react with diverse organomagnesium or -lithium reagents to yield differentially-masked *anti*-1,2-diols, in many cases with >20:1 diastereomeric ratio.[9] In the course of that study, we noticed that the NMR chemical shift of the hydroxyl proton in 2,2,6,6-tetramethylpiperidinyl-masked 1,2-diols is strongly dependent on the stereochemistry of the diol. ((For clarity, throughout this paper 2,2,6,6-

tetramethylpiperidinyl-masked 1,2-diols are referred to simply as diols. There are no unprotected diols in this paper.) The hydroxyl chemical shift in $CDCl_3$ is ca. 6 ppm for primary alcohols **1** (Figure 1), ca. 7 ppm for *syn* diols **2**, and ca. 2 ppm for *anti* diols **3**. Herein we provide computational and NMR spectroscopic evidence that this chemical shift anomaly reflects differences in the ground state conformations of such compounds.

Figure 1. 2,2,6,6-Tetramethylpiperidinyl-masked diols.

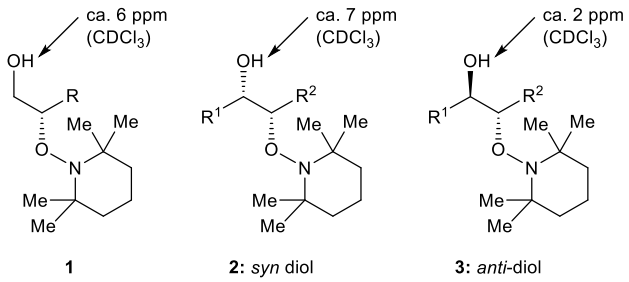

Results and Discussion

The ^1H NMR spectra for differentially-masked diols **1a**, **2a**, and **3a** are shown in Figure 2. Synthetic diols **2a** (*syn*) and **3a** (*anti*) were chosen for NMR spectroscopic studies because the ^1H NMR signals for the two hydrogens next to the oxygen-bound carbons could be unambiguously assigned since only one is allylic. Secure assignment of these two signals was critical for enabling coupling constant-based conformational analysis.[10] The identity of the hydroxyl protons was confirmed by deuterium exchange with D_2O. Whereas hydroxyl protons in $CDCl_3$ typically display variable chemical shifts and often are absent due to their rapid exchange with protons from adventitious water, the

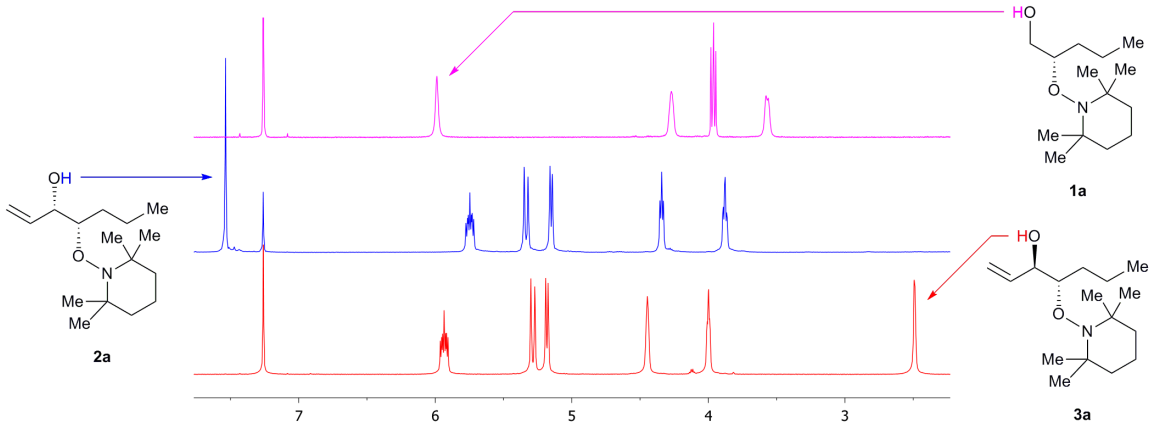

Figure 2. Partial ^{1}H NMR spectra of diols **1a**, **2a**, and **3a**. See Supporting Information for full-width spectra.

hydroxyl protons in diols **1**–**3** had reproducible chemical shifts and did not undergo rapid proton exchange with water. The slow rate of proton exchange suggested the presence of intramolecular hydrogen bonding. The hydroxyl proton could hydrogen bond to the oxygen of the masked alcohol to form a five-membered ring or to the nitrogen of the piperidine ring to form a six-membered ring. The large chemical shift differences between *syn* diols **2** and *anti* diols **3** suggested that these diastereomeric compounds may adopt different ground state conformations.

Since the unusual hydroxyl proton NMR chemical shifts were observed across all compounds of structures **1**–**3** that we have characterized thus far,[9] computational studies could be performed using the simplest possible carbon backbones. The computational analysis of primary alcohol **1b**, *syn* diol **2b**, and *anti* diol **3b** (all with R = R^1 = R^2 = Me) began with a systematic identification of the low energy conformations. Three to five of the lowest energy conformations were chosen for each compound as starting points for higher-level analysis. All structures shown in this paper are at the MP2/6-311G(d,p) level and all energies include zero point energy (ZPE) corrections. The element colors in the

figures are as follows: nitrogen is blue, oxygen is red, carbon is grey, and hydrogen is white.

After the final round of geometry optimizations, a low energy geometry emerged for each of the compounds (**1b**–**3b**). The structures shown in Figures 3 and 4 do not emphasize visualization of the piperidinyl ring, but in all cases this ring possesses a chair conformation with the oxygen substituent in an equatorial position. The computed geometry of primary alcohol **1b** (Figure 3a) shows an intramolecular hydrogen bond between the hydroxyl proton and the piperidine nitrogen (1.85 Å). The six-membered

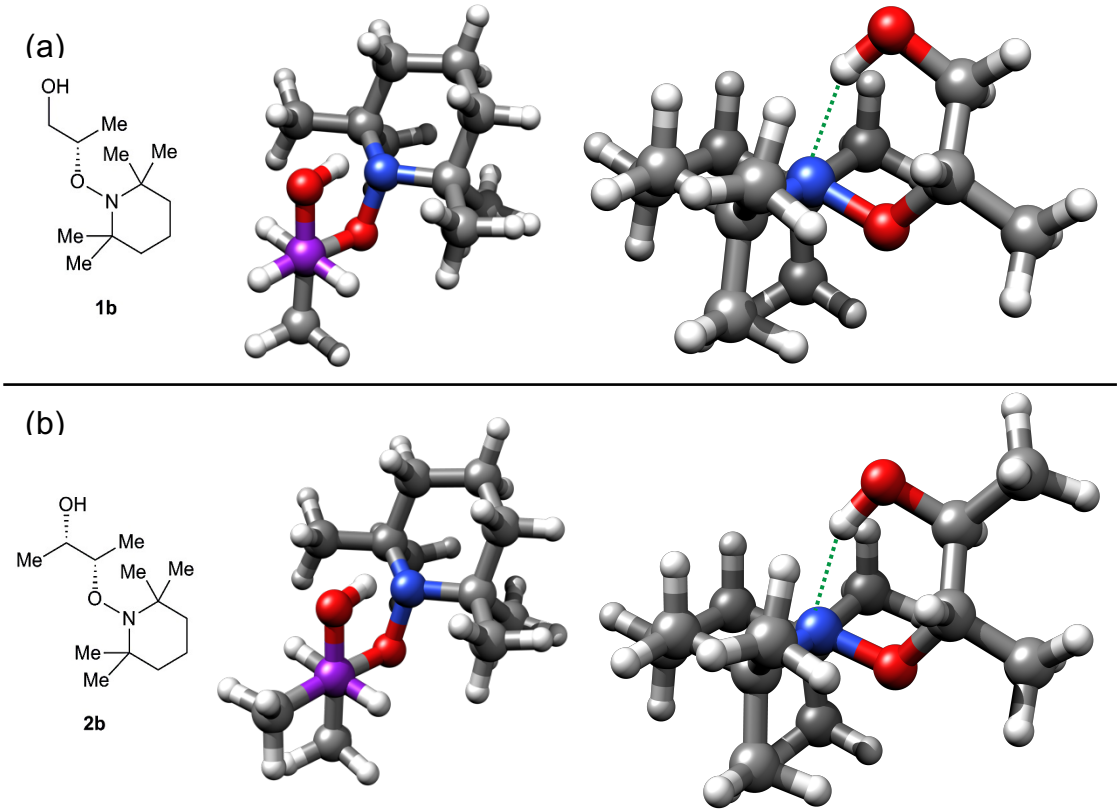

Figure 3. Computed ground state conformations of (a) primary diol **1b** and (b) *syn* diol **2b**. Two different views are given for each conformation. The purple atom is a carbon directly in front of another carbon in a Newman projection-like view.

ring formed by hydrogen bonding adopts a twist boat conformation, and the alkyl chain of the diol backbone is *anti* to the free hydroxyl group. While the lowest energy conformation contains a six-membered ring hydrogen bond, the lowest energy conformation with a five-membered ring hydrogen bond is only 3.3 kcal mol^{-1} higher in energy (see Table 1). The computed geometry of *syn* diol **2b** (Figure 3b) is virtually identical to that of primary alcohol **1b** (1.85 Å hydrogen bond for **1b**; 1.81 Å for **2b**) save for the presence of an additional alkyl group *anti* to the masked hydroxyl group. The *anti* relationship between the two methine protons (and thus the gauche relationship of the diol alkyl groups) was experimentally validated by the observation of a large $^{3}J_{H-H}$ coupling constant (8.7 Hz) between these two protons in the ^{1}H NMR spectrum of *syn* diol **2a**.[10] The lowest energy five-membered ring hydrogen bond conformation is 3.4 kcal mol^{-1} higher in energy than the lowest six-membered ring structure.

Table 1. Relative energy of five- and six-membered ring hydrogen bond conformations[a]

Compound	ΔE / kcal mol^{-1}
1b	+3.3
2b	+3.4
3b	–2.7

[a] The energy difference is calculated for the lowest energy five- and six-membered ring hydrogen bond conformations. A positive energy indicates that the six-membered ring hydrogen bond conformation is lower in energy.

As shown in Figure 4, the two lowest energy computed geometries of *anti* diol **3b** possess a five-membered ring hydrogen bond between the hydroxyl proton and the oxygen of the masked hydroxyl. The two five-membered ring geometries were calculated to have similar energies (separated by only 0.9 kcal mol^{-1}) and hydrogen bond distances

(2.21 Å for the lower energy geometry; 2.25 Å for the higher energy geometry). This hydrogen bond length is significantly longer than those for **1b** and **2b** and is likely due to the need to minimize torsional strain in the five-membered ring. A transition state between these two geometries was located computationally at 6.3 kcal mol^{-1} above the lower energy geometry, suggesting that these two structures rapidly equilibrate at ambient temperature. The hydrogen bond to oxygen shortens in the transition state to 1.87 Å. HETLOC NMR spectroscopy of *anti* diol **3a** revealed a 4 Hz $^{3}J_{H-H}$ coupling constant between the methine protons, consistent with a gauche relationship between these two protons (and thus a gauche relationship between the diol alkyl groups).

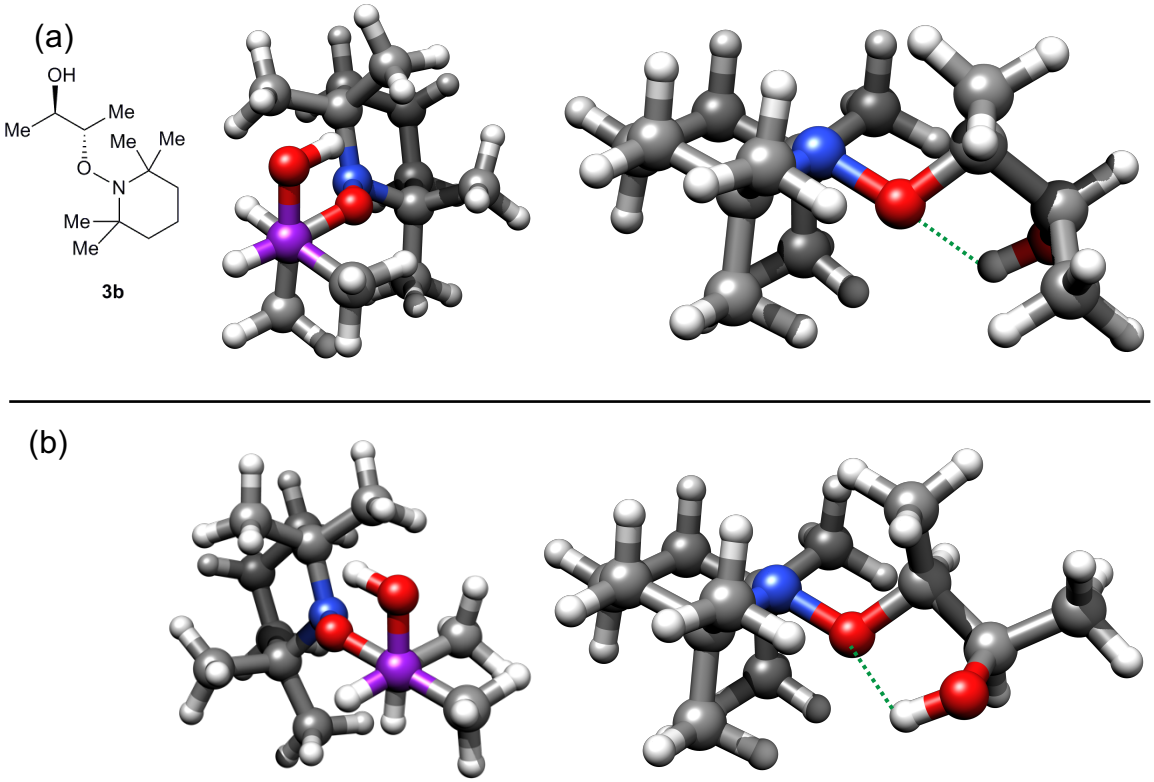

Figure 4. Computed geometries for (a) the lowest energy conformation of *anti* diol **3b** and (b) the second-lowest energy conformation of diol **3b**. Two different views are given for each conformation. The purple atom is a carbon directly in front of another carbon in a Newman projection-like view.

Measurement of $^{2}J_{C–H}$ and $^{3}J_{C–H}$ coupling constants by HETLOC and PS-HMBC NMR spectroscopy, respectively,[10] did not allow unambiguous identification of the major conformation, but 1D NOE data provided evidence for the presence of both conformations shown in Figure 4. The lowest energy six-membered ring hydrogen bond conformation is 2.7 kcal mol^{-1} higher in energy than the lowest energy five-membered ring.

Isotropic chemical shifts were calculated for the lowest energy conformations of diols **1b**–**3b** (see Table 2). The KT2 functional was favored over B3LYP because KT2 was designed specifically for the calculation of magnetic properties. The computed proton chemical shifts for diols **1b**−**3b** are in good qualitative agreement with the experimental chemical shifts for diols **1a**–**3a** in $CDCl_3$. Interestingly, even though the computed low energy geometries of diols **1b** and **2b** are very similar, the computed hydroxyl proton chemical shifts nonetheless correctly reflect not only the experimentally-observed relative shielding of the hydroxyl protons, but even the magnitude of the difference. This close agreement provides strong evidence that the computed gas phase conformations of diols **1b**–**3b** are relevant in solution.

Similar differences in shielding between the hydroxyl protons of diols **1a**–**3a** are observed in other solvents with weak Lewis basicity, suggesting that the calculated conformational preferences are retained. The chemical shift of the hydroxyl protons of primary alcohol **1a** and *syn* diol **2a** are little affected by solvents with stronger Lewis basicity, but the hydroxyl proton of *anti* diol **3a** shifts downfield. This change might be due to a competition between intramolecular hydrogen bonding and hydrogen bonding to the more Lewis basic solvents; alternatively, these solvents might reduce the energy gap

between the five- and the six-membered ring intramolecular hydrogen bond conformations. Nonetheless, the relative shielding as compared with *syn* diol **2a** is preserved, and thus this chemical shift difference is a useful stereochemical probe across a broad range of solvents. Interestingly, despite the ability to compensate for loss of intramolecular hydrogen bond by hydrogen bonding to CD_3OH, the proton exchange for diols **1a** and **2a** is sufficiently slow that their characteristic hydroxyl proton chemical

Table 2. Computed and experimental hydroxyl proton chemical shifts

Solvent	Primary alcohol / ppm	*syn* Diol / ppm	*anti* Diol / ppm
Gas phase (computed)	5.51 (**1b**)[a]	6.98 (**2b**)[a]	0.00 (**3b**)[b] 2.05 (**3b**)[a][c]
$CDCl_3$	5.99 (**1a**)	7.55 (**2a**)	2.49 (**3a**)
Benzene-d_6	5.40 (**1a**)	7.16 (**2a**)[d]	1.87 (**3a**)
Cyclohexane-d_{12}	4.68 (**1a**)	6.49 (**2a**)	1.75 (**3a**)
CD_3CN	5.94 (**1a**)	6.66 (**2a**)	2.71 (**3a**)
THF-d_8	4.44 (**1a**)	6.36 (**2a**)	3.54 (**3a**)
Acetone-d_6	4.75 (**1a**)	6.93 (**2a**)	3.46 (**3a**)
DMF-d_7	4.58 (**1a**)	6.00 (**2a**)	4.50 (**3a**)
DMSO-d_6	4.59 (**1a**)	6.42 (**2a**)	4.51 (**3a**)
Pyridine-d_5	5.94 (**1a**)	7.17 (**2a**)	6.06 (**3a**)
CD_3OH:$CDCl_3$ (1:1)	5.51 (**1a**)	6.98 (**2a**)	[e]

[a] Referenced to the calculated isotropic chemical shift of the lower energy conformation of diol **3b**. [b] The calculated isotropic chemical shift for the lower energy conformation of diol **3b** was set to 0.00 ppm. [c] Calculated for the higher energy conformation of diol **3b**. [d] Hydroxyl proton signal is hidden under the solvent residual peak. Blending in a small amount of $CDCl_3$ shifts the hydroxyl proton signal downfield. [e] Hydroxyl proton signal is either hidden under the CD_3OH hydroxyl proton signal or rapidly exchanging with the CD_3OH hydroxyl proton signal.

shifts can be observed even in a 1:1 CD_3OH:$CDCl_3$ mixture. ($CDCl_3$ was added in order to improve solubility.) Therefore, the 6-membered ring hydrogen bond conformation of primary alcohol **1a** and *syn* diol **2a** appears to be surprisingly stable even in protic solvent.

To try to understand why diastereomeric diols **2** and **3** favor different conformations, we investigated the role of the *gem*-dimethyl groups on the 2,2,6,6-tetramethylpiperidinyl moiety by computing the low energy geometries for diols **1′**–**3′** (Figure 5). In all cases, a six-membered ring hydrogen bond conformation is favored, but the energy difference between five- and six-membered ring hydrogen bond conformations is smaller than the corresponding energy difference for diols **1b**–**3b** (see Table 3). The *syn* pentane interaction between the axial methyl groups on the piperidine ring of diols **1**–**3** forces these methyl groups apart (N–C–C_{axial} angle for **1b**: 115.0° and 115.3°; N–C–H_{axial} angles for **1′**: 109.6° and 109.9°; all angles measured on the lowest energy conformation) and flattens the chair conformation at nitrogen (C–N–C angle for **1b**: 117.2°; for **1′**: 110.9°). Similar angles are observed for all five- and six-membered

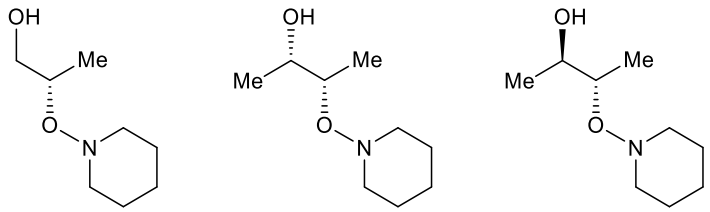

1′ **2′:** *syn* diol **3′:** *anti*-diol

Figure 5. Diols masked by unmethylated piperidinyl moieties.

Table 3. Relative energy of five- and six-membered ring hydrogen bond conformations[a]

Compound	ΔE / kcal mol^{-1}
1′	+1.2
2′	+0.5
3′	+1.3

[a] The energy difference is calculated for the lowest energy five- and six-membered ring hydrogen bond conformations. A positive energy indicates that the six-membered ring hydrogen bond conformation is lower in energy.

ring conformations of diols **1b**–**3b** and for diols **1′**–**3′**. This *syn* pentane-induced distortion does not consistently favor a five- or six-membered ring hydrogen bond conformation, but nonetheless appears to be causing diols **1**–**3** to have distinct preferred conformations and NMR spectroscopic signatures.

Conclusion

The stereochemistry-dependent hydroxyl proton chemical shift of 2,2,6,6-tetramethylpiperidinyl-masked 1,2-diols was shown by a combination of computational and NMR spectroscopic methods to be the result of differences in ground state conformations. Primary alcohols **1** and *syn* diols **2** favor a six-membered ring hydrogen bond, but *anti* diols **3** favor a five-membered ring hydrogen bond. Computed isotropic chemical shifts of the hydroxyl protons show good correlation with experimental chemical shifts. The hydroxyl proton of *syn* diols **2** is downfield of the hydroxyl proton of *anti* diols **3** in a broad range of solvents, making this difference in chemical shift useful for assigning relative stereochemistry. These stereochemistry-dependent conformational and spectroscopic differences appear to stem from a *syn* pentane interaction on the tetramethylpiperidine ring.

The internal hydrogen bonding forces the carbon chain of the diol to adopt a gauche conformation in both *syn* diols **2** and *anti* diols **3**. This bending of the carbon chain is expected to enhance ring closure rates of substrates containing a 2,2,6,6-tetramethylpiperidinyl-masked 1,2-diol. Furthermore, the predictable direction of the bend for *syn* diols **2** may be useful for remote stereoinduction in cyclization reactions. Studies to explore these potential synthetic consequences of the conformational preferences discovered herein are under way.

Experimental Section

Computation

The General Atomic and Molecular Electronic Structure System (GAMESS) software package[11] was used for all structure analysis calculations. The systematic identification of low energy conformations was performed using Restricted Hartree-Fock (RHF) and the small basis set 3-21G(d).[12] The optimization process began with finding a stable, low-energy conformation for the tetramethylpiperidine ring. The carbon chain was then attached with each diol's required stereochemistry and a systematic rotor search followed. Between 15 and 20 different conformations of each compound were optimized. All equilibrium coordinates are provided in the Supporting Information. Three to five geometries were then chosen for each of the diols of interest; only the lowest energy geometries within a 3-4 kcal/mol window were used in higher-level calculations. Further optimizations were performed using both B3LYP[13] density functional theory and Møller–Plesset second-order perturbation theory (MP2)[14] using the 6-311G(d,p) basis set.[15] Since the B3LYP and MP2 geometries were very similar, Hessians were only computed at the

B3LYP/6-311G(d,p) level to confirm that minima were found and to obtain the zero point energy (ZPE) corrections. The images in the paper are the MP2-optimized coordinates and were generated using Chimera.[16]

Chemical shielding calculations were performed using the NWChem computational software package.[17] The Gauge-Independent Atomic Orbital (GIAO) method[18] was employed with the KT2 functional[19] and the aug-cc-pVTZ basis set[20] using the MP2/6-311G(d,p) optimized geometries. Shielding tensors of the lowest energy structure for each compound were calculated and the isotropic shielding values were then used to calculate the chemical shifts. For completeness, all shielding calculations were also performed using the B3LYP functional. The results using B3LYP provided the same trend in chemical shifts and are available in the Supporting Information.

Synthesis

See Scheme 1. All reactions were performed with stirring under an argon atmosphere under anhydrous conditions. Vinylmagnesium bromide solution was purchased from Aldrich. All other reagents were purchased at the most economical grade. Dry tetrahydrofuran (THF), was obtained by passing HPLC grade solvent through a commercial solvent purification system. All other chemicals were used as received, without purification. Flash column chromatography was performed using Grace Davison Davisil silica gel (60 Å, 35–70 μm). Yields refer to chromatographically- and spectroscopically- (1H NMR) homogeneous samples of single diastereomers. Thin-layer chromatography (TLC) was performed on Grace Davison Davisil silica TLC plates using UV light and common stains for visualization. NMR spectra were calibrated using

residual undeuterated solvent as an internal reference. Apparent couplings were determined for multiplets that could be deconvoluted visually.

Scheme 1. Synthesis of diols **1a**–**3a**.

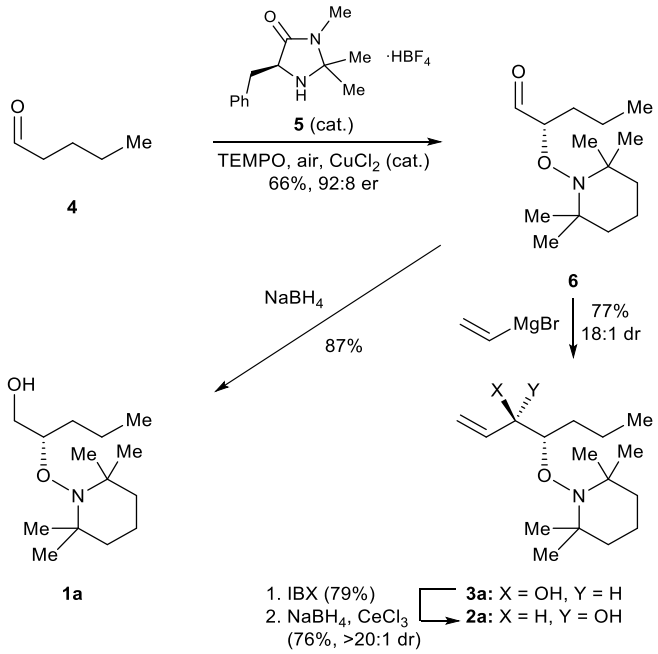

α-Oxyaldehyde 6

((*S*)-2-((2,2,6,6-tetramethylpiperidin-1-yl)oxy)pentanal). To a mixture of activated 4 Å molecular sieves (100 mg, powdered) and imidazolidinone catalyst **5** ((*S*)-5-benzyl-2,2,3-trimethylimidazolidin-4-one) (500 mg, 1.6 mmol, 0.2 equiv.) in 5 mL of acetone was added $CuCl_2 \cdot 2H_2O$ (139 mg, 0.81 mmol, 0.1 equiv.). The green reaction mixture was stirred open to air for 5 minutes until the copper salt dissolved and the mixture turned dark orange. The reaction was cooled to 0 °C for 10 minutes, then pentanal (**4**, 0.87 mL, 8.1 mmol, 1.0 equiv.) was added dropwise over 2 minutes. The reaction was stirred at 0 °C for 10 minutes, then a solution of TEMPO (1.51 g, 9.7 mmol,

1.2 equiv.) in 2 mL of acetone was added dropwise over 3 minutes. The reaction mixture was capped with a rubber septum and an air inlet line was attached via an 18-gauge needle. The reaction was stirred at 0 °C for 24 hours, then partitioned between ether (15 mL) and saturated NH_4Cl (45 mL). The aqueous layer was extracted with ether (2 × 45 mL) and the combined organic layers were washed with brine (90 mL). The organic layer was dried over Na_2SO_4, filtered, and concentrated to give an orange oil. Flash column chromatography (5% EtOAc / hexanes) gave α-oxyaldehyde **6** (1.30 g, 66% yield) as a colorless oil. A sample was derivatized [1. $NaBH_4$, MeOH; 2. *m*-nitrobenzoyl chloride, Et_3N, DMAP (cat.), CH_2Cl_2; 3. Zn, AcOH, THF, H_2O] and determined by chiral HPLC [Chiraltech IC column, 2.1 × 100 mm, 3 μm; 10% *i*-PrOH / hexanes, 0.2 mL / min, 25 °C; 280 nm UV detection; R_t = 8.8 (major), 9.9 (minor) minutes] to have 92:8 er. **6:** R_f = 0.47 (5% EtOAc / hexanes); $[\alpha]_D^{23}$ = –90.5 ° (*c* = 1.00, $CHCl_3$); IR (thin film): ν_{max} = 2933, 1732 cm^{-1}; ^1H NMR (600 MHz, $CDCl_3$): δ = 9.77 (d, *J* = 4.5 Hz, 1H), 4.08 (m, 1H), 1.70 (m, 1H), 1.64 (m, 1H), 1.50–1.08 (m, 20H), 0.92 (t, *J* = 7.4Hz, 3H) ppm; ^{13}C NMR (150 MHz, $CDCl_3$): δ = 204.6, 88.5, 40.2, 34.5, 33.9, 32.2, 20.5, 20.3, 17.8, 17.3, 14.3 ppm; HRMS (ESI-QTOF) calcd for $C_{14}H_{28}NO_2^+$ [M + H^+]: 242.2100, found: 242.2102.

Primary alcohol 1a

((*S*)-2-((2,2,6,6-tetramethylpiperidin-1-yl)oxy)pentan-1-ol). To a solution of α-oxyaldehyde **6** (96 mg, 0.4 mmol, 1.0 equiv.) in 5 mL ethanol was added sodium borohydride (101 mg, 3.6 mmol, 9.0 equiv.). The reaction mixture was stirred for five minutes, then partitioned between ether (20 mL) and water (20 mL). The aqueous layer was extracted with ether (20 mL), and the combined organic layers were washed with

brine (10 mL), dried over Na_2SO_4, and concentrated to give a colorless oil. Flash column chromatography (5% EtOAc / hexanes) gave primary alcohol **1a** (85 mg, 87%) as a colorless oil. **1a:** R_f = 0.27 (10% EtOAc / hexanes) $[\alpha]_D^{23}$ = –62.3 ° (*c* = 1.00, $CHCl_3$); IR (thin film): ν_{max} = 3576, 3018, 2925, 1465 cm^{-1}; ^1H NMR (600 MHz, $CDCl_3$): δ = 5.99 (s, 1H), 4.27 (s, 1H), 3.96 (dd, *J* = 11.9, 10.0 Hz, 1H), 3.57 (d, *J* = 9.5 Hz, 1H), 1.70–1.01 (m, 22H), 0.93 (t, *J* = 7.2 Hz, 3H) ppm; ^{13}C NMR (150 MHz, CDCl3): δ = 68.8, 40.5, 39.8, 34.8, 33.5, 32.5, 20.6, 19.3, 17.3, 14.4 ppm; HRMS (ESI-QTOF) calcd for $C_{14}H_{30}NO_2^+$ [M + H^+]: 244.2300, found: 244.2271.

anti Diol 3a

((3*R*,4*S*)-4-((2,2,6,6-tetramethylpiperidin-1-yl)oxy)hept-1-en-3-ol). To a solution of aldehyde **6** (100 mg, 0.4 mmol, 1.0 equiv.) in 400 μL of THF at –78 °C was added vinylmagnesium bromide (1.0 M in THF, 600 μL, 0.6 mmol, 1.5 equiv.) dropwise over 3 minutes. The resultant solution was stirred at –78 °C for 30 minutes, then warmed to ambient temperature. The reaction mixture was partitioned between saturated NH_4Cl (5 mL) and ether (10 mL). The organic phase was washed with water (2 × 10 mL) and brine (10 mL), dried over Na_2SO_4, and concentrated to give a colorless oil. Flash column chromatography (5% EtOAc / hexanes) gave alcohol **3a** (77 mg, 71% yield) and a mixture of alcohol **3a** and the epimeric alcohol **2a** (7 mg, 6% yield) as colorless oils. **3a:** R_f = 0.42 (10% EtOAc / hexanes); $[\alpha]_D^{23}$ = –10.3 ° (*c* = 1.00, $CHCl_3$); IR (thin film): ν_{max} = 3450, 1642 cm^{-1}; ^1H NMR (600 MHz, $CDCl_3$): δ = 5.93 (ddd, *J* = 17.4 , 10.5, 6.2 Hz, 1H), 5.28 (d, *J* = 17.3 Hz, 1H), 5.18 (d, *J* = 10.7 Hz, 1H), 4.44 (s, 1H), 3.98 (m, 1H), 2.49 (d, *J* = 3.6 Hz, 1H), 1.76 (m, 1H), 1.63–1.04 (m, 21 H), 0.90 (t, *J* = 7.3 Hz, 3H) ppm; ^{13}C

NMR (150 MHz, $CDCl_3$): δ = 137.5, 115.9, 84.2, 73.9, 60.4, 40.8, 34.4, 31.1, 19.9, 17.3, 14.7, 14.3 ppm; $^3J_{H3–H4}$ = 4 Hz, $^2J_{H3–C4}$ = –3.1 Hz, $^2J_{H4–C3}$ = –1.0 Hz, $^3J_{H3–C5}$ = +1.2 Hz, $^3J_{H4–C2}$ = +3.1 Hz; HRMS (ESI-QTOF) calcd for $C_{16}H_{32}NO_2^+$ [M + H+]: 270.2400, found: 270.2431.

syn Diol 2a

((3*S*,4*S*)-4-((2,2,6,6-tetramethylpiperidin-1-yl)oxy)hept-1-en-3-ol). To alcohol **3a** (1.56 g, 5.8 mmol, 1.0 equiv.) in 12 mL of THF was added a solution of IBX (2.45 g, 8.7 mmol, 1.5 equiv.) in 10 mL of DMSO. The reaction mixture was stirred for 1.5 hours, then diluted with 20 mL of ether and filtered. The organic phase was washed with water (2 × 20 mL) and brine (20 mL), dried over Na_2SO_4, and concentrated to give an enone ((*S*)-4-((2,2,6,6-tetramethylpiperidin-1-yl)oxy)hept-1-en-3-one) (1.20 g, 79%) as a colorless oil. The enone was used without purification in the next reaction.

To this enone (1.20 g, 4.5 mmol, 1.0 equiv.) in 6 mL of THF and 18 mL of MeOH was added $CeCl_3 \cdot 7H_2O$ (3.36 g, 9.0 mmol, 2.0 equiv.). The reaction mixture was stirred for 15 minutes, then cooled to –20 °C. $NaBH_4$ (513 mg, 13.6 mmol, 3.0 equiv.) was added, and the resultant mixture was stirred for 2 hours. The reaction mixture was partitioned between ether (50 mL) and water (100 mL). The aqueous layer was extracted with ether (100 mL), and the combined organic layers were washed with brine (50 mL), dried over Na_2SO_4, and concentrated to give a colorless oil. Flash column chromatography (5% EtOAc / hexanes) gave allylic alcohol **2a** (800 mg, 67%) and a mixture of alcohol **2a** and epimeric alcohol **3a** (110 mg, 9%) as colorless oils. **2a:** R_f = 0.36 (10% EtOAc / hexanes); $[\alpha]_D^{23}$ = –28.6 ° (*c* = 1.00, $CHCl_3$); IR (thin film): ν_{max} = 3438, 1641 cm^{-1}; ^1H NMR (600 MHz, $CDCl_3$): δ = 7.55 (br s, 1H), 5.74 (ddd, *J* = 17.1,

10.5, 6.8 Hz, 1H), 5.33 (d, J = 17.0 Hz, 1H), 5.14 (d, J = 10.4 Hz, 1H), 4.33 (t, J = 7.7 Hz, 1H), 3.87 (dt, J = 2.8, 8.7 Hz, 1H), 1.65–1.08 (m, 22H), 0.90 (t, J = 7.2 Hz, 3H) ppm; ^{13}C NMR (150 MHz, $CDCl_3$): 137.8, 116.8, 82.7, 78.1, 61.8, 60.3, 40.5, 40.0, 34.6, 33.6, 32.0, 20.73, 20.67, 18.9, 17.3, 14.5 ppm; HRMS (ESI-QTOF) calcd for $C_{16}H_{32}NO_2^+$ [M + H^+]: 270.2400, found: 270.2434.

Acknowledgments

This research is supported by the National Science Foundation (TLW and ELF: OCI-1216566; JSC and SC: CHE-1453896; NMR instrument: MRI-1040098). We thank Shu Xu (Iowa State University) for assistance with 2D NMR.

Supporting Information

^{1}H and ^{13}C NMR spectra, and calculated Cartesian coordinates and total energies. This material is available free of charge via the Internet at http://pubs.acs.org.

References

1. (a) Schröder, M. *Chem. Rev.* **1980**, *80*, 187. (b) Kolb, H. C.; VanNieuwenhze, M. S.; Sharpless, K. B. *Chem. Rev.* **1994**, *94*, 2483.

2. (a) Rabjohn, N. *Org. React.* **1976**, *24*, 261. (b) Umbreit, M. A.; Sharpless, K. B. *J. Am. Chem. Soc.* **1977**, *99*, 5526.

3. (a) Prein, M.; Adam, W. *Angew. Chem. Int. Ed. Engl.* **1996**, *35*, 477. (b) Stratakis, M.; Orfanopoulos, M. *Tetrahedron* **2000**, *56*, 1595.

4. Davis, F. A.; Chi, B. C. *Chem. Rev.* **1992**, *92*, 919.

5. (a) Sibi, M. P.; Hasegawa, M. *J. Am. Chem. Soc.* **2007**, *129*, 4124. (b) Pouliot, M.; Renaud, P.; Schenk, K.; Studer, A.; Vogler, T. *Angew. Chem. Int. Ed.* **2009**, *48*, 6037. (c) Kano, T.; Mii, H.; Marouka, K. *Angew. Chem. Int. Ed.* **2010**, *49*, 6638. (d) Van Humbeck, J. F.; Simonovich, S.; Knowles, R. R.; MacMillan, D. W. C. *J. Am. Chem. Soc.* **2010**, *132*, 10012. (e) Simonovich, S. P.; Van Humbeck, J. F.; MacMillan, D. W. C. *Chem. Sci.* **2012**, *3*, 58. (f) Dinca, E.; Hartmann, P.; Smrček, J.; Dix, I.; Jones, P. G.; Jahn, U. *Eur. J. Org. Chem.* **2012**, 4461. (g) Xie, Y.-X.; Song, R.-J.; Liu, Y.; Liu, Y.-Y.; Xiang, J.-N.; Li, J.-H. *Adv. Synth. Catal.* **2013**, *355*, 3387. (h) Ho, X.-H.; Jung, W.-J.; Shyam, P. K.; Jang, H.-Y. *Catal. Sci. Technol.* **2014**, *4*, 1914.

6. (a) Liu, H.; Feng, W.; Kee, C. W.; Zhao, Y.; Leow, D.; Pan, Y.; Tan C.-H. *Green Chem.* **2010**, *12*, 953. (b) Koike, T.; Yasu, Y.; Akita, M. *Chem. Lett.* **2012**, *41*, 999. (c) Luo, X.; Wang, Z.-L.; Jin, J.-H.; An, X.-L.; Shen, Z.; Deng, W.-P. *Tetrahedron* **2014**, *70*, 8226.

7. (a) Fuller, P. H.; Kim, J.-W.; Chemler, S. R. *J. Am. Chem. Soc.* **2008**, *130*, 17638. (b) Karyakarte, S. D.; Smith, T. P.; Chemler, S. R. *J. Org. Chem.* **2012**, *77*, 7755. (c) Sanjaya, S.; Chua, S. H.; Chiba, S. *Synlett* **2012**, 1657. (d) Han, B.; Yang, X.-L.; Fang, R.; Yu, W; Wang, C.; Duan, X.-Y.; Liu, S. *Angew. Chem. Int. Ed.* **2012**, *51*, 8816. (e) Hartmann, M.; Li, Y.; Studer, A. *J. Am. Chem. Soc.* **2012**, *134*, 16516. (f) Zhang, B.; Studer, A. *Org. Lett.* **2013**, *15*, 4548. (g) Dutta, U.; Maity, S.; Kancherla, R.; Maiti, D. *Org. Lett.* **2014**, *16*, 6302.

8. (a) Yoon, H.-S.; Ho, X.-H.; Jang, J.; Lee, H.-J.; Kim, S.-J.; Jang, H.-Y. *Org. Lett.* **2012**, *14*, 3272. (b) Li, Y.; Vogler, T.; Renaud, P.; Studer, A. *Org. Lett.* **2012**, *14*, 4474. (c) Shyam, P. K.; Jang, H.-Y. *Eur. J. Org. Chem.* **2014**, 1817.

9. Abeykoon, G. A.; Chatterjee, S.; Chen, J. S. *Org. Lett.* **2014**, *16*, 3248.

10. Matsumori, M.; Kaneno, D.; Murata, M.; Nakamura, H.; Tachibana, K. *J. Org. Chem*. **1999**, *64*, 866.

11. Allen, M. J.; Keal, T. W.; Tozer, D. J. *Chem. Phys. Lett.* **2003**, *380*, 70.

12. Stephens, P. J.; Devlin F. J.; Chablowski C. F.; Frisch M. *J. Phys. Chem.* **1994**, *98*, 11623.

13. Schmidt, M. W.; Baldridge, K. K.; Boatz, J. A.; Elbert, S. T.; Gordon, M. S.; Jensen, J. H.; Koseki, S.; Matsunaga, N.; Nguyen, K. A.; Su S. J.; Windus, T. L.; Dupuis, M.; Montgomery, J. A. *J. Comput. Chem*. **1993**, *14*, 1347.

14. Binkley, J. S.; Pople, J. A., Hehre, W. J. *J. Am. Chem. Soc.* **1980**, *102*, 939.

15. Head-Gordon, M.; Pople, J. A.; Frisch, M. J. *Chem. Phys. Lett.* **1988**, *153*, 503.

16. Frisch, M. J.; Pople, J. A.; Binkley, J. S. *J. Chem. Phys*. **1984**, *80*, 3265. Matsumori, M.; Kaneno, D.; Murata, M.; Nakamura, H.; Tachibana, K. *J. Org. Chem*. **1999**, *64*, 866.

17. Pettersen, E. F.; Goddard, T. D.; Huang, C. C.; Couch, G. S.; Greenblatt, D. M.; Meng, E. C.; Ferrin, T. E. *J. Comput. Chem.* **2004**, 25, 1605.

18. Valiev, M.; Bylaska, E. J.; Govind, N.; Kowalski, K.; Straatsma, T. P.; Van Dam, H. J. J.; Wang, D.; Nieplocha, J.; Apra, E.; Windus, T. L.; De Jong, W. A. *Comput. Phys. Commun.* **2010**, *181*, 1477.

19. Wolinski, K.; Hinton, J. F.; Pulay, P. *J. Am. Chem. Soc.* **1990**, *112*, 8251.

20. Kendall, R. A.; Dunning, Jr., T. H.; Harrison, R. J. *J. Chem. Phys.* **1992**, *96*, 6796.

CHAPTER 7: CHARACTERIZATION OF SILICON NANOCRYSTAL SURFACES BY MULTIDIMENSIONAL SOLID-STATE NMR SPECTROSCOPY

A paper published in *Chemistry of Materials* 2017, 29, 10339-10351

Michael P. Hanrahan, Ellie L. Fought, Theresa L. Windus, Lance M. Wheeler, Nicholas C. Anderson, Nathan R. Neale and Aaron J. Rossini

Abstract

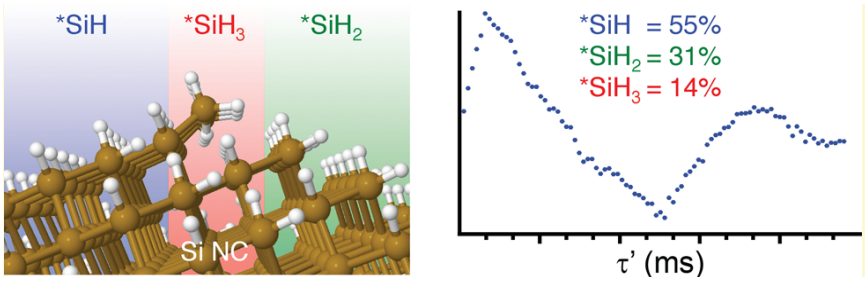

The chemical and photophysical properties of silicon nanocrystals (Si NCs) are strongly dependent on the chemical composition and structure of their surfaces. Here we use fast magic angle spinning (MAS) and proton detection to enable the rapid acquisition of dipolar and scalar 2D $^{1}H-^{29}Si$ heteronuclear correlation (HETCOR) solid-state NMR spectra and reveal a molecular picture of hydride-terminated and alkyl-functionalized surfaces of Si NCs produced in a nonthermal plasma. 2D $^{1}H-^{29}Si$ HETCOR and dipolar $^{1}H-^{1}H$ multiple-quantum correlation spectra illustrate that resonances from surface mono-, di-, and trihydride groups cannot be resolved, contrary to previous literature assignments. Instead the 2D NMR spectra illustrate that there is a large distribution of ^{1}H and ^{29}Si chemical shifts for the surface hydride species in both the as-synthesized and

functionalized Si NCs. However, proton-detected $^{1}H-^{29}Si$ refocused INEPT experiments can be used to unambiguously differentiate NMR signals from the different surface hydrides. Varying the ^{29}Si evolution time in refocused INEPT experiments and fitting the oscillation of the NMR signals allows for relative populations of the different surface hydrides to be estimated. This analysis confirms that monohydride species are the predominant surface species on the as-synthesized Si NCs. A reduction in the populations of the di- and trihydrides is observed upon functionalization with alkyl groups, consistent with our previous hypothesis that the trihydride, or silyl ($*SiH_3$), group is primarily responsible for initiating surface functionalization reactions. Density functional theory (DFT) calculations were used to obtain structural models of the Si NC surface and reproduce observed ^{1}H and ^{29}Si chemical shifts. The approaches outlined here will be more useful to obtain a more detailed picture of surface structures for Si NCs and other hydride-passivated nanomaterials.

Introduction

Semiconductor nanocrystals (NCs) comprised of group II-VI, III-V, and IV-VI elements are widely explored and, in some cases, commercialized for their unique optoelectronic properties; however, the majority of these materials are toxic, and there is a desire to develop alternatives.[1] The group IVb (silicon, germanium, etc.) materials show promise as a potential replacement owing to their low toxicity and high earth abundance. In particular silicon (Si) NCs are appealing for a diverse range of applications such as photovoltaics,[2,3] LEDs,[4-7] batteries,[8] heterogeneous catalysts,[9] bioimaging,[10] etc.[1,11-13] The surface of Si NCs can be terminated with a variety of species such as

halogens,[14,15] oxides,[15-18] hydrogen,[14,19-21] alkyl and aryl groups,[14-16,19-21] and amides,[1,22] all of which can be used to tune the Si NC photophysical properties.[1,13,23-28] Functionalized Si NCs are traditionally characterized and studied using a variety of techniques including photoluminescence,[20,22,29] X-ray diffraction (XRD),[30] Fourier transform infrared spectroscopy (FTIR),[19,30] transmission electron microscopy,[19,31] and 1D ^{1}H, ^{13}C, and ^{29}Si solution and solid-state nuclear magnetic resonance (NMR) spectroscopy.[9,14,16-18,21,22,32-38]

Though many of these techniques can probe the general surface chemical composition and help us understand how it impacts the NC optical properties, determining the molecular-level composition and chemical structure of the surface is challenging.[23,26] Solid-state NMR spectroscopy could be an ideal probe of the Si NC surface since it directly interrogates the elements commonly found in Si NCs an surface ligands. Historically, 1D direct excitation ^{29}Si solid-state NMR spectroscopy has been applied to characterize bulk crystalline silicon,[39,40] porous silicon,[39-45] and Si NCs.[9,14,16-18,21,22,32-34] However, direct excitation NMR spectra cannot easily distinguish surface signals from those in the bulk. Maciel and co-workers demonstrated that since ^{1}H nuclei are not present in the bulk of inorganic materials, 1D ^{1}H–^{29}Si cross-polarization magic angle spinning (CPMAS)[46] solid-state NMR experiments could be used to selectively obtain NMR spectra of surface nuclei in silica by selective excitation of the surface ^{29}Si nuclei that are adjacent to ^{1}H nuclei.[47] Surface selective 1D ^{1}H–^{29}Si CPMAS solid-state NMR experiments are routinely applied to probe the surface of silicon microparticles, porous silicon, and Si NCs.[9,14,21,22,34] Figure 1 contains a summary of the different isotropic ^{29}Si chemical shifts that have been assigned for amorphous silicon,[48-51] porous

silicon,[39-45] Si NCs, [9,14,16-18,21,22,32-34] and silica. [17,40,41,43,45,47,52,53] A more detailed list of the chemical shift assignments is presented in Table S1.

1D surface-selective ^{29}Si solid-state NMR spectra of silicon and silica materials can potentially resolve the chemical structure of the surface; however, the information content of these spectra is often limited due to low resolution surface-selective ^{29}Si solid-state NMR spectra. Additionally, the ^{29}Si chemical shifts of distinct surface species found in silicon and silica systems are very similar (Figure 1). A more detailed picture of the surface structure of Si NCs could potentially be obtained with multidimensional solid-state NMR experiments and/or by applying NMR methods that allow for the observation of different surface species on the basis of near-neighbor interactions. For example, with modern solid-state NMR methods such as fast MAS[54-58] and ^{1}H homonuclear decoupling schemes,[59-62] it is now possible to obtain scalar (through-bond) or dipolar (through-space) 2D heteronuclear correlation (HETCOR) solid-state NMR spectra of surface species.[63-68]

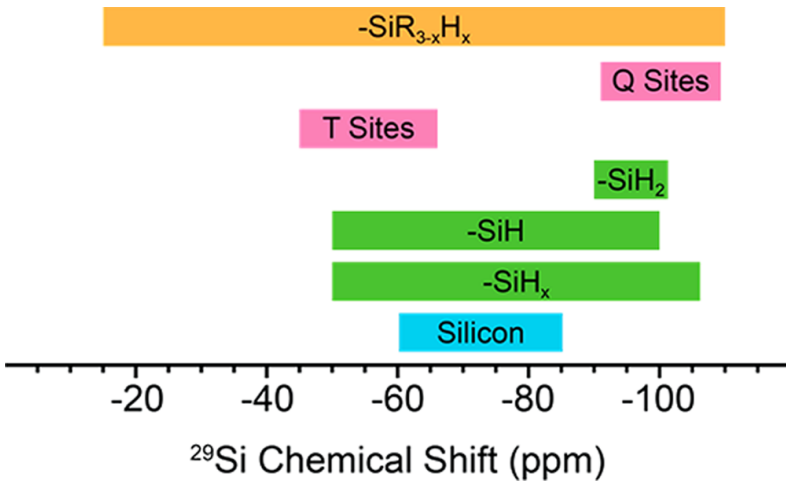

Figure 1. Summary of the different ^{29}Si chemical shifts previously assigned to various silicon and silica surface species.[9,14,16-18,21,22,32-34,39-45,47-53] "Q Sites" refer to $(Si\text{-}O)_{4-x}Si\text{-}(OH)_x$ and "T Sites" refer to $(Si\text{-}O)_{3-x}(OH)_xSiR$.

Here we characterize the surface structure of Si NCs synthesized from the reduction of silane gas (SiH_4) in a radio frequency (RF), nonthermal plasma reactor[37,69] using state-of-the-art solid-state NMR spectroscopy experiments. We show that proton detection and fast MAS[54,55,57,64] enable the acquisition of surface-selective 2D $^1H-^1H$, and $^1H-^{29}Si$, and $^1H-^{13}C$ correlation solid-state NMR spectra. Notably, we demonstrate that proton-detected refocused insensitive nuclei enhanced by polarization transfer (INEPT) pulse sequences[65,66,70] resolve silicon mono-, di- and trihydride surface species, allowing the proportions of surface hydride species in as-synthesized and functionalized Si NCs to be estimated. 1D and 2D ^1H, ^{13}C, and ^{29}Si solid-state NMR spectra of functionalized Si NCs show that the trihydride, or silyl ($*SiH_3$), groups previously invoked to participate in functionalization with alkenes[37] have been transferred from the Si NC surface to the alkyl ligands upon functionalization. Quantum chemical models of the Si NC surface were also created, and the predicted ^{29}Si and ^1H chemical shifts are in reasonable agreement with the experimentally observed shifts.

Results And Discussion

Description of Si NCs studied

As-synthesized 3.7 nm diameter Si NCs were prepared using our previously described plasma-synthesis procedure (Scheme 1A).[37] Throughout this work, **1** refers to as-synthesized Si NCs terminated by surface hydride species (denoted as $*SiH_x$ with x = 1, 2, or 3). **2** refers to ligand-functionalized **1**, which was obtained by reaction of **1** with

Scheme 1. (A) Schematic of Si NC Synthesis from RF Plasma Reduction of Silane Gas (SiH_4) and Silicon Hydride Surface Termination of the As-Synthesized Si NCs (samples 1 and 3) and (B) Si NC Surface Functionalization Scheme with 1-Dodecene Initiated by Surface Silyl ($*SiH_3$) Group Abstraction To Form a Silyl Radical ($^{\bullet}SiH_3$)[37,a]

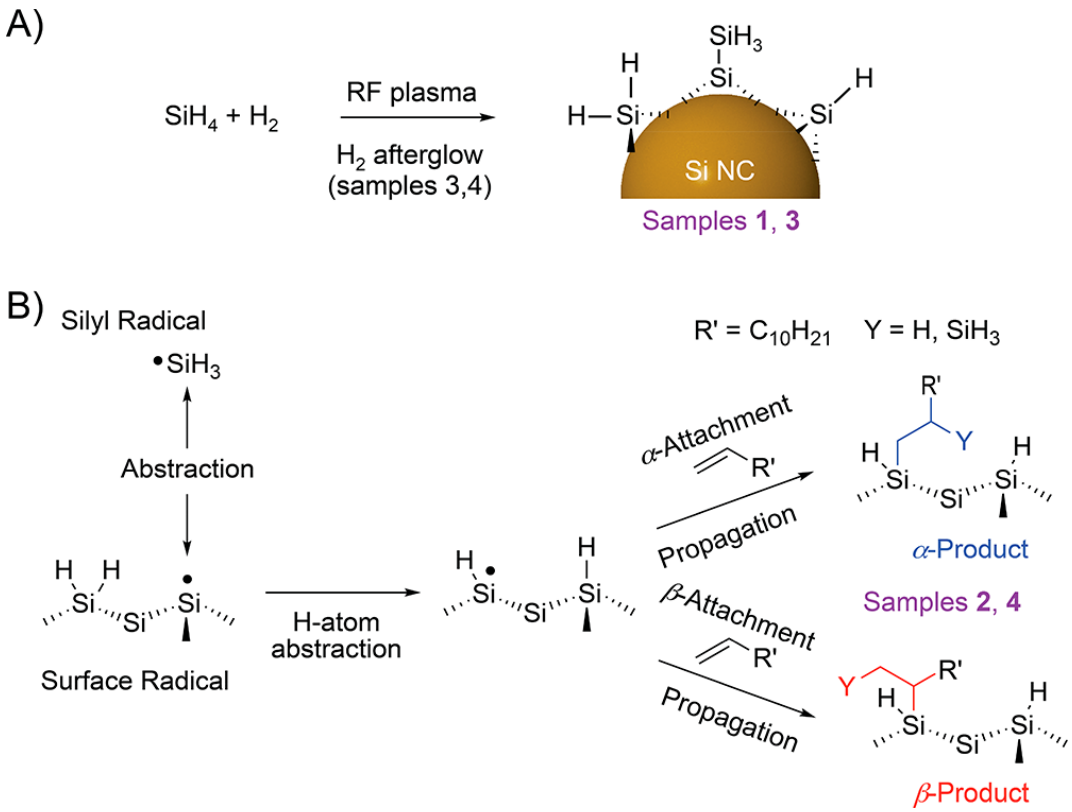

[a]Both α- and β-alkyl products from hydrosilylation and silylsilylation are shown in addition to a possible route to $*SiHR$ species via adjacent H-atom abstraction from $*SiH_2$ during propagation (samples **2** and **4**).

1-dodecene via the thermally initiated method to yield functionalized Si NCs with dodecyl and silyldodecyl groups attached at the α- or β-carbon as previously described (Scheme 1B).[37] The reaction proceeds through radical propagation along the Si NC surface until it is ultimately quenched by the abstracted silyl radical ($^{\bullet}SiH_3$) or other radical trap. Experiments were also performed on a second set of samples that were prepared in a similar manner as **1**, but with a secondary H_2 gas injection into the plasma afterglow region. This procedure is known to increase the coverage of surface silyl

groups (this is also confirmed here with FTIR spectroscopy, Figure S1).[71] We refer to as-synthesized Si NCs with a greater proportion of *SiH_3 as **3**, and **4** refers to ligand-functionalized **3** generated and purified in an identical manner to **2**.

^{1}H Solid-State NMR Spectroscopy

We begin our investigation of the surface structures of **1** and **2** with ^{1}H solid-state NMR experiments since these experiments offer the highest sensitivity and could possible probe and differentiate the different surface hydride species. ^{1}H solid-state NMR spectra of **1** and **2** were obtained with an MAS frequency of 25 kHz (Figure 2). The ^{1}H solid-state NMR spectrum of **1** shows a broad ^{1}H NMR signal which covers a chemical shift range of ca. 2 to 6 ppm (Figure 2A). ^{1}H chemical shifts between 3.0 and 6.0 ppm

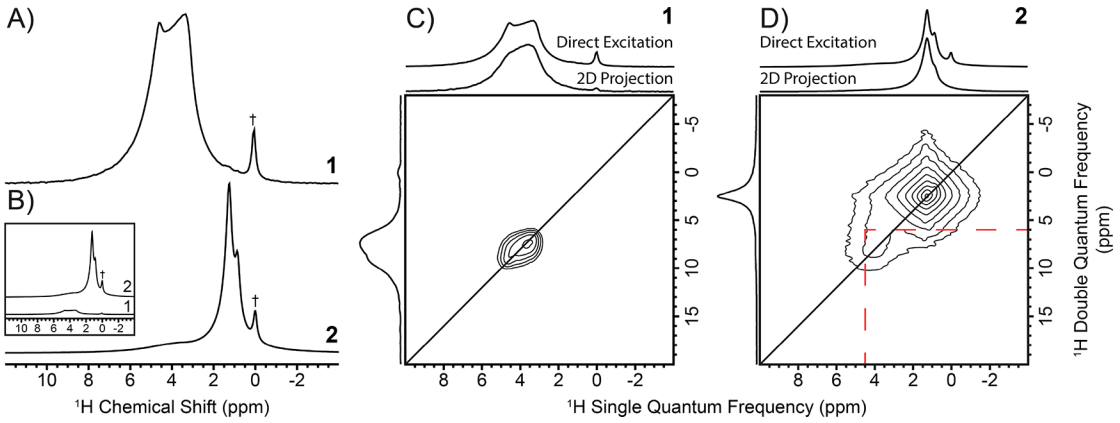

Figure 2. Spin echo MAS ^{1}H solid-state NMR spectra of (A) as-synthesized hydride terminated Si NCs (**1**) and (B) functionalized Si NCs (**2**). The inset shows the spectra plotted with absolute signal intensities. (C, D) 2D ^{1}H−^{1}H dipolar double-quantum single-quantum (DQ-SQ) homonuclear correlation spectra of (C) **1** and (D) **2**, obtained with the BABA pulse sequence. The diagonal black line indicates the autocorrelation line. The dashed red lines in (D) indicate correlations between surface hydrides (*SiH_x) and the hydrocarbons in the alkyl ligands. All spectra were acquired with a 25 kHz MAS frequency. The signal marked by a † is due to an unidentified impurity.

have previously been observed in the solution ^{1}H NMR spectra of molecular silicon hydrides[37,38,72] and in the ^{1}H solid-state NMR spectra of silicon hydride materials.[17,21,34]

^{1}H solid-state NMR spectra of **1** obtained with multiple MAS frequencies indicate that the signal broadening is mainly inhomogeneous (Figure S2). The inhomogeneous broadening likely arises because there are multiple types of surface hydride species present, and there will also be many different exposed surface facets on the Si NCs, each of which likely have distinct silicon hydride ^{1}H chemical shifts. The minimal homogeneous broadening likely occurs because the surface mainly consists of silicon hydrides (*SiH/*SiH$_2$/*SiH$_3$) that are distant from the other surface hydrides. Consequently, the ^{1}H−^{1}H homonuclear dipolar couplings will be small compared to the MAS frequency. For example, if the surface was capped with *SiH species arranged such that the internuclear ^{1}H−^{1}H distances were larger than 3 Å (cf. *SiH on the (111) surface are spaced 3.3 Å apart),[73] then the ^{1}H−^{1}H homonuclear dipolar coupling constants would be less than 5 kHz. In this scenario, the homogeneous broadening due to the homonuclear dipolar could be averaged out by MAS frequencies on the order of 25 kHz. We rule out the possibility that surface hydride species are mobile since the proton longitudinal relaxation time (T_1) is ca. 20 s.

We next employed 2D double-quantum single-quantum (DQ-SQ) and triple-quantum single-quantum (TQ-SQ) dipolar homonuclear ^{1}H−^{1}H correlation experiments in an attempt to distinguish *SiH, *SiH$_2$, and *SiH$_3$ surface species since dipolar 2D DQ-SQ ^{1}H−^{1}H correlation spectra have been previously applied to characterize molecules on surfaces,[74,75] including hydride species.[76,77] In a dipolar DQ-SQ ^{1}H−^{1}H correlations

experiment, only NMR signals from ^{1}H nuclei that are dipolar coupled to another ^{1}H nucleus will be observed. We hypothesized that this would selectively attenuate the ^{1}H NMR signals from *SiH species and allow us to observe the ^{1}H NMR signals of *SiH_2 and *SiH_3 in **1**. However, the projection of the direct dimension of the dipolar 2D DQ-SQ ^{1}H–^{1}H correlation spectrum (Figure 2C) is very similar in appearance to the 1D ^{1}H NMR spectrum. As discussed below, most of the surface is passivated with silicon monohydride (*SiH) species. Therefore, the similarity of the dipolar DQ-filtered ^{1}H NMR spectrum and the 1D ^{1}H NMR spectrum suggests that the *SiH are close enough to each other on the surface to give rise to appreciable dipolar DQ signals; i.e., there is likely no preferential enhancement of the relative intensity of signals from *SiH_2 and *SiH_3 species. Therefore, alternative methods were required to differentiate and quantify the different surface hydride species, as discussed below.

We now turn to characterization of **2**, which was obtained by reaction of **1** with 1-dodecene. In our previous report, we hypothesized that some of the *SiH_3 groups on the surface of **1** are transferred to the alkyl chain of **2** upon functionalization via a silylsilylation process that competes with conventional hydrosilylation (Scheme 1B).[37] The ^{1}H solid-state NMR spectrum of **2** (Figure 2B) contains two sharp components with chemical shifts of ca. 0.88 and 1.27 ppm, which are absent from the ^{1}H NMR spectrum of **1**. These chemical shifts are consistent with those we observed previously for the ^{1}H nuclei in the alkyl chains in the dodecyl and silyldodecyl ligands in the ^{1}H solution NMR spectrum from **2** suspended in toluene.[37] A broad, low intensity of ^{1}H NMR signal centered around 4 ppm was also observed, and its shape, position, and intensity are very similar to that observed from the surface hydrides *SiH_x in the ^{1}H solid-state NMR

spectra of **1**. Comparison of the ^{1}H solid-state NMR spectra of **1** and **2** plotted on the same absolute intensity scale shows that the intensity of the hydride ^{1}H NMR signals is similar in both samples (Figure 2B, inset). Therefore, the increase in intensity of the ^{1}H NMR signal of **2** as compared to **1** reflects an increase in the ^{1}H concentration resulting from attachment of alkyl ligands to the surface. The proton T_1 measurements on **2** yielded a T_1 of 0.87 s for all resonances. The proton T_1 for **2** is over an order of magnitude smaller than that measured for **1** (T_1 = 20 s, see above). The short proton T_1 is most likely due to rotation of the terminal methyl groups on the alkyl ligands and/ or motion of the alkyl chains. The proton T_1 of the hydride signal of **2** is the same as that observed for the alkyl resonances, suggesting that the surface and alkyl protons can exchange magnetization by ^{1}H spin diffusion and that they are in close spatial proximity on the surface of the Si NC.

Our prior work reported a Si NC surface silyl abstraction activation mechanism.[37] The FTIR spectrum of **2** showed a high-frequency shoulder in the *SiH_x stretching region (~2120 cm^{-1}) that we hypothesized resulted from transfer of surface-bound silyl groups in **1** (*SiH_3) to silyl groups on the alkyl ligands of **2** (SiH_3–R, Scheme 1B).[37] Here we obtained a 2D dipolar DQ-SQ ^{1}H–^{1}H correlation spectrum of **2** to test this hypothesis (Figure 2D). The 2D DQ-SQ correlation spectrum mainly shows intensity along the diagonal, which is expected since the ^{1}H nuclei in the alkyl chain will be in close proximity to one another and the 2D DQ-SQ correlation spectrum of **1** primarily shows that the hydrides give rise to autocorrelation (diagonal) signals. There is clearly some off diagonal intensity visible in the DQ-SQ correlation spectrum of **2** (indicated with dashed red lines, Figure 2D). The DQ dimension chemical shift represents the sum of the

chemical shifts of the two ^{1}H nuclei that are dipolar coupled. Therefore, the signal observed in the 2D DQ-SQ correlation at a direct dimension chemical shift of 4.5 ppm and an indirect dimension chemical shift of 6 ppm likely arises from proximity of surface hydrides (cs. 4.5 ppm) and alkyl protons with a chemical shift of ca. 1.5 ppm. This dipolar correlation indicates that the protons on the surface of the Si NCs are near the alkyl chain protons. However, this does not provide confirmation that the *SiH_3 group is transferred to the alkyl chains of **2** upon functionalization of **1**. Therefore, standard 1D and 2D ^{1}H solid-state NMR experiments cannot validate the structures proposed in Scheme 1.

As noted above, secondary H_2 gas injection increases the *SiH_3 coverage in **3** relative to **1**. The FTIR spectrum of **4**, following reaction of **3** with 1-dodecene, reveals a much more intense peak at ~2120 cm^{-1} (relative to **2**) consistent with silyl group transfer to the alkyl ligand SiH_3−R (Figure S1). However, a similar set of 1D and 2D ^{1}H solid-state NMR experiments performed on **3** and **4** (see Supporting Information) were identical to those obtained for the corresponding samples **1** and **2** (i.e., they do not resolve SiH_3−R) and are not discussed further.

2D ^{1}H–^{29}Si Dipolar and Scalar HETCOR Solid-State NMR Spectra

A clearer picture of the surface structures of the Si NCs was obtained by using proton-detected 2D dipolar and scalar ^{1}H–^{29}Si HETCOR spectroscopy. The 2D *dipolar* ^{1}H–^{29}Si HETCOR solid-state NMR spectra were obtained using a proton-detected CP-HETCOR pulse sequence (Figure 3A), which allows correlation to be observed between *spatially proximate* ^{1}H and ^{29}Si nuclei.[54,55,64] In contrast, the 2D *scalar* ^{1}H–^{29}Si HETCOR spectra were obtained using a proton-detected, CP-refocused INEPT pulse

sequence (Figure 3B), which exclusively provides correlations only between *chemically bonded* ^{1}H and ^{29}Si nuclei.[65,66,70] In both types of experiments proton detection[54,55,57,64] gives a substantial gain in sensitivity and allows the 2D solid-state NMR spectra to be obtained in reasonable experimental times (4−12 h for each spectrum), despite the unfavorable proton T_1 associated with **1** and **3**. Note that the ^{29}Si solid-state NMR spectra of **1** and **2** obtained from the indirect dimension of the 2D HETCOR spectra are similar to the spectra obtained with direct detection of ^{29}Si with a CP-CPMG pulse sequence (Figure S6),[78] demonstrating the validity of this indirect detection approach.

The 2D dipolar ^{1}H−^{29}Si HETCOR spectrum of the native hydride-terminated sample **1** shows a broad ^{29}Si solid-state NMR with a chemical shift range of ca. −70 ppm to −120 ppm (Figure 4A). Previously reported ^{29}Si solid-state NMR spectra of hydride-passivated silicon materials are similarly broad and featureless with ^{29}Si isotropic

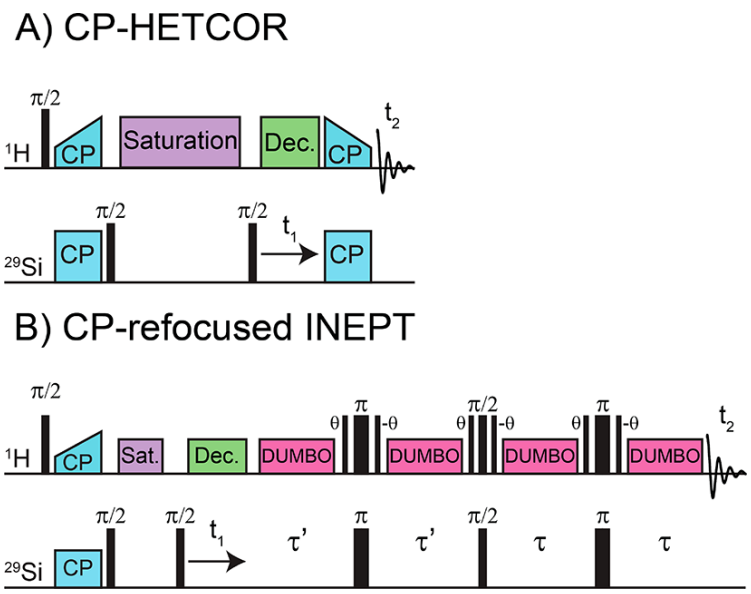

Figure 3. Pulse programs for fast MAS proton-detected dipolar-detected dipolar and scalar HETCOR experiments used to study **1**,**2**,**3**, and **4**. (A) CP-HETCOR and (B) CP-refocused INEPT pulse programs used to acquire 2D scalar HETCOR spectra and observe the evolution of the ^{29}Si Magnetization under scalar coupling to ^{1}H.

HETCOR spectrum (Figure 4C). Gleason and co-workers observed a similar ^{29}Si NMR

chemical shifts between −85 ppm and −111 ppm.[21,34] Thus, the 2D dipolar $^{1}H–^{29}Si$ HETCOR spectrum does not improve the resolution of the ^{1}H or ^{29}Si solid-state NMR spectra. However, the broad 2D correlation pattern indicates that ^{1}H and ^{29}Si nuclei with a range of isotropic chemical shifts are proximate to one another. We also found a well-resolved peak of low intensity with an isotropic chemical shift of ca. −51 ppm in the ^{29}Si solid-state NMR spectrum of **1**, which is also observed in the scalar 2D $^{1}H–^{29}Si$ signal in $^{1}H–^{29}Si$ CPMAS spectrum of porous silicon that, as noted above, exhibits a similar heterogeneous surface to Si NCs.[39] They attributed this ^{29}Si NMR signal with a chemical shift of −50 ppm to partially oxidized surface monohydride species, $(O_2Si)SiH$ (i.e., a surface *SiH bonded to two O atoms and one Si atom).[39,41] Therefore, this minor peak could indicate trace oxidation of the sample during handling. The presence of this peak in the scalar 2D HETCOR spectrum is consistent with it originating from a silicon hydride.

The scalar (through-bond) 2D $^{1}H–^{29}Si$ HETCOR (Figure 4C) spectrum of **1** is essentially identical to the dipolar HETCOR spectrum. In fact, the ^{29}Si solid-state NMR spectra extracted from 2D dipolar HETCOR spectra acquired with different back CP step contact times (Figure S7) are all similar in appearance to the 2D scalar HETCOR spectrum. If the samples were highly oxidized, then the 2D dipolar HETCOR spectrum could show additional ^{1}H and ^{29}Si NMR signals from hydroxyl groups and highly oxidized silicon atoms. The similarity of the dipolar and scalar 2D $^{1}H–^{29}Si$ HETCOR NMR spectra of **1** suggests that the observed ^{1}H and ^{29}Si NMR signals can be primarily attributed to surface hydride species.

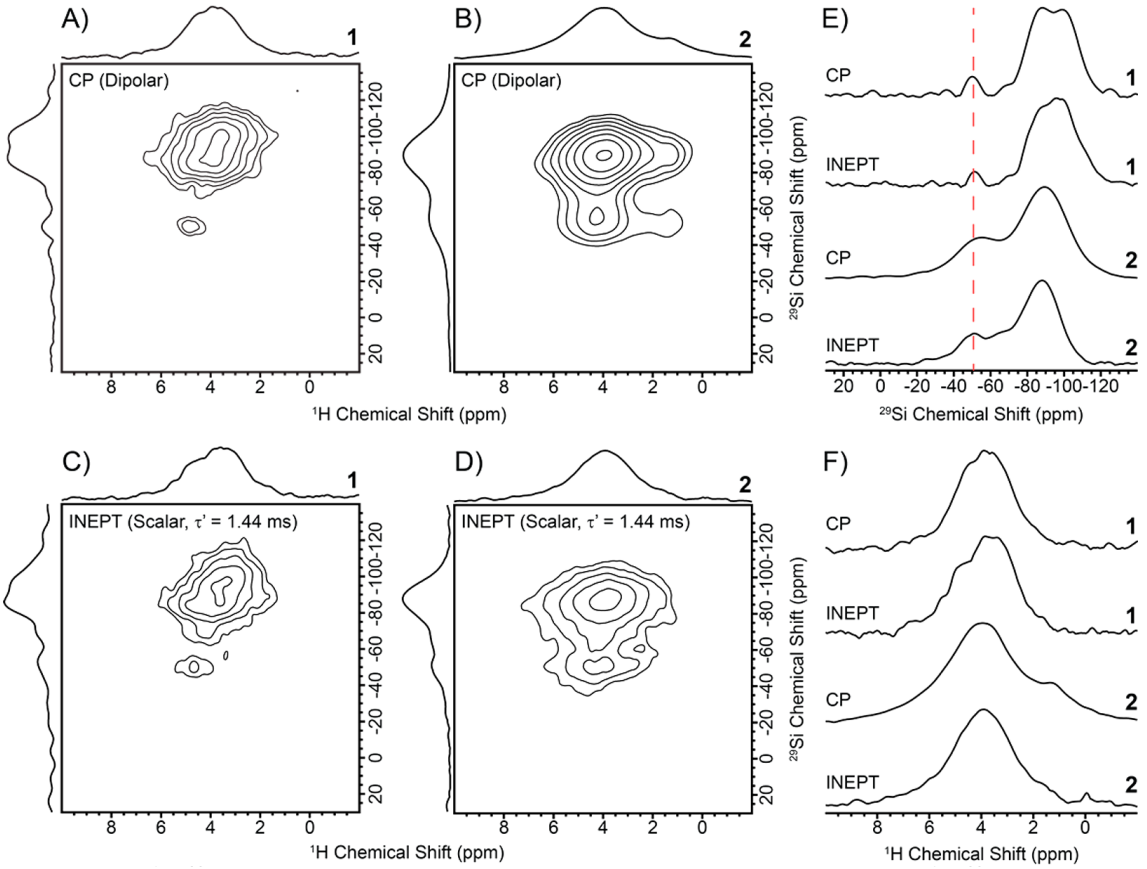

Figure 4. 2D $^{1}H–^{29}Si$ HETCOR solid-state NMR spectra of **1** and **2**. (A, B) 2D dipolar $^{1}H–^{29}Si$ CP-HETCOR NMR spectra of **1** and **2** acquired with a 25 kHz MAS frequency. (C, D) 2D Scalar $^{1}H–^{29}Si$ CP-refocused INEPT HETCOR spectra of **1** and **2** acquired with a 22 kHz MAS frequency. (E) ^{29}Si solid-state NMR spectra and (F) ^{1}H solid-state NMR spectra obtained from the projections of the dipolar and scalar 2D HETCOR NMR spectra. The dashed red line in (E) highlights the intense signals at ca. −50 ppm attributed to silicon atoms bonded to carbon atoms in the functionalized Si NCs.

Both the 2D dipolar and scalar $^{1}H–^{29}Si$ HETCOR spectra of the functionalized Si NC sample **2** exhibits a broad, intense region from ca. −70 ppm to −120 ppm, which is smaller to the ^{29}Si solid-state NMR spectrum of **1** (Figure 4B). However, ^{29}Si NMR spectra of **2** now show that the signal centered at a chemical shift of ca. −51 ppm is significantly broader and much more intense (indicated with a dashed red line, Figure 4E). The absence of a high intensity O−Si−H stretch in the FTIR spectrum of **2** eliminates the possibility that this broad peak is solely from oxidation (Figure S8). We

propose that the broad ^{29}Si NMR signal centered at −51 ppm in **2** is mainly attributed to silicon that is covalently bonded to a carbon atom because ^{29}Si NMR signals at chemical shifts of ca. −50 ppm have previously been assigned to the silicon atoms covalently bonded to alkyl groups at the surface of silicon.[21] There are two plausible silicon sites that explain this chemical shift. One is that corresponds to a surface silicon hydride attached to an alkyl group via either the α- or β-C atom (Scheme 1B). Another plausible species is silyl groups that have been transferred to the dodecyl chain leading to *SiH_3−R (Scheme 1B). Both types of sites should be observable in the ^{1}H−^{29}Si refocused INEPT experiments because they have directly bonded silicon and hydrogen atoms. The INEPT experiments performed with variable scalar coupling evolution times indicate that both of these types of silicon sites could be present (vide infra). Finally, the observation of a correlation between the ^{29}Si NMR signal at −51 ppm and the ^{1}H NMR signal at 1.3 ppm in the 2D dipolar HETCOR spectrum suggests the silicon species are located near the ligand alkyl protons (Figure 4B).

2D ^{1}H−^{13}C dipolar HETCOR spectra of the ligand-functionalized Si NCs **2** and **4** were also obtained (Figure S9). However, they are of limited utility for determining the structure of the surface ligands because the intense ^{13}C signals arising from the –CH_2– and –CH_3 groups of the alkyl chain obscure any signals from dilute carbon atoms that are directly bonded to silicon.

Detecting and Differentiating Hydride Species with ^{1}H–^{29}Si Refocused INEPT Experiments

To obtain more definitive ^{1}H and ^{29}Si resonance assignments for as-synthesized and ligand-functionalized Si NCs, we performed 2D scalar ^{1}H−^{29}Si HETCOR

experiments with variable ^{29}Si evolution times in the refocused INEPT block (τ', Figure 3B). By varying τ' in the refocused INEPT block it is possible to selectively enhance or attenuate the relative intensity of NMR signals on the basis of the stoichiometry of the spin system.[70,79,80] Figure 5A shows the expected variation in the ^{1}H–^{29}Si INEPT NMR signal as a function of τ' for mono-, di-, and trihydrides. The ^{1}H–^{29}Si *J*-couplings used to calculate the curves in Figure 5A were obtained from fits of INEPT signal evolution curves (vide infra). The 2D scalar ^{1}H–^{29}Si HETCOR spectra of **1** and **2** shown in Figure 4 were obtained with a τ' period of 1.44 ms to observe NMR signals from all types of surface hydrides. Note that a τ' of 1.44 ms will slightly attenuate the relative intensity of *SiH signals compared to those of *SiH_2 and *SiH_3 (Figure 5A).

Figure S10 shows 2D scalar ^{1}H–^{29}Si HETCOR spectra of **1** and **2** obtained with τ' values of 2.21 ms to observe only correlation signals from the monohydride *SiH. The ^{29}Si solid-state NMR spectra of **1** and **2** extracted from the 2D scalar ^{1}H–^{29}Si HETCOR spectra obtained with τ' values of 1.44 and 2.21 ms are shown in Figure 5B,C. In general, the 2D scalar ^{1}H–^{29}Si HETCOR spectra and extracted ^{29}Si solid-state NMR spectra obtained with the different τ' values are very similar in appearance because most of the surface hydrides in **1** and **2** are monohydrides (vide infra). By taking the difference of the ^{29}Si solid-state NMR spectra obtained with τ'=1.44 ms (all *SiH_x) and τ' = 2.21 ms (*SiH only), it is possible to generate a selective ^{29}Si solid-state NMR spectrum that only shows NMR signals originating from *SiH_2 and *SiH_3 (Figure 5B,C) for **1** and **2.** Note that the ^{29}Si solid-state NMR spectra obtained with a τ' value of 2.21 ms scaled by a factor of 0.91 and 0.89 for **1** and **2**, respectively, to account for the increased intensity that the *SiH signals have with a ^{29}Si evolution time of 2.21 ms.

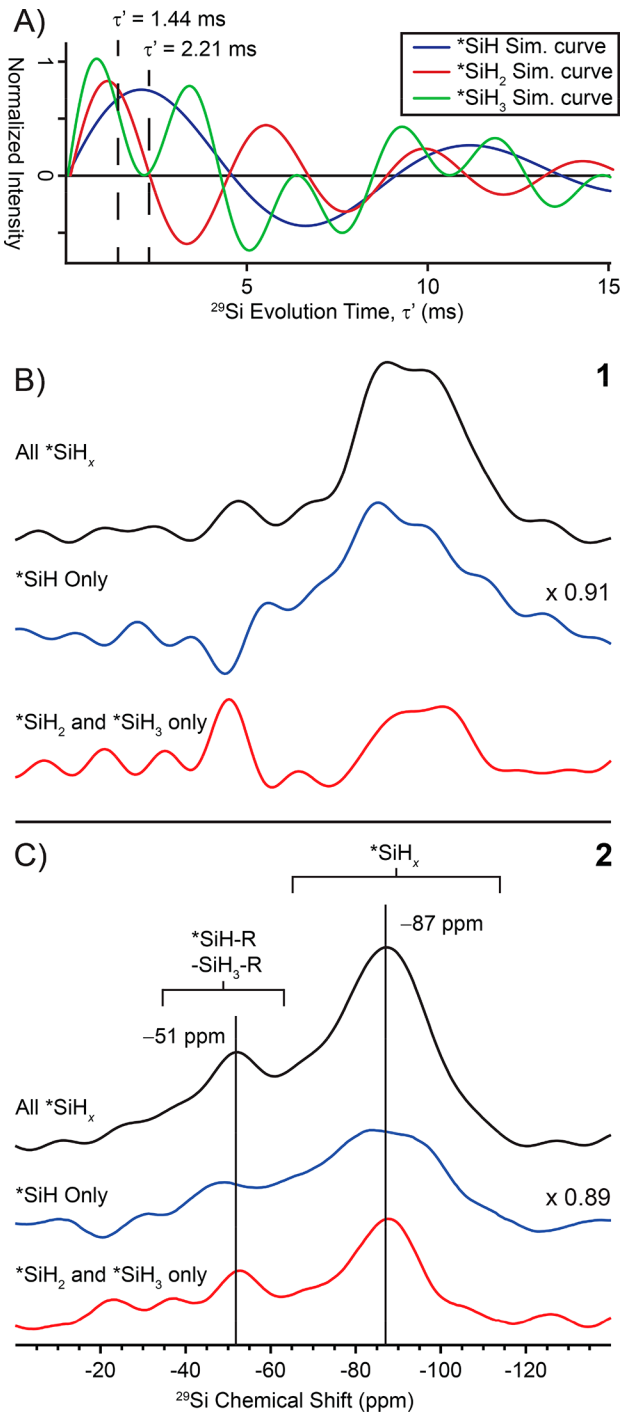

Figure 5. (A) Simulation of *τ'* evolution curves from the $^{1}H–^{29}Si$ refocused INEPT pulse sequence for the different surface hydride groups. ^{29}Si solid-state NMR spectra extracted from the 2D $^{1}H–^{29}Si$ INEPT HETCOR spectra obtained with *τ'* values of 1.44 ms (black trace—all *SiH_x) or 2.21 ms (blue trace—*SiH only) for (B) **1** and (C) **2**. The difference spectra (red traces) were obtained by subtraction and only show signals from *SiH_2 and *SiH_3.

The *SiH_2 and *SiH_3 difference subspectrum obtained in this way **1** shows reduced signal intensity because most of the surface hydrides are monohydrides (Figure 5B). Additionally, the main silicon hydride ^{29} Si NMR signals of **1** in the difference spectrum are now slightly more negatively shifted, suggesting that *SiH_2 and *SiH_3 have a slight tendency to have more negative ^{29}Si chemical shifts compared to *SiH. This is in agreement with previous ^{29}Si chemical shift assignments based upon DFT calculations.[21] Note that in the ^{29}Si solid-state NMR spectrum of **1** obtained with τ' = 2.21 ms the resonance at ca. −51 ppm is negative. The negative signal may occur because this site has a larger ^{1}H–^{29}Si *J*-coupling constant, or it is a dihydride species (Figure 5B). These observations are consistent with assignment of this peak to a small amount of oxidized silicon hydride species such as (O_2Si)***Si**H (vide supra) or possibly an oxidized dihydride such as (OSi)***Si**H_2.

The ^{29}Si solid-state NMR spectra of **2** acquired with τ' = 2.21 ms and τ' = 1.44 ms show similar ^{29}Si chemical shifts; however, there are substantial variations in intensity (Figure 5C). The ^{1}H–^{29}Si refocused INEPT solid-state NMR spectra of **2** with all hydride signals show two sets of broad signals centered at ca. −90 ppm and ca. −50 ppm. The former is assigned to surface hydrides *SiH_x, while the latter are assigned to silicon atoms directly bonded to carbon atoms, ***Si**H−R and ***Si**H_3−R (vide supra). The observation of substantial signal intensity at ca. −50 ppm in the monohydride bonded to one C atom from the dodecyl ligand and two Si atoms, (CSi_2)**Si**H, denoted as *SiH−R (Scheme 1B). This group likely forms via surface- based radical propagation chemistry during functionalization where *SiH_2 undergoes H$^{\bullet}$ abstraction, and the resulting *Si(H)$^{\bullet}$ reacts with 1-dodecene to give *SiH−R (Scheme 1B). The *SiH_2 and *SiH_3 only ^{29}Si

NMR subspectrum of **2** also shows substantial signal intensity at ca. −90 ppm and ca. −56 ppm. We assign the former to *SiH_2 that remain following functionalization and the latter to silyl groups that are transferred to the alkyl chains upon functionalization (i.e., SiH_3−R) as we proposed previously based on FTIR and solution ^{1}H NMR data.[37]

Additional evidence for these assignments is provided by 2D dipolar ^{1}H−^{29}Si HETCOR solid-state NMR experiments performed on samples **3** and **4**, which possess greater percentages of *SiH_3 and SiH_3−R, respectively (vide supra). The 2D dipolar ^{1}H−^{29}Si HETCOR solid-state NMR spectrum of **3** showed the absence of trace oxidation (no peak at −51 ppm, Figure S11A), while the spectrum of **4** showed very strong correlation between the ^{29}Si NMR signal with a chemical shift of −51 ppm and the ^{1}H nuclei in the surface-bound alkyl groups with a ^{1}H chemical shift of ca. 1.3 ppm (Figure S11B). This correlation is significantly stronger than that observed in Figure 3B and is consistent with the assignment of ^{29}Si NMR signals at ca. −50 ppm to *SiH−R and SiH_3−R. Below, we use ^{1}H−^{29}Si scalar refocused-INEPT experiments to quantify the relative populations of different surface hydride species.

Estimating the Relative Surface Hydride Populations on the Si NCs

Next, we performed a pseudo-2D experiment with the CP-refocused INEPT pulse sequence to identify and estimate the relative populations of the different types of surface hydrides in samples **1**−**4**. Proton-detected refocused INEPT ^{1}H−^{29}Si NMR spectra were acquired with a fixed value of τ and different values of τ' which was varied in a pseudo-2D experiment (Figure 6). The oscillation of the refocused INEPT NMR signals with τ' depends upon the stoichiometry of each hydride species. Equations 1 – 3 predict the variation in the refocused INEPT NMR signals for IS (−SiH), I_2S (−SiH_2), and I_3S

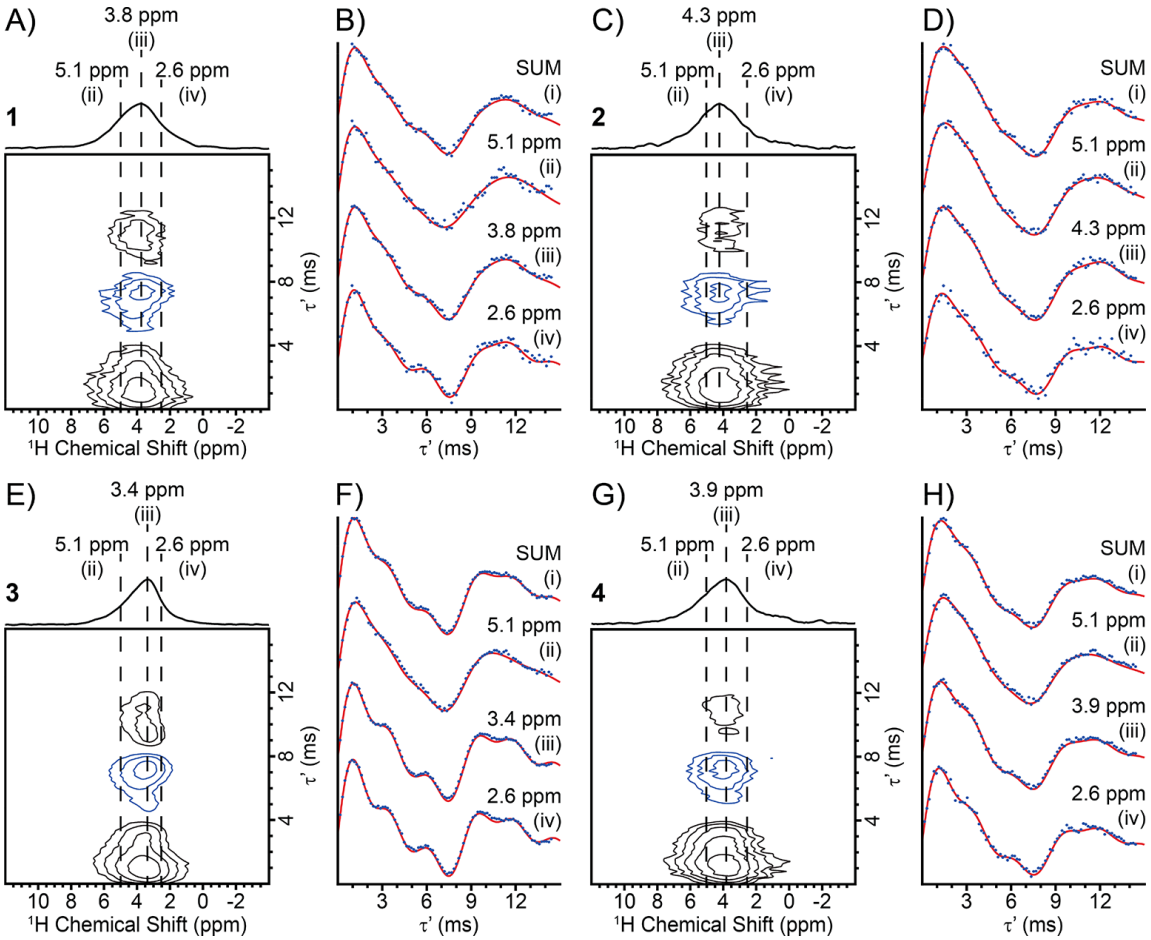

Figure 6. Plots of the ^{1}H signal intensity as a function of the ^{29}Si evolution time (τ') in the CP-refocused INEPT pulse sequence. Individual τ' signal evolution curves extracted from the 2D contour plots show the variation of signal intensity due to evolution of ^{29}Si scalar coupling to ^{1}H. Experiments were performed on (A, B) **1**, (C, D) **2**, (E, F) **3**, and (G, H) **4**. (B, D, F, and H) Experimental τ' evolution curves extracted at different ^{1}H chemical shifts were obtained by (i) summing all ^{1}H NMR signals in the chemical shift range of 1.5 to 6.5 ppm, or individual τ' evolution curves were extracted from columns with ^{1}H chemical shifts of (ii) 5.1 ppm, (iii) the ^{1}H chemical shift with the most intense signal (ca. 3.5 to 4 ppm), and (iv) 2.6 ppm. Experimental data points are given as blue dots and fits are shown as solid red lines.

(−SiH_3) spin systems as a function of the $^1H–^{29}Si$ scalar coupling constants (J'), and the transverse relaxation times (T_2') of ^1H and ^{29}Si under homonuclear decoupling:[70,79,80]

$$M_{IS}(J', t, \tau', T_2') = (\gamma_H/\gamma_{Si})\sin(2\pi J'\tau')e^{-(2\tau'/T'^{Si}_2)} \sin(2\pi J'\tau)\, e^{-(2\tau/T'^{H}_2)} \quad (1)$$

$$M_{I_2S}(J', t, \tau', T_2') = (\gamma_H/\gamma_{Si})\sin(4\pi J'\tau')e^{-(2\tau'/T'^{Si}_2)} \sin(2\pi J'\tau)\, e^{-(2\tau/T'^{H}_2)} \quad (2)$$

$$M_{I_3S}(J', t, \tau', T_2') = \left(3\gamma_H/4\gamma_{Si}\right)[\sin(2\pi J'\tau') + \sin(6\pi J'\tau')] \times \quad (3)$$

$$e^{-(2\tau'/T'^{Si}_2)} \sin(2\pi J'\tau)\, e^{-(2\tau/T'^{H}_2)}$$

The predicted variation in the refocused INEPT NMR signal intensities as a function of τ' for mono-, di-, and trihydrides is shown in Figure 5A. The real $^1H–^{29}Si$ scalar coupling constant ($^1J(^1H–^{29}Si)$) is related to the scaled coupling constant (J') by the homonuclear decoupling sequence scaling factor ($J' = s \times J$). The homonuclear decoupling scaling factor s was independently determined to be 0.61 by performing CP-refocused INEPT experiments on adamantane and tetrakis-(trimethylsilyl)silane (TMSS) (Figures S12−S14). Using a scaling factor of 0.61 and fitting of the τ' curves of **1**−**4** (vide infra) yields average $^1J(^1H–^{29}Si)$ values of 180 Hz, 186 Hz, and 198 Hz for mono-, di-, and trihydrides, respectively. These values of the $^1J(^1H–^{29}Si)$ are in very good agreement with those measured for small molecule silanes in solution NMR.[72]

The experimental variation in the refocused INEPT $^1H–^{29}Si$ NMR signal as a function of τ' for samples **1**−**4** is shown in Figure 6. We refer to these plots as "τ' curves". We assume that T'^{H}_2 the experimental τ' curves can be fit to a function that is the weighted sum of the individual theoretical τ' curves given by eqs 1 – 3:

$$M_{\mathrm{Total}} = a \times M_{\mathrm{IS}} + b \times M_{\mathrm{I_2S}} + c \times M_{\mathrm{I_2}S} \qquad (4)$$

The coefficients *a*, *b*, and *c* determined from fits of the experimental τ' curves allow the relative populations of the different hydrides to be estimated. We assume that T_2' is the same for all ^{1}H spins because all the surface ^{1}H spins are strongly coupled. This assumption is based upon the observations that there was a single monoexponential proton T_1 measured in **1** and **2** and the 2D dipolar homonuclear correlation spectra were similar in appearance to the direct excitation ^{1}H NMR spectra.

The accuracy of the τ' evolution curve fitting for the quantifying the population of different spin systems was investigated by performing ^{1}H–^{13}C refocused INEPT experiments on adamantane. Fits of the τ' curves for adamantane yielded populations with substantial relative errors of ca. 20% of the experimental values for the relative populations of the methylene bridge group (–CH_2–) and the methanetriyl group (C_3C–H) group (Table S3 and Figures S12–S14). A Monte Carlo fitting procedure was also used to assess the uncertainty in the relative populations determined from fitting the τ' evolution curves of adamantane and **1**–**4** (see Supporting Information). The Monte Carlo procedure suggested that the fits of the τ' curves yield very accurate J' values, while larger relative uncertainties on the order of 20–30% of the measured values are associated with the relative populations and T_2' obtained from fits (see Table 1 for uncertainties). However, for adamantane, the uncertainties associated with fits of the τ' curve are less than the experimental error in the relative populations, suggesting that other sources of error that are difficult to quantify also affect the accuracy of the measured populations. For example, imperfections in experimental τ' curves could conceivably occur due to MAS instability and RF inhomogeneity. The different surface hydrides could also have

different CP dynamics and relaxation properties. Therefore, we stress the uncertainties derived from Monte Carlo fitting procedure for the hydride populations that are reported in Table 1 should be considered as lower estimates of the uncertainty. However, for **1** excellent agreement is observed between the hydride populations determined from fitting

Table 1. Estimated Relative Populations of Surface Hydride Species Determined from Fits of INEPT τ' Evolution Curves

spin system	J'[a] (Hz)	T_2' (ms)	population Coefficients (a, b, c)	normalized populations[b] (%)
		Sample **1**		
−SiH	106 ± 1	20 ± 3	0.77 ± 0.06	55 ± 7
$-SiH_2$	108 ± 2	9 ± 3	0.44 ± 0.09	31 ± 7
$-SiH_3$	119 ± 4	10 ± 8	0.20 ± 0.09	14 ± 6
		Sample **2**		
−SiH	102 ± 1	15 ± 2	1.16 ± 0.08	76 ± 7
$-SiH_2$	108 ± 3	12 ± 6	0.26 ± 0.07	17 ± 5
$-SiH_3$	114 ± 4	24 ± 21	0.10 ± 0.05	7 ± 4
		Sample **3**		
−SiH	110 ± 1	17 ± 1	0.86 ± 0.02	56 ± 2
$-SiH_2$	114 ± 1	14 ± 1	0.39 ± 0.02	26 ± 1
$-SiH_3$	118 ± 1	19 ± 3	0.28 ± 0.02	18 ± 1
		Sample **4**		
−SiH	105 ± 1	13 ± 1	1.19 ± 0.06	71 ± 6
$-SiH_2$	110 ± 2	11 ± 4	0.29 ± 0.06	17 ± 4
$-SiH_3$	117 ± 2	15 ± 8	0.19 ± 0.05	12 ± 4

[a] $J' = s \times J$ where s is the scaling factor of the homonuclear decoupling pulse sequence. By fitting the τ' INEPT curves of adamantane and comparing them to the previously reported values of $^1J(^1H–^{13}C)$ from solution NMR, s was determined to be 0.61. [b] Normalized populations were determined using the population coefficients: Population(*SiH) = 100% × $a/(a + b + c)$, Population(*SiH_2) = 100% × $b/(a + b + c)$, and Population(*SiH_3) = 100% × $c/(a + b + c)$. The a, b, and c coefficients were corrected for slight differences in signal expected because each group has a different optimal value of τ. This was done by dividing each coefficient by $\sin(2\pi J'\tau)$, where τ was the fixed evolution time that was used to acquire the τ' curves (see Figure 3B). The uncertainties were determined with a Monte Carlo fitting procedure (see Supporting Information for details).

the Si−H stretching peak in the FTIR spectrum (see Table S8 and Figure S15). The relative populations determined by NMR and FTIR spectroscopies are within 1% of one another suggesting that the hydride populations measured from fits of τ' curves are at least as accurate as those determined by fitting FTIR spectra.

The results from the fits of the experimental τ' curves of **1**−**4** are summarized in Table 1, and the main results of this analysis are as follows: In all samples, the monohydride is clearly the primary surface hydride species. In the hydride terminated Si NCs, **1** and **3**, the monohydrides were found to make up more than 50% of the surface hydride species. **3** was prepared by performing an injection of H_2 gas in the reactor downstream from the main plasma where the particles are synthesized, which is known to increase trihydride coverage.[71] Comparison of the FTIR spectra of **1** and **3** shows that for **3** the peak at 2138 cm^{-1}, assigned to trihydride groups, has increased intensity (Figure S1). Consistent with the FTIR spectra, fits of the τ' curves for **1** and **3** indicate an increase in the population of the trihydride species in **3** (18%) relative to that in **1** (14%). This is reflected by the observation of better defined "shoulders" near to 3 and 6 ms of evolution in the τ' curve of **3**.

The relative ratios of mono-, di-, and trihydride species between as-synthesized **1** and ligand functionalized **2** agree will with the FTIR data and our previously proposed reaction scheme.[37] Upon functionalization, there is a substantial decrease in the populations of the *SiH_2 and *SiH_3 groups relative to the *SiH population (cf. **2** vs **1**, Table 1). The large reduction in the proportion of *SiH_3 reflects the fact that the silyl groups will undergo different reaction pathways that result in their loss (e.g., they may couple to form volatile disilane gas (Si_2H_6) or react with trace impurities such as H_2O and

O_2) or they will react with the alkyl group (either 1-dodecene or surface-bound dodecyl radical) to form SiH_3−R. The cause for the decrease in the *SiH_2 groups upon functionalization fits well with the proposed $H^{\bullet}$ abstraction from *SiH_2 and subsequent reaction with 1-dodecene to form a monohydride species *SiH−R as described above (Figure 1B). This transformation of some dihydride to monohydride groups, along with the relatively low reactivity of *SiH compared with *SiH_3 and *SiH_2, also explains the increase in the proportion of monohydrides relative to the other groups.[37]

Another interesting observation is that τ' curves extracted at different isotropic ^{1}H chemical shift positions suggest that there are differences in the estimated populations of *SiH, *SiH_2, *SiH_3 (Figure 6 and Table S4−S6). *SiH always maintains the highest estimated population regardless of the ^{1}H chemical shift. However, the *SiH_2 and *SiH_3 groups generally have greater relative populations at lower ^{1}H chemical shifts, whereas the *SiH have larger relative populations at higher ^{1}H chemical shifts. Therefore, on the basis of the τ' curve fitting, it is possible to conclude that there is a tendency for the *SiH_2 and *SiH_3 groups to resonate at lower ^{1}H chemical shifts.

Probing the Surface of Partially Oxidized Functionalized Si NCs

Solid-state NMR experiments were performed on a partially oxidized sample of **2** to test if ^{1}H−^{29}Si scalar correlation experiments could detect oxidation and to determine if oxidation affects the hydride groups differently. Partial Oxidation of **2** was achieved by exposing the sample to air for several days after synthesis. The oxidized sample of **2** is denoted $\mathbf{2_{ox}}$. The FTIR spectra of $\mathbf{2_{ox}}$ show low intensity peaks attributed to Si−O stretching models suggesting that partial oxidation of the surface has occurred (Figure S16). The 2D scalar and dipolar ^{1}H−^{29}Si HETCOR spectra of **2** and $\mathbf{2_{ox}}$ were very similar

in appearance (Figure S17). Likewise, fits of the τ' curves obtained from **2** and $\mathbf{2_{ox}}$ yielded very similar relative hydride populations that are within experimental error (Table 1, Tables S4−S7, and Figure S18). Taken together the NMR and FTIR measurements suggest that after several days of air exposure the oxidation of the functionalized Si NC surface is minimal, and that oxidation appears to affect all hydrides equally because there was no change in the relative populations.

^{1}H−^{29}Si CP-HETCOR experiments with an added *J*-dephasing period were also performed in order to selectively observe ^{29}Si solid-state NMR signals from nonprotonated silicon sites such as oxidized surface species (Figures S20−S23). The *J*-dephased ^{1}H−^{29}Si CP-HETCOR pulse program is described in Figure S20. When the *J*-evolution time (τ_J) is set to $1/(2J')$ the ^{29}Si NMR signals of silicon atoms with attached protons will be eliminated. A reference spectrum with NMR signals from all silicon sites was obtained by acquiring a spectrum without the central ^{1}H π- and θ-pulses. 2D *J*-dephased ^{1}H−^{29}Si CP-HETCOR spectra of **2** and $\mathbf{2_{ox}}$ were acquired with back CP contact times of 0.5 and 0.8 ms. With a short back CP contact time of 0.5 ms the ^{1}H and ^{29}Si NMR signals from hydride groups will primarily be observed because they have large ^{1}H−^{29}Si dipolar couplings and undergo correspondingly fast CP transfers (Figure S21). Consequently, the *J*-dephased HETCOR spectra of both **2** and $\mathbf{2_{ox}}$ obtained with a contact time of 0.5 ms show very low signal intensity because all of the silicon atoms detected with this contact time are likely bonded to hydrogen atoms. The *J*-dephased ^{1}H−^{29}Si CP-HETCOR spectra of **2** and $\mathbf{2_{ox}}$ obtained with a back CP contact time of 8 ms give ^{29}Si NMR signals that are nearly 50% of the integrated intensity of the reference signal (Figure S22). However, both the reference and *J*-dephased ^{1}H−^{29}Si CP-HETCOR NMR

spectra of **2** and $\mathbf{2_{ox}}$ are very similar in appearance, which is again consistent with minimal oxidation of the surface (Figure S23). The large ^{29}Si NMR signal observed in the *J*-dephased HETCOR NMR spectra can most likely be assigned to surface or subsurface silicon atoms without attached protons, e.g., "bulk" [$Si(Si_4)$], surface Si atoms bonded to carbon [$Si(Si_3R)$], and possibly oxidized sites [$Si(O)_{4-x}(OH)_x$].

DFT Models of Si NCs Surfaces and Calculation of ^{1}H and ^{29}Si Chemical Shifts

Preliminary density functional theory (DFT) calculations were performed to generate basic model structures of the Si NC surfaces. We have calculated the ^{1}H and ^{29}Si chemical shifts of these DFT models to determine if specific structural features and distinct surface hydride groups can be assigned to different chemical shifts. Lee et al. have also recently applied DFT calculations to generate structural models of Si surfaces and predict ^{13}C and ^{29}Si chemical shifts of functionalized Si nanoparticles.[21]

The four different silicon crystal faces (001, 010, 100, and 110) used for calculations were obtained by taking slabs from the crystal structure of silicon, terminating all silicon edge atoms with hydrogen atoms, and then geometry optimizing all atoms in the cluster. ^{1}H and ^{29}Si chemical shifts are reported for the central silicon atom of the cluster which is either a *SiH or *SiH_2 depending upon the crystal face. *SiH_3 groups were obtained by grafting a *SiH_3 group onto the central atom and then optimizing the geometry of the *SiH_3 group only. The geometry optimized 001 and 110 silicon faces that were used for the DFT calculations of NMR parameters are shown in Figure 7, and coordinates for all optimized structures are provided in the Supporting Information. The calculated ^{1}H and ^{29}Si chemical shifts are plotted on top of the scalar 2D ^{1}H–^{29}Si HETCOR of **1** for the 001

(blue), 010 (green), 100 (red), and 110 (yellow) crystal faces with the different central hydride groups, *SiH (star), *SiH_2 (square), and *SiH_3 (circle) (Figure 7).

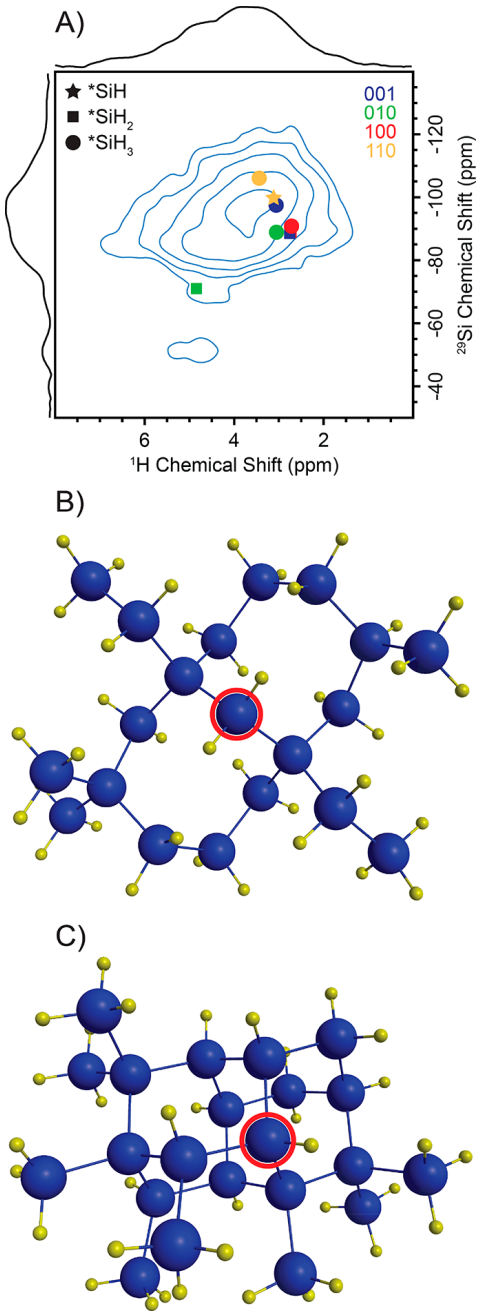

Figure 7. (A) Calculated ^{1}H and ^{29}Si isotropic chemical shifts overlaid on the ^{1}H–^{29}Si scalar HETCOR of **1** for the different *SiH_x species on various silicon crystal faces. Examples of geometry optimized clusters used to model the different silicon crystal faces, (B) 001 face with central *SiH_2, and (C) 110 face with central *SiH. Silicon atoms are blue, and hydrogen atoms are yellow. The central Si atom used for the chemical shift calculations is highlighted in red.

All of the calculated ^{1}H and ^{29}Si chemical shifts fit within the 2D correlation spectrum suggesting the calculated chemical shifts are reasonably accurate. The calculated chemical shifts show that the different types of surface hydride groups on different crystal faces may have the same chemical shift. This prediction is consistent with the refocused INEPT experiments that unambiguously demonstrated that the ^{1}H or ^{29}Si chemical shifts of the different surface hydride species overlap. This also potentially explains why the dipolar $^{1}H-^{1}H$ multiple-quantum correlation spectra primarily show signal intensity along the diagonal of the 2D spectrum (autocorrelations). Autocorrelations would be expected from the proximate hydrides of the same type that are bonded to the same crystal face.

Conclusions

In conclusion, we have shown that high resolution solid-state NMR spectroscopy may be applied to probe the surface of as-synthesized and ligand-functionalized Si NCs. MAS ^{1}H solid- state NMR spectra show that there is a relatively broad isotropic chemical shift range for the surface hydrides on the Si NCs. 2D dipolar $^{1}H-^{1}H$ multiple-quantum homonuclear correlation spectra were unable to resolve the different ^{1}H NMR signals that arise from *SiH, *SiH_2, and *SiH_3. However, these spectra confirm that the alkyl ligands are proximate to surface hydride species in the functionalized Si NCs. The application of fast MAS and proton detection enabled acquisition of 2D $^{1}H-^{29}Si$ dipolar and scalar HETCOR NMR spectra of the Si NCs in experiment times of less than 12 h. By varying the scalar evolution period in a refocused INEPT pulse sequence, it was possible to generate ^{29}Si NMR subspectra of mono-, di-, or trihydride groups. By observing the

oscillation of $^{1}H–^{29}Si$ INEPT NMR signals the relative populations of surface mono-, di-, and trihydride species could be estimated. The estimated relative populations showed that the monohydrides made up 55−76% of the surface hydrides $*SiH_x$ in both the as-synthesized and functionalized Si NCs. Upon functionalization with 1-dodecene there is a significant reduction in the relative amounts of $*SiH_3$ and $*SiH_2$, which is consistent with our previously proposed surface functionalization scheme where silylsilylation resulting in surface-bound silylalkyl ligands competes with conventional hydrosilylation.[37] The analysis of the τ' curves and 2D $^{1}H–^{29}Si$ INEPT HETCOR spectra shows that the ^{1}H and ^{29}Si chemical shifts for surface *SiH, $*SiH_2$, and $*SiH_3$ are similar; however, there was a slight tendency for $*SiH_2$ and $*SiH_3$ to resonate at more negative ^{1}H and ^{29}Si chemical shifts. DFT calculations on model hydride-terminated Si NCs suggest that different crystal facets can have a strong influence on the chemical shifts of $*SiH_x$ species such that mono-, di-, and trihydrides can appear at the same ^{1}H and ^{29}Si chemical shifts depending on the particular crystal face they terminate. This is consistent with experimental results that demonstrate a broad range of chemical shifts for the individual surface silicon hydrides.

We anticipate that the approaches outlined here should be generally applicable for the study of functionalized Si NCs and other nanomaterials, especially those passivated with hydride groups. In particular proton-detected scalar 2D HETCOR experiments should provide a way to more reliably assign NMR signals in silicon nanomaterials and provide a definitive identification and determination of surface hydride species.

Experimental Section

Samples of tetrakis(trimethylsilyl)silane (TMSS) and adamantane were purchased from Sigma-Aldrich and used without further purification. Samples **1** and **2** were prepared following our previously reported procedure,[37] with samples **3** and **4** prepared identically except for the addition of 20 sccm H_2 into the afterglow region downstream of the electrodes. Samples **1**−**4** were packed into rotors in a nitrogen atmosphere glovebox, and MAS experiments were performed with nitrogen gas to minimize oxidation or hydration. Acquisition of 1D ^{1}H solid-state NMR spectra was periodically performed over the course of the experiments to check for oxidation, and no visible changes in signal intensities or positions were observed. Partial oxidation of samples **1** and **2** was achieved by exposing them to air for 2 days before the FTIR spectra were collected. Partially oxidized **2** (**2$_{ox}$**) was exposed to air for 6 days before solid-state NMR measurements were performed.

All solid-state NMR experiments were performed on a Bruker wide-bore 9.4 T (ν_0(^{1}H) = 400 MHz) NMR spectrometer equipped with a Bruker Avance III HD console and Bruker 2.5 mm HXY MAS probe. MAS frequencies between 22 and 25 kHz were used for all experiments. ^{29}Si RF pulses were calibrated on tetrakis(trimethylsilyl)- silane. ^{1}H and ^{13}C RF pulses were calibrated on adamantane. ^{1}H chemical shifts were referenced to neat tetramethylsilane through the use of adamantane (δ_{iso}(^{1}H) = 1.82 ppm) as a secondary chemical shift standard. ^{13}C and ^{29}Si chemical shifts were indirectly referenced to the established chemical shift standards using the previously published relative NMR frequencies.[81] DEPTH,[82] back to back (BABA),[83−85] proton detected (dipolar) CP-HETCOR,[54,55,64] proton detected (scalar) CP-refocused INEPT,[65,66,70] and rotor

synchronized MAS CP-CPMG[74] experiments were performed with the previously described pulse sequences. ^{1}H DEPTH experiments were utilized to suppress unwanted ^{1}H NMR signals from the probe and rotor drive cap. The 2D ^{1}H−^{1}H dipolar DQ-SQ or TQ-SQ experiments were acquired with the BABA pulse sequence. The DEPTH and BABA experiments were performed with 100 kHz RF field ^{1}H pulses. The recycle delays, number of scans, and acquisition times for ^{1}H NMR experiments are given in Table S9.

All proton detected CP-HETCOR experiments were acquired with a 25 kHz MAS frequency. CP experiments used ^{1}H $\pi/2$ pulses with 100 kHz RF fields, ^{29}Si $\pi/2$ pulses with 45−69 kHz RF fields, and ^{13}C $\pi/2$ pulses with RF fields of 74−96 kHz. The ^{1}H CP spin lock pulses were linearly ramped from 85% to 100% of the spin lock RF field, and the direction of the ramp was reversed for the back CP step. The RF fields for CP matching conditions were experimentally optimized to give maximum signal on each sample. The ^{1}H−^{29}Si CP experiments used spin lock pulses with RF fields between 53 and 61 kHz RF and 29−41 kHz RF for ^{1}H and ^{29}Si, respectively. The ^{1}H−^{13}C CP experiments on **2** and **4** used spin lock pulses with RF fields between 77−121 kHz and 77−100 kHz for ^{1}H and ^{13}C, respectively. In the rotor synchronized ^{1}H−^{29}Si CP-CPMG experiments each full echo was typically 800−1200 μs in duration, and a total of 30−50 echoes were collected. SPINAL-64 heteronuclear decoupling[86] was applied with an RF field of ca. 100 kHz in all cases. The recycle delay, CP contact time, number of scans, number of indirect dimension points, and acquisition times for CP-HETCOR experiments are given in Table S9.

The eDUMBO-1_{22} homonuclear decoupling scheme[87] was applied during the scalar coupling evolution periods (τ and τ') of the proton detected CP-refocused INEPT. The eDUMBO-1_{22} pulses were 32 μs in duration with a ^{1}H RF field of ca. 100 kHz. 2D ^{1}H–^{29}Si scalar HETCOR spectra with all hydride signals present were obtained with τ' = 1.44 ms and τ = 1.6−1.92 ms. Monohydride, selective NMR spectra were obtained with τ' = 2.21 ms. The recycle delay, CP contact time, number of scans, number of indirect points, and acquisition times for INEPT experiments are given in Table S9. Proton detected CP-refocused INEPT experiments were also used to estimate the relative populations of *SiH_x. In these experiments the τ period was set to the optimal value that yielded maximum signal. The τ' period was then incremented by steps of 5 eDUMBO-1_{22} cycles (160 μs), and 90 points were acquired for each τ' curve up to a maximum τ' of 14.4 ms. The τ' curves were fit in MATLAB R2015b using the curve fitting application. The accuracy of the method for measuring populations/ relative concentrations was separately tested on adamantane using both ^{1}H and ^{13}C detected versions of the pulse program. A description of this data can be found in the Supporting Information. A scaling factor of 0.61 was determined for the *e*-$DUMBO_{1\text{-}22}$ by fitting the ^{13}C τ' curves of both adamantane and TSS and comparing the scaled scalar coupling constants (J') to the established literature values of $^{1}J(^{1}H–^{13}C)$.[88,89]

All calculations were performed with the NWChem Computational Chemistry Package.[90] See the main text for a description of how models were generated. All geometry optimizations were completed using density functional theory with B3LYP[91–94] and the aug-cc-pVTZ basis sets.[95] ^{1}H and ^{29}Si chemical shielding values were computed with the KT2 functional,[96] the aug-cc-pVTZ basis set, and the GIAO method. The KT2

functional was designed specifically for NMR property calculations.[96] DFT calculations of ^{1}H and ^{29}Si chemical shielding values (σ) were performed on small molecule silanes with known experimental ^{1}H and ^{29}Si chemical shifts (δ, see Supporting Information).[72] Plots of ^{1}H and ^{29}Si chemical shift as a function of chemical shielding and a linear regression fit gave a calibration curve which was then used to convert calculated chemical shielding to chemical shift values (Figure S24 and S25).

Acknowledgments

A.J.R. and M.P.H. were supported by the U.S. Department of Energy (DOE), Office of Science, Basic Energy Sciences, Materials Science and Engineering Division. The Ames Laboratory is operated for the U.S. DOE by Iowa State University under Contract No. DE-AC02-07CH11358. L.M.W., N.C.A., and N.R.N. were supported by the U.S. DOE, Office of Science, Office of Basic Energy Sciences, Division of Chemical Sciences, Geosciences and Biosciences, Solar Photochemistry Program, under Contract No. DE-AC36-08GO28308 to NREL. E.L.F. and T.L.W. were supported by the Air Force Office of Scientific Research under the AFOSR award FA9550-12-1- 0476. A.J.R. thanks Iowa State University and the Ames Laboratory (Royalty Account) for additional support. We are grateful to Prof. Aaron Sadow and Mr. Zachary Weinstein (Iowa State University, Chemistry Department) for providing access to the glovebox used for packing rotors and storage of Si NC samples.

References

1. Dasog, M.; Kehrle, J.; Rieger, B.; Veinot, J. G. Silicon Nanocrystals and Silicon-Polymer Hybrids: Synthesis, Surface Engineering, and Applications. *Angew. Chem., Int. Ed*. **2016**, 55, 2322−2339.

2. Beard, M. C.; Knutsen, K. P.; Yu, P. R.; Luther, J. M.; Song, Q.; Metzger, W. K.; Ellingson, R. J.; Nozik, A. J. Multiple Exciton Generation in Colloidal Silicon Nanocrystals. *Nano Lett*. **2007**, 7, 2506−2512.

3. Liu, C. Y.; Holman, Z. C.; Kortshagen, U. R. Hybrid Solar Cells from P3HT and Silicon Nanocrystals. *Nano Lett*. **2009**, 9, 449−452.

4. Walters, R. J.; Bourianoff, G. I.; Atwater, H. A. Field-Effect Electroluminescence in Silicon Nanocrystals. *Nat. Mater*. **2005**, 4, 143−146.

5. Cheng, K. Y.; Anthony, R.; Kortshagen, U. R.; Holmes, R. J. Hybrid Silicon Nanocrystal-Organic Light-Emitting Devices for Infrared Electroluminescence. *Nano Lett*. **2010**, 10, 1154−1157.

6. Cheng, K. Y.; Anthony, R.; Kortshagen, U. R.; Holmes, R. J. High-Efficiency Silicon Nanocrystal Light-Emitting Devices. *Nano Lett*. **2011**, 11, 1952−1956.

7. Maier-Flaig, F.; Rinck, J.; Stephan, M.; Bocksrocker, T.; Bruns, M.; Kubel, C.; Powell, A. K.; Ozin, G. A.; Lemmer, U. Multicolor Silicon Light-Emitting Diodes (SiLEDs). *Nano Lett*. **2013**, 13, 475− 480.

8. Lin, Y. M.; Klavetter, K. C.; Abel, P. R.; Davy, N. C.; Snider, J. L.; Heller, A.; Mullins, C. B. High Performance Silicon Nanoparticle Anode in Fluoroethylene Carbonate-Based Electrolyte for Li-Ion Batteries. *Chem. Commun*. **2012**, 48, 7268−7270.

9. El-Demellawi, J. K.; Holt, C. R.; Abou-Hamad, E.; Al-Talla, Z. A.; Saih, Y.; Chaieb, S. Room-Temperature Reactivity Of Silicon Nanocrystals With Solvents: The Case Of Ketone And Hydrogen Production From Secondary Alcohols: Catalysis? *ACS Appl. Mater. Interfaces* **2015**, 7, 13794−13800.

10. Erogbogbo, F.; Yong, K. T.; Roy, I.; Hu, R.; Law, W. C.; Zhao, W. W.; Ding, H.; Wu, F.; Kumar, R.; Swihart, M. T.; Prasad, P. N. In Vivo Targeted Cancer Imaging, Sentinel Lymph Node Mapping and Multi-Channel Imaging with Biocompatible Silicon Nanocrystals. *ACS Nano* **2011**, 5, 413−423.

11. Buriak, J. M. Organometallic Chemistry on Silicon and Germanium Surfaces. *Chem. Rev*. **2002**, 102, 1271−1308.

12. Buriak, J. M. Illuminating Silicon Surface Hydrosilylation: An Unexpected Plurality of Mechanisms. *Chem. Mater*. **2014**, 26, 763− 772.

13. Sun, W.; Qian, C. X.; Chen, K. K.; Ozin, G. A. Silicon Nanocrystals: It's Simply a Matter of Size. *ChemNanoMat* **2016**, 2, 847−855.

14. Carter, R. S.; Harley, S. J.; Power, P. P.; Augustine, M. P. Use of NMR spectroscopy in the Synthesis and Characterization of Air- and Water-Stable Silicon Nanoparticles from Porous Silicon. *Chem. Mater*. **2005**, 17, 2932−2939.

15. Atkins, T. M.; Cassidy, M. C.; Lee, M.; Ganguly, S.; Marcus, C. M.; Kauzlarich, S. M. Synthesis of Long T-1 Silicon Nanoparticles for Hyperpolarized Si-29 Magnetic Resonance Imaging. *ACS Nano* **2013**, 7, 1609−1617.

16. Baldwin, R. K.; Pettigrew, K. A.; Ratai, E.; Augustine, M. P.; Kauzlarich, S. M. Solution Reduction Synthesis of Surface Stabilized Silicon Nanoparticles. *Chem. Commun*. **2002**, 1822−1823.

17. Faulkner, R.; DiVerdi, J.; Yang, Y.; Kobayashi, T.; Maciel, G. The Surface of Nanoparticle Silicon as Studied by Solid-State *NMR. Materials* **2013**, 6, 18−46.

18. Kolyagin, Y. G.; Zakharov, V. N.; Yatsenko, A. V.; Aslanov, L. A. Studies of Silicon Nanocluster Ligand Coating by Solid-State NMR. *Russ. Chem. Bull*. **2015**, 64, 1829−1832.

19. Nelles, J.; Sendor, D.; Bertmer, M.; Ebbers, A.; Petrat, F. M.; Simon, U. Surface Chemistry of n-Octane Modified Silicon Nanoparticles Analyzed by IR, C-13 CPMAS NMR, EELS, and TGA. *J. Nanosci. Nanotechnol*. **2007**, 7, 2818−2822.

20. Fuzell, J.; Thibert, A.; Atkins, T. M.; Dasog, M.; Busby, E.; Veinot, J. G. C.; Kauzlarich, S. M.; Larsen, D. S. Red States versus Blue States in Colloidal Silicon Nanocrystals: Exciton Sequestration into Low-Density Traps. *J. Phys. Chem. Lett.* **2013**, 4, 3806−3812.

21. Lee, D.; Kaushik, M.; Coustel, R.; Chenavier, Y.; Chanal, M.; Bardet, M.; Dubois, L.; Okuno, H.; Rochat, N.; Duclairoir, F.; Mouesca, J. M.; De Paepe, G. Solid-State NMR and DFT Combined for the Surface Study of Functionalized Silicon Nanoparticles. *Chem. Eur. J.* **2015**, 21, 16047−16058.

22. Giuliani, J. R.; Harley, S. J.; Carter, R. S.; Power, P. P.; Augustine, M. P. Using Liquid and Solid State NMR and Photoluminescence to Study the Synthesis and Solubility Properties of Amine Capped Silicon Nanoparticles. Solid State *Nucl. Magn. Reson.* **2007**, 32, 1−10.

23. Dasog, M.; Yang, Z. Y.; Regli, S.; Atkins, T. M.; Faramus, A.; Singh, M. P.; Muthuswamy, E.; Kauzlarich, S. M.; Tilley, R. D.; Veinot, J. G. C. Chemical Insight into the Origin of Red and Blue Photoluminescence Arising from Freestanding Silicon Nanocrystals. *ACS Nano* **2013**, 7, 2676−2685.

24. Svrcek, V.; Dohnalova, K.; Mariotti, D.; Trinh, M. T.; Limpens, R.; Mitra, S.; Gregorkiewicz, T.; Matsubara, K.; Kondo, M. Dramatic Enhancement of Photoluminescence Quantum Yields for Surface-Engineered Si Nanocrystals within the Solar Spectrum. *Adv. Funct. Mater*. **2013**, 23, 6051−6058.

25. Wheeler, L. M.; Neale, N. R.; Chen, T.; Kortshagen, U. R. Hypervalent Surface Interactions for Colloidal Stability and Doping of Silicon Nanocrystals. *Nat. Commun.* **2013**, 4, 2197.

26. Wen, X.; Zhang, P.; Smith, T. A.; Anthony, R. J.; Kortshagen, U. R.; Yu, P.; Feng, Y.; Shrestha, S.; Coniber, G.; Huang, S. Tunability Limit of Photoluminescence in Colloidal Silicon Nanocrystals. *Sci. Rep*. **2015**, 5, 12469.

27. Zhou, T.; Anderson, R. T.; Li, H.; Bell, J.; Yang, Y.; Gorman, B. P.; Pylypenko, S.; Lusk, M. T.; Sellinger, A. Bandgap Tuning of Silicon Quantum Dots by Surface Functionalization with Conjugated Organic Groups. *Nano Lett*. **2015**, 15, 3657−3663.

28. Sinelnikov, R.; Dasog, M.; Beamish, J.; Meldrum, A.; Veinot, J. G. C. Revisiting an Ongoing Debate: What Role Do Surface Groups Play in Silicon Nanocrystal Photoluminescence? *ACS Photonics* **2017**, 4, 1920−1929.

29. Hessel, C. M.; Reid, D.; Panthani, M. G.; Rasch, M. R.; Goodfellow, B. W.; Wei, J.; Fujii, H.; Akhavan, V.; Korgel, B. A. Synthesis of Ligand-Stabilized Silicon Nanocrystals with Size-Depend- ent Photoluminescence Spanning Visible to Near-Infrared Wave- lengths. *Chem. Mater*. **2012**, 24, 393−401.

30. Yu, Y.; Hessel, C. M.; Bogart, T. D.; Panthani, M. G.; Rasch, M. R.; Korgel, B. A. Room Temperature Hydrosilylation of Silicon Nanocrystals with Bifunctional Terminal Alkenes. *Langmuir* **2013**, 29, 1533−1540.

31. Panthani, M. G.; Hessel, C. M.; Reid, D.; Casillas, G.; Jose-Yacamań,M.;Korgel,B.A.Graphene-SupportedHigh-Resolution TEM and STEM Imaging of Silicon Nanocrystals and their Capping Ligands. *J. Phys. Chem. C* **2012**, 116, 22463−22468.

32. Mayeri, D.; Phillips, B. L.; Augustine, M. P.; Kauzlarich, S. M. NMR Study of the Synthesis of Alkyl-Terminated Silicon Nanoparticles from the Reaction of SiCl4 with the Zintl Salt, NaSi. *Chem. Mater*. **2001**, 13, 765−770.

33. Kravitz, K.; Kamyshny, A.; Gedanken, A.; Magdassi, S. Solid State Synthesis of Water-Dispersible Silicon Nanoparticles from Silica Nanoparticles. *J. Solid State Chem.* **2010**, 183, 1442−1447.

34. Neiner, D.; Kauzlarich, S. M. Hydrogen-Capped Silicon Nanoparticles as a Potential Hydrogen Storage Material: Synthesis, Characterization, and Hydrogen Release. *Chem. Mater*. **2010**, 22, 487− 493.

35. Biesta, W.; van Lagen, B.; Gevaert, V. S.; Marcelis, A. T. M.; Paulusse, J. M. J.; Nielen, M. W. F.; Zuilhof, H. Preparation, Characterization, and Surface Modification of Trifluoroethyl Ester- Terminated Silicon Nanoparticles. *Chem. Mater.* **2012**, 24, 4311−4318.

36. Xu, Z.; Wang, D.; Guan, M.; Liu, X.; Yang, Y.; Wei, D.; Zhao, C.; Zhang, H. Photoluminescent Silicon Nanocrystal-Based Multi- functional Carrier for pH-Regulated Drug Delivery. *ACS Appl. Mater. Interfaces* **2012**, 4, 3424−3431.

37. Wheeler, L. M.; Anderson, N. C.; Palomaki, P. K. B.; Blackburn, J. L.; Johnson, J. C.; Neale, N. R. Silyl Radical Abstraction in the Functionalization of Plasma-Synthesized Silicon Nanocrystals. *Chem. Mater*. **2015**, 27, 6869−6878.

38. Zhukhovitskiy, A. V.; Mavros, M. G.; Queeney, K. T.; Wu, T.; Voorhis, T. V.; Johnson, J. A. Reactions of Persistent Carbenes with Hydrogen-Terminated Silicon Surfaces. *J. Am. Chem. Soc*. **2016**, 138, 8639−8652.

39. Chang, W. K.; Liao, M. Y.; Gleason, K. K. Characterization of Porous Silicon by Solid-State Nuclear Magnetic Resonance. *J. Phys. Chem*. **1996**, 100, 19653−19658.

40. Brandt, M. S.; Ready, S. E.; Boyce, J. B. Si-29 Nuclear Magnetic Resonance of Luminescent Silicon. *Appl. Phys. Lett*. **1997**, 70, 188− 190.

41. Chang, W. K.; Gleason, K. K. Relationship of Processing Parameters to Photoluminescence Intensity and Mechanical Failure in Thick Porous Silicon Layers. *J. Electrochem. Soc*. **1997**, 144, 1441− 1446.

42. Petit, D.; Chazalviel, J. N.; Ozanam, F.; Devreux, F. Porous Silicon Structure Studied by Nuclear Magnetic Resonance. *Appl. Phys. Lett*. **1997**, 70, 191−193.

43. Tsuboi, T.; Sakka, T.; Ogata, Y. H. Structural Study of Porous Silicon and its Oxidized States by Solid-State High-Resolution Si-29 NMR Spectroscopy. *Phys. Rev. B: Condens. Matter Mater. Phys*. **1998**, 58, 13863−13869.

44. Buriak, J. M.; Stewart, M. P.; Geders, T. W.; Allen, M. J.; Choi, H. C.; Smith, J.; Raftery, D.; Canham, L. T. Lewis Acid Mediated Hydrosilylation on Porous Silicon Surfaces. *J. Am. Chem. Soc*. **1999**, 121, 11491−11502.

45. Tsuboi, T.; Sakka, T.; Mabuchi, M.; Ogata, Y. H. Spin-Lattice Relaxation of Si-29 Near Porous Silicon Surface. *Appl. Surf. Sci*. **2000**, 153, 268−274.

46. Pines, A. Proton-Enhanced NMR of Dilute Spins in Solids. *J. Chem. Phys*. **1973**, 59, 569−590.

47. Maciel, G. E.; Sindorf, D. W. SI-29 Nuclear Magnetic Resonance Study of the Surface of Silica-Gel by Cross Polarization and Magic Angle Spinning. *J. Am. Chem. Soc*. **1980**, 102, 7606−7607.

48. Reimer, J. A.; Vaughan, R. W.; Knights, J. C. Proton Magnetic Resonance Spectra of Plasma-Deposited Amorphous Si: H Films. *Phys. Rev. Lett.* **1980**, 44, 193−196.

49. Jeffrey, F. R.; Murphy, P. D.; Gerstein, B. C. Si-29 NMR-Spectra for Reactively Sputtered Amorphous-Silicon. *Phys. Rev. B: Condens. Matter Mater. Phys.* **1981**, 23, 2099−2101.

50. Hayashi, S.; Hayamizu, K.; Yamasaki, S.; Matsuda, A.; Tanaka, K. Interpretation of 29Si Nuclear Magnetic Resonance Spectra of Amorphous Hydrogenated Silicon. *J. Appl. Phys*. **1986**, 60, 1839−1841.

51. Cheung, M. K.; Petrich, M. A. Si-29 Magnetic-Resonance Study of Amorphous Hydrogenated Silicon Plasma Deposited at 50-Degrees- C. *J. Appl. Phys*. **1993**, 73, 3237−3241.

52. Balmer, M. L.; Bunker, B. C.; Wang, L. Q.; Peden, C. H. F.; Su, Y. L. Solid-State Si-29 MAS NMR Study of Titanosilicates. *J. Phys. Chem. B* **1997**, 101, 9170−9179.

53. Kriesel, J. W.; Tilley, T. D. Synthesis and Chemical Functionalization of High Surface Area Dendrimer-Based Xerogels and Their Use as New Catalyst Supports. *Chem. Mater*. **2000**, 12, 1171−1179.

54. Ishii, Y.; Tycko, R. Sensitivity Enhancement in Solid State N-15 NMR by Indirect Detection with High-Speed Magic Angle Spinning. *J. Magn. Reson*. **2000**, 142, 199−204.

55. Ishii, Y.; Yesinowski, J. P.; Tycko, R. Sensitivity Enhancement in Solid-State C-13 NMR of Synthetic Polymers and Biopolymers by H-1 NMR Detection with High-Speed Magic Angle Spinning. *J. Am. Chem. Soc*. **2001**, 123, 2921−2922.

56. Schnell, I.; Spiess, H. W. High-Resolution 1H NMR Spectroscopy in the Solid State: Very Fast Sample Rotation and Multiple-Quantum Coherences. *J. Magn. Reson*. **2001**, 151, 153−227.

57. Zhou, D. H.; Rienstra, C. M. Rapid Analysis of Organic Compounds by Proton-Detected Heteronuclear Correlation NMR Spectroscopy with 40 kHz Magic Angle Spinning. *Angew. Chem., Int. Ed.* **2008**, 47, 7328−7331.

58. Nishiyama, Y. Fast Magic Angle Sample Spinning Solid-State NMR at 60−100kHz for Natural Abundance Samples. Solid State *Nucl. Magn. Reson*. **2016**, 78, 24−36.

59. Gerstein, B. C.; Pembleton, R. G.; Wilson, R. C.; Ryan, L. M. High Resolution NMR in Randomly Oriented Solids with Homonuclear Dipolar Broadening: Combined Multiple Pulse NMR and Magic Angle Spinning. *J. Chem. Phys*. **1977**, 66, 361−362.

60. Elena,B.;dePaepe,G.;Emsley,L.DirectSpectralOptimisation of Proton-Proton Homonuclear Dipolar Decoupling in Solid-State NMR. *Chem. Phys. Lett*. **2004**, 398, 532−538.

61. Vinogradov, E.; Madhu, P. K.; Vega, S. Strategies for High-Resolution Proton Spectroscopy in Solid-State NMR. In New Techniques in Solid-State NMR; Klinowski, J., Ed., Springer: Berlin, Heidelberg, **2005**; pp 33−90.

62. Mote, K. R.; Agarwal, V.; Madhu, P. K. Five Decades of Homonuclear Dipolar Decoupling in Solid-State NMR: Status and Outlook. *Prog. Nucl. Magn. Reson. Spectrosc*. **2016**, 97, 1−39.

63. Lesage, A.; Emsley, L.; Chabanas, M.; Coperet, C.; Basset, J. M. Observation of a H-Agostic Bond in a Highly Active Rhenium-Alkylidene Olefin Metathesis Heterogeneous Catalyst by Two-Dimensional Solid-State NMR Spectroscopy. *Angew. Chem., Int. Ed*. **2002**, 41, 4535−4538.

64. Wiench, J. W.; Bronnimann, C. E.; Lin, V. S. Y.; Pruski, M. Chemical Shift Correlation NMR Spectroscopy with Indirect Detection in Fast Rotating Solids: Studies of Organically Functionalized Mesoporous Silicas. *J. Am. Chem. Soc*. **2007**, 129, 12076−12077.

65. Mao, K.; Pruski, M. Directly and Indirectly Detected Through- Bond Heteronuclear Correlation Solid-State NMR Spectroscopy Under Fast MAS. *J. Magn. Reson.* **2009**, 201, 165−174.

66. Mao, K.; Wiench, J. W.; Lin, V. S.; Pruski, M. Indirectly Detected Through-Bond Chemical Shift Correlation NMR Spectroscopy in Solids Under Fast MAS: Studies of Organic-Inorganic Hybrid Materials. *J. Magn. Reson*. **2009**, 196, 92−95.

67. Conley, M. P.; Lapadula, G.; Sanders, K.; Gajan, D.; Lesage, A.; del Rosal, I.; Maron, L.; Lukens, W. W.; Coperet, C.; Andersen, R. A. The Nature of Secondary Interactions at Electrophilic Metal Sites of Molecular and Silica-Supported Organolutetium Complexes from Solid-State NMR Spectroscopy. J. *Am. Chem. Soc*. **2016**, 138, 3831− 3843.

68. Coperet, C.; Estes, D. P.; Larmier, K.; Searles, K. Isolated Surface Hydrides: Formation, Structure, and Reactivity. *Chem. Rev*. **2016**, 116, 8463−8505.

69. Kortshagen, U. R.; Sankaran, R. M.; Pereira, R. N.; Girshick, S. L.; Wu, J. J.; Aydil, E. S. Nonthermal Plasma Synthesis of Nanocrystals: Fundamental Principles, Materials, and Applications. *Chem. Rev*. **2016**, 116, 11061−127.

70. Elena, B.; Lesage, A.; Steuernagel, S.; Bockmann, A.; Emsley, L. Proton to Carbon-13 INEPT in Solid-State NMR Spectroscopy. *J. Am. Chem. Soc*. **2005**, 127, 17296−17302.

71. Anthony, R. J.; Rowe, D. J.; Stein, M.; Yang, J.; Kortshagen, U. Routes to Achieving High Quantum Yield Luminescence from Gas-Phase-Produced Silicon Nanocrystals. *Adv. Funct. Mater*. **2011**, 21, 4042−4046.

72. Hahn, J. Contributions to the Chemistry of Silicon and Germanium XXIX [1] Si-29 NMR Spectroscopic Investigations on Straight and Branched Silanes. Z. Naturforsch., B: *J. Chem. Sci*. **1980**, 35, 282−296.

73. Baski, A. A.; Erwin, S. C.; Whitman, L. J. The Structure of Silicon Surfaces from (001) to (111). *Surf. Sci*. **1997**, 392, 69−85.

74. Trebosc, J.; Wiench, J. W.; Huh, S.; Lin, V. S. Y.; Pruski, M. Solid-State NMR Study of MCM-41-Type Mesoporous Silica Nanoparticles. *J. Am. Chem. Soc*. **2005**, 127, 3057−3068.

75. Avenier, P.; Lesage, A.; Taoufik, M.; Baudouin, A.; De Mallmann, A.; Fiddy, S.; Vautier, M.; Veyre, L.; Basset, J. M.; Emsley, L.; Quadrelli, E. A. Well-Defined Surface Imido Amido Tantalum(V) Species from Ammonia and Silica-Supported Tantalum Hydrides. *J. Am. Chem. Soc*. **2007**, 129, 176−186.

76. Rataboul, F.; Baudouin, A.; Thieuleux, C.; Veyre, L.; Coperet, C.; Thivolle-Cazat, J.; Basset, J. M.; Lesage, A.; Emsley, L. Molecular Understanding of the Formation of Surface Zirconium Hydrides upon Thermal Treatment under Hydrogen of [(SiO)Zr(CH(2)tBU)(3)] by Using Advanced Solid-State NMR Techniques. *J. Am. Chem. Soc*. **2004**, 126, 12541−12550.

77. Larabi, C.; Merle, N.; Norsic, S.; Taoufik, M.; Baudouin, A.; Lucas, C.; Thivolle-Cazat, J.; de Mallmann, A.; Basset, J. M. Surface Organometallic Chemistry of Titanium on Silica-Alumina and Catalytic Hydrogenolysis of Waxes at Low Temperature. *Organometallics* **2009**, 28, 5647−5655.

78. Trebosc, J.; Wiench, J. W.; Huh, S.; Lin, V. S. Y.; Pruski, M. Studies of Organically Functionalized Mesoporous Silicas Using Heteronuclear Solid-State Correlation NMR Spectroscopy Under Fast Magic Angle Spinning. *J. Am. Chem. Soc*. **2005**, 127, 7587−7593.

79. Sorensen, O. W.; Ernst, R. R. Elimination of Spectral Distortion in Polarization Transfer Experiments - Improvements and Comparison of Techniques. *J. Magn. Reson.* **1983**, 51, 477−489.

80. Coelho, C.; Azais, T.; Bonhomme-Coury, L.; Laurent, G.; Bonhomme, C. Efficiency of the Refocused P-31-Si-29 MAS-J-INEPT NMR Experiment for the Characterization of Silicophosphate Crystalline Phases and Amorphous Gels. *Inorg. Chem*. **2007**, 46, 1379−1387.

81. Harris, R. K.; Becker, E. D.; de Menezes, S. M. C.; Goodfellow, R.; Granger, P. NMR Nomenclature. Nuclear Spin Properties and Conventions for Chemical Shifts - (IUPAC Recommendations 2001). *Pure Appl. Chem*. **2001**, 73, 1795−1818.

82. Cory, D. G.; Ritchey, W. M. Suppression of Signals from the Probe in Bloch Decay Spectra. *J. Magn. Reson*. **1988**, 80, 128−132.

83. Feike, M.; Demco, D. E.; Graf, R.; Gottwald, J.; Hafner, S.; Spiess, H. W. Broadband Multiple-Quantum NMR Spectroscopy. *J. Magn. Reson*., *Ser. A* **1996**, 122, 214−221.

84. Schnell, I.; Lupulescu, A.; Hafner, S.; Demco, D. E.; Spiess, H. W. Resolution Enhancement in Multiple-Quantum MAS NMR Spectroscopy. *J. Magn. Reson*. **1998**, 133, 61−69.

85. Schnell, I. Dipolar Recoupling in Fast-MAS Solid-State NMR Spectroscopy. *Prog. Nucl. Magn. Reson. Spectrosc*. **2004**, 45, 145−207.

86. Fung, B. M.; Khitrin, A. K.; Ermolaev, K. An Improved Broadband Decoupling Sequence for Liquid Crystals and Solids. *J. Magn. Reson.* **2000**, 142, 97−101.

87. Sakellariou, D.; Lesage, A.; Hodgkinson, P.; Emsley, L. Homonuclear Dipolar Decoupling in Solid-State NMR Using Continuous Phase Modulation. *Chem. Phys. Lett.* **2000**, 319, 253−260.

88. Gilman, H.; Smith, C. L. Tetrakis(Trimethylsilyl)Silane. *J. Organomet. Chem*. **1967**, 8, 245.

89. Terao, T.; Miura, H.; Saika, A. Measurements of the C-13-H-1 Coupling-Constants in Solid Adamantane: Resolution Enhancement by Multiple-Pulse Decoupling. *J. Magn. Reson*. **1982**, 49, 365−367.

90. van Dam, H. J. J.; de Jong, W. A.; Bylaska, E.; Govind, N.; Kowalski, K.; Straatsma, T. P.; Valiev, M. NWChem: Scalable Parallel Computational Chemistry. *Wiley Interdiscip Comput. Mol. Sci*. **2011**, 1, 888−894.

91. Vosko, S. H.; Wilk, L.; Nusair, M. Accurate Spin-Dependent Electron Liquid Correlation Energies for Local Spin-Density Calculations: A Critical Analysis. *Can. J. Phys*. **1980**, 58, 1200−1211.

92. Lee, C.; Yang, W.; Parr, R. G. Development of the Colle-Salvetti Correlation-Energy Formula into a Functional of the Electron Density. Phys. Rev. B: *Condens. Matter Mater. Phys*. **1988**, 37, 785−789.

93. Becke, A. D. Density-Functional Thermochemistry. III. The Role of Exact Exchange. *J. Chem. Phys*. **1993**, 98, 5648−5652.

94. Stephens, P. J.; Devlin, F. J.; Chabalowski, C. F.; Frisch, M. J. Ab Initio Calculation of Vibrational Absorption and Cicular Dichroism Spectra Using Density Functional Force Fields. *J. Phys. Chem*. **1994**, 98, 11623−11627.

95. Kendall, R. A.; Dunning, T. H.; Harrison, R. J. Electron Affinities of the First-Row Atoms Revisited. Systematic Basis Sets and Wave Functions. *J. Chem. Phys*. **1992**, 96, 6796−6806.

96. Allen, M. J.; Keal, T. W.; Tozer, D. J. Improved NMR Chemical Shifts in Density Functional Theory. *Chem. Phys. Lett*. **2003**, 380, 70− 77.

CHAPTER 8: RAPID AND ORDERED CARBONYLATION AND OXYGENATION OF A COBALT(II) METHYL

A Communication published in *Chemical Communications* 2017, 53, 11020-11023

Regina R. Reinig, Ellie L. Fought, Arkady Ellern, Theresa L. Windus, and Aaron D. Sadow

ELF and TLW performed all DFT and TDDFT calculations. RRR, AE, and ADS performed all synthetic and spectroscopic work.

Abstract

The oxidative carbonylation of ToMCoMe (**1**; ToM = tris(4,4-dimethyl-2-oxazolinyl)phenylborate) involves its rapid, reversible reaction with CO to form ToMCo{C(O)Me}CO (**2**) followed by rapid reaction with O_2 yielding ToMCoOAc (**3**), in contrast to the slow direct carboxylation of ToMCoMe by CO_2.

Introduction

Catalytic oxidative carbonylation reactions are generally proposed to involve metal-based oxidations[1,2]. Consider, for example, catalytic production of benzoic acid from benzene, CO, and an oxidant. Palladium(II) mediates the combination of the arene, CO and water to afford benzoic acid, with palladium(0) generated as a byproduct. Then, the suggested catalytic cycle is completed by metal-based oxidation, rather than oxygenation of an acylpalladium intermediate. Interestingly, the proposed biosynthesis of

the energy-carriers acetate or acetyl-CoA follows a conceptually similar outline, involving insertion of CO into a metal-methyl bond followed by metal-based oxidation and thiolysis (reductive elimination of the C–S bond) to form acetyl-CoA.[3,4]

Oxygenation of metal-carbon bonds (or the reductive coupling followed by oxidation pathway) is key to many hydrocarbon functionalization schemes. On the other hand, acetate may be derived directly from CO_2 and methyl transition metal compounds. Although CO_2 is a substrate for acetogenesis, it is reduced by carbon monoxide dehydrogenase (CODH) to CO prior to its interaction with the metal-methyl.[4] Likewise, oxidative carbonylation yields are sometimes improved under CO_2, yet CO is the ultimate source of carbonyl in the transformation. The distinction between CO/[O] in oxidative carbonylation versus CO_2 in carboxylation, in terms of their kinetic and thermodynamic parameters, is critical for the development of sustainable processes that utilize C_1 starting materials, such as methane, carbon monoxide, or carbon dioxide, because the processes must balance atom and energy economy with rate, yield, and selectivity to be viable.

Four-coordinate organocobalt(II) species are expected to be reactive toward CO, O2 and CO2 based on studies of bulky $Tp^{t\text{-}Bu,Me}$, $Tp^{i\text{Pr}}$, $Tp^{i\text{Pr2}}$, and [$PhTt^{t\text{Bu}}$] ($Tp^{R,\,R'}$ = $HB(3R,5R'\text{-}N_2C_3HR_2)_3$; $PhTt^{t\text{Bu}}$ = $PhB(CH_2S\textit{t}Bu)_3$).[5-10] These reactions give either reduction or carbonylation products, oxidation or oxygenation, or carboxylation, respectively. CO affects one-electron reductions to give $Tp^{t\text{Bu}}$CoCO or $Tp^{i\text{Pr,Me}}Co(CO)_2$,[6,11] while carbonylation to cobalt(II) acyl species is also reported.[7,8] Oxygenation of organocobalt(II) to a cobalt alkyl peroxide could follow our observations for related zinc compounds, where kinetics of zinc alkyl oxygenation to alkylperoxides or alkoxides are consistent with a turnover-limiting bimolecular substitution of zinc alkyl

with alkylperoxy radical (S_H2).[12] This oxygenation pathway avoids metal-centered oxidation. Indeed, alkylperoxy and acylperoxy metal compounds are intermediates in oxygenation reactions.[13,14] In the present work, a comparison of oxygenation, carbonylation and oxygenation, and carboxylation of To^MCoMe (**1**; To^M = tris(4,4-dimethyl-2-oxazolinyl)phenylborate) reveals that the kinetically favored pathway selectively produces acetate through an ordered, multistep sequence.

Results and Discussion

The reaction of To^MCoCl[15] and MeLi at room temperature affords To^MCoMe as a deep aquamarine solid (equation (1)).

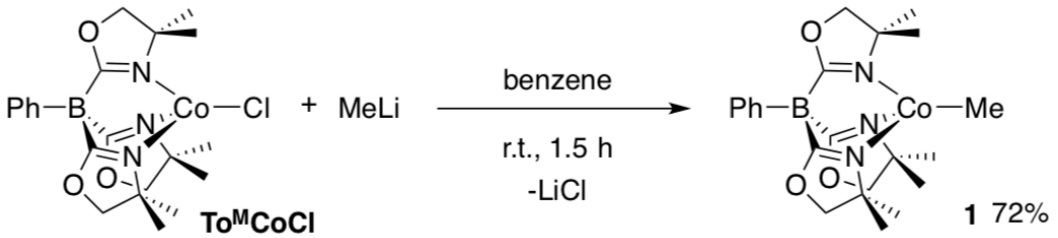

(1)

The ^{1}H NMR spectrum of **1** showed signals at 15.44 and –12.05 ppm assigned to the oxazoline's methylene and methyl groups, respectively, on the basis of integration. These signals were shifted downfield compared to To^MCoCl (24.88 and 8.38 ppm, respectively). A resonance for the methyl ligand was not detected. The ^{11}B signal at 100 ppm was significantly shifted in comparison to the peak of To^MCoCl (–29 ppm). A single ν_{CN} band at 1594 cm^{-1} in the IR spectrum suggested tridentate ToMCo coordination. The UV-Vis spectrum of 1 (in Et2O) revealed intense absorptions at 346 (ε: 1412 $M^{-1}cm^{-1}$) and 697 (ε: 1078 $M^{-1}cm^{-1}$) assigned to charge transfer transitions associated with the alkyl ligand on the basis of their large molar absorptivities (>1000 $M^{-1}cm^{-1}$) and the lack

of similar signals in To^{M}CoCl. Weaker absorptions at 581 (ε: 388 $M^{-1}cm^{-1}$) and 617 (ε: 424 $M^{-1}cm^{-1}$) were attributed to d ← d transitions. The effective magnetic moment of **1** (4.2(2) μ_B), determined by Evans method, is consistent with a high-spin cobalt(II) (S = 3/2). The EPR spectrum of **1**, acquired at 5 K in glassed toluene, showed a rhombic spectrum with hyperfine coupling to the ^{59}Co center (I = 7/2) in a characteristic eight-line pattern.

The identity of **1** as the cobalt(II) methyl is unambiguously established by X-ray diffraction (Figure 1). The compound is slightly distorted from the C_{3v} symmetry suggested by solution-phase spectroscopy, with the C22 (methyl) displaced from the B–Co vector (∠B–Co–Me: 172.83°). The Co1–C22 distance in To^{M}CoMe (1.994(2) Å) is within the range of similar pseudotetrahedral methylcobalt(II) species, which vary from 1.9 to 2.1 Å.[5,6,6d,16,10, 17]

DFT calculations show that the quartet state (S = 3/2) is lowest energy and 49 kcal mol^{-1} lower than the doublet state. A TDDFT-calculated electronic transition at 310 nm (using implicit solvation) allows the experimental band at 346 nm to be classified as LMCT. This transition involves excitation from occupied orbitals mostly on the methyl carbon to unoccupied orbitals delocalized over Co, B, and the unsaturated C in the To^{M} ligand. Additional peaks at 602 nm, 740 nm and 743 nm, found both in To^{M}CoMe and To^{M}CoCl calculations, support the assignment of the weaker signals in the experimental spectra as d ← d transitions. The strong, experimentally observed band at 697 nm was not evident, which may be due to the single configuration approach of TDDFT.

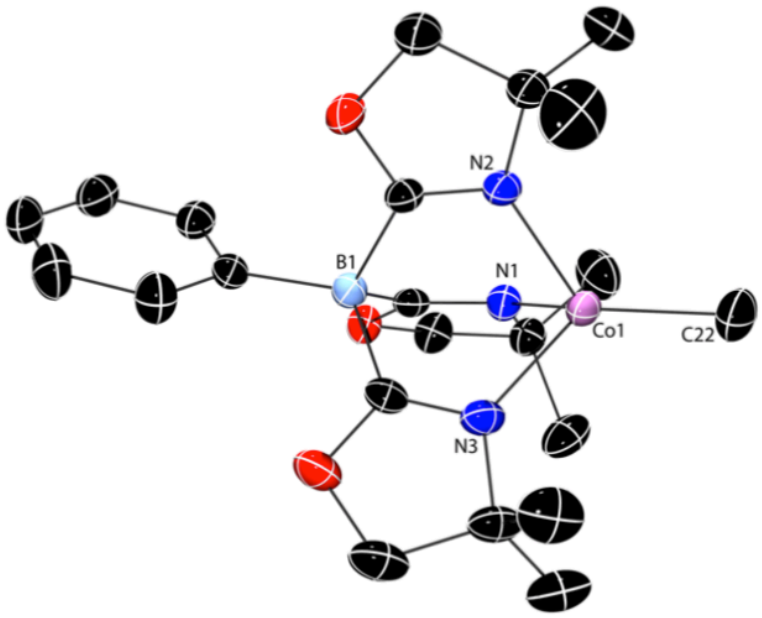

Figure 1. Rendered thermal ellipsoid diagram of To^{M}CoMe (**1**) with ellipsoids plotted at 50% probability. H atoms are omitted for clarity.

To^{M}CoMe and CO (1 atm) rapidly react in benzene-d_6 or THF at room temperature, as evidenced by an immediate color change from blue to orange. The possible products of To^{M}CoMe and CO include reduced To^{M}CoCO or To^{M}Co(CO)$_2$ species, To^{M}Co(Me)CO or its inserted isomer To^{M}CoC(O)Me, To^{M}Co{C(O)Me}CO, or To^{M}Co{C(O)Me}(CO)$_2$. A single ^{11}B NMR signal at -4 ppm, shifted upfield by 104 ppm from the value for **1**, suggested the formation of a single To^{M}Co-containing product (**2**). The ^{1}H and ^{11}B NMR spectra did not vary from room temperature to -80 °C.

Evaporation of a solution of **2** to dryness overnight gives **1** as the only detectable To^{M}Co-containing species, indicating that the reaction of **1** and CO is reversible. This reversibility hampers the isolation of **2**. Compound **2** persists in partially degassed solutions, while evaporation of all solvent and immediate redissolution affords a mixture of **1** and **2**. The reversible inter- action of **1** and CO rules out formation of To^{M}CoCO

because the byproducts of 1 e^- reduction of **1** are unlikely to persist in a form that could re-methylate To^MCoCO.

An *in situ* IR spectrum of the orange THF solution, collected on a ZnSe ATR crystal, revealed bands at 1984, 1886, 1687, and 1655 cm^{-1}. The two higher energy peaks were assigned to coordinated CO ligands, with the higher energy peak at 1984 cm^{-1} significantly more intense. The lower energy absorptions were assigned to rotamers of the cobalt acyl group, and the signal at 1655 cm^{-1} was notably non-Gaussian shaped with a shoulder tailing toward the red. On the basis of DFT calculations (see below), we assign this shoulder to the ν_{CN} of a weakly or non-coordinated oxazoline, which typically appears at 1630 cm^{-1}.[15] In addition, a peak at 1590 cm^{-1}, corresponding to the ν_{CN} of cobalt-coordinated oxazoline, was red-shifted by ~4 cm^{-1} in comparison to the To^MCoMe starting material. For comparison, the IR spectrum of isolated $Tp^{iPr2}Co\{C(O)Et\}CO$ contained a single CO band at 1999 cm^{-1} and an acyl peak at 1636 cm^{-1}.[7] The IR spectrum of $PhTt^{tBu}Co(C(O)Me)CO$ contained carbonyl ν_{CO} at 1993 cm^{-1} and acyl ν_{CO} at 1684 and 1663 cm^{-1} (assigned to rotomers).[10] Thus, the interaction of To^MCoMe and CO affords a mixture of $To^MCo\{C(O)Me\}CO$ (**2**; major, 1984, 1687, and 1655 cm^{-1}) and $To^MCo(Me)CO$ (minor, 1886 cm^{-1}; Scheme 1).

Scheme 1. Reversible reaction of To^MCoMe (**1**) and CO.

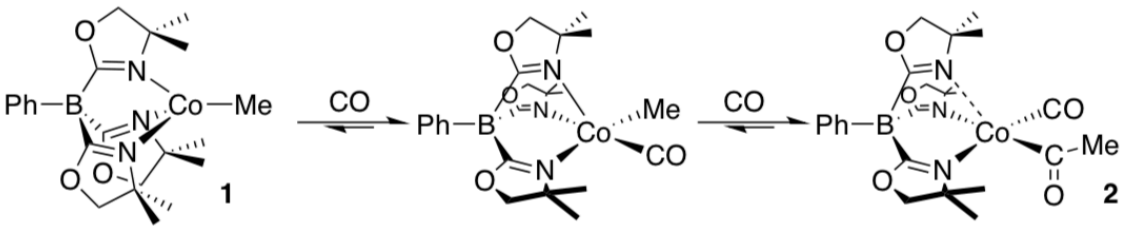

The effective magnetic moment of 2 is 2.7(**1**) μ_B (determined by Evans method). This value is reduced with respect to high spin To^{M}CoMe and is distinct from that of low-spin acyls PhTt^{tBu}Co{C(O)R}CO (R = Me, Et, Ph; μ_{eff} = 1.9–2.1 μ_B).[10] The result for **2** does not fit the spin-only μ_{eff} for low spin Co(II) (S = 1/2 is 1.73 μ_B). While high spin Co(I) (S = 1) would give a spin-only value of 2.83 μ_B (*e.g.*, for Tp^{Np}CoCO and Tp^{iPr,Me}CoCO, μ_{eff} = 3.1(1) μ_B), this type of product is ruled out above.[11,18] Instead, the effective magnetic moment of **2** is rationalized by a square pyramidal structure with a long axial Co–N interaction on the basis of the typical moments for square planar cobalt(II) complexes.[19–21] While a trigonal bipyramidal structure is also consistent with the magnetic moment, DFT calculations (described below) are more consistent with the square pyramidal geometry. A room temperature isotropic signal (g_{iso} ≈2.1) in the EPR spectrum of **2** further supported the low spin assignment.[22,23] The UV-vis spectrum of **2** was distinct from **1** and contained a broad, weak band from 760 to 1100 nm with a λ_{max} at 885 nm (ε: 305 M^{-1} cm^{-1}). In addition, a strong absorption tails from 200 to 600 nm.

DFT calculations of To^{M}Co{C(O)Me}CO suggest a square pyramidal geometry for the optimized structure. The low spin state is 33 kcal mol^{-1} lower in energy than the high spin state. A TDDFT calculation with implicit solvation finds strong electronic transitions at 448 and 462 nm, with multiple smaller contributing transitions between 300 nm and 400 nm, consistent with experimental findings. In a DFT Hessian calculation, the frequency corresponding to the acyl carbonyl stretching mode is found at 1731 cm^{-1} and the terminal carbonyl stretch is located at 2117 cm^{-1}. In addition, the calculated ν_{CN} stretches occur at 1636, 1667, and 1693 cm^{-1} with the highest energy ν_{CN} being associated

with the non-coordinated oxazoline.

The lowest energy calculated structure of $To^{M}Co(Me)CO$ adopts a square pyramidal geometry. The doublet spin state for this species is 30 kcal mol^{-1} below the high spin state. TDDFT calculations identify electronic transitions at 386 nm and 395 nm, which could be obscured by the multiple excitations found with the $To^{M}Co\{C(O)Me\}CO$ species. The calculated frequency for the CO stretch at 2030 cm^{-1} is lower energy than in $To^{M}Co\{C(O)Me\}CO$, providing support for the assignment of the experimental spectrum.

The orange carbonylated cobalt **2** rapidly reacts with O_2 to give purple $To^{M}CoOAc$ (**3**, eqn (2)), identified by comparison with an authentic sample's electronic spectrum (l_{max} = 486 and 585 nm), ^{1}H and ^{11}B NMR spectra, and X-ray diffraction pattern.[15] This reaction is sufficiently rapid and selective (and $To^{M}CoOAc$ is easily crystallized) that this product is typically isolated from attempted crystallizations of the monocarbonyl acyl complex at -80 °C due to trace O_2 impurities. *In situ*-generated **2** reacts with O_2 to afford **3** under a range of conditions, including 1 atm of O_2 at room temperature (analyzed by ^{1}H and ^{11}B NMR spectroscopy) or addition of O_2 as a THF solution (5–20 equiv. O_2, with or without excess CO, analyzed by UV-vis spectroscopy) at room temperature. Also, addition of a solution of O_2 (10–20 equiv.) to **2** at -100 °C provides an intermediate (l_{max} = 511, 550, and 585 nm) that converts into **3** upon warming to room temperature. That is, the transformation of equation (2) is fairly robust.

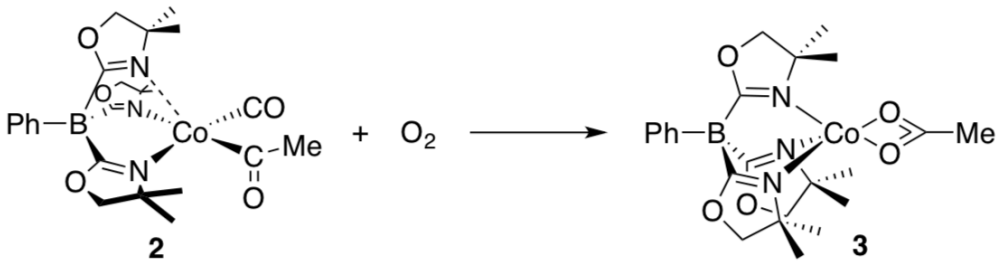

(2)

The reverse order of addition of reagents to To^{M}CoMe, oxidation followed by carbonylation, is not nearly so robust, selective or efficient. Reactions of **1** and O_2 at room temperature in THF or toluene-d_8 give a mixture of unidentified species that are unreactive toward CO. At -100 °C, a new, single ^{11}B NMR signal at -25 ppm suggests one species forms from addition of To^{M}CoMe and O_2 (1 atm). This species persists (based on unchanged ^{11}B NMR and EPR spectra) and is unreactive toward CO until the mixture is warmed to -20 °C. At that point, the solution becomes purple and To^{M}CoOAc forms as a minor component in a mixture of To^{M}Co-containing species.

The direct carboxylation reaction of **1** with CO_2 (1 atm or 85 psi) to form **3** requires 2 weeks (equation (3)), as monitored by ^{1}H NMR spectroscopy and a gradual color change from blue to purple.

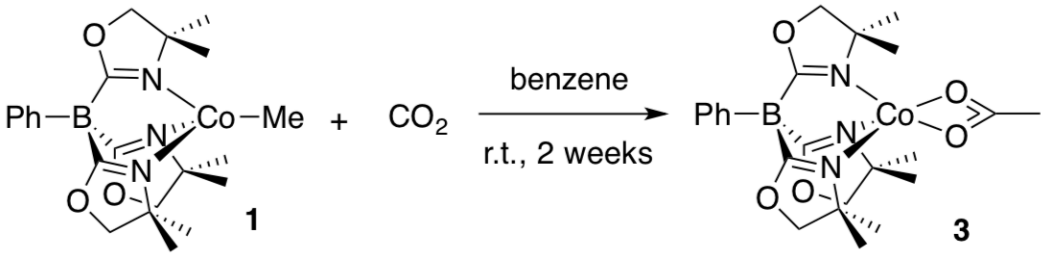

(3)

The rate of this conversion is significantly slower than the rapid carbonylation/oxidation chemistry described above. A related reaction of **2** and CO_2 also sluggishly provides

$To^{M}CoOAc$ at room temperature over ~2 weeks. Thus, while CO_2 insertion is possible, carbonylation and oxygenation by O_2 is the kinetically favored pathway.

These three sets of experiments provide considerable insight into the oxidative carbonylation sequence. First, a pathway from **2** to **3** involving **1** as an intermediate is unlikely because complete decarbonylation appears to be slow as indicated by the long drying times needed to fully convert **2** to **1**. Second, catalytic oxidation of CO to CO_2 by $To^{M}Co^{II}/O_2$ followed by carboxylation is ruled out as kinetically unfeasible by the experiment of equation (3).

Conclusion

We conclude that the sequence involving carbonylation of **1** to produce **2** followed by oxygenation to form 3 is kinetically favored. These results suggest that strategies for utilization of CO_2 involving carboxylation of organic compounds could benefit from an enzyme-inspired approach involving initial reduction to CO, CO migratory insertion, and finally oxidation rather than a direct, one-step carboxylation. At least in this case, a multistep compulsory-ordered pathway is considerably faster and more selective than random addition or direct insertion. Because acetate is important as a privileged ligand in oxidation catalysis and in CH activation pathways, the oxidative carbonylation studied here may be useful as part of selective hydrocarbon functionalization schemes. We are currently investigating related cobalt(II) alkyl and aryl compounds in pursuit of catalytic conversions.

Acknowledgments

This research was supported by the U.S. Department of Energy, Office of Basic Energy Sciences, Division of Chemical Sciences, Geosciences, and Biosciences. The Ames Laboratory is operated for the U.S. Department of Energy by Iowa State University under Contract No. DE-AC02-07CH11358.

References

1. B. Gabriele, G. Salerno and M. Costa, in *Catalytic Carbonylation Reactions*, ed. M. Beller, Springer Berlin Heidelberg, Berlin, Heidelberg, **2006**, pp. 239- 272.

2. D. J. Díaz, A. K. Darko and L. McElwee-White, *Eur. J. Org. Chem.*, **2007**, 4453-4465.

3. P. A. Lindahl, *J. Biol. Inorg. Chem.*, **2004**, *9*, 516-524.

4. S. W. Ragsdale and E. Pierce, *Biochim. Biophys. Acta, Proteins Proteomics*, **2008**, *1784*, 1873-1898. Kunishita, T. L. Gianetti and J. Arnold, *Organometallics*, **2012**, *31*, 372-380.

5. J. D. Jewson, L. M. Liable-Sands, G. P. A. Yap, A. L. Rheingold and K. H. Theopold, *Organometallics*, **1999**, *18*, 300-305.

6. N. Shirasawa, M. Akita, S. Hikichi and Y. Moro-oka, *Chem. Commun.*, **1999**, 417-418.

7. N. Shirasawa, T. T. Nguyet, S. Hikichi, Y. Moro-oka and M. Akita, *Organometallics*, **2001**, *20*, 3582-3598.

8. S. Yoshimitsu, S. Hikichi and M. Akita, *Organometallics*, **2002**, *21*, 3762- 3773.

9. J. A. DuPont, M. B. Coxey, P. J. Schebler, C. D. Incarvito, W. G. Dougherty, G. P. A. Yap, A. L. Rheingold and C. G. Riordan, *Organometallics*, **2007**, 971-979.

10. J. L. Detrich, O. M. Reinaud, A. L. Rheingold and K. H. Theopold, *J. Am. Chem. Soc.*, **1995**, *117*, 11745-11748.

11. D. Mukherjee, A. Ellern and A. D. Sadow, *J. Am. Chem. Soc.*, **2012**, *134*, 13018-13026.

12. S. Hikichi, H. Komatsuzaki, M. Akita and Y. Moroka, *J. Am. Chem. Soc.*, **1998**, *120*, 4699-4710.

13. S. Hikichi, K. Hanaue, T. Fujimura, H. Okuda, J. Nakazawa, Y. Ohzu, C. Kobayashi and M. Akita, *Dalton Trans.*, **2013**, *42*, 3346-3356.

14. R. R. Reinig, D. Mukherjee, Z. B. Weinstein, W. Xie, T. Albright, B. Baird, T. S. Gray, A. Ellern, G. J. Miller, A. H. Winter, S. L. Bud'ko and A. D. Sadow, *Eur. J. Inorg. Chem.*, **2016**, 2486-2494.

15. R. E. Cowley, R. P. Bontchev, E. N. Duesler and J. M. Smith, *Inorg. Chem.*, **2006**, *45*, 9771-9779.

16. P. J. Schebler, B. S. Mandimutsira, C. G. Riordan, L. M. Liable-Sands, C. D. Incarvito and A. L. Rheingold, *J. Am. Chem. Soc.*, **2001**, *123*, 331-332.

17. J. L. Detrich, R. Konečný, W. M. Vetter, D. Doren, A. L. Rheingold and K. H. Theopold, *J. Am. Chem. Soc.*, **1996**, *118*, 1703-1712.

18. E. K. Barefield, D. H. Busch and S. M. Nelson, *Q. Rev. Chem. Soc.*, **1968**, *22*, 457-498.

19. R. Poli, *Chem. Rev.*, **1996**, *96*, 2135-2204.

20. M. Cibian and G. S. Hanan, *Chem. Eur. J.*, **2015**, *21*, 9474-9481.

21. P. H. Haffner and J. E. Coleman, *J. Biol. Chem.*, **1973**, *248*, 6630-6636.

22. D. M. Jenkins, A. J. Di Bilio, M. J. Allen, T. A. Betley and J. C. Peters, *J. Am. Chem. Soc.*, **2002**, *124*, 15336-15350.

CHAPTER 9: COBALT(II) ACYL INTERMEDIATES IN CARBON-CARBON BOND FORMATION AND OXYGENATION

A paper published in *Dalton Transactions* **2018**, 47, 12147-12161

Regina R. Reinig, Ellie L. Fought, Arkady Ellern, Theresa L. Windus, and Aaron D. Sadow

ELF and TLW performed all DFT, TDDFT, and CI calculations. RRR, AE, and ADS performed all synthetic and spectroscopic work.

Abstract

The organocobalt scorpionate compounds $To^{M}CoR$ (To^{M} = tris(4,4-dimethyl-2-oxazolinyl)phenylborate; R = Bn, **1**; CH_2SiMe_3, **2**; Ph, **3**; Et, **4**; ^{n}Bu, **5**; Me, **6**) react in carbonylation, oxidation, and carboxylation reactions via pathways that are distinctly influenced by the nature of the organometallic moiety. The compounds are prepared by reaction of $To^{M}CoCl$ with the corresponding organolithium or organopotassium reagents. Compounds **1–6** were characterized by 8-line hyperfine coupling to cobalt in EPR spectra and solution phase magnetic measurements (μ_{eff} = 4–5μ_B) as containing a high-spin cobalt(II) center. The UV-Vis spectra revealed an intense diagnostic band at ca. 700 nm ($\varepsilon > 1000$ M^{-1} cm^{-1}) associated with the tetrahedral organocobalt(II) center that was assigned to a d ← d transition on the basis of configuration interaction (CI) calculations. Complexes **1–6** react rapidly with CO to form equilibrating mixtures of the low spin organocobalt carbonyl $To^{M}Co(R)CO$, acyl $To^{M}CoC(=O)R$, and acyl carbonyl

$To^{M}Co\{C(=O)\ R\}CO$. The ^{1}H and ^{11}B NMR spectra contained only one set of signals for the CO-treated solutions, whereas the solution-phase IR spectra contained up to two $\nu_{C\equiv O}$ and three $\nu_{C(=O)R}$ signals with intensities varying depending on the R group (R = Bn, **7**; CH_2SiMe_3, **8**; Ph, **9**; Et, **10**; ^{n}Bu, **11**; Me, **12**). Single crystal X-ray diffraction of $To^{M}Co\{C(=O)Et\}CO$ (**10**) supports its assignment as a square pyramidal cobalt(II) acyl carbonyl complex. Upon evaporation of volatiles, solutions of **8–12** revert to the CO-free organocobalt starting materials **2–6**, whereas attempts to isolate benzyl-derived **7** provide an unusual α-alkoxyketone species, characterized by single crystal X-ray diffraction. Despite the differences observed in the carbonylation of **1–6** as a result of varying the R group, compounds **7–12** all react rapidly with O_2 through an oxygenation pathway to afford the corresponding carboxylate compounds $To^{M}CoO_2CR$ (R = Bn, **13**; CH_2SiMe_3, **14**; Ph, **15**; Et, **16**; ^{n}Bu, **17**; Me, **18**). In contrast, the insertion of CO_2 into the Co–C bond in **1–6** requires several days to weeks.

Introduction

Oxidative carbonylation, an organotransition metal-mediated route to carboxylates, typically proceeds by a sequence in which a metal hydrocarbyl reacts with CO to form an acyl, followed by hydrolysis and reductive elimination. Under catalytic conditions, metal-centered oxidation and metalation steps complete the cycle to generate a new metal hydrocarbyl. This kind of pathway has been proposed for palladium-catalyzed oxidative carbonylation of arenes,[1] as well as catalytic carboxylations of amides to give carbamates and ureas.[2] Remarkably, the biological synthesis of acetate also involves carbonylation of an organometallic nickel methyl to give an acetyl group

that is transferred to acetyl Co-A to form a thioacetate and then subsequently hydrolyzed.[3–5] The fact that carbon dioxide, which serves as the source of both carbon atoms in acetate, is not incorporated into acetate by direct insertion into the metal-methyl is perhaps even more remarkable. Instead, CO_2 is reduced both to the methyl and to CO by CO dehydrogenase.[6,7] Similarly, in synthetic chemistry, the synthesis of acetate or acetic acid *via* the Monsanto process involves CO, reductive elimination and hydrolysis rather than direct insertion of CO_2.[8] These carbonylations result in oxygenation of an acyl to carboxylate, but the pathways invoke hydrolysis followed by oxidation at the metal center rather than by direct oxygenation of the metal acyl species. The distinction between oxidation catalysis (including reactions mediated by oxidases)[9] and oxygenation catalysis (catalyzed by oxygenases) affects the choice of reagent as the oxygen source and oxidant, as well as the conditions and occasions for their use. Nonetheless, acyl species are proposed as likely intermediates in multiple pathways, therefore identification of the conditions by which acyl metal compounds form and their subsequent reaction pathways are key to developing new transformations.

A seemingly straightforward and well-established route to acyl compounds involves an insertive combination of CO and organometallic compounds. For tetrahedral organometallic compounds, however, a number of species and pathways can result from interactions with CO. In one pathway, the coordination of CO to the metal center gives a metal hydrocarbyl carbonyl adduct, which can undergo insertion to form an isomeric acyl species. Further coordination of one or two CO ligands is likely influenced by the steric properties of the ancillary ligand or acyl group and by the electronic configuration of the metal center. For example, acyl derivatives of $Tp^{R'}CoEt$, $Tp^{R'}CoC_3H_5$ and

$Tp^{R'}CoCH_2C_6H_4OMe$ are isolable ($Tp^{R'}$ = Tp^{iPr2} or Tp^{Me3}; Tp^{iPr2} = tris(3,5-diisopropylpyrazolyl)borate; Tp^{Me3} = tris(3,4,5-trimethylpyrazolyl)borate).[10,11]

Alternatively, reactions of tetrahedral divalent organometallics with CO can result in 1*e*– reduction to form carbonyl adducts.[12,13] Reduction is typically observed with bulky ancillary ligands, such as in the reactions of CO and $Tp^{tBu,Me}CoMe$ ($Tp^{tBu,Me}$ = tris(3-*t*-butyl-5-methylpyrazolyl)borate) or $PhTp^{tBu}FeMe$ ($PhTp^{tBu}$ = tris(3-t-butylpyrazolyl)phenylborate) that form cobalt(I) or iron(I) carbonyls, respectively. Homolysis of tetrahedral cobalt alkyls is also proposed as the first step in the rearrangement of $Tp^{Ph,Me}Co$*t*Bu ($Tp^{Ph,Me}$ = tris(3-phenyl-5-methylpyrazolyl)borate) to $Tp^{Ph,Me}CoCH_2CHMe_2$.[14] Interestingly, $Tp^{R'}CoEt$ and CO provides first the acylcobalt carbonyl species, which forms $Tp^{R'}CoCO$ upon removal of volatiles,[11] and this is suggested to occur by homolysis of $Tp^{R'}CoEt(CO)$. The fate of the organometallic ligand in these reductive pathways has not been established.

Recently, we reported the synthesis of $To^{M}CoMe$ (To^{M} = tris (4,4-dimethyl-2-oxazolinyl)phenylborate) by reaction of $To^{M}CoCl$ with MeLi. $To^{M}CoMe$ reacts readily with CO to form $To^{M}Co\{C(=O)Me\}CO$ followed by rapid reaction with O_2 to produce $To^{M}CoOAc$.[15] Direct insertion of CO_2 into $To^{M}CoMe$ also affords $To^{M}CoOAc$, but the reaction requires several weeks. The observation that the multistep pathway is, at least in this case, significantly faster than direct insertion, motivated us to expand the study to other organocobalt species supported by To^{M} to determine if this reactivity is general to other alkyl and aryl groups.

Herein, we prepare a series of alkyl, aryl, and benzyl cobalt(II) compounds supported by a tris(oxazolinyl)borate ligand. The spectroscopic, electronic, and structural

features are compared within the series of organocobalt(II) compounds and with halide and pseudo-halide analogues to discover distinguishing features that might parallel reactivity differences within the series of compounds and to related four-coordinate cobalt alkyls. The products of carbonylation are characteristic of the hydrocarbyl ligand, as identified by signals observed in the infrared spectra in carbonyl and acyl C=O stretching regions. These carbonylation products are oxygenated in reactions with O_2, which occurs rapidly, in contrast to sluggish reactions of the organocobalt compounds and carbon dioxide.

Results and Discussion

Synthesis and Characterization Of To^{M}CoR

The organometallic cobalt(II) complexes To^{M}CoR (R = Bn, **1**; CH_2SiMe_3, **2**; Ph, **3**; Et, **4**; ^{n}Bu, **5**; Me, **6**) are prepared by salt metathesis reactions involving To^{M}CoCl and excess (1.4–1.7 equiv.) organopotassium ($PhCH_2K$) or organolithium (Me_3SiCH_2Li, PhLi, EtLi, ^{n}BuLi, MeLi) reagents (Scheme 1).[15] To^{M}CoMe and To^{M}CoBn are the most straightforward to prepare and form in good yields at room temperature under dilute conditions. For example, To^{M}CoBn (**1**, 0.129 g, 0.242 mmol, 79%) is synthesized from To^{M}CoCl (0.308 mmol, 0.031 M) and 1.7 equiv. of KBn in THF at room temperature.

Dilute conditions (~0.02 M) are also effective on a ~0.03 mmol scale for synthesizing organocobalt(II) complexes **2–5** in good yield (>50%). Unfortunately, preparative scale reactions for **2–5** (>0.06 mmol) under these dilute conditions consistently give less than 30% yield. Instead, **2–5** require more concentrated conditions (~0.1 M) and low temperature reactions. Using 0.1 M To^{M}CoCl, 1.4 equiv. of alkyllithium, and mixtures cooled to −78 °C, To^{M}CoCH$_2$SiMe$_3$ (**2**), To^{M}CoPh (**3**),

To^{M}CoEt (**4**) and ToMConBu (**5**) are reproducibly synthesized in greater than 0.20 mmol quantities and >60% yields. These conditions provide spectroscopically and analytically pure To^{M}CoR. Signals for To^{M}CoCl in NMR and UV-Vis spectra, even as a trace impurity, were not detected for these samples (see below).

NMR spectroscopy provided an initial assay for alkyl- or arylation of To^{M}CoCl. Despite the paramagnetic nature of these cobalt(II) complexes, both ^{1}H and ^{11}B NMR spectroscopy clearly distinguished To^{M}CoCl from the organocobalt(II) complexes by their chemical shifts (Table 1). The To^{M}-based pattern of signals was consistent with C_{3v}-symmetric species, and their chemical shifts appeared in similar regions for all six

Scheme 1. Synthesis of To^{M}CoBn (**1**), To^{M}CoCH$_2$SiMe$_3$ (**2**), To^{M}CoPh (**3**), To^{M}CoEt (**4**), To^{M}Co^{n}Bu (**5**), and To^{M}CoMe (**6**).

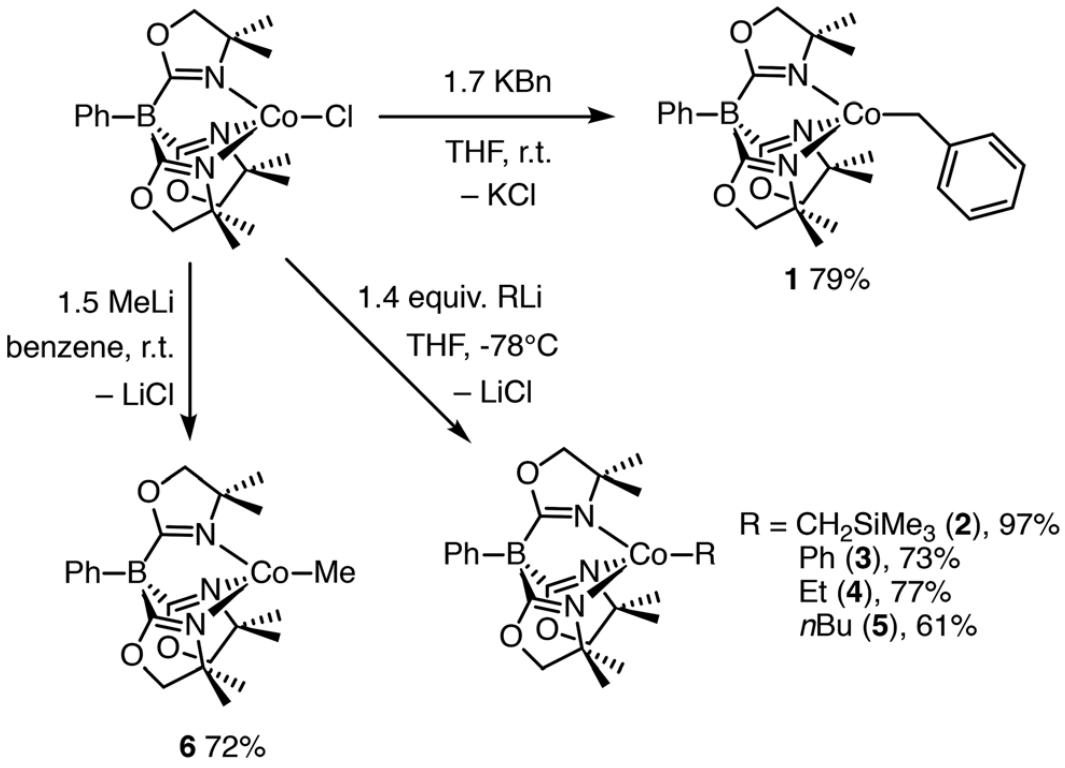

organocobalt compounds. The signals attributed to the oxazoline methyl groups ranged from −9.6 to −14.5 ppm, which was more than 15 ppm lower frequency compared to the corresponding signal in $To^{M}CoCl$ at 8.38 ppm. The oxazoline methylene peaks' range was even smaller, from 14.8–16.7 ppm, whereas the corresponding resonance in $To^{M}CoCl$ was observed at 24.9 ppm. While the chemical shifts for the To^{M} ligand were similar across **1–6**, the detected signals for the alkyl and aryl ligands were wide ranging. For example, the benzyl ligand resonances in **1**, were observed at 34, −77, and −89 ppm. ^{1}H NMR peaks that might be attributed to hydrogen on the α-carbon were not detected in any of the alkyl compounds. The ^{11}B NMR spectra of these complexes each contained one peak, the chemical shift of which ranged from 87 to 117 ppm. These signals had far higher frequency chemical shifts compared to the resonances of the chloride (−29 ppm)

Table 1. NMR data for $To^{M}CoR$

	^{1}H NMR[a] (ppm)			
Compound	To^{M} (CH_2)	To^{M} (CH_3)	R	^{11}B NMR (ppm)
$To^{M}CoBn$ (**1**)	16.3	−12.5	34.5, −77.5, −89.0	100.4
$To^{M}CH_2SiMe_3$ (**2**)	15.7	−9.6	8.5	86.6
$To^{M}CoPh$ (**3**)	16.7	−13.7	74.0, 10.6	107.7
$To^{M}CoEt$ (**4**)	14.9	−14.5	−31.3	116.7
$To^{M}Co^{n}Bu$ (**5**)	14.9	−14.3	14.2, −2.7	115.0
$To^{M}CoMe$[b] (**6**)	15.4	−12.1	Not detected	100.3
$To^{M}CoCl$[c]	24.9	8.4	Not applicable	−29

[a] See experimental for Ph resonances. [b] See ref. 15. [c] See ref. 16.

as well as diamagnetic species resulting from transmetalation of To^{M}(ca. −17 ppm). Overall, the ^{1}H and ^{11}B NMR spectra associated with the To^{M} ligand in the series of organometallic species are comparable, whereas the chemical shifts for the oxazolinylborate ligand in $To^{M}CoX$ (e.g. X = Cl, O^{t}Bu, OAc) complexes vary

considerably. These data suggest that the organometallic compounds' electronic structures, which are responsible for the paramagnetic chemical shifts, are similar between simple alkyl, *β*-H containing alkyl, trimethylsilyl-substituted alkyl, aryl, and benzyl ligands.

A single band at ~1590 cm^{-1} in the IR spectra of **1–6**, assigned to the oxazoline $\nu_{C=N}$, provided additional support for tridentate coordination of the To^M ligand to cobalt. Signals at higher frequency (~1630 cm^{-1}) associated with C=N stretching modes of non-coordinated oxazolinyl groups were not detected. In addition, the IR spectrum of 1 contained a new band at 3012 cm^{-1} that was assigned to an aromatic ν_{C-H} mode and taken as additional evidence of benzylation. This peak was distinct from the signals at 3070 and 3050 cm^{-1} present in all the compounds that were attributed to aromatic ν_{C-H} modes from the phenyl group in the To^M ligand. In contrast, the aromatic region in the IR spectrum of phenylcobalt 3 did not reveal new aromatic ν_{C-H} signals.

The UV-Vis spectra (Fig. 1 and Table S1‡) of 1–6 contained intense absorptions at *ca.* 350 (ε: 1400–3200 M^{-1} cm^{-1}) and 700 nm (ε: 1100–1500 M^{-1} cm^{-1}) and two weaker bands at *ca*. 570 (ε: 200–400 M^{-1} cm^{-1}) and 620 nm (ε: 200–450 M^{-1} cm^{-1}). The former, intense features are not detected in spectra of To^MCoCl and are characteristic of these organometallic complexes. The bands in the region of 500–650 nm were similar to those observed for To^MCoCl at 568 (ε = 362 M^{-1} cm^{-1}) and 635 nm (ε = 641 M^{-1} cm^{-1}) and were assigned to d ← d transitions. These bands are related to the $^4T_1(P) \leftarrow {}^4A_2$ (F) transition in $[CoCl_4]^{2-}$ that split in lower symmetry. Across the organometallic compounds, the wavelengths of these d ← d bands do not vary very much, further

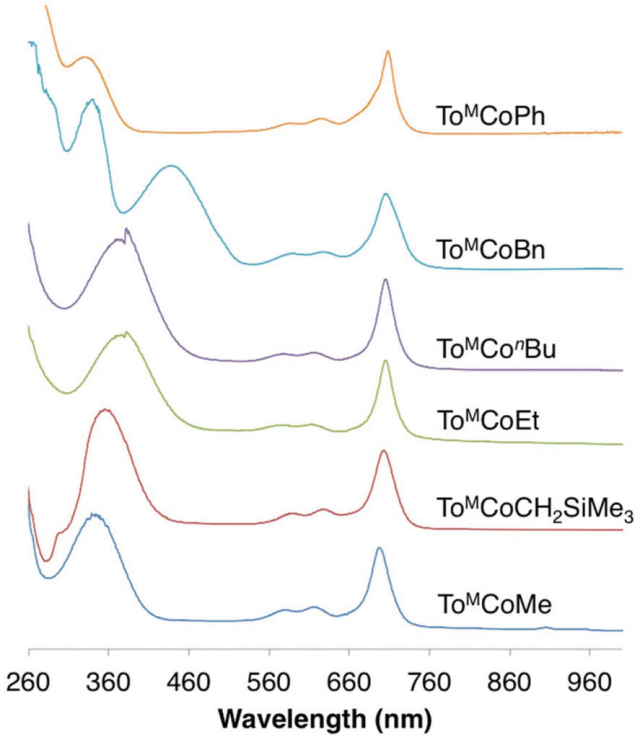

Figure 1. UV-Vis spectra of To^{M}CoPh (**3**), To^{M}CoBn (**1**), To^{M}ConBu (**5**), To^{M}CoEt (**4**), To^{M}CoCH$_2$SiMe$_3$ (**2**), and To^{M}CoMe (**6**) measured in diethyl ether.

supporting the idea, from the NMR chemical shift analysis discussed above, that their electronic structures are similar. The benzyl compound **1**, which also showed unique reactivity (see below), contained an additional intense absorption at 439 nm (ε: 1964 M^{-1} cm^{-1}; see Fig. 1).

A few four-coordinate tris(pyrazolyl)borate organocobalt species show similar features in their electronic spectra. For example, the spectrum of Tp^{iPr2}CoEt had four bands at 388 (1030 M^{-1} cm^{-1}), 580, 610, and 690 (810 M^{-1} cm^{-1}) nm (ref. 11) and p-tolyl Tp^{iPr2}CoC$_6$H$_4$Me contained an intense absorption at 697 nm (1304 M^{-1} cm^{-1}).[17] This intense ~700 nm absorption, however, is not a universal features of tetrahedral cobalt(II) alkyl complexes. In contrast, other tris(pyrazolyl) borate organocobalt species revealed weaker bands around 700 nm, such as Tp^{tBu,Me}CoMe (685 nm, 499 M^{-1} cm^{-1}),

Tp$^{t\text{Bu}}$CoMe (688 nm, 839 M^{-1} cm^{-1}; TptBu = tris(3-t-butyl- pyrazolyl)borate), and Tp$^{t\text{Bu,Me}}$CoEt (688 nm, 510 M^{-1} cm^{-1}).[12] Also, visible-region transitions were more intense for the chloride than for methyl, phenyl, or benzyl compounds in the tris(tert-butylthio)methyl borate cobalt(II) compounds PhTt$^{t\text{-Bu}}$CoX.[18,19]

The absorption spectra for the series of tris(oxazolinyl) borato organocobalt and heteroatom-bonded species were further studied with representative electronic structure calculations. Gas-phase models for To^{M}CoBn (**1-calc**), To^{M}CoMe (**6-calc**) and To^{M}CoCl (**To^{M}CoCl-calc**) were optimized (PBE0, 6-311+G* and Stuttgart RSC 1997)[20,21] using the coordinates from X-ray diffraction (see below) as initial geometries. The average Co–N distances (To^{M}CoCl, 2.02 Å; To^{M}CoCl-calc, 2.04 Å; **1**, 2.05 Å; **1-calc**, 2.06 Å; **6**, 2.05 Å; **6-calc**, 2.08 Å), B–Co–X angle (To^{M}CoCl, 171°; To^{M}CoCl-calc, 178.59°; **1**, 171.3°; **1-calc**, 173.4°; **6**, 172.8°; **6-calc**, 179.3°) and τ_4 values (To^{M}CoCl, 0.76; To^{M}CoCl-calc, 0.80; **1**, 0.75; **1-calc**, 0.75; **6**, 0.76**; 6-calc**, 0.79) were in reasonably good agreement with the results from X-ray diffraction, although comparison of the latter two parameters indicated gas-phase DFT structures are more symmetrical than solid-state structures, as assessed by diffraction. The τ_4 scale for accessing distortions of four-coordinate compounds, is defined as $\tau_4 = 1$ for a T_d geometry, 0.85 for a trigonal pyramid (C_{3v}), and 0.0 for a square planar geometry.[22] The vibrational calculations for **6-calc** and To^{M}CoCl-calc contained peaks at 1667 and 1677 cm^{-1}, respectively, which corresponded to the symmetric ν_{CN} mode (the asymmetric ν_{CN} mode was low intensity). The high spin state for **1-calc** and **6-calc** were calculated to be 46 and 48 kcal mol^{-1} lower in energy than the low spin, respectively, as expected for tetrahedral cobalt(II).

TDDFT calculations on To^{M}CoCl-calc and **6-calc** revealed transitions at 602, 740 and 743 nm for both species. The intense low-energy experimental band at 697 nm in **6**, however, was not present in the TDDFT method. We previously postulated that the single configuration TDDFT approach was insufficient to correctly describe the electronic features of these compounds.[15] In fact, configuration interaction (CI) singles calculations show that the ground state wave functions of organocobalt **1-calc** and **6-calc** are distinct from that of To^{M}CoCl-calc. The ground state electronic structure of To^{M}CoCl-calc is best described by a single-reference wavefunction. In contrast, the ground state wave functions of **1-calc** and **6-calc** contain multireference character (*i.e.*, the ground state has more than one contributing electronic configuration). The primary distinction between the To^{M}CoCl-calc compared to **1-calc** and **6-calc** is the location of two molecular orbitals with nodal planes of the phenyl ring on the To^{M} ligand (Fig. 2) within the molecular orbital space manifold.

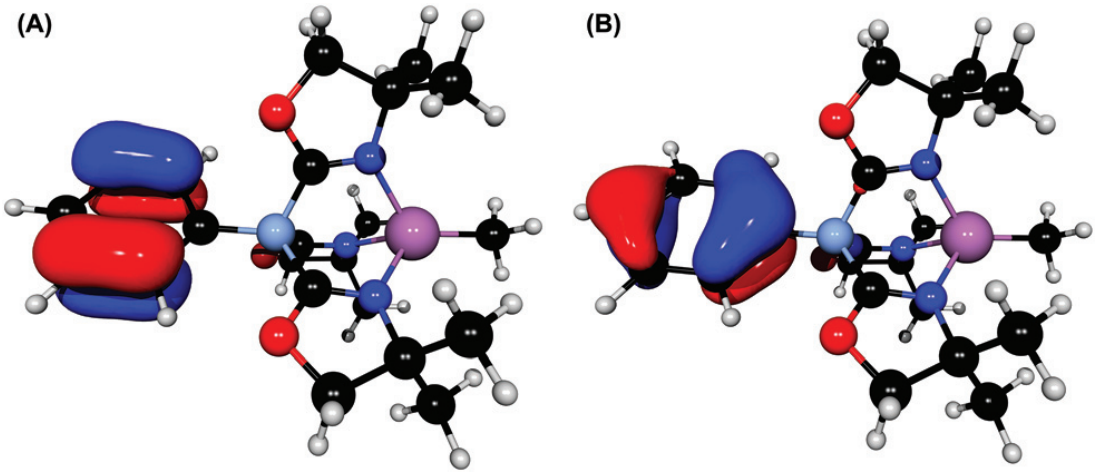

Figure 2. Three-dimensional rendering of molecular orbitals showing the nodal planes of the phenyl ring of **6-calc** calculated using configuration interaction singles.

In the To^{M}CoCl-calc system, these two orbitals are lower in energy than in **1-calc** and **6-calc**, nearly degenerate, and are both doubly occupied. In a single reference calculation for **1-calc** and **6-calc**, these two orbitals are split – one in the doubly occupied space and the other in the singly occupied space, thus creating an artificial preference of one orbital over another to be singly occupied. Multireference character in the ground state wavefunction of **6-calc** helps to explain why the excitation at 697 nm from the experimental UV-Vis was not found in earlier TDDFT calculations. The CI singles calculation of **1-calc** contain an excited state (3rd excited state) with an energy difference from the ground state corresponding to an excitation at 661 nm. The excitation is from a doubly occupied bonding orbital to a singly occupied anti-bonding orbital centered on the cobalt. The orbitals involved in this excitation are mostly, but not purely, d orbitals and include contributions from the oxazolines and the methyl group; however, the d orbitals have the largest changes in electron density. Thus, this transition is identified as essentially a d ← d transition. The conclusions from CI calculations on **1-calc** are also consistent with those from the study of **6-calc**.

Solution-phase magnetic moments of compounds **1–6** range from 4.0 to 4.9μ_B (Table S1‡) at room temperature, measured using Evans method, and were consistent with high-spin cobalt(II) (S = 3/2, spin-only μ_{eff} = 3.87μ_B) and the calculated electronic structures. With the exception of To^{M}CoPh, the effective magnetic moments are within the range reported for other pseudo-tetrahedral organocobalt(II) complexes.[10,12] In high spin, tetrahedral cobalt(II) with an $e^4t_2^3$ configuration, orbital contributions to the magnetic moment are expected to be quenched in the ground state, but low-lying excited state mixing results in μ_{eff} ranging from 4–5μ_B.[23] EPR spectra for **1–6** (Fig. S62‡) all

contain striking eight-line patterns resulting from hyperfine coupling (54 G) to the ^{59}Co center (I = 7/2). Other four-coordinate $\{\kappa^3\text{-To}^M\}\text{Co}^{II}$ species, namely To^MCoCl and $\text{To}^M\text{CoO}^t\text{Bu}$, produced rhombic signals that were devoid of hyperfine coupling.

The spectroscopically assigned structures of compounds **1–6** are validated by X-ray diffraction studies of single crystals (Fig. 3–5 and ESI‡). The molecular structures are similar to previously reported tris(oxazolinyl)borate magnesium (d^0) and zinc (d^{10}) organometallic compounds.[24,25] In each cobalt complex, the tris(oxazolinyl)borate ligand is coordinated in a tridentate motif, and the To^M and alkyl or aryl ligands provide a distorted tetrahedral geometry for the cobalt centers (τ_4 = 0.75–0.82), which is similar to To^MMgMe (τ_4 = 0.75) and To^MZnMe (τ_4 = 0.76). The ∠B–M–Me in To^MMgMe (172.89°), To^MZnMe (174.74) and To^MCoMe (172.83°) are similar. The τ_4 scale, the ∠N–Co–C angles, and the ∠B–M–C angles describe similar distortions of the alkyl ligand away from the C3 axis in the $\{\kappa^3\text{-To}^M\}$M motif. That is, the three unpaired d electrons in the high spin cobalt(II) compounds appear to have little consequence on the coordination geometry. In addition, the Co–C distances in compounds **1–6** vary only from 1.994(2) (**6**) to 2.023(2) Å for **1** (see Table S2‡). The Co–N interatomic distances are also similar across the series, varying from 2.019(2) to 2.062(3) Å. That is, the similar electronic features identified by UV-Vis, EPR, and NMR spectroscopies are also reflected in similar structural parameters.

Complexes **1–6** persist in solution at elevated temperatures (in the absence of air and moisture). For example, ethyl and butyl compounds **4** and **5** do not eliminate detectable quantities of ethylene or butene, respectively, after thermal treatment at 120 °C despite the possibility for *β*-hydrogen elimination or Co–C bond homolysis. Similar

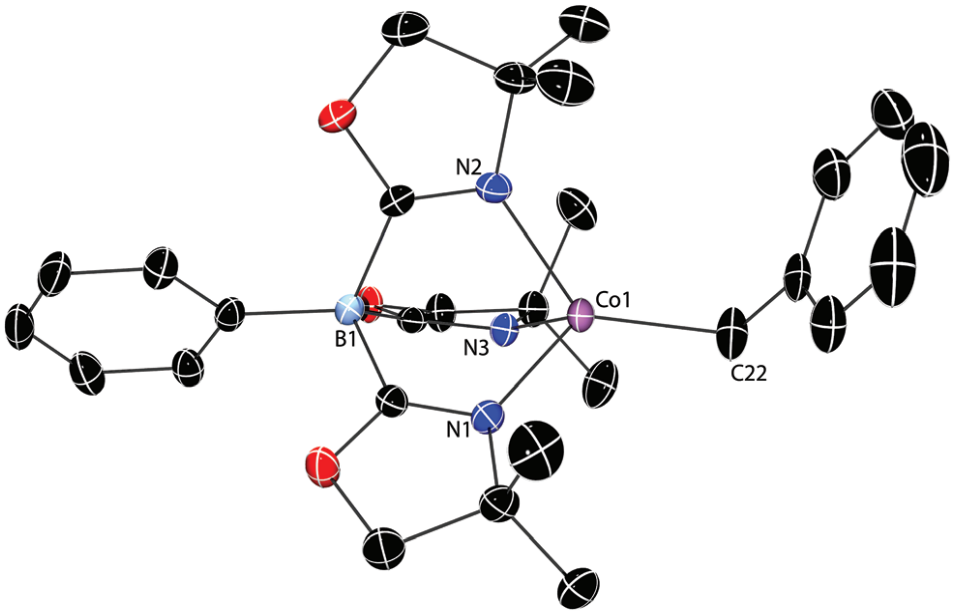

Figure 3. Thermal ellipsoid diagram of To^{M}CoBn (**1**) with ellipsoids plotted at 50% probability. H atoms are omitted for clarity. Selected interatomic distances (Å) and angles (°): Co1–C22, 2.023(2); Co1–N1, 2.040(1); Co1– N2, 2.055(1); Co1–N3, 2.041(1); N1–Co1–C22, 122.94(6); N2–Co1–C22, 131.33(6); N3–Co1–C22, 116.37(6); N1–Co1–N2, 91.68(5); N1–Co1–N3, 94.00(5); N2–Co1–N3, 91.00(5), B1–Co1–C22, 171.27(6).

resistance toward *β*-hydrogen elimination in a bulkier tris(pyrazolyl)borato cobalt ethyl, Tp^{iPr2}CoEt, was attributed to its high spin electronic configuration.[10,26] Products of Co–C bond homolysis, such as ethane or butane, are also not formed.

Crude samples of **2–5**, apparently pure and To^{M}CoCl-free as determined by ^{1}H NMR, ^{11}B NMR and UV-Vis spectroscopy, revealed small amounts of To^{M}CoCl (<10%) as a contaminant after addition of CO. In contrast, reactions of either **1** or **6** and CO or CO_2 provide acyl or carboxylate products that are free of To^{M}CoCl impurity, implying that the source of To^{M}CoCl is not present in either the cobalt benzyl or methyl samples. Ultimately, recrystallization of organocobalt(II) species **2**–**5** afforded isolable organometallic species that did not generate detectable To^{M}CoCl in subsequent reactions.

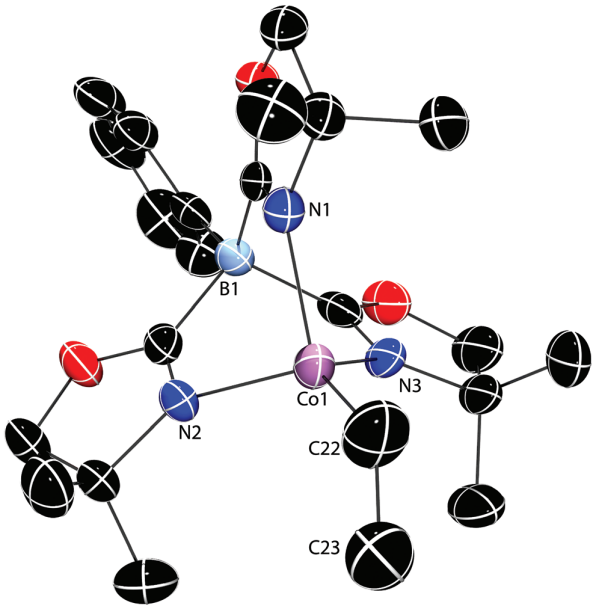

Figure 4. Thermal ellipsoid plot of To^{M}CoEt (**4**) with ellipsoids rendered at 50% probability. Hydrogen atoms are omitted for clarity. Selected interatomic distances (Å) and angles (°): Co1–C22, 1.980(3); Co1–N1, 2.046(2); Co1–N2, 2.045(2); Co1–N3, 2.046(2); N1–Co1–C22, 119.7(1); N2–Co1– C22, 126.9(1); N3–Co1–C22, 125.2(1); N1–Co1–N2, 92.52(9); N1–Co1– N3, 91.07(9); N2–Co1–N3, 91.77(9); B1–Co1–C22, 175.4(1).

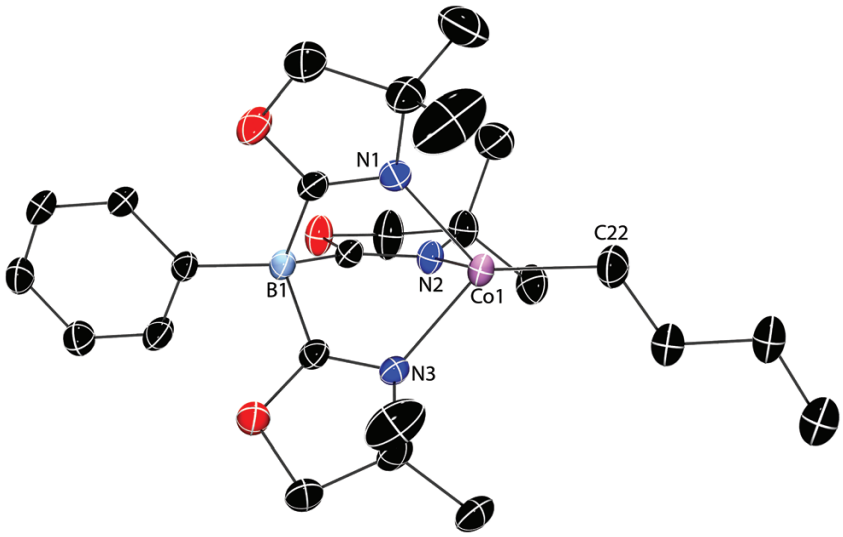

Figure 5. Thermal ellipsoid plot of ToMConBu (5) with ellipsoids rendered at 50% probability. H atoms are omitted for clarity. Selected interatomic distances (Å) and angles (°): Co1–C22, 2.010(4); Co1–N1, 2.046(2); Co1– N2, 2.047(2); Co1–N3, 2.054(3); N1–Co1–C22, 121.4(1); N2–Co1–C22, 124.4(1); N3–Co1–C22, 126.3(1); N1–Co1–N2, 91.2(1); N1–Co1–N3, 91.5(1); N2–Co1–N3, 92.4(1), B1–Co1–C22, 176.9(1).

Carbonylation Of To^{M}CoR

Complexes **1–6** rapidly react with CO (1 atm) in benzene-d_6 at room temperature (Scheme 2), as evidenced by an immediate change from blue/green to orange, to give mixtures containing organocobalt carbonyl To^{M}CoR(CO) (**7a–12a**; 7, Bn; **8**, CH_2SiMe_3; **9**, Ph; **10**, Et; **11**, ^{n}Bu; **12**, Me), acyl To^{M}CoC(=O)R (**7b–12b**), and acyl carbonyl To^{M}Co{C(=O)R}CO (**7c–12c**). Species **a**, **b**, and **c** interconvert by insertion and CO coordination, or CO dissociation and decarbonylation, and the relative amounts of **a**, **b**, and **c** present in **7–12** vary depending on the alkyl or aryl group, as determined by IR spectroscopy. The results from analysis of the IR spectra are summarized in eqn (1)–(4) in Scheme 2. Multiple $\nu_{C\equiv O}$ and $\nu_{(C=O)R}$ in the IR spectra indicate that several species are present in each reaction mixture, whereas ^{1}H and ^{11}B NMR spectroscopy suggest only a single species is formed. Together, NMR and IR spectroscopy suggest that organocobalt carbonyl **a**, acyl **b**, and acyl carbonyl **c** species interconvert through a process that is faster than the NMR timescale and slower than the IR timescale.

Compounds **8–12** gave similar ^{1}H NMR spectra that contained five, broad signals from 10 to −7 ppm, which were distinct from the spectra for the organocobalt(II) starting materials. Four of the ^{1}H NMR signals were attributed to the To^{M} ligand on the basis of their consistent chemical shifts across complexes **8–12** (9.6, 8.1, 7.7, and −1.2 ppm). The fifth peak was assigned to the organocobalt group on the basis of its varying chemical shift among the complexes (e.g., −0.09 ppm for the CH_2SiMe_3 group in **8**, and −7.7 ppm for the ethyl group in **10**). In contrast, the ^{1}H NMR spectrum of cobalt benzyl-derived **7** contained many (>15) signals from 82 to −28 ppm that were not readily assigned to specific moieties in the complex.

Scheme 2. Carbonylation of 1–6 to form interconverting mixtures of organocobalt(II) carbonyl (**a**), acyl (**b**), and acyl carbonyl (**c**) complexes. Species observed by IR spectroscopy are enclosed in boxes, and equilibrium arrows indicate favored and disfavored compounds. [Co] = κ^3-To^{M}Co.

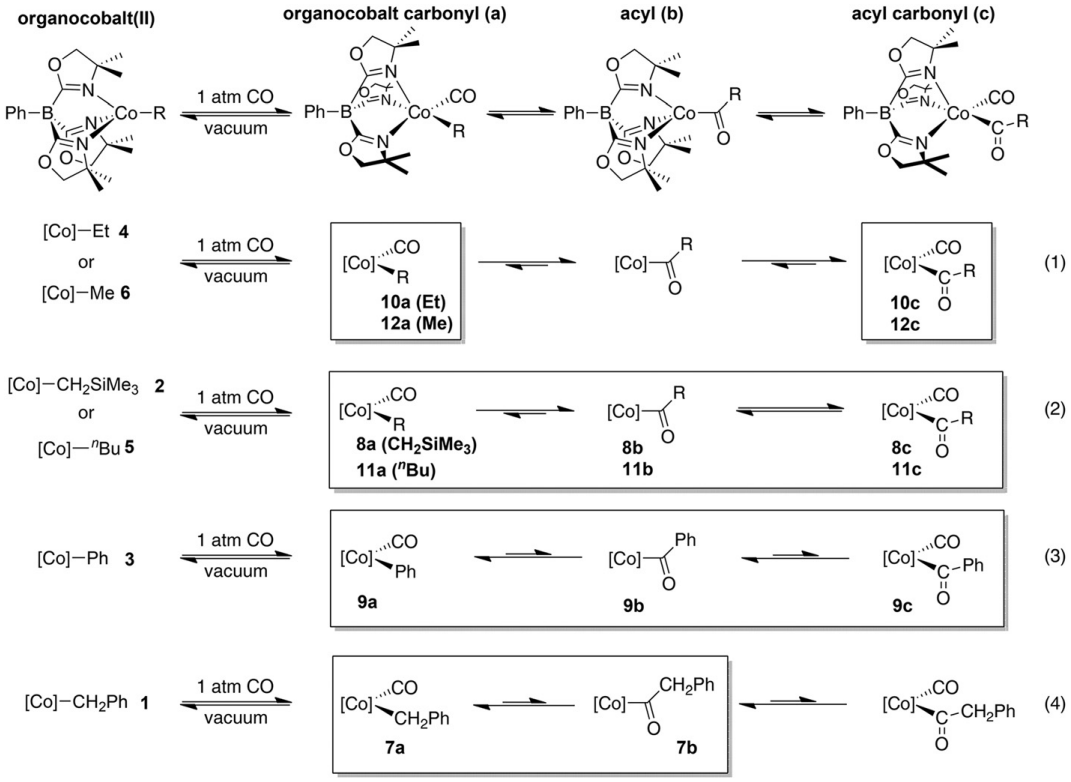

Benzene-d_6 solutions of **7–12** were also assayed by ^{11}B NMR spectroscopy in the presence of excess CO (1 atm). The ^{11}B NMR resonance for **8–12** appeared at ca. −4 ppm, which was distinct from the 87 to 116 ppm chemical shift range of organocobalt species **1–6**. Unexpectedly, the 88 ppm ^{11}B NMR chemical shift for the carbonylated benzyl derivative **7** was located in the region associated with four-coordinate cobalt alkyl/aryl or five-coordinate cobalt carboxylate compounds (*e.g.*, To^{M}CoO$_2$CCH$_2$Ph: 84 ppm).

The infrared spectra of **7–12**, recorded in THF solutions saturated with CO at atmospheric pressure in an ATR cell (compiled in Table 2), contained signals that were assigned to terminal carbonyl ($\nu_{C\equiv O}$, 1886 and 1973 to 1986 cm^{-1}), acyl ($\nu_{C(=O)R}$, 1650 to

1718 cm^{-1}), and the oxazoline regions (ν_{CN}: 1582 to 1594 cm^{-1}). First, the spectra of all of the compounds **7–12** contained a $\nu_{C\equiv O}$ band at ca. 1886 cm^{-1} (see Fig. S36– S41‡). This signal was the only $\nu_{C\equiv O}$ in benzyl **7**, the dominant $\nu_{C\equiv O}$ in phenyl-derived **9**, a significant signal in **8** and **11** from trimethylsilyl- and *n*-butylcobalt species, and the minor signal in ethyl **10** and methyl **12**. A higher energy $\nu_{C\equiv O}$ band, at approximately 1980 cm^{-1}, was observed for complexes **8–12** and appeared at the expense of the 1886 cm^{-1} signal. The 1886 and 1980 cm^{-1} peaks were assigned to organocobalt carbonyl $To^{M}Co(R)CO$ (**a**) and acylcobalt $To^{M}Co\{C(=O)R\}CO$ (**c**), respectively, on the basis of the expected increased π-back donation from organocobalt compared to acylcobalt species. This idea was supported by DFT calculations of $To^{M}Co(Me)CO$ (**12a**) and $To^{M}Co\{C(=O)Me\}CO$ (**12c**), which reproduced the trend in $\nu_{C\equiv O}$ with **12a** (2030 cm^{-1}) < **12c** (2117 cm^{-1}).

The acyl ($\nu_{C(=O)R}$) signals were less intense than $\nu_{C\equiv O}$ and appeared as one (R = CH_2SiMe_3 or Ph) or two signals (R = Et, ^{n}Bu, or Me) in the region from 1650 to 1690 cm^{-1}, but were absent for R = Bn (**7**). Instead, a band in the spectrum for **7** at 1717 cm^{-1} was assigned to terminal carbonyl-free acyl species (**b**) because the spectrum lacked the $\nu_{C\equiv O}$ band associated with **c** (see Table 2). These assignments were further supported by the IR spectra of **8**, **9**, and **11**, which contained IR signals associated with all three species **a**, **b**, and **c**.

Table 2. Infrared spectroscopic data of **7–12** collected in CO-saturated THF using a ZnSe crystal in ATR mode. Not detected (N.D.) in the IR spectrum

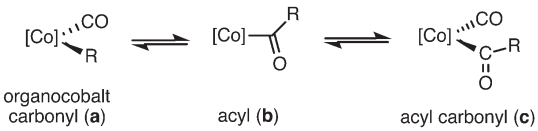

organocobalt carbonyl (**a**) acyl (**b**) acyl carbonyl (**c**)

R	$\nu_{C=O}$ (cm^{-1}) (**7a–12a**)	$\nu_{(C=O)R}$ (cm^{-1}) (**7b–12b**)	$\nu_{C=O}$ and $\nu_{C=O}$ (cm^{-1}) (**7c–12c**)	
Bn (**7**)	1887	1716	n.d.	
CH_2SiMe_3 (**8**)	1887	1718	1973	1673
Ph (**9**)	1886	1715	1986	1686
Et (**10**)	1887	n.d.	1980	1667
				1650
^{n}Bu (**11**)	1887	1717	1979	1687
				1662
Me (**12**)	1887	n.d.	1984	1687
				1655

The region from 1630–1500 cm^{-1} is typically associated with ν_{CN} modes of the oxazoline. The IR spectra of compounds **7–12** all contained an intense band from 1590 to 1600 cm^{-1}, assigned to the coordinated oxazolines. In the spectrum of ethyl **10**, a lower energy shoulder accompanied the peak at 1591 cm^{-1}, whereas a higher energy shoulder at 1630 cm^{-1} was evident in the spectrum of methyl species **12**. The shoulder in **12** was previously assigned to a weakly-coordinated oxazoline group based on the Hessian calculation of a DFT-optimized square pyramidal structure of **12c-calc** (see below).[15] Two peaks were observed at 1597 and 1556 cm^{-1} for benzyl-derived **7** and at 1594 and 1556 cm^{-1} for phenyl derived **9**. In contrast, the only notable signal in the IR spectra of trimethylsilylmethyl **8** and butyl-derived **11** within that region appeared at 1590 cm^{-1}. Based on comparison of these patterns with those for the carbonyl, we assign the 1590 cm^{-1} band to ν_{CN} in terminal carbonyl-containing **a** and **c** structures, and the 1556 cm^{-1} band to ν_{CN} in $To^{M}CoC(=O)R$ species.

The orange carbonylated compounds **7–12** have distinct UV-Vis spectra from their blue or green starting materials. The dominating bands at 350 nm and 700 nm in the starting materials, discussed above, are absent in the carbonylated product. Instead **7–12** are characterized by weak signals from 700 to 500 nm (ε: 100–170 $M^{-1}cm^{-1}$) and a strong, tailing absorption from 200 to 500 nm. In addition, compounds **7–12** are low spin (μ_{eff} = 2.4–3.4(2)μ_B) as determined by the Evans method. The magnetic moments are higher than the spin-only μ_{eff} value (1.73μ_B) for low spin Co(II) (S = 1/2). Square pyramidal compounds, with long axial Co–N interactions, typically have magnetic moments in this range (2.1–2.9μ_B) that are higher than those expected for spin-only, low-spin, square planar Co(II) complexes.[27] Alternatively, contributions from the acyl species **7b–12b** could also result in higher-than-expected magnetic moments. This idea suggests that methyl (**12**) and ethyl (**10**) derivatives would have the lowest μ_{eff} values, because their IR spectra are dominated by the CO-coordinated species. Instead, experimental μ_{eff} values for **10** and **12** are in the middle of the series (2.7μ_B). Despite the spectroscopic similarities between cobalt methyl and ethyl derived acyl species, as seen below, the coordination geometries of even **10c** and **12c** are not equivalent.

A pentane solution of **10** cooled to −30 °C provides X-ray quality crystals, and a single crystal diffraction study reveals the five-coordinate, acyl carbonyl form $To^{M}Co\{C(=O)Et\}CO$ (**10c**) as a square pyramidal complex (τ_5 = 0.15; Fig. 6).28 Although the oxazolines are disposed *trans* to either CO, an acyl, or an open coordinate site, the Co1–N1 (2.037(3) Å), Co1–N2 (2.067(2) Å) and Co1–N3 (2.050(2) Å) distances are similar to each other and to the four-coordinate tris(oxazolinyl) borato organocobalt(II) compounds described above. Related $PhTt^{tBu}Co\{C(=O)R\}CO$ (R = Me,

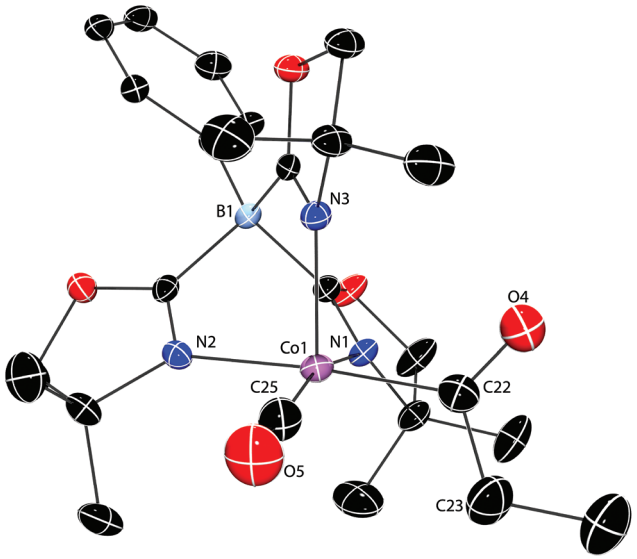

Figure 6. Thermal ellipsoid plot of To^{M}Co{C(=O)Et}CO (**10**) plotted at 35% probability. H atoms are omitted for clarity. Selected interatomic distances (Å) and angles (°): Co1–C22 1.973(4), Co1–C25 1.751(4), Co1–N1 2.037(3), Co1–N2 2.066(3), Co1–N3 2.050(2), C22–O4, 1.207(5), C25– O5 1.156(5), N1–Co1–C22 89.7(1), N2–Co1–C22 174.0(1), N3–Co1–C22 97.1(1), N1–Co1–N2 87.0(1), N1–Co1–N3 92.6(1), N2–Co1–N3 88.1(1), C22–Co1–C25 85.5(2).

Et, or Ph) are also square pyramidal, with similar Co–S distances for basal and apical groups.[19]

We have not been able to obtain X-ray quality crystals of any of the other species in the mixture of **10**, nor have acyl or carbonyl containing compounds of **7–9**, **11**, or **12** been isolated. Attempts to crystallize **12**, for example, provide either To^{M}CoMe (**6**) or To^{M}CoOAc (**18**, see below). The reversibility of the carbonylation of the organocobalt(II) alkyls posed challenges to the compounds' isolation. Thus, evaporation and exhaustive drying of To^{M}Co{C(=O)Me}CO provides **6** after 24 h under dynamic vacuum, whereas complexes **9–11** show only partial conversion back to **3–5** under these condition as assessed by ^{11}B NMR spectroscopy. Complex **8** is fully consumed upon evaporation, with To^{M}CoCH$_2$SiMe$_3$ as one of several other products that remain unidentified, as determined by ^{1}H and ^{11}B NMR spectroscopy.

Coupling of CO with To^{M}CoBn

An entirely unique outcome occurs upon exposure of **7** to vacuum. Unlike the evaporation of **8–12**, which produces the corresponding organocobalt compounds **2–6**, a mixture is obtained from **7** that gives two signals in the ^{11}B NMR spectrum at 86 and 87 ppm. The former signal may be from residual To^{M}CoBn(CO) in equilibrium with ToMCoC(=O)Bn (**7a/b**) or from To^{M}Co(CO) (**7e**, see below). The other signal, as well as a dominant peak in the ^{1}H NMR spectrum at −18 ppm, was attributed to an alkoxy ketone cobalt(II) species (**7d**, Scheme 3). The evidence for that structure is provided by X-ray diffraction studies of crystals grown from degassed solutions of To^{M}CoBn and CO (Fig. 7). In that compound, one To^{M}Co, two CO, and three benzyl groups combine to form To^{M}Co{*O*,*O*- κ$_2$-O–C(Bn)$_2$–C(=O)Bn}.

Scheme 3. Carbonylation of To^{M}CoBn (**1**) followed by removal of volatile materials provides **7d** as confirmed by X-ray crystallography and a species tentatively assigned as To^{M}CoCO (**7e**) as determined by IR spectroscopy.

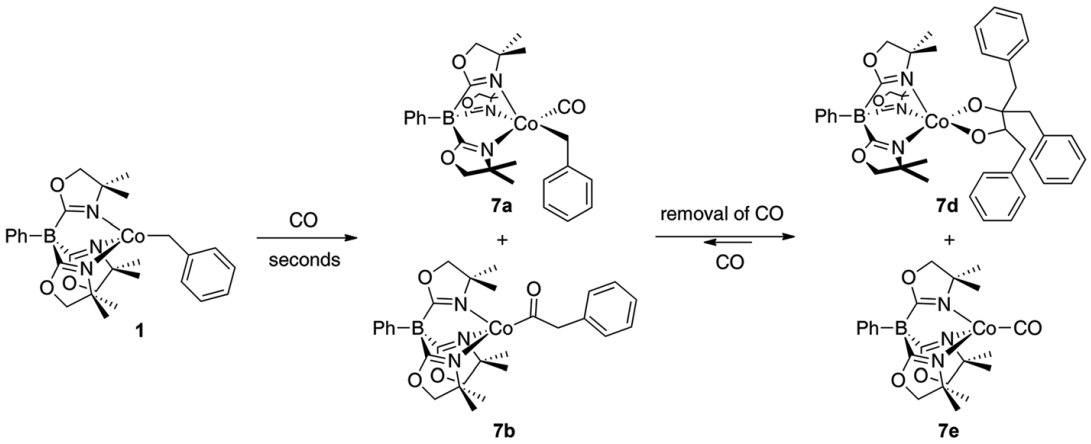

The coordination geometry of **7d** is distorted trigonal bipyramidal (τ_5 = 0.5). Two oxazolines (N1 and N2) and the alkoxide (O4) of the alkoxyketone are coordinated in the equatorial plane. The third oxazoline (N3) and the ketone oxygen (O5) are in axial sites

(N3–Co1–O5, 172.8(1)°). The cobalt–alkoxide distance (Co1–O4, 1.972(2) Å) is shorter than that of the cobalt–ketone (Co1–O5, 2.212(2) Å), while the carbon–oxygen distances vary as expected for a ketone (O5–C37, 1.231(4) Å) and alkoxide (O4–C22, 1.386(4) Å). The distance C22–C37, between ketone and alkoxide carbon atoms, is long (1.635(4) Å). The Co–N distances (Co1–N1 2.098(3), Co1–N2 2.086(3), Co1–N3 2.136(3) Å; Co–$N_{average}$ = 2.11 Å) are all longer than other structurally characterized Co(II) complexes supported by To^M (*e.g.*, Co–$N_{average}$ = 2.055 Å in **1** and 2.053 Å in To^MCoO_2CBn (13)). In contrast to the square pyramidal **10** whose apical Co1–N3 distance is similar to the equatorial cobalt–oxazoline distances, the axial Co1–N3 in **7d** is longer than the corresponding equatorial distances.

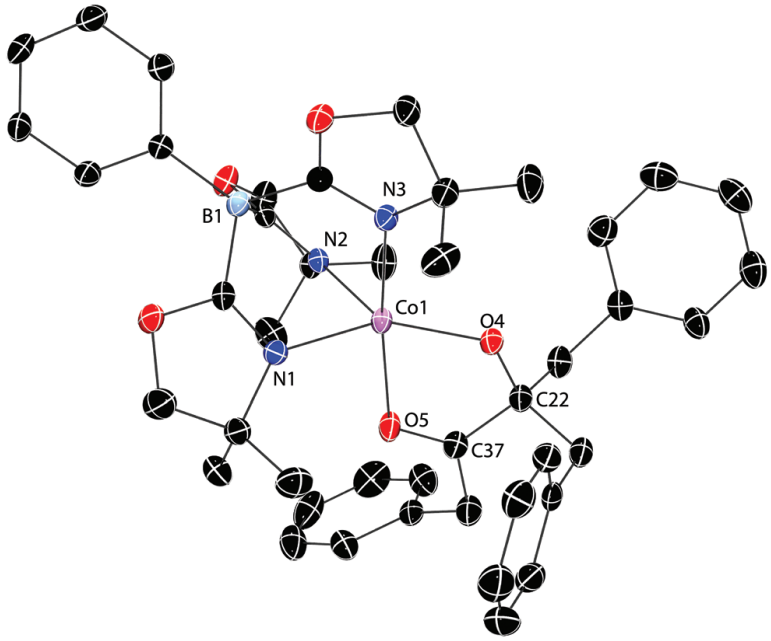

Figure 7. Thermal ellipsoid plot of **7d** at 35% probability. H atoms and a pentane molecule in the unit cell are omitted for clarity. Selected interatomic distances (Å) and angles (°): Co1–O4, 1.927(2); Co1–O5, 2.212(2); Co1–N1, 2.098(3); Co1–N2, 2.086(3); Co1–N3, 2.136(3); C22–O4, 1.386(4); C37–O5, 1.231(4); C22–C37, 1.635(4); N1–Co1–N2 88.8(1); N2–Co1–O4, 129.4(1); N1–Co1–O4, 141.4(1); N3–Co1–O5, 172.8(1); O4–Co1–O5, 77.52(9).

IR spectroscopy (KBr) of the crystalline solid obtained after evaporation of **7** contained a $\nu_{C\equiv O}$ band (1943 cm−1) and $\nu_{C(=O)R}$ band (1671 cm^{-1}). The $\nu_{C(=O)R}$ band is assigned to the alkoxy ketone species **7d** while the $\nu_{C\equiv O}$ band is tentatively assigned to a reduced $To^{M}CoCO$ (**7e**) species based upon its similar frequency to signals in $Tp^{Np}CoCO$ ($\nu_{C\equiv O}$ = 1950 cm^{-1}; Tp^{Np} = tris(3-neopentylpyrazolyl)borate),[29] $Tp^{iPr,Me}CoCO$ ($\nu_{C\equiv O}$ = 1946 cm^{-1}; $Tp^{iPr,Me}$ = tris(3-isopropyl-5methyl-pyrazolyl)borate),[30] and $Tp^{iPr2}CoCO$ ($\nu_{C\equiv O}$ ~ 1950 cm^{-1}).[11] In these Co(I) compounds, the $\nu_{C\equiv O}$ appears at lower energy than in the cobalt(II) acyl carbonyls (e.g., $Tp^{iPr2}Co\{C(=O)Et\}CO$, $\nu_{C\equiv O}$ = 1999 cm^{-1}). Unfortunately, X-ray quality crystals of $To^{M}CoCO$ were not obtained to support this assignment. The diagnostic ^{1}H NMR signal at −18 ppm assigned to the alkoxy ketone species **7d** disappeared upon addition of CO, and the remaining signals match those that have been assigned to **7a/b** suggesting that formation of **7d** is reversible.

Compound **7d** is remarkable, in that two molecules of carbon monoxide and three benzyl groups have been coupled into an α-alkoxyketone ligand. Compounds containing such ligands are typically synthesized by coordination of pre-formed α-hydroxyketones to metal centers.[31–33] For example, 3,4-hydroxy-pyridinone (3,4-HOPO) and $Tp^{Ph,Me}CoCl$ react under basic conditions to provide $Tp^{Ph,Me}Co$(3,4-HOPO). Unlike trigonal bipyramidal **7d**, $Tp^{Ph,Me}Co$(3,4-HOPO) forms a square pyramidal solid state structure.[31]

Alternatively, the *α*-hydroxyketone core of the ligand is related to benzoin condensation products, although the tertiary alkoxide (which containing *α*-hydrogen), is unlikely to be synthesized from a benzoin-like condensation of phenylacetaldehyde and dibenzylketone. Acyl anions, however, may be generated by reaction of alkyllithium and CO in the presence of electrophiles, such as ketones, to form α-hydroxyketones at low

temperature (−100 to −135 °C).[34] Acylzirconium reagents, formed from hydrozirconation followed by carbonylation, also react with aldehydes to give α-hydroxyketones.[35] In contrasting chemistry, acylzirconium species are proposed to react as electrophiles with $Cp^*_2ZrH_2$ via hydrozirconation to give [Zr]–CH2– O–[Zr].[36] A possible pathway to generate **7d** involves the combination of a cobalt acyl and a ketone, which is suggested based on these examples with early metals (Scheme 4).

Scheme 4. Proposed formation of **7d** and **7e** by reaction of To^MCoBn (**1**) and CO.

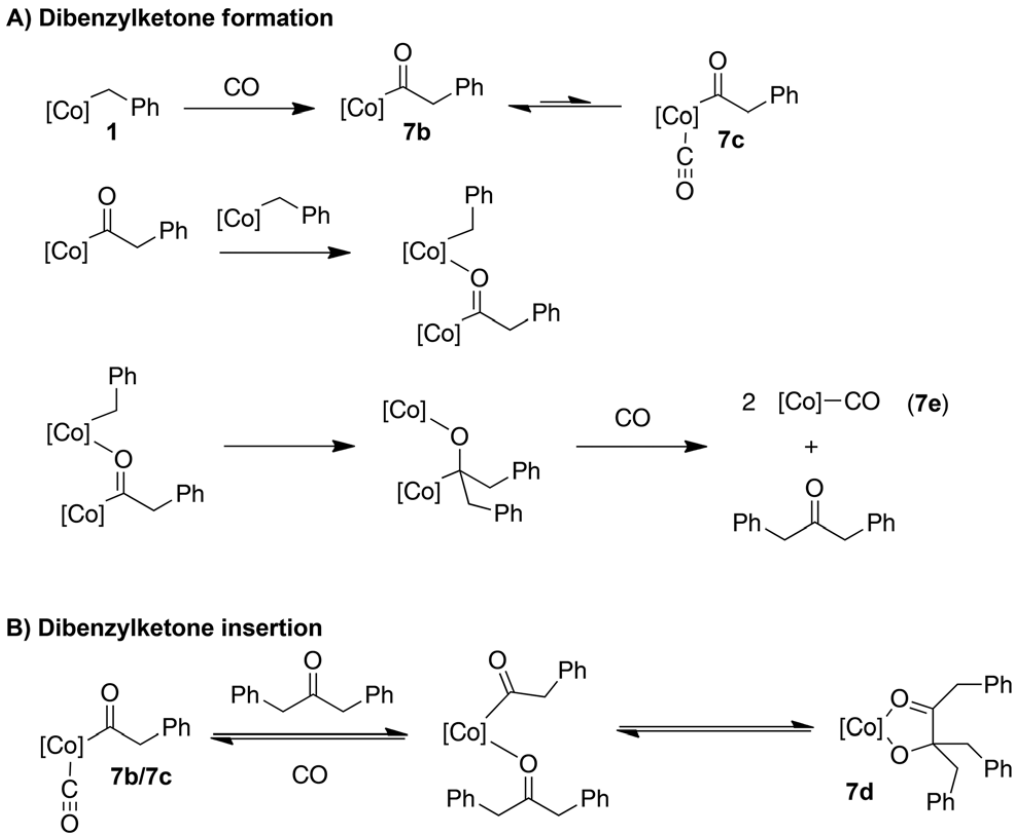

The first step of the multistep process would provide dibenzyl ketone, via combination of the cobalt(II) acyl **7b** with cobalt(II) benzyl **1** to give [Co]–O–$C(Bn)_2$–[Co] in analogy to the reaction of $Cp^*_2Zr\{C(=O)H\}H$ and $Cp^*_2ZrH_2$. Extrusion of dibenzylketone would

produce two equivalents of reduced To^{M}CoCO species. Then, species **7d** could form by insertion of dibenzylketone into the cobalt–carbon bond of the cobalt acyl species (**7b**). This reaction appears to be at least partly reversed upon addition of CO, suggesting that the process requires an additional ligand to displace dibenzylketone from the coordination sphere of cobalt. Alternatively, removal of CO and crystallization provides **7d**. That the *α*-alkoxyketone product is only observed in reactions of benzyl-based **1** (and not **2–6**) suggested the possibility of cobalt–carbon bond homolysis and trapping of To^{M}Co and benzyl radical with CO. However, no evidence of benzyl radical elimination (*e.g.*, bibenzyl) could be obtained in solutions of **1**, and bibenzyl was not detected in reaction mixtures that produce **7d**.

Oxygenation Of To^{M}Co{C(=O)R}Co And Carboxylation Of To^{M}CoR

Complexes **7–12** rapidly react with O_2 to form the corresponding carboxylate complexes To^{M}CoO$_2$CBn (**13**), To^{M}CoO$_2$CCH$_2$SiMe$_3$ (**14**), To^{M}CoO$_2$CPh (**15**), To^{M}CoO$_2$CEt (**16**), To^{M}CoO$_2$CnBu (**17**), and To^{M}CoO$_2$CMe (**18**) (eqn (5)).

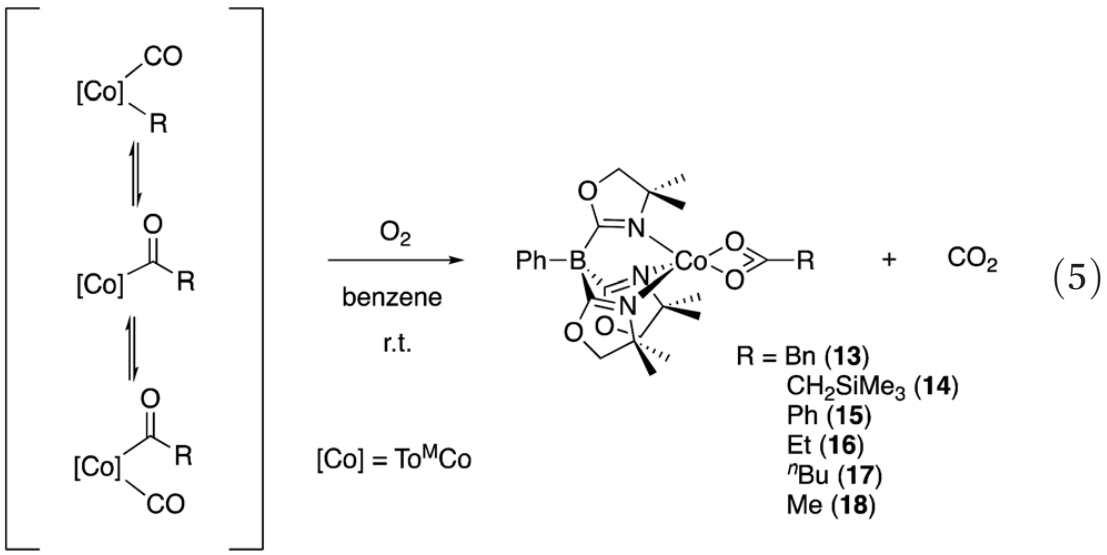

(5)

An immediate color change occurs upon addition of O_2 to the orange mixtures of **7a/b/c**–**12a/b/c** to provide purple solutions, accompanied by dramatic changes in the ^{1}H and ^{11}B NMR spectra. The ^{1}H NMR spectra of the products **14–18** were characteristic, with an unusual upfield chemical shift of ca. −45 ppm (18 H) assigned to the methyl from the oxazoline, as well as straightforward assignment of methylene (6 H) groups. The ^{1}H NMR spectrum of benzyl-derived **13** also revealed an intense signal at −40.8 ppm, but the methylene signal was not readily assigned, and the spectrum contained a large number of peaks. For comparison, the oxazoline methyl signals in the organocobalt starting materials appear at *ca.* −12 ppm (Table 1). The ^{11}B NMR spectra of **13–18** displayed a single signal in the region from 86 to 112 ppm, which were also distinct from the spectra measured for the exchanging carbonylated species 7–12 at *ca*. −4 ppm.

The NMR assignments of $To^{M}CoO_2CR$ are supported by their independent generation from reaction of $To^{M}CoCl$ and MO_2CR (M = Na or K; R = Bn, Ph, Et, Me). The ^{1}H and ^{11}B NMR spectra, UV-Vis spectra (as THF solutions), and IR spectra (as KBr pellets) of crude samples of **13**, **15**, **16**, and **18** matched the spectra obtained from the route of eqn (5) *via* sequential carbonylation and oxygenation. The cobalt carboxylate products are not easily isolated from this route, although X-ray crystals of **13** were obtained (see below). $TlTo^{M}$ and $CoOAc_2$ most conveniently provide $To^{M}CoOAc$ (**18**).[16] Alternatively, the reactions of **2–6** and CO_2 provide carboxylates **14–18**. Again, the ^{1}H and ^{11}B NMR spectra, UV-Vis spectra, and IR spectra matched the spectra of materials obtained from reactions of **2–6** with CO and then O_2. Strangely, the reaction of benzylcobalt **1** and CO_2 affords an unidentified species whose ^{11}B NMR signal of 108 ppm does not match the chemical shift of isolated **13** at 86 ppm.

Notably, direct insertion of CO_2 into the cobalt–carbon bond requires longer reaction times, which vary depending on the organocobalt species. Compound **3** reacts with CO_2 to form To^MCoO_2CPh (**15**) over 3 days, whereas compounds **2**, and **4–6** react with carbon dioxide over two weeks.

The carboxylate assignments of **13** and **15–18** are supported by X-ray diffraction studies of crystals grown from saturated pentane solutions at −40 °C (Fig. 8 and 9 and ESI‡). The crystals of **13** were obtained from reaction of To^MCoCl with KO_2Bn, **16–18** were isolated from reactions of To^MCoR (R = Et, ^{n}Bu, and Me) with CO followed by O_2, and **15** was prepared by reaction of To^MCoPh with CO_2. All five compounds are five coordinate and form distorted square pyramidal structures, in which one oxazoline donor is located in the apical site and the bidentante carboxylate is located in the equatorial plane. Compound **13** crystallizes with two independent molecules in the unit cell, both of which adopt distorted square pyramidal geometry (τ_5 = 0.08 and 0.34, Fig. 8).[28] Two crystallizations of **18** afford different $P\bar{1}$ unit cells, although both molecules are distorted square pyramidal (τ_5 = 0.35 and 0.03). Compound **16** crystallizes with two, similarly distorted square pyramidal molecules in the unit cell (Fig. 9, τ_5 = 0.43 and 0.33).
In general, the apical Co–N distance is shorter than the equatorial Co–N distances. An extreme example of this appears in one of the two co-crystallized molecules of the ethyl derivative **16** (τ_5 = 0.33), in which the apical Co1–N3 distance (1.837(4) Å) is considerably shorter than equatorial Co1–N1 (2.138(4) Å) and Co1–N2 (2.200(5) Å). The cobalt–oxygen interatomic distances associated with the carboxylate moiety are inequivalent in all of these structures. In the same molecule of **16**, for example, the difference between Co1–O4 (1.993(4) Å) and Co1–O5 (2.410(5) Å) is 0.42 Å. In

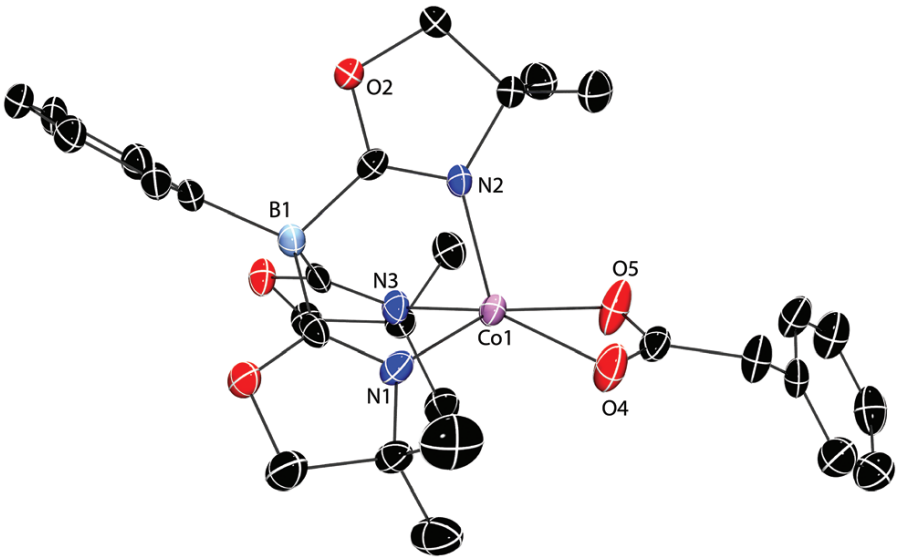

Figure 8. Thermal ellipsoid plot of To^{M}CoO$_2$CBn (**13**) at 50% probability. A second, crystallographically-independent molecule of **13** and H atoms are omitted for clarity. Selected interatomic distances (Å) and angles (°): Co1–O4, 2.040(2); Co1–O5, 2.214(2); Co1–N1, 2.067(3); Co1–N2, 2.023(3); Co1–N3, 2.059(3); N1–Co1–N2, 92.2(1); N1–Co1–N3, 88.6(1); N2–Co1–N3, 89.9(1); N1–Co1–O5 155.4(1); N2–Co1–O4, 118.2(1); N3–Co1–O4 150.6(1); N3–Co1–O5, 102.9(1).

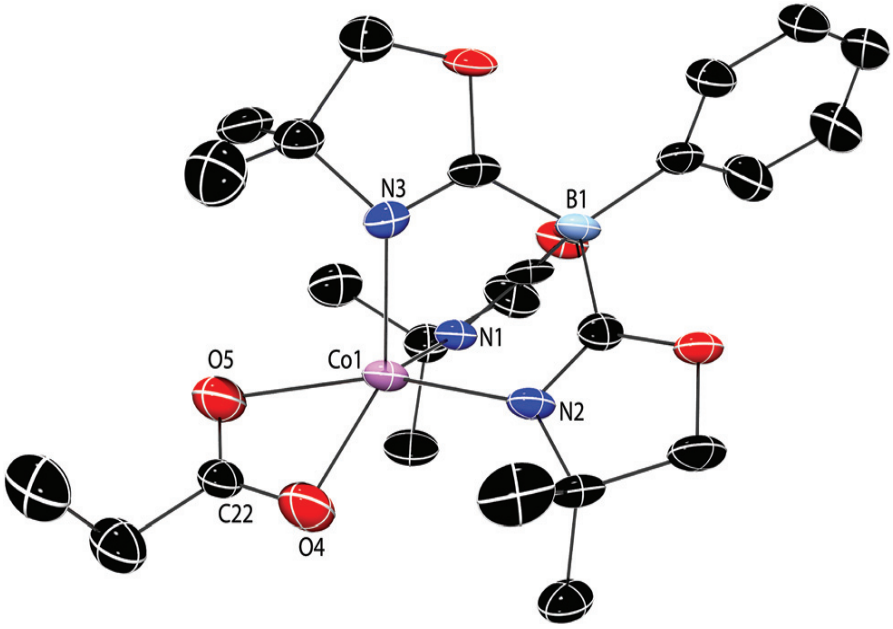

Figure 9. Thermal ellipsoid diagram illustrating one of two molecules of To^{M}CoO$_2$CEt (**16**) at 50% probability. Hydrogen atoms are omitted for clarity. Selected interatomic distances (Å) and angles (°): Co1–O4, 1.993(4); Co1–O5, 2.410(5); Co1–N1, 2.138(4); Co1–N2, 2.200(5); Co1–N3, 1.837(4); N1–Co1–N2, 85.0(2); N1–Co1–N3, 92.3(2); N2–Co1–N3, 90.6(2); N1–Co1–O4, 140.9(2); N2–Co1–O5, 160.5(2).

addition, the carbon–oxygen distances in the carboxylate ligand are unequal, with C22–O4 (1.325(8) Å) much longer than C22–O5 (1.176(7) Å). These distances and differences in distances, however, are extreme in this example, whereas the difference in cobalt–oxygen distances (Co2–O9, 2.184(6) and Co2–O10, 2.005(5) Å) in the other molecule of **16** is much smaller (0.18 Å). The latter set of cobalt–oxygen distances is much more representative of the series. For example, in the two benzylcarboxylate molecules in the unit cell of **13**, the distances are Co1–O4 (2.040(3) Å) and Co1–O5 (2.214(3) Å) (Δ_{Co-O} = 0.17 Å), and Co2–O9 (2.026(3) Å) and Co2–O10 (2.214(3) Å) (Δ_{Co-O} = 0.19 Å).

As noted in the Introduction, the oxidative transformation of a metal acyl into carboxylate, either under abiotic conditions or in acetate biosynthesis, often involves reductive elimination, followed by oxidation of the metal center rather than oxygenation. Unlike the oxidative carbonylation systems that contain two *cis*-disposed ligands that can undergo reductive elimination, **7–12** do not contain hydroxide, alkoxide, or halide ligands that could reductively eliminate with the acyl group. We envisioned a possible route to reductive elimination of carboxylate through heterolytic cleavage of H–OR (R = H, alkyl, aryl) across an oxazoline–cobalt bond (Scheme 5). A related addition of HCl to To^{M}CoCl

Scheme 5. Possible pathways for oxidative conversion to cobalt carboxylate via (A) protonation, elimination, and oxidation or (B) oxygenation via an acylperoxy intermediate.

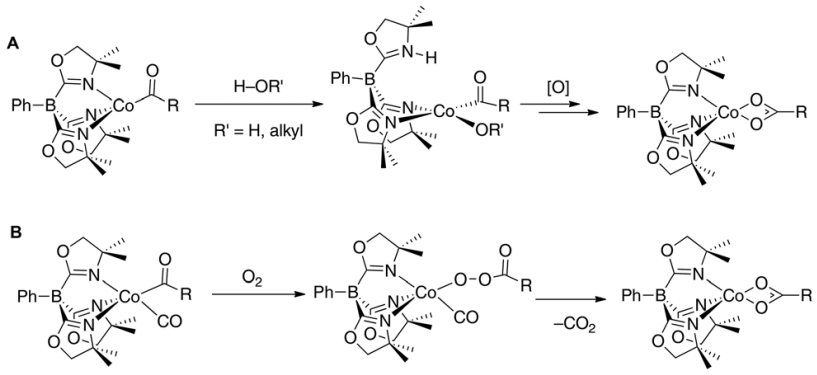

can provide $\{HTo^M\}CoCl_2$, which contains a zwitterionic HTo^M ligand that coordinates to cobalt in a bidentate fashion, with the third oxazoline donor protonated at nitrogen.

This idea was tested with two experiments. First, compound **12** persists in the presence of H_2O. The ^1H NMR spectrum of mixtures containing **12** and over 10 equiv. of

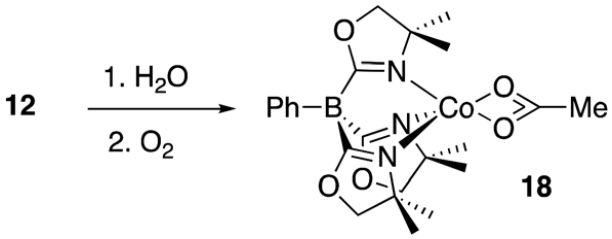

(6)

H_2O revealed only signals corresponding to starting materials after 30 min. This experiment did not provide evidence for protonation of an oxazoline; however, reaction of this mixture and O_2 provides compound **18** within seconds (eqn (6)).

In a second experiment, ^{13}C-labeled **12**, generated by combination of **6** and ^{13}CO, and O_2 reacted to give two new signals in the $^{13}C\{^1H\}$ NMR spectrum at 124 and 82 ppm. The former signal was assigned to $^{13}CO_2$,[37] and the latter to $To^MCoO_2{}^{13}CMe$ (**18***). The formation of CO_2 is unlikely to accompany either hydrolysis or reduction steps associated with oxidative carbonylation, and these results suggest that the cobalt acyl reacts with O_2 via oxygenation. In addition, the detection of carbon dioxide as a product of oxidation suggests that the acyl carbonyl species **12c** reacts with O_2 to provide oxygen atoms for both CO and C(=O)R ligand oxygenation. This process could involve insertion of O_2 into the [Co]–C(=O) R to give an acylperoxy cobalt [Co]–OO–C(=O)R, which was proposed for a related oxygenation of a cobalt acyl.[17]

Conclusion

These studies of organocobalt(II) complexes **1–6** reveal similar spectroscopic features with variation of the hydrocarbyl ligand. Despite the distinct reaction chemistry of compound **1**, the solution-phase spectroscopic data suggests a mono-hapto benzyl coordination and similar four-coordinate structure to that found for aliphatic methyl, ethyl, and butyl complexes. While there are differences in speciation of exchanging mixtures of organocobalt carbonyl, acylcobalt, and acylcobalt carbonyl in the presence of CO and more significant changes in reactivity upon removal of CO across the series, oxygenation with O_2 consistently afford carboxylates.

First, the series of organocobalt(II) complexes **1–6** share similar features in their ^{1}H and ^{11}B NMR, EPR, and UV-Vis spectra that suggest similar electronic structures. Particularly, intense absorptions at *ca*. 350 and 700 nm in the UV-Vis spectra are a general feature of tetrahedral alkyl and aryl $To^{M}Co(II)$ complexes that distinguishes them from other four- coordinate compounds lacking a cobalt–carbon bond, including $To^{M}CoOAc$, $To^{M}CoO^{t}Bu$ or $To^{M}CoCl$.

Reactions of **1–6** and CO afford mixtures containing organocobalt carbonyl, cobalt acyl, and/or cobalt acyl carbonyl species that interconvert. The speciation of the mixture varies, depending upon the R group with only the benzyl **7** favoring organocobalt carbonyl and cobalt acyl, whereas ethyl **10** and methyl **12** favor cobalt acyl and its carbonyl adduct. The spontaneous formation of α-alkoxyketone ligand is postulated to involve coupling of dibenzylketone and cobalt acyl. We are currently pursuing related reactions of acyl species and ketones as a promising synthetic route to a range of substituted derivatives, as well as providing evidence that supports or rules out the

proposed pathway. We also note that the carboxylate products of oxidation could be exchanged for organometallic ligands via transmetalation reactions; we are also investigating these reactions toward catalytic oxygenative hydrocarbon functionalizations.

Experimental

Materials And Methods

All reactions were performed using standard Schlenk techniques under an atmosphere of dry argon. Benzene and diethyl ether were dried and deoxygenated using an IT PureSolv system. Benzene-d_6 was degassed with freeze–pump–thaw cycles, heated to reflux over a Na/K alloy, and then vacuum transferred. $To^{M}CoCl$, $To^{M}CoMe$ (**6**), $To^{M}Co\{C(=O)\ Me\}CO$ (**12**), and $To^{M}CoOAc$ (**18**) were synthesized or generated following the reported procedures.[15,16] ^{1}H and ^{11}B NMR spectra were collected on a Bruker Avance III 600 spectrometer. ^{11}B NMR spectra were referenced to an external sample of $BF_3{\cdot}Et_2O$. Infrared spectra were measured on a Bruker Vertex 80 FTIR spectrometer. EPR spectra were obtained on an X-band Elexsys 580 FT-EPR spectrometer in continuous wave mode. UV-Vis spectra were recorded on an Agilent 8453 UV-Vis spectrophotometer. Magnetic moments were measured by Evans Method at room temperature. Elemental analyses were performed using a PerkinElmer 2400 Series II CHN/S. Single crystal X-ray diffraction data was collected on an APEX II diffractometer.

Synthetic Procedures

To^{M}CoBn (1). To^{M}CoCl (0.147 g, 0.308 mmol) and KBn (0.067 g, 0.515 mmol) were stirred in tetrahydrofuran (10 mL) for 2 h. The green solution was evaporated to dryness under vacuum, the residue was extracted with benzene (10 mL), and the extracts were dried *in vacuo* to afford To^{M}CoBn as a green solid (0.129 g, 0.242 mmol, 79%). ^{1}H NMR (benzene-d_6, 600 MHz): δ 34.47 (s, 2 H), 16.33 (s, 6 H, CNCMe$_2$*CH*$_2$O), 14.90 (s, 2 H), 10.96 (s, 2 H), 9.14 (s, 1 H), −12.46 (s, 18 H, CNC*Me*$_2$CH$_2$O), −77.45 (s, 1 H), −89.01 (s, 1 H). ^{11}B NMR (benzene-d_6, 128 MHz): δ 100.4. IR (KBr, cm^{-1}): ν 3072 (w), 3046 (w), 3012 (w), 2966 (m), 2926 (m), 2897 (m), 2869 (m), 1701 (w), 1588 (s, ν_{CN}), 1482 (m), 1459 (m), 1384 (m), 1366 (m), 1351 (m), 1271 (m), 1194 (m) 1160 (m), 1027 (m), 1008 (m), 963 (m). UV-vis (Et$_2$O): λ_{max} = 339 (ε 3205 M^{-1}cm^{-1}), 439 (ε 1964 M^{-1}cm^{-1}) 589 (ε 332 M^{-1}cm^{-1}), 628 (ε 365 M^{-1}cm^{-1}), 704 (ε 1444 M^{-1}cm^{-1}). μ_{eff}(benzene-d_6) = 4.2(7)μ_B. Anal. calcd for $C_{28}H_{36}BCoN_3O_3$: C, 63.17; H, 6.82; N, 7.89. Found: C, 62.71; H, 7.10; N, 8.19. Mp 151–153 °C, dec.

To^{M}CoCH$_2$SiMe$_3$ (2). LiCH$_2$SiMe$_3$ (0.041 g, 0.44 mmol) dissolved in pentane (1 mL) was added dropwise to a solution of To^{M}CoCl (0.150 g, 0.31 mmol) in tetrahydrofuran (3 mL) cooled to −78 °C. The purple reaction mixture was stirred for 15 min at −78 °C, warmed to room temperature, and then stirred for an additional 45 min. The solvent was evaporated, and the residue was extracted with benzene. Evaporation of benzene afforded To^{M}CoCH$_2$SiMe$_3$ as a blue solid (0.161 g, 0.30 mmol, 97% yield). X-ray quality crystals were obtained from a saturated pentane solution at −40 °C. ^{1}H NMR (benzene-d_6, 600 MHz): δ 15.73 (s, 6 H, CNCMe$_2$*CH*$_2$O), 12.72 (s, 2 H, C$_6$H$_5$), 10.08 (s, 2 H, C$_6$H$_5$), 8.54 and 8.48 (s, 10 H, CH$_2$Si*Me*$_3$, *p*-C$_6$H$_5$), −9.58 (s, 18 H, CNC*Me*$_2$CH$_2$O).

^{11}B NMR (benzene-d6, 128 MHz): δ 86.6. IR (KBr, cm^{-1}): ν 2966 (m), 2892 (m), 1586 (s, ν_{CN}), 1490 (m), 1462 (m), 1434 (m), 1386 (m), 1366 (m), 1275 (m), 1251 (m) 1195 (m), 1159 (m), 1020 (m), 1001 (m), 966 (m). UV-vis (Et2O): λ_{max} = 355 (ε 2228 M^{-1} cm^{-1}), 591 (ε 374 M^{-1} cm^{-1}), 628 (ε 448 M^{-1} cm^{-1}), 703 (ε 1495 M^{-1} cm^{-1}). μ_{eff}(benzene-d_6) = 4.9(3)μ_B. Anal. calcd for $C_{25}H_{40}BCoN_3O_3Si$: C, 56.82; H, 7.63; N, 7.95. Found: C, 56.26; H, 7.72; N, 7.54. Mp 234–235 °C, dec.

To^{M}CoPh (3). Phenyllithium (1.8 M in dibutyl ether, 0.250 mL, 0.45 mmol) was added dropwise to a solution of To^{M}CoCl (0.151 g, 0.317 mmol) in THF (3 mL) cooled to −78 °C. The dark blue reaction mixture was stirred for 15 min at −78 °C, warmed to room temperature, and stirred for an additional 45 min. The solvent was evaporated, and the residue was extracted with benzene. Evaporation of benzene provided To^{M}CoPh as a blue solid (0.119 g, 0.230 mmol, 73% yield). X-ray quality crystals were obtained from pentane solutions cooled to −40 °C. ^{1}H NMR (benzene-d_6, 600 MHz): δ 73.95 (s, 1 H), 16.73 (s, 6 H, CNCMe$_2$*CH*$_2$O), 15.74 (s, 2 H, C$_6$H$_5$), 11.30 (s, 2 H, C$_6$H$_5$), 10.61 (s, 1 H, *p*-C$_6$H$_5$), 9.42 (s, 1 H, *p*-C$_6$H$_5$), −13.68 (s, 18 H, CNC*Me*$_2$CH$_2$O). ^{11}B NMR (benzene-d_6, 128 MHz): δ 107.7. IR (KBr, cm^{-1}): ν 3042 (m), 2967 (m), 2927 (m), 2890 (m), 2869 (m), 1582 (s, ν_{CN}), 1494 (m), 1461 (m), 1433 (m), 1388 (m), 1368 (m), 1352 (m), 1274 (m), 1196 (m), 1159 (m), 964 (m), 951 (m). UV-vis (Et$_2$O): λ_{max} = 330 (ε 1245 M^{-1} cm^{-1}), 587 (ε 176 M^{-1} cm^{-1}), 625 (ε 252 M^{-1} cm^{-1}), 708 (ε 1333 M^{-1} cm^{-1}). μ_{eff}(benzene-d_6) = 4.0(1)μ_B. Anal. calcd for $C_{27}H_{34}BCoN_3O_3$: C, 62.57; H, 6.61; N, 8.11. Found: C, 63.05; H, 6.81; N, 7.75. Mp 194–197 °C, dec.

ToMCoEt (4). Ethyllithium (0.5 M in a mixture of benzene and cyclohexane, 0.880 mL, 0.44 mmol) was added dropwise to a solution of To^{M}CoCl (0.150 g, 0.31

mmol) in THF (3 mL) cooled to −78 °C. The purple reaction mixture was stirred for 15 min at −78 °C, warmed to room temperature, and stirred for an additional 45 min. Evaporation of volatiles, extraction of the solid residue with benzene, and evaporation of the benzene afforded $To^{M}CoEt$ as a green solid (0.114 g, 0.24 mmol, 77% yield). X-ray quality crystals were obtained from pentane at −40 °C. ^{1}H NMR (benzene-d_6, 600 MHz): δ 15.95 (s, 2 H, C_6H_5), 14.85 (s, 6 H, $CNCMe_2CH_2O$), 11.33 (s, 2 H, C6H5), 9.42 (s, 1 H, *p*-C_6H_5), −14.45 (s, 18 H, $CNCMe_2CH_2O$), −31.31 (s, 1 H, CH_2CH_3). 11B NMR (benzene-d_6, 128 MHz): δ 116.7. IR (KBr, cm^{-1}): ν 3078 (w), 3045 (w), 2967 (m), 2929 (m), 2895 (m), 2870 (m), 2837 (m), 1592 (s, νCN), 1495 (m), 1461 (m), 1434 (m), 1385 (m), 1366 (m), 1351 (m), 1268 (m), 1193 (m), 1159 (m), 1101 (w), 1017 (w), 961 (m). UV-vis (Et_2O): λ_{max} = 382 (ε 1935 M^{-1} cm^{-1}), 579 (ε 268 M^{-1} cm^{-1}), 615 (ε 286 M^{-1} cm^{-1}), 705 (ε 1255 M^{-1} cm^{-1}). μ_{eff}(benzene-d_6) = 4.1(6)μ_B. Anal. calcd for $C_{23}H_{34}BCoN_3O_3$: C, 58.74; H, 7.29; N, 8.94. Found: C, 58.83; H, 7.07; N, 8.64. Mp 179–181 °C, dec.

$To^{M}Co^{n}Bu$ (5). $To^{M}CoCl$ (0.155 g, 0.33 mmol) was dissolved in THF (3 mL), cooled to −78 °C, and *n*-butyllithium (2.5 M in hexanes, 0.19 mL, 0.48 mmol) was added in a dropwise fashion. The dark purple reaction mixture was stirred at −78 °C for 15 min, warmed to room temperature, and stirred for an additional 45 min. THF was removed *in vacuo*, the residue was extracted with benzene, and benzene was evaporated to afford $To^{M}Co^{n}Bu$ as a dark green solid (0.100 g, 0.20 mmol, 61% yield). X-ray quality crystals were obtained from pentane cooled to −40 °C. ^{1}H NMR (benzene-d_6, 600 MHz): δ 15.91 (s, 2 H, C_6H_5), 14.88 (s, 6 H, $CNCMe_2CH_2O$), 14.21 (s, 2 H, $(CH_2)_3CH_3$), 11.34 (s, 2 H, C_6H_5), 9.47 (s, 1 H, *p*-C_6H_5), −2.67 (s, 3 H, $(CH_2)_3CH_3$), −14.31 (s, 18 H,

CNC*Me*$_2$CH$_2$O). ^{11}B NMR (benzene-d_6, 128 MHz): δ 115.0. IR (KBr, cm^{-1}): ν 3083 (w), 3047 (w), 2966 (m), 2928 (m), 2890 (m), 2871 (m), 1587 (s, ν_{CN}), 1495 (m), 1462 (m), 1434 (m), 1386 (m), 1368 (m), 1351 (m), 1271 (m), 1198 (m), 1159 (m), 1104 (w), 1025 (m), 995 (m). UV-vis (Et$_2$O): λ_{max} = 382 (ε 1679 M^{-1} cm^{-1}), 576 (ε 406 M^{-1} cm^{-1}), 613 (ε 422 M^{-1} cm^{-1}), 705 (ε 1291 M^{-1} cm^{-1}). μ_{eff}(benzene-d_6) = 4.5(2)μ_B. Anal. calcd for $C_{25}H_{38}BCoN_3O_3$: C, 60.26; H, 7.69; N, 8.43. Found: C, 60.25; H, 7.37; N, 8.32. Mp 244–246 °C, dec.

To^{M}CoO$_2$CBn (13). Compound **7** was generated from To^{M}CoBn (0.038 g, 0.072 mmol) and CO. The CO was removed under reduced pressure, and O_2 (1 atm) was added to give a purple solution. The volatiles were evaporated in vacuo yielding To^{M}CoO$_2$CBn as a purple solid (0.038 g, 0.066 mmol, 92% yield). ^{1}H NMR (benzene-d_6, 600 MHz): δ 49.61, 32.02, 28.01, 23.86, 23.64, 17.32, 13.17, 10.93, 9.68, −40.84. ^{11}B NMR (benzene-d_6, 128 MHz): δ 86.4. IR (KBr, cm^{-1}): ν 3080 (w), 3040 (w), 2964 (m), 2928 (m), 2891 (m), 1667 (m), 1591 (s, ν_{CN}), 1517 (m), 1495 (m), 1462 (m), 1402 (m), 1367 (m), 1351 (m), 1275 (m), 1196 (m), 1160 (m), 1126 (m), 1095 (m), 1029 (m), 961 (m). UV-vis (THF): λ_{max} = 663 (ε: 200 M^{-1} cm^{-1}). μ_{eff}(benzene-d_6) = 4.7(2)μ_B. Anal. calcd for $C_{29}H_{36}BCoN_3O_5$: C, 60.43; H, 6.30; N, 7.29. Found: C, 60.09; H, 6.30; N, 6.89. Mp 230–232 °C.

To^{M}CoO$_2$CCH$_2$SiMe$_3$ (14). To^{M}CoCH$_2$SiMe$_3$ (0.046 g, 0.092 mmol) was dissolved in toluene (2 mL), the headspace was removed *in vacuo*, and then CO (1 atm) was introduced. An immediate color change from green to orange was observed. Evacuation of CO followed by introduction of O_2 (1 atm) resulted in a color change from orange to purple. Toluene was evaporated *in vacuo* to afford To^{M}CoO$_2$CCH$_2$SiMe$_3$ as a

purple solid (0.043 g, 0.075 mmol, 82% yield). ^{1}H NMR (benzene-d_6, 600 MHz): δ 208.77 (s, 2 H, $O_2CCH_2SiMe_3$), 37.30 (s, 2 H, C_6H_5), 19.31 (s, 2 H, C_6H_5), 16.20 (s, 1 H, *p*-C_6H_5), 15.92 (s, 9 H, $O_2CCH_2SiMe_3$), 11.34 (s, 6 H, $CNCMe_2CH_2O$), −49.53 (s, 18 H, $CNCMe_2CH_2O$). ^{11}B NMR (benzene-d_6, 128 MHz): δ 113.2. IR (KBr, cm^{-1}): *v* 3080 (w), 3049 (w), 2965 (m), 2929 (m), 2896 (m), 2872 (m), 1595 (s, ν_{CN}), 1520, 1464 (m), 1434 (m), 1368 (m), 1354 (m), 1273 (m), 1251 (m), 1196 (m), 1162 (m), 1104 (m), 1024 (m), 958 (m). UV-vis (THF): λ_{max} = 588 (ε: 98 M^{-1} cm^{-1}). μ_{eff}(benzene-d_6) = 4.7(2)μ_B. Anal. calcd for $C_{26}H_{40}BCoN_3O_5Si$: C, 54.55; H, 7.04; N, 7.34. Found: C, 54.41; H, 7.18; N, 7.26. Mp 186–188 °C.

To^{M}CoO$_2$CPh (15). To^{M}CoPh (0.020 g, 0.039 mmol) was dissolved in toluene (2 mL), the headspace was removed *in vacuo*, and then CO (1 atm) was introduced. An immediate color change from green to orange was observed. Evacuation of CO followed by introduction of O_2 (1 atm) resulted in a color change from orange to purple. Toluene was evaporated *in vacuo* to afford To^{M}CoO$_2$CPh as a purple solid (0.019 g, 0.034 mmol, 87% yield). ^{1}H NMR (benzene-d_6, 600 MHz): δ 48.80 (s, 2 H), 31.55 (s, 2 H), 23.34 (s, 2 H), 17.16 (s, 2 H), 14.48 (s, 1 H), 13.16 (s, 6 H, $CNCMe_2CH_2O$), 12.83 (s, 1 H), −40.00 (s, 18 H, $CNCMe_2CH_2O$). ^{11}B NMR (benzene-d_6, 128 MHz): δ 83.6. IR (KBr, cm^{-1}): *v* 3074 (w), 3045 (w), 2965 (m), 2927 (m), 2893 (m), 2870 (m), 1589 (s, ν_{CN}), 1536 (m, ν_{CN}), 1496 (m), 1462 (m), 1408 (m), 1368 (m), 1352 (m), 1273 (m), 1197 (m), 1159 (m), 1101 (m), 1069 (m), 1025 (m), 962 (m), 949 (m). UV-vis (THF): λ_{max} = 587 (ε: 157 M^{-1} cm^{-1}). μ_{eff}(benzene-d_6) = 4.6(2)μ_B. Anal. calcd for $C_{28}H_{34}BCoN_3O_5$: C, 59.81; H, 6.09; N, 7.47. Found: C, 59.44; H, 6.03; N, 6.46. Mp 238–240 °C.

To^{M}CoO$_2$CEt (16). To^{M}CoEt (0.029 g, 0.062 mmol) was dissolved in toluene (2 mL), the headspace was removed *in vacuo*, and then CO (1 atm) was introduced. An immediate color change from green to orange was observed. Evacuation of CO followed by introduction of O_2 (1 atm) resulted in a color change from orange to purple. Toluene was evaporated *in vacuo* to afford To^{M}CoO$_2$CEt as a purple solid (0.024 g, 0.047 mmol, 76% yield). X-ray quality crystals were obtained from pentane cooled to −40 °C. ^{1}H NMR (benzene-d_6, 600 MHz): δ 35.16 (s, 4 H), 33.81 (s, 2 H, C_6H_5), 18.05 (s, 2 H, C_6H_5), 15.20 (s, 1 H, C_6H_5), 12.32 (s, 6 H, CNCMe$_2$*CH*$_2$O), −43.62 (s, 18 H, CNC*Me*$_2$CH$_2$O). ^{11}B NMR (benzene-d_6, 128 MHz): δ 95.0. IR (KBr, cm^{-1}): ν 3080 (w), 3045 (w), 2965 (m), 2932 (m), 2893 (m), 2874 (m), 1588 (s, ν_{CN}), 1544 (m, ν_{CN}), 1466 (m), 1437 (m), 1387 (w), 1369 (m), 1352 (m), 1276 (m), 1199 (m), 1160 (m), 1074 (w), 1027 (w), 964 (m), 949 (m). UV-vis (THF): λ_{max} = 584 (ε: 98 M^{-1} cm^{-1}). μ_{eff}(benzene-d_6) = 4.8(2)μ_B. Anal. calcd for $C_{24}H_{34}BCoN_3O_5$: C, 56.05; H, 6.66; N, 8.17. Found: C, 56.25; H, 6.46; N, 8.02. Mp 174–176 °C.

To^{M}CoO$_2$C^{n}Bu (17). To^{M}Co^{n}Bu (0.030 g, 0.060 mmol) was dissolved in toluene (2 mL), the headspace was removed *in vacuo*, and then CO (1 atm) was introduced. An immediate color change from green to orange was observed. Evacuation of CO followed by introduction of O_2 (1 atm) resulted in a color change from orange to purple. Toluene was evaporated *in vacuo* to afford To^{M}CoO$_2$C^{n}Bu as a purple solid (0.032 g, 0.059 mmol, 98% yield). X-ray quality crystals were obtained from pentane cooled to −40 °C. ^{1}H NMR (benzene-d_6, 600 MHz): δ 161.09 (s, 2 H, O$_2$C*CH*$_2$CH$_2$CH$_2$CH$_3$), 34.53 (s, 2 H, O$_2$C(*CH*$_2$)$_3$CH$_3$), 33.72 (s, 2 H, O$_2$C(*CH*$_2$)$_3$CH$_3$), 19.24 (s, 2 H, C_6H_5), 17.93 (s, 2 H, C_6H_5), 15.08 (s, 1 H, *p*-C_6H_5), 12.27 (s, 6 H, CNCMe$_2$*CH*$_2$O), 10.83 (s, 3 H,

$O_2C(CH_2)_3CH_3$), −43.55 (s, 18 H, $CNCMe_2CH_2O$). ^{11}B NMR (benzene-d_6, 128 MHz): δ 95. IR (KBr, cm^{-1}): ν 3079 (w), 3055 (w), 2963 (m), 2930 (m), 2893 (m), 2871 (m), 1595 (s, ν_{CN}), 1540 (m, ν_{CN}), 1498 (w), 1461 (m), 1437 (m), 1385 (m), 1365 (m), 1355 (m), 1316 (w), 1274 (m), 1107 (w), 1024 (w), 956 (s). UV-vis (THF): λ_{max} = 584 (ε: 101 M^{-1} cm^{-1}). μ_{eff}(benzene-d_6) = 4.3(2)μ_B. Anal. calcd for $C_{26}H_{38}BCoN_3O_5$: C, 57.58; H, 7.06; N, 7.75. Found: C, 56.47; H, 7.16; N, 7.43. Mp 197–199 °C (Tables 3 and 4).

Table 3. Summary of single crystal X-ray diffraction data for cobalt hydrocarbyl compounds **1–5**

Compound	To^MCoCH_2Ph	$To^MCoCH_2SiMe_3$	To^MCoPh	To^MCoEt	To^MCo^nBu
Compound label	**1**	**2**	**3**	**4**	**5**
Chemical formula	$C_{28}H_{36}BCoN_3O_3$	$C_{25}H_{40}BCoN_3O_3Si$	$C_{27}H_{34}BCoN_3O_3$,C_7H_8	$C_{23}H_{35}BCoN_3O_3$	$C_{25}H_{38}BCoN_3O_3$
CCDC	1845865	1845870	1845864	1845869	1845866
Crystal system	Monoclinic	Monoclinic	Triclinic	Monoclinic	Monoclinic
a	14.3233(7)	12.2663(6)	11.2319(9)	11.683(2)	13.592(2)
b	13.3449(6)	14.2328(7)	11.442(1)	13.302(3)	11.081(1)
c	15.9647(7)	42.322(2)	14.056(1)	16.168(3)	17.801(2)
α	90	90	88.211(2)	90	90
β	114.139(1)	90.904(1)	87.338(2)	93.68(3)	95.162(2)
γ	90	90	63.393(1)	90	90
Volume	2784.7(2)	7448.0(6)	1613.33	2507.4(9)	2670.1(6)
Space group	$P2_1/c$	$P2_1/n$	$P\bar{1}$	$P2_1/c$	$P2_1/c$
Z	4	8	2	4	4
Reflections	7191	19 203	6545	2627	6888
R	3.17	7.51	4.82	3.17	6.15

Table 4. Summary of single crystal X-ray diffraction data for cobalt alkoxyketone **7d**, acyl carbonyl **10**, and carboxylate compounds **13**, **15–17**

Compound	$To^MCo\{\kappa^2$-$OCBn_2C(=O)Bn\}$	$To^MCo\{C(=O)Et\}CO$	$To^MCoO_2CCH_2Ph$	To^MCoO_2CPh	To^MCoO_2CEt	$To^MCoO_2C^nBu$
Compound label	**7d**	**10**	**13**	**15**	**16**	**17**
Chemical formula	$C_{44}H_{50}BCoN_3O_5$,C_5H_{12}	$C_{25}H_{34}BCoN_3O_5$, $(C_5H_{12})_{0.5}$	$C_{29}H_{36}BCoN_3O_5$	$C_{28}H_{34}BCoN_3O_5$	$C_{24}H_{34}BCoN_3O_5$	$C_{26}H_{38}BCoN_3O_5$
CCDC	1845867	1845874	1845871	1845868	1845872	1845873
Crystal system	Monoclinic	Triclinic	Triclinic	Triclinic	Monoclinic	Triclinic
a	10.051(8)	10.1610(8)	12.233(3)	10.3916(9)	14.271(3)	10.8101(6)
b	20.29(2)	10.5368(9)	14.313(4)	12.2557(9)	23.235(5)	11.5931(7)
c	23.00(2)	13.713(1)	17.118(5)	13.357(1)	15.881(3)	13.7312(8)
α	90	89.764(2)	74.05(2)	94.681(7)	90	90.193(3)
β	100.73(1)	78.934(2)	80.17(4)	110.553(6)	99.79(3)	112.684(2)
γ	90	81.773(2)	87.18(2)	112.444(5)	90	114.132(2)
Volume	4627(6)	1425.6(2)	2840(1)	1425.7(2)	5189(2)	1422.2(2)
Space group	$P2_1/c$	$P\bar{1}$	$P\bar{1}$	$P\bar{1}$	$P2_1/c$	$P\bar{1}$
Z	4	2	4	2	8	2
Reflections	5048	5032	7979	4038	6317	7665
R	3.9	4.62	4.52	4.82	6.63	3.85

Computational Methods

Density Functional Theory (DFT) optimizations were performed using NWChem[38] on **1-calc**, **6-calc**, **10c-calc**, **12a-calc**, **12c-cal**, and To^{M}CoCl-calc using the PBE0 hybrid functional,[20] the 6-311+G* basis for first and second row elements,[39] and the Stuttgart RSC 1997 effective core potential for cobalt.[21] Single-point energy calculations were also performed on both the high-spin and low-spin configurations to determine the lowest energy spin state for each structure. DFT Hessians were performed on **6-calc**, **12a-calc**, and **12c-calc** to compute vibrational frequencies for comparison with experiment. A Time-Dependent DFT (TDDFT) calculation using implicit solvation was initially performed to calculate excited states for **6-calc**,[40] but it was determined that a more robust method allowing for multiple electronic configurations was needed due to missing excitations in the results. Gas-phase configuration interaction (CI) singles calculations were performed using the GAMESS quantum chemistry package on **6-calc** and To^{M}CoCl-calc to compute the first 25 excited states for each structure.[41]

Acknowledgements

This research was supported by the U.S. Department of Energy, Office of Basic Energy Sciences, Division of Chemical Sciences, Geosciences, and Biosciences through the Ames Laboratory Catalysis and Chemical Physics programs. The Ames Laboratory is operated for the U.S. Department of Energy by Iowa State University under Contract No. DE-AC02- 07CH11358.

References

1. Q. Liu, H. Zhang and A. Lei, *Angew. Chem., Int. Ed*., **2011**, 50, 10788–10799.

2. D. J. Díaz, A. K. Darko and L. McElwee-White, *Eur. J. Org. Chem*., **2007**, 4453–4465.

3. S. W. Ragsdale and H. G. Wood, *J. Biol. Chem*., **1985**, 260, 3970–3977.

4. P. A. Lindahl, *J. Biol. Inorg. Chem*., **2004**, 9, 516–524.

5. T. C. Harrop and P. K. Mascharak, *Coord. Chem. Rev.,* **2005**, 249, 3007–3024.

6. S. W. Ragsdale, *Chem. Rev.*, **2006**, 106, 3317–3337.

7. S. W. Ragsdale and E. Pierce, *Biochim. Biophys. Acta, Proteins Proteomics*, **2008**, 1784, 1873–1898.

8. A. Haynes, in *Adv. Catal*, ed. B. C. Gates and H. Knözinger, Academic Press, **2010**, vol. 53, pp. 1–45.

9. S. S. Stahl, *Angew. Chem., Int. Ed*., **2004**, 43, 3400–3420.

10. N. Shirasawa, M. Akita, S. Hikichi and Y. Moro-oka, *Chem. Commun*., **1999**, 417–418.

11. N. Shirasawa, T. T. Nguyet, S. Hikichi, Y. Moro-oka and M. Akita, *Organometallics*, **2001**, 20, 3582–3598.

12. J. D. Jewson, L. M. Liable-Sands, G. P. A. Yap, A. L. Rheingold and K. H. Theopold, *Organometallics*, **1999**, 18, 300–305.

13. J. L. Kisko, T. Hascall and G. Parkin, *J. Am. Chem. Soc*.,**1998**, 120, 10561–10562.

14. A. Kunishita, T. L. Gianetti and J. Arnold, *Organometallics*, **2012**, 31, 372–380.

15. R. R. Reinig, E. L. Fought, A. Ellern, T. L. Windus and A. D. Sadow*, Chem. Commun.*, **2017**, 53, 11020–11023.

16. R. R. Reinig, D. Mukherjee, Z. B. Weinstein, W. Xie, T. Albright, B. Baird, T. S. Gray, A. Ellern, G. J. Miller, A. H. Winter, S. L. Bud'ko and A. D. Sadow, *Eur. J. Inorg. Chem*., **2016**, 2486–2494.

17. S. Yoshimitsu, S. Hikichi and M. Akita, *Organometallics*, **2002**, 21, 3762–3773.

18. P. J. Schebler, B. S. Mandimutsira, C. G. Riordan, L. M. Liable-Sands, C. D. Incarvito and A. L. Rheingold, *J. Am. Chem. Soc*., **2001**, 123, 331–332.

19. J. A. DuPont, M. B. Coxey, P. J. Schebler, C. D. Incarvito, W. G. Dougherty, G. P. A. Yap, A. L. Rheingold and C. G. Riordan, *Organometallics*, **2007**, 26, 971–979.

20. J. P. Perdew, M. Ernzerhof and K. Burke, *J. Chem. Phys*., **1996**, 105, 9982–9985.

21. M. Dolg, H. Stoll, H. Preuss and R. M. Pitzer, *J. Phys. Chem*., **1993**, 97, 5852–5859.

22. L. Yang, D. R. Powell and R. P. Houser, *Dalton Trans*., **2007**, 955–964.

23. R. S. Drago, *Physical methods for chemists*, Saunders College Pub., Ft. Worth, 2nd edn, **1992**.

24. J. F. Dunne, D. B. Fulton, A. Ellern and A. D. Sadow, *J. Am. Chem. Soc*., **2010**, 132, 17680–17683.

25. D. Mukherjee, R. R. Thompson, A. Ellern and A. D. Sadow, *ACS Catal*., **2011**, 698–702.

26. S. M. Bellows, T. R. Cundari and P. L. Holland, *Organometallics*, **2013**, 32, 4741–4751.

27. E. K. Barefield, D. H. Busch and S. M. Nelson, *Q. Rev., Chem. Soc*., **1968**, 22, 457–498.

28. A. W. Addison, T. N. Rao, J. Reedijk, J. van Rijn and G. C. Verschoor, J. Chem. Soc., *Dalton Trans*., **1984**, 1349–1356.

29. J. L. Detrich, R. Konečný, W. M. Vetter, D. Doren, A. L. Rheingold and K. H. Theopold, *J. Am. Chem. Soc*., **1996**, 118, 1703–1712.

30. J. L. Detrich, O. M. Reinaud, A. L. Rheingold and K. H. Theopold, *J. Am. Chem. Soc*., **1995**, 117, 11745–11748.

31. F. E. Jacobsen, R. M. Breece, W. K. Myers, D. L. Tierney and S. M. Cohen, *Inorg. Chem*., **2006**, 45, 7306–7315.

32. F. Lu, A. L. Rheingold and J. S. Miller, *Chem. – Eur. J.*, **2013**, 19, 14795–14797.

33. H. S. Ahn, T. C. Davenport and T. D. Tilley, *Chem. Commun*., **2014**, 50, 3834–3837.

34. D. Seyferth, R. M. Weinstein, R. C. Hui, W. L. Wang and C. M. Archer, *J. Org. Chem*., **1992**, 57, 5620–5629.

35. S. Harada, T. Taguchi, N. Tabuchi, K. Narita and Y. Hanzawa, *Angew. Chem., Int. Ed*., **1998**, 37, 1696–1698.

36. P. T. Wolczanski and J. E. Bercaw, *Acc. Chem. Res*., **1980**, 13, 121–127.

37. G. R. Fulmer, A. J. M. Miller, N. H. Sherden, H. E. Gottlieb, A. Nudelman, B. M. Stoltz, J. E. Bercaw and K. I. Goldberg, *Organometallics*, **2010**, 29, 2176–2179.

38. M. Valiev, E. J. Bylaska, N. Govind, K. Kowalski, T. P. Straatsma, H. J. J. Van Dam, D. Wang, J. Nieplocha, E. Apra, T. L. Windus and W. A. de Jong*, Comput. Phys. Commun*., **2010**, 181, 1477–1489.

39. R. Krishnan, J. S. Binkley, R. Seeger and J. A. Pople, *J. Chem. Phys*., **1980**, 72, 650–654.

40. A. Klamt and G. Schuurmann, *J. Chem. Soc*., Perkin Trans., **1993**, 799–805.

41. M. W. Schmidt, K. K. Baldridge, J. A. Boatz, S. T. Elbert, M. S. Gordon, J. H. Jensen, S. Koseki, N. Matsunaga, K. A. Nguyen, S. Su, T. L. Windus, M. Dupuis and J. A. Montgomery, *J. Comput. Chem*., **1993**, 14, 1347–1363.

GENERAL CONCLUSIONS

In the first of three computational studies, the power consumption characteristics of the three most common implementations of MP2 within the NWChem software package were examined. On two different Intel microarchitectures, multiple DVFS strategies were deployed in an attempt to reduce energy consumption of an algorithm with minimal performance losses. Both processor and memory frequency scaling were implemented with a limited set of available frequencies. Energy savings as high as 10% were observed with 3-10% drops in performance. With these results more finely tuned strategies should be explored, taking advantage of a wider range of frequencies.

Following this analysis of the power consumption habits of the different MP2 implementations, a pair of computational studies were performed to evaluate the effects of oversubscription on the semi-direct MP2 energy and gradient algorithms. Using one node, oversubscription was used on both Intel and AMD platforms with different MPI implementations testing a wide range of molecular shapes and sizes. The same Intel platform was also used evaluate the effects of oversubscription when using multiple nodes. Using oversubscription in conjunction with semi-direct MP2 algorithms on both single and multiple nodes resulted in significant energy savings of up to 20% with the additional benefit of dramatically reducing the time to solution. Time savings of up to 45% were observed for the semi-direct MP2 energy and up to 15% for the semi-direct MP2 gradient. These significant improvements in performance can be attributed to more efficient use of the CPUs throughout the molecular integral transformations, eliminating much of the lag time during extended periods of I/O.

Collaboration between the various disciplines of chemistry is necessary to obtain a more complete picture of the chemical processes being studied. Several collaborative works involving computational and experimental chemists are presented. In the first, electronic structure calculations and molecular electrostatic potentials provided understanding for the highly regioselective products of a Diels-Alder reaction. In another organic collaboration, NMR calculations corroborated experimental findings, and optimized geometries provided a structural basis for the chemical shifts observed. In another extensive study of the 2D NMR characterization of silicon nanocrystals, several crystal faces were constructed and calculated NMR shielding values reinforced experimental findings. Finally, in a pair of works involving organocobalt complexes, computational analyses provided structural analysis, vibrational frequencies, and configuration interaction singles excited states for the identification of previously unidentified UV-Vis absorption peaks.